Development of an Apparatus for a Strontium Optical Lattice Optical Frequency Standard

Ian Robert Hill
MSci, ARCS, Physics, Imperial College London, 2007

Department of Physics

Imperial College London

A thesis submitted in partial fulfilment of
the requirements for the degree of

Doctor of Philosophy

June, 2012

Declaration

I hereby declare that the work presented here as my own is my own, and in all other cases appropriate references are given.

Abstract

Hill, Ian R. (PhD. Physics)
Development of an Apparatus for a Strontium Optical Lattice Optical Frequency Standard

Accurate time keeping is critical to the function and advancement of many human endeavours. Atomic clocks based on a microwave transition in atomic Cs have served as primary frequency standards to realise the SI second since their formal adoption in 1967. State-of-the-art, laser cooled, Cs fountains now routinely operate with fractional frequency uncertainties below the 10^{-15} level in laboratories throughout the world. Over the last decade, efforts to build frequency standards based on optical transitions have come to fruition and potential inaccuracies below the 10^{-17} level have been demonstrated. Such standards point to the future of time keeping and much development is being pursued to realise the potential of these 'next generation' optical clocks. One such approach, on which this work focusses, relies on a 'magic' wavelength optical lattice trap to provide (almost) Doppler- and recoil-free confinement of atoms during clock interrogation. At this 'magic' wavelength, light induced perturbation of the clock states is equal and so cancels precisely. This thesis describes the design and implementation of an optical lattice frequency standard apparatus based on ^{88}Sr held in a 1D optical lattice. A review of the development of atomic frequency metrology is given from a historical viewpoint and the technology and limitations of current methods discussed. To tackle the blackbody radiation shift, which currently presents the greatest limitation to the Sr lattice clock, imposing at the 10^{-16} level, a scheme to measure the blackbody radiation shift coefficient at the 10^{-17} level is developed. Techniques to laser cool and trap atomic strontium are described and the implementation detailed. All laser systems required for clock operation are described including the design and implementation of extended-cavity diode lasers for precision spectroscopy. Details relevant to the eventual operation of the apparatus are discussed.

To my loving parents Rennie and Elizabeth,
"Back off man, I'm a scientist!".

Acknowledgements

Acknowledging in isolation all those who have steered me towards the successful completion my Ph.D. thesis is a difficult task in itself. As the son of an electronics technician I was exposed to a host of 'cool stuff' from a very early age, or what my Mam often refers to as "a house full of junk". After mastering cardboard and Sellotape construction methods I graduated to Technic Lego where I learnt much of my early trade. Throughout my school days my Dad took me radio controlled car racing every week which served as a great playground for my growing interest in physics and engineering. I benefited greatly from the enthusiasm and ambition of several great teachers, such as my middle school DT teacher Mr Crawford and in later years my high school physics teacher Mr Thompson and maths teacher Mrs Heaton. In particular, my headmaster Andrew Wright, an all round great guy, provided my first great role model of a physicist.

During my time as an undergraduate at Imperial College London my interest in the area of atomic physics was born, which I first pursued as a MSci student within the QOLS group under the guidance of Jon Marangos. I owe identification of my thesis project to my eventual academic supervisor Ben Sauer who has subsequently provided an efficient, stress free interface to the mysterious world of college administration. My thesis would not of course have been possible without the opportunity provided by Patrick Gill who welcomed me into the Time and Frequency group at NPL, where the work of this thesis was carried out.

Throughout my time at NPL I benefited greatly from my interaction with several talented scientists. Yuri Ovchinnikov, with whom I have enjoyed many great (and humorous) discussions, has played an essential role in the development of my laser cooling knowledge and provided some great ideas for the lab. Guido Wilpers, whose dedicated and thorough approach to science (and in particular vacuum technology!) set a great example to myself as a young student and whose company often resulted in stimulating and enjoyable discussions. Likewise, I thank Stephen Webster for his expertly considered responses to my numerous questions on laser stabilisation, which were key to the development of my understanding in this area. I thank also Alastair Sinclair, Rachel Godan,

Geoffrey Barwood, Hugh Klein, Helen Margolis, and Christopher Edwards who have provided help and support on numerous occasions.

My work could not have been accomplished without the efforts of others and I thank Paul Stevens and Keith Burgon and the machinists at the NPL Engineering Workshop for providing a fantastic service. It was really a joy to see drawings brought to life in the finest manner. Producing electronic devices has been a large part of setting up the NPL Strontium Lattice lab, a task in itself, and would have been all the more of a challenge without the generous assistance of Barry Thomas and Pravin Patel.

I have had the pleasure of getting to know fellow graduate students Liz Bridge, Ben Parker, and Steven King, with whom I shared many hours of entertaining discussion about physics amongst other things. In particular I thank my lab partner Liz Bridge who toughed it out with me throughout the good and the bad, proving two minds are better than one, and has grown to be a great friend. I thank of course my industrial supervisor Anne Curtis, the instigator of 'Team Lattice', who has supported me throughout my time at NPL and has always acted with my best interests at heart. Thank you!

I reserve a very special acknowledgement to my family. Growing up, I have had the benefit of following in the path of my talented elder sister Jennifer Hill, whose abilities have created great expectations for my own. My parents, Rennie and Elizabeth Hill, have guided and supported me in my pursuit of education and always encouraged me to "just do it". Through their example I have learned the value of honest hard work owe my well-being and much of who I am and what I may become to them (that's right, it's your fault!). During my time in London I was lucky enough to acquire a second family; Amy, Paul, and Luisa Lewis, who welcomed me into their home and looked after me for most part of my Ph.D..

Finally, my greatest discovery throughout my time as a student in London has been my first love Amy Lewis. It has been a valuable journey and I'm glad we took it together!

Contents

Contents 6

List of Tables 9

List of Figures 10

Nomenclature 11

1 Introduction to the Measurement of Time 12
- 1.1 A Brief History of Timekeeping . . . 12
  - 1.1.1 The Birth of Atomic Time . . . 12
  - 1.1.2 Perfecting the Second . . . 16
- 1.2 Clocks in Context . . . 23
- 1.3 Thesis Outline . . . 24

2 Optical Frequency Standards 25
- 2.1 Better Clocks Q Up . . . 25
  - 2.1.1 Clock Characteristics . . . 26
  - 2.1.2 Narrowing the 'Line' . . . 27
- 2.2 A Clock in Pieces . . . 29
  - 2.2.1 Oscillator: The Clock Laser . . . 29
  - 2.2.2 Reference . . . 31
  - 2.2.3 Frequency Counter . . . 35
- 2.3 Single Ion Clocks: Quality over Quantity . . . 35
  - 2.3.1 Doppler- and Recoil-Free Spectroscopy . . . 36
  - 2.3.2 Current Status of Ion Optical Clocks . . . 37
- 2.4 Optical Lattice Clocks: Quality and Quantity . . . 40
  - 2.4.1 Ballistic Clock . . . 40
  - 2.4.2 Light-shift cancellation at the "magic-wavelength" . . . 41
  - 2.4.3 Optical lattice trap and higher order effects . . . 44
  - 2.4.4 Current Status of Neutral Atom Optical Clocks . . . 48
- 2.5 Conclusion . . . 55

3 A Strontium Optical Lattice Clock **56**
3.1 Electronic atomic structure . . . 56
3.1.1 Strontium . . . 59
3.2 A Strontium Source . . . 59
3.2.1 Vapour source . . . 60
3.2.2 Atomic beam apparatus . . . 62
3.3 Laser Cooling Neutral Atoms . . . 69
3.3.1 Atom-Light Interaction: The Basics . . . 69
3.3.2 Velocity dependent scattering force . . . 70
3.3.3 Optical Molasses . . . 71
3.3.4 Compensation of the Doppler shift . . . 73
3.3.5 Magneto-optical trap (MOT) . . . 76
3.4 Laser Cooling Divalent Atoms . . . 80
3.5 $^1S_0$ – $^1P_1$: Initial cooling and trapping Sr . . . 80
3.5.1 Blue MOT . . . 80
3.5.2 Repumping schemes . . . 84
3.5.3 Experimental details: Laser sources . . . 85
3.5.4 Experimental details: Apparatus . . . 92
3.5.5 Experimental results of the first cooling stage . . . 96
3.6 $^1S_0$ – $^3P_1$: Second-stage cooling Sr . . . 99
3.6.1 Red MOT . . . 99
3.6.2 Experimental details: 689 nm light source . . . 99
3.7 One-Dimensional Optical Lattice Trap . . . 103
3.7.1 Dipole force . . . 103
3.7.2 Lattice Potential . . . 106
3.7.3 Spectroscopic effects of the trapping potential . . . 109
3.7.4 813 nm laser source . . . 110
3.8 The $^1S_0$ – $^3P_0$ Clock Transition: Allowing the forbidden . . . 110
3.8.1 Magnetically Induced Spectroscopy . . . 111
3.8.2 BBR Quenching . . . 114

4 Diode Lasers for Precision Spectroscopy **118**
4.1 Extended Cavity Diode Lasers . . . 118
4.1.1 Littrow Grating Configuration . . . 120
4.1.2 Synchronous Tuning of the Extended Cavity . . . 121
4.1.3 Extended Cavity Opto-Mechanical Design . . . 124
4.1.4 Environmental Considerations . . . 127
4.1.5 Characterisation of the ECDL . . . 134

5 Atomic Polarisability: Magic wavelengths, probe light shifts, and the BBR shift **143**

5.1 Calculation of the ac Dipole Polarisability 143

5.2 The Dynamic Stark Shift in a BBR Field 148

5.3 Measurement of the BBR shift 156

6 Conclusions and Outlook **163**

Appendix A **165**

.1 Flow characteristics 165

.1.1 Beam flux and angular spread 165

.1.2 Beam velocity 170

References **171**

List of Tables

2.1 Q comparison of ion optical clocks . . . 38
2.2 Ion optical clock status as of the year 2010 . . . 39
2.3 Neutral-atom optical clocks current status as of mid 2011 . . . 48
2.4 Q comparison of neutral atom optical clock candidates . . . 50
2.5 Comparison of BBR-induced shifts of the $^1S_0 \rightarrow ^3P_0$ clock transition in neutral atom optical clocks. . . . 53

3.1 Sr transition properties. . . . 57
3.2 Stable isotopes of Sr and their natural abundance. . . . 59
3.3 Properties of Sr cooling transitions for divalent neutral atoms. . . . 81
3.4 Laser cooling properties for first and second stage cooling transitions in Sr. 81
3.5 Isotope shifts of the $5s^2\,^1S_0 \rightarrow 5s5p\,^1P_1$ transition . . . 85
3.6 MIS example parameters . . . 115
3.7 Branching terms of relevant to the BBR quenching of metastable states. . . . 116

4.1 ECDL parameters . . . 128
4.2 ECDL tuning range . . . 136

5.1 Parameters for calculation of the clock state polarisabilities. . . . 149
5.2 Individual contributions (ICs) to the ground and excited clock state polarisabilities. . . . 151
5.3 Calculated polarisabilities at key optical wavelengths. . . . 155
5.4 Lattice trapping parameters . . . 158

List of Figures

1.1 Early Cs Thermal-Beam Frequency Standard Apparatus 15
1.2 Atomic fountain apparatus 21

2.1 Rulers 26
2.2 A High-Performance Clock 30
2.3 Optical Cavities for Highly-Stabilised Lasers 31
2.4 Electron Shelving Detection Scheme 34
2.5 Lamb-Dicke Confinement 37
2.6 Ballistic Clock Interrogation 41
2.7 Stark-Free Trapping at the Magic-Wavelength 43
2.8 EM Standing Wave 46
2.9 Blue Detuned Lattice Potential 48
2.10 ^{87}Sr Clock Frequency Measurement Comparison 49
2.11 Looking into the oven 54

3.1 Strontium Energy Level Scheme 58
3.2 Vapour Pressures 60
3.3 NPL Sr oven 65
3.4 Atomic beam velocity distribution 66
3.5 Atomic beam flux 68
3.6 Optical Molasses 72
3.7 Mechanism of a magneto-optical trap 76
3.8 Particle trajectories in 1D MOT 77
3.9 3D MOT configuration 78
3.10 Capture velocity for various MOT parameters 79
3.11 Reduced Sr energy level scheme 82
3.12 Fluorescence of $5s^2\,{}^1S_0 \rightarrow 5s5p\,{}^1P_1$ line measured in a well-collimated Sr atomic beam 86
3.13 461 nm light source 88
3.14 Four wavelength locking scheme 93
3.15 Vacuum Apparatus 95

3.16 MOT Isotope Scan . . . 97
3.17 Second-Stage Cooling . . . 98
3.18 689 nm Light Source . . . 100
3.19 1D Optical Lattice Potential . . . 108
3.20 Trap Anharmonicity . . . 110
3.21 State mixing . . . 112
3.22 Magnetic induced spectroscopy . . . 115
3.23 BBR quenching of metastable states . . . 117

4.1 Littrow and Littman ECDL configurations . . . 119
4.2 Simplified Littrow geometry . . . 124
4.3 The collimator assembly. . . . 125
4.4 Pictures of Assembled ECDLs . . . 129
4.5 ECDLs . . . 130
4.6 The loop filter . . . 132
4.7 In-Loop Temperature Instability . . . 134
4.8 Compensating the system response. . . . 135
4.9 Determination of the clock ECDL linewidth . . . 136
4.10 Laser Stabilisation Scheme . . . 137
4.11 Cavity Transmission Fringe . . . 138
4.12 ECDL and Cavity Transfer Functions . . . 139
4.13 System, Loop Filter, and Total Transfer Functions . . . 140
4.14 Laser Stabilisation Loop Filter . . . 141

5.1 Atomic dynamic polarisabilities . . . 150
5.2 BBR shift. . . . 154
5.3 Experiment apparatus for measurement of the BBR shift. . . . 157
5.4 Optics schematic of transport and magic lattices. . . . 159
5.5 Transport optical lattice potential. . . . 160

1 Sr collisional mean free path versus source temperature . . . 166

1

Introduction to the Measurement of Time

"We are measuring something with extreme precision...
...but who know's what?" – Tom O'Brian, Chief of the Time and Frequency Division, NIST.

1.1 A Brief History of Timekeeping

For millennia mankind has puzzled over the concept of time, pursued with great interest its measure, and endeavoured to use its passing wisely. The apparent predictable nature of time, which is so readily observed within the periodic mechanisms of our solar system and beyond, has played a key role in the success of civilisation. Through tracking the motion of celestial bodies in the sky, such as star constellations, the sun, and the moon and its phases, time-scales of years, months, days, or even hours have been maintained allowing for the organisation and synchronisation of events to take place within society. However, an ever increasingly complex society demands an ever increasing division of time and devices to count smaller intervals of time have been and continue to be developed.

1.1.1 The Birth of Atomic Time

For a great many years the duration of the mean solar day defined a universal time scale (UT) where 1/86 400 of a mean solar day represented 1 mean solar second. Thought at one time to be invariable, this provided a reference for mechanical clocks serving as time interval standards for both civil and scientific duties well into the early part of the 20th century. As the precision of astronomical observation improved, it became apparent that the rate of the Earth's rotation fluctuated on a number of characteristic time scales, deviating from the mean by as much as one second in a year ($\Delta T/T \sim 3 \times 10^{-8}$).

By the 1900s it was generally accepted that a long-term deceleration of the Earth's

angular velocity existed due to tidal friction. In addition to a periodic nutation, stellar observations revealed the effects of an irregular polar motion, unpredictably shifting the Earth's rotation axis. However, it wasn't until the invention of William H. Shortt's dual pendulum clock in 1920, typically losing or gaining no more than 1 second in a year ($\Delta T/T \sim 3 \times 10^{-8}$), that horologists were finally able to perceive the Earth's rotational variation.

A few years later, time-interval standards based on piezoelectric resonances in quartz-crystal oscillators were established, demonstrating fractional frequency instabilities of a few parts in 10^{10}. The development marked a significant step in the use of time interval standards in national laboratories, as now the frequency at which the time interval was generated leapt from a single cycle per second as for the pendulum clock to hundreds of thousands of cycles per second in quartz, allowing time interval standards to operate simultaneously as standards of frequency.

Discrepancies evident between astronomical observation (using UT based on the mean solar day) and the internationally agreed ephemerides, derived from celestial mechanics, led the International Astronomical Union (IAU), in 1952, to recommend the second of ephemeris time (ET), defined by the orbital motion of the Earth around the Sun, be used as the basis of uniform astronomical time. In practice, ET was more conveniently obtained by observing the orbit of the Moon around the Earth. A dual-rate moon position camera, designed and operated by Dr. William Markowitz, Director of the Time Division at the US Naval Observatory (USNO), enabled precise observation of the epoch of a lunar ephemeris in terms of UT. Photographic zenith tubes (PZT), operated at the USNO and Richmond Naval Air Base, provided Markowitz with a version of UT to which the comparisons with ET at a number of epochs were made [1]. The difference, quantified by $\Delta T = ET - UT$, revealed a lag in UT with a year upon year increase of approximately 0.17 s owing to a decline in the Earths rotation period [2]. The standard second of UT was no longer adequate.

Shown to offer greater stability, the International Committee of Weights and Measures (CIPM), in 1956, adopted the second of ET and defined it as the fraction 1/31 556 925.9747 of the tropical year 1900 [3]. This was not especially well received in the field of radio communications due to the necessarily lengthy and tedious practical means of obtaining the unit, which was not directly or easily accessible, and with little prospect for improvement.

As early as 1879 Sir William Thomson (later to become Lord Kelvin) alluded to the use of a mode of vibration intrinsic to a particular element, referring to the strong spectral lines at 589 nm in sodium, to serve as an abundant and universal reference of time. Following on from this idea, in 1945, Isidor Isaac Rabi proposed possibly the first apparatus of an atomic frequency standard. It was to be based on his technique of magnetic resonance spectroscopy [4] applied to the ground state hyperfine microwave transition in caesium[1]

[1]Cs being relatively heavy and with high vapour pressure meant it was relatively easy to produce

in an atomic-beam apparatus, but was not realised for several years. Instead, claim to the first atomic frequency standard was held by Harold Lyons and his 'ammonia clock' at the US National Bureau of Standards (NBS) which was based on the nitrogen inversion transition at 23.870 GHz in the ammonia molecule [5]. It consisted of a quartz-crystal oscillator electronically stabilised to the 'absorption line' of the inversion transition, and while it caused quite a stir at the time, it failed to improve upon quartz-crystal oscillators and in its final revision only achieved a stability of 2 parts in 10^8.

In 1955 at the National Physical Laboratory (NPL) Louis Essen[1] and John V. L. Parry demonstrated the first atomic frequency standard[2] with accuracy exceeding the best astronomical observations, based on the ^{133}Cs microwave ground state hyperfine transition ($|F = 3,\ m_F = 0\rangle \rightarrow |F = 4,\ m_F = 0\rangle$, where F is the vector sum of total angular momentum J and nuclear spin I and m_F is the Zeeman sub-state) [6]. The apparatus exploited Ramsey spectroscopy[3] of a magnetically state selected thermal caesium-beam, with two 'identical' spatially separated 'Ramsey cavities' providing the required separated field excitation to achieve the desired narrow resonance feature of the 'clock' transition [7]. Prior attempts to build an atomic clock using Rabi's atomic beam magnetic resonance technique were thwarted by prohibitively broad resonance features, resulting from a failure to realise in an atomic beam apparatus sufficient length of homogeneous interrogation of the clock transition.

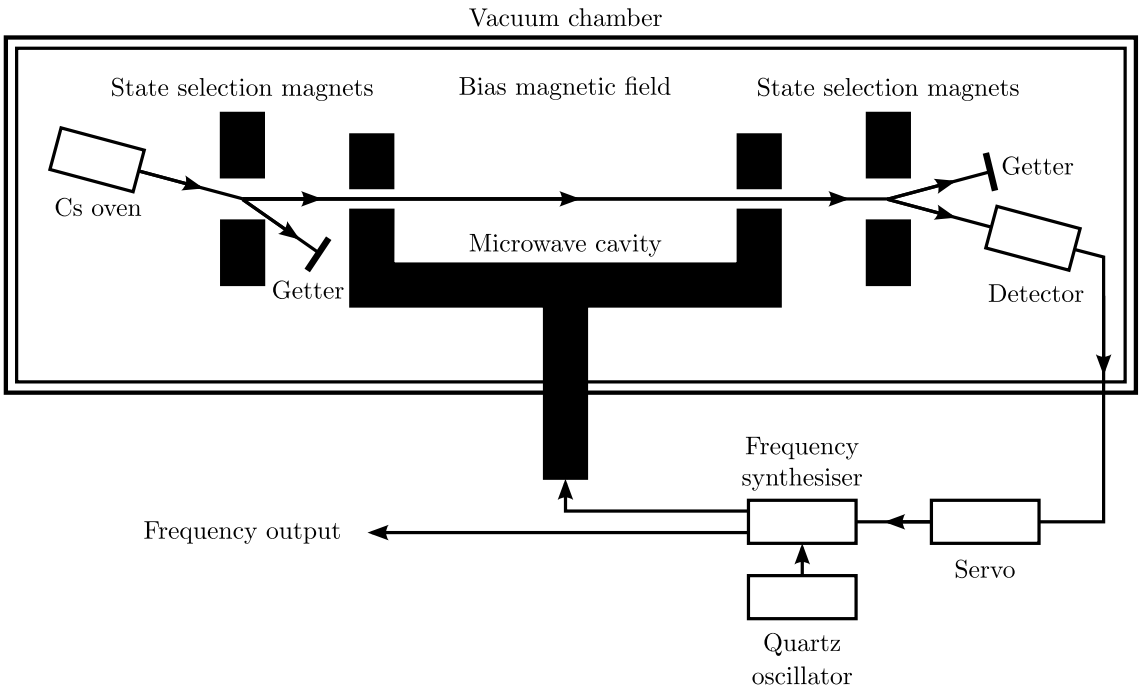
A comprehensive appraisal of systematic frequency biases with reference to an ensemble of Essen ring 'flywheel' oscillators allowed Essen to measure the 'second' of caesium to an accuracy of 1 part in 10^{10}, limited largely by the stability of the flywheel reference over the period of days required to assess the biases [8]. It should be noted that astronomical observations required significantly greater time periods to reach comparable uncertainties. A PZT could resolve UT to an uncertainty approaching 1 part in 10^9 after a month of averaging and further to that some four years would be required to match the precision of the caesium standard.

intense atomic beams with moderate velocities $\sim 130\,\mathrm{m\,s^{-1}}$. The clock transition was also convenient benefiting from its relatively high frequency while still easily accessible with microwave technology.

[1] Essen was already well known for his highly stable piezoelectric quartz-ring oscillators, or Essen rings, as they were known.

[2] A similar standard was simultaneously under development at the NBS but its completion was delayed partly due to it moving labs from Washington to the then new facilities in Boulder.

[3] Here, the atomic ensemble is interrogated by two coherent-field excitations of frequency ω, separated by time T, with duration of each corresponding to a Rabi $\pi/2$ pulse. When tuned to resonance, $\omega = \omega_0$, the first pulse excites the atoms, initially prepared in the ground state, to an equal superposition of the ground and excited states. During time T, the ensemble evolves with frequency ω_0 and develops a phase offset relative to the excitation field of $\Delta\omega T$; $\Delta\omega = (\omega - \omega_0)$. Clearly this is zero for the resonant case and the subsequent $\pi/2$ pulse completes the excitation. Varying ω for a fixed T, or T for a fixed detuning $\Delta\omega$, results in the ensemble acquiring a phase offset relative to the excitation field, such that the projection onto the axis of excitation transition probability shows sinusoidal variation as a function of $\Delta\omega T$. A narrow Ramsey fringe resolution can therefore be achieved for long transit time interactions, independent of the duration of the interrogating pulses. The result is a Ramsey spectrum which consists of many fringes imposed on a Rabi pedestal.



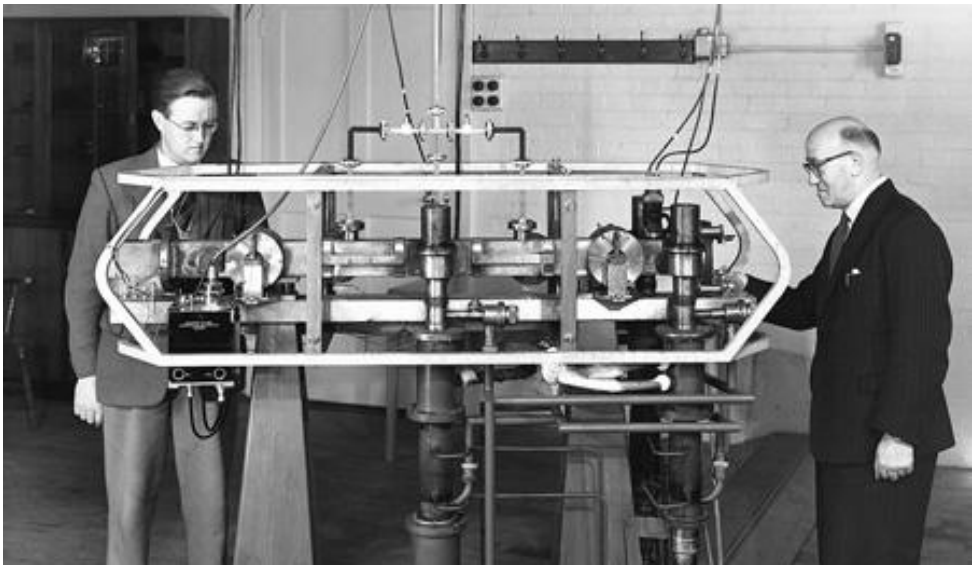


Figure 1.1: **Early Cs Thermal-Beam Frequency Standard Apparatus** - (Top) Schematic of apparatus: An effusive oven source provides a collimated stream of atomic Cs in a mixture of $F = 3$ and $F = 4$ states. State selection occurs by magnetic deflection, with strong field seeking $F = 3$ state atoms guided towards the apparatus centre, and atoms in the weak field seeking state $F = 4$ rejected from the beam. Centre guided atoms experience a two-pulse, spatially separated, Ramsey excitation and the excitation fraction at the exit of the microwave cavity is measured with the aid of a second state selection magnet and hot wire ionising detector. A control loop is used to maintain resonance of the microwave cavity and the atomic frequency is readout directly. (Bottom) The NPL Cs apparatus with Louis Essen (right) and colleague John Parry.

From June 1955 to January 1957 Essen compared the second of UT against that of his caesium standard. Similarly to Markowitz, a suitably agreeable drift in UT of approximately $0.16\,\mathrm{s\,yr^{-2}}$, compared to atomic time (AT), defined in the literature as $\Delta A = AT - UT$, was clearly evident in the data [9]. Collaboration between Essen and Markowitz, detailed in various review papers [10, 11], in which the quantity $\Delta T - \Delta A$ was evaluated (in this way eliminating UT), finally led to a value of the caesium second in terms of the ephemeris second, published in 1958, of $9\,192\,631\,770 \pm 20\,\mathrm{Hz}$ [9]. The uncertainty was largely due to the difficulty associated with obtaining ET. In 1967 at the 13th meeting of the General Conference on Weights and Measures (CGPM) this value was formally adopted as the International Standard (SI) second. An atomic time standard, eventually to be known as International Atomic Time (TAI) – regulated by the International Bureau of Weights and Measures (BIPM) and later adjusted to correspond to proper time at the geoid – was quickly established. Many atomic clocks located worldwide now contribute to TAI which provides the time-interval standard for Coordinated Universal Time (UTC), adjusted to track UT1 (a global realisation of UT) to a convenient degree by the addition or subtraction of a leap second, as recommended by the International Earth Rotation and Reference Systems Service (IERS).

1.1.2 Perfecting the Second

1.1.2.1 Thermal-Beam Frequency Standards

In 1956, Jerrold Zacharias at MIT together with the National Company announced the worlds first commercially available atomic clock (also the first self-contained portable clock), named the Atomichron, which was based on a 200 cm vertical Ramsey cavity design derived from Zacharias's failed earlier work on atomic fountains (see Sec. 1.1.2.2). Over 50 were sold, primarily to the US military and some to metrology laboratories [12]. Subsequently, and with the prospect of a redefinition of the second based on Cs in sight, various universities, national laboratories and scientific industries worked to 'perfect' and miniaturise the technology.

In 1964 Hewlett-Packard released their first in a line of commercially available atomic frequency standards, the HP 5060, which weighed less than 30 kg, with a horizontal Ramsey cavity of only 12.4 cm, and fit into a standard equipment rack. By 1966 the specified accuracy had reached 1 part in 10^{11} making it suitable for use as a primary frequency standard in many calibration and metrology laboratories worldwide. A collaborative effort between Hewlett-Packard and NBS (renamed the National Institute of Standards and Technology or NIST in 1988) saw the development of the NBS-4; the smallest of all NBS built primary frequency standards with a Ramsey cavity of just 52.4 cm [13]. The most recent design iteration, the HP 5071, introduced in 1991, implemented microprocessor control of many of the key operating parameters that could sway the determined frequency,

which when coupled to an improved caesium beam tube increased the specified accuracy to 5 parts in 10^{13} with long-term stability better than 1 part in 10^{14} at 5 days of averaging.

'No-compromise' high performance clocks, built and operated at national laboratories, utilised various combinations of beam velocity and microwave cavity separation, with some laboratories, such as PTB (in Braunschweig, Germany), opting for shorter beam paths $\sim 0.8\,\mathrm{m}$ and slower atomic beams $\sim 90\,\mathrm{m\,s^{-1}}$ and others, for example NIST, SYRTE (in Paris, France), and NICT (in Tokyo, Japan), utilising higher velocity beams $\sim 230\,\mathrm{m\,s^{-1}}$ and longer beam paths $\sim 1.5\,\mathrm{m}$, each with the view to maintaining a long transit time between microwave cavities. While this aided achieving narrow resonance features, various physical effects needed to be addressed to improve the standard's accuracy.

The accuracy of early thermal-beam standards was limited by the uncertainty of the perturbation caused by the quadratic Zeeman effect, which provided the largest of all known frequency shifts. The combination of large state selection fields and the bias field required to separate the magnetic sub-states and define the quantisation axis made the appraisal and control of the shift difficult, with the uncertainty determined by the extent of magnetic field inhomogeneity and imprecise knowledge of the field. A related effect resulting from an overlap in the excitation probability of neighbouring transitions (of differing m_F), termed frequency- or line-pulling, is reduced for a larger Zeeman-splitting of the magnetic sub-states. Later, optical state-preparation schemes removed the need for magnetic state selection, allowing for much improved uniformity of the bias field. Instead of filtering out atoms in unwanted states, atoms are 'optically pumped' by selective population transfer into the desired $m_F = 0$ sub-state of the chosen hyperfine level, depleting population in the unwanted $m_F \neq 0$ sub-states [14]. As no atoms are lost, the atomic beam is prepared in the desired state while retaining the familiar Maxwell-Boltzmann distribution, thereby simplifying the estimation of velocity-related shifts, and with increased atom flux a higher signal-to-noise ratio is achieved. In addition, lower population of unwanted $m_F \neq 0$ states, responsible for line pulling effects, allows for a reduction of the bias field, further reducing the quadratic Zeeman shift.

Two of the largest uncertainties are usually attributed to cavity phase shifts caused by non-ideal physical properties of the Ramsey cavity. The cavity consists of two 'identical' microwave cavities situated at the end zones of a U-shaped waveguide resonator. An asymmetry in the length of the waveguide arms of ΔL introduces a so-called end-to-end phase shift of $\delta\phi = k\Delta L$, resulting in a frequency shift of $\delta\nu = \delta\phi/2\pi T$, where k is the wave-vector of the microwave radiation and T is the transit time between cavities. The shift can be measured by reversing the direction of the beam. For example, the CS2 at PTB was built with an oven and detector at each end so that the direction of beam can be easily reversed without breaking vacuum. They estimated the fractional uncertainty of this shift in CS2 as 1 part in 10^{14} [15]. Phase shifts also arise due to ohmic losses in the microwave cavity where a finite conductivity in the walls of the waveguide leads to

a reduction in the reflected wave compared to the incident wave. This imbalance results in a small travelling wave contribution to the ideal standing wave, producing a spatial variation in the phase of the microwave field, which is larger nearer the cavity walls. The shift experienced by an atom, similar in nature to the Doppler shift, is thus dependent on its transverse position in the beam and for this reason is often termed the distributed cavity phase shift. Ring cavities, where a standing wave split into two opposing travelling waves superimpose to form a standing wave at the interaction region, have successfully acted to reduce the distributed cavity phase shift [16].

Ultimately, velocity related problems inherent to the operation of thermal-beam standards limit the final achievable accuracy of the standard. Finite velocity distributions both transverse and longitudinal to the atomic beam direction act to reduce the coherence of the Ramsey spectroscopy resulting in a 'wash out' of the fringes[1]. Second-order Doppler shifts arising from relativistic time-dilation phenomena are significantly reduced for slow atomic beams, however without sufficient beam collimation much of the signal would be lost. Potentially, increasing the transit time by lengthening the Ramsey cavity would decrease the Ramsey fringe width, but due to difficulties in maintaining a homogeneous magnetic field over a larger extent, and velocity related signal losses, nothing would be gained. The 'best' published accuracy of a caesium-beam standard is of 5 parts in 10^{15} belonging to the NIST-7 apparatus [17], although standards at SYRTE, PTB, NRLM and NICT are very close and in some cases offer greater stability; summerised in the review article by Vanier and Audoin [18].

1.1.2.2 Laser Cooling and the Atomic Fountain

In 1953 Zacharias proposed (unpublished) a novel method of increasing the transit time of atoms in the Ramsey cavity. By launching the atoms vertically against gravity they would follow a ballistic flight path, passing once through a single excitation cavity on the way up and, crucially, the same cavity again some time later on return. Zacharias' fountain promised to eradicate problems associated with end-to-end cavity phase shifts, as each interrogation would take place in the same cavity, and so only distributed cavity phase shifts would remain. However, at the time of conception, techniques to control atomic velocities proved inadequate and his attempts to realise such an experiment were unsuccessful – the flux of returning atoms was insufficient to detect [12].

The advent of laser cooling techniques allowing experimenters to cool and trap atomic vapours at the μK level revived interest in the Zacharias fountain [19]. Detailed analyses were carried out with the view to establishing the fountain as an improved frequency standard, addressing the fundamental problems of the thermal Cs beam apparatus [20, 21].

[1] This is easily understood by considering the conditions required to obtain a π rotation of the pseudo spin vector. Atoms of non-zero transverse velocity experience a first order Doppler shift away from resonance and those with a longitudinal velocity other than the mean result in a spread in transit times through each cavity; both effects leading to non-ideal excitation coherence.

In 1989 the first successful realisation of the Zacharias fountain was demonstrated by Mark Kasevich and co-workers using laser cooled sodium atoms [22]. The atoms were first cooled, to around 1 mK, and held in a magneto optical trap (MOT) consisting of 6 intersecting optical molasses (OM) beams and a magnetic field gradient trap produced using an anti-helmholtz coil pair. The magnetic field was then switched off allowing further cooling by molasses to $\sim 50\,\mu$K corresponding to a velocity of $14\,\mathrm{cm\,s^{-1}}$. An additional upward facing "pushing" beam was used to launch the atomic cloud to a mean vertical velocity of $240\,\mathrm{cm\,s^{-1}}$. A Ramsey fringe linewidth of 2 Hz, corresponding to a flight time of 0.25 s and a peak height above the cavity of 77 mm, was achieved for the clock transition in Na, measured to an accuracy of 1 part in 10^9. With an integration time of 1000 s the central fringe could be resolved to within ± 10 mHz. The measured instability was at 1 part in 10^{10} at 1 s; two orders of magnitude worse than thermal beam standards of the time, the NBS-6 and the commercial Hewlett-Packard 5061B, but clearly demonstrated the potential of the technique.

Meanwhile, Christopher Monroe and Carl Weiman, of JILA and NIST respectively, measured the clock-transition of laser cooled Cs atoms in a vapour cell MOT. The apparatus was compact with just two diffraction grating-stabilised diode lasers operating to cool and optically pump the atoms. Using a MOT/OM configuration, temperatures of $10\,\mu$K were reached after the molasses phase and on completion of optical pumping to the $F = 4, m_F = 0$ excited state atoms were released at an estimated $20\,\mu$K. A single microwave horn was used to provide time-separated Ramsey interrogation of the clock-transition. For the duration of the Ramsey spectroscopy, the MOT was switched off to avoid light induced ac Stark shifts and magnetic field related Zeeman shifts. Without the presence of the trapping fields the atom cloud undergoes ballistic expansion, due to thermally related velocities resulting from the finite temperature of the atoms, and acceleration due to gravity takes place. The fall results in a phase shift of the second interrogation pulse, relative to the first, caused by a slight curvature of the microwave radiation wavefront. Expansion of the atom cloud leads to reduction of the excitation coherence, as in the Cs beam standards, acting to 'wash-out' the pattern of Ramsey fringes. It is therefore necessary to reduce the temperature of the atoms maximally before spectroscopy and avoid any potential heating mechanisms during the process. Nevertheless, in Monroe's and Weiman's experiment, an 8 Hz linewidth and a short-term fractional frequency instability of 6.5 parts in 10^{12} at 1 s was measured [23]. Shortly afterwards André Clairon et al. published results from their caesium fountain [24]. Using similar techniques to prepare and launch the atoms they achieved a linewidth of 2 Hz and instability of 2 parts in 10^{12} at 1 s, at least as good as contemporary thermal beam standards. Fountains were soon being built for use in metrology and by the late 1990's several were operating as primary frequency standards [25–27]. Flight chambers are now typically ~ 1 m with the Ramsey cavity located about half way up providing interaction times of over half a second

corresponding to Ramsey fringe linewidths of $\sim 1\,\mathrm{Hz}$ ($\Delta\nu = 1/2T$), depicted in Fig. 1.2.

With velocity related problems somewhat under control in laser-cooled atomic fountains, the contribution of density related collisional (spin-exchange) shifts, to the uncertainty budget, becomes significant (see for example details in Ref. [26]). The shift may be measured by operating the fountain at various atomic densities and an extrapolation to zero density provides the unperturbed frequency, with some error. To this end, a new state selection technique was developed at SYRTE exploiting the adiabatic rapid passage method allowing preparation of the atomic sample at a repeatable ratio of 1:2 with precision 10^{-3} [28]. However such a method potentially limits the stability of the fountain as time must be spent measuring at two differing frequencies. At NIST the shift has been reduced by cooling the atoms in an extended molasses to give a cigar shaped atom cloud, thereby increasing the volume and decreasing the density while maintaining atom number. Additionally, a lin-perp-lin cooling geometry is adopted as opposed to the conventional σ^+/σ^- molasses, reaching temperatures $< 500\,\mathrm{nK}$, leading to a higher fraction of atoms being detected after the launch. As a result, fewer atoms can be launched to maintain a given signal to noise ratio [29].

Shifts caused by collisions of atoms in the $F = 4$ state have an opposite sign to those in the $F = 3$ state but with different magnitude. By carefully preparing the relative populations of the upper and lower states in the correct proportions it should be possible to cancel the shift [30, 31]. An NPL led collaboration with PTB and NIST confirmed experimentally this result [32]. However, the technique relies on an initial pre-measurement and an assumption that conditions thereafter are unchanged, which at present is not satisfied and so has not yet been implemented in normal operation.

In 1997 theoretical work of Gibble[1] and co-workers predicted a factor of 15 reduction in the collision-induced fractional frequency shift of ultracold atomic ^{87}Rb [34], spurring on construction of the first Rb fountains, built at SYRTE and Yale University. Further encouragement came from experimental measurements of the collision-induced frequency shift in ^{87}Rb which gave closer to a factor of 30 reduced sensitivity in comparison to ^{133}Cs atoms [35, 36]. Fountains operated with Rb atoms therefore offer intrinsically greater stability and have allowed measurement of the clock transition frequency in ^{87}Rb with associated uncertainty currently comparable to that of the primary Cs standard and with scope to surpass them by almost an order of magnitude [37]. As a result six Rb fountains are currently under construction at the USNO to be used as part of the Master Clock ensemble, which contributes approximately one third of UTC, exploiting the robust operation of Rb to characterise more rapidly the frequency drift of the 'flywheel' hydrogen maser [38]. Following measurements of the Rb frequency relative to Cs [39, 40], a recommendation by the Consultative Committee for Time and Frequency (CCTF) to adopt the frequency $6\,834\,682\,610.904\,324\,\mathrm{Hz}$ of ^{87}Rb as a secondary representation of the SI second

[1] Previous work of Gibble dealt with frequency shifts in Cs due to ultracold collisions [33].

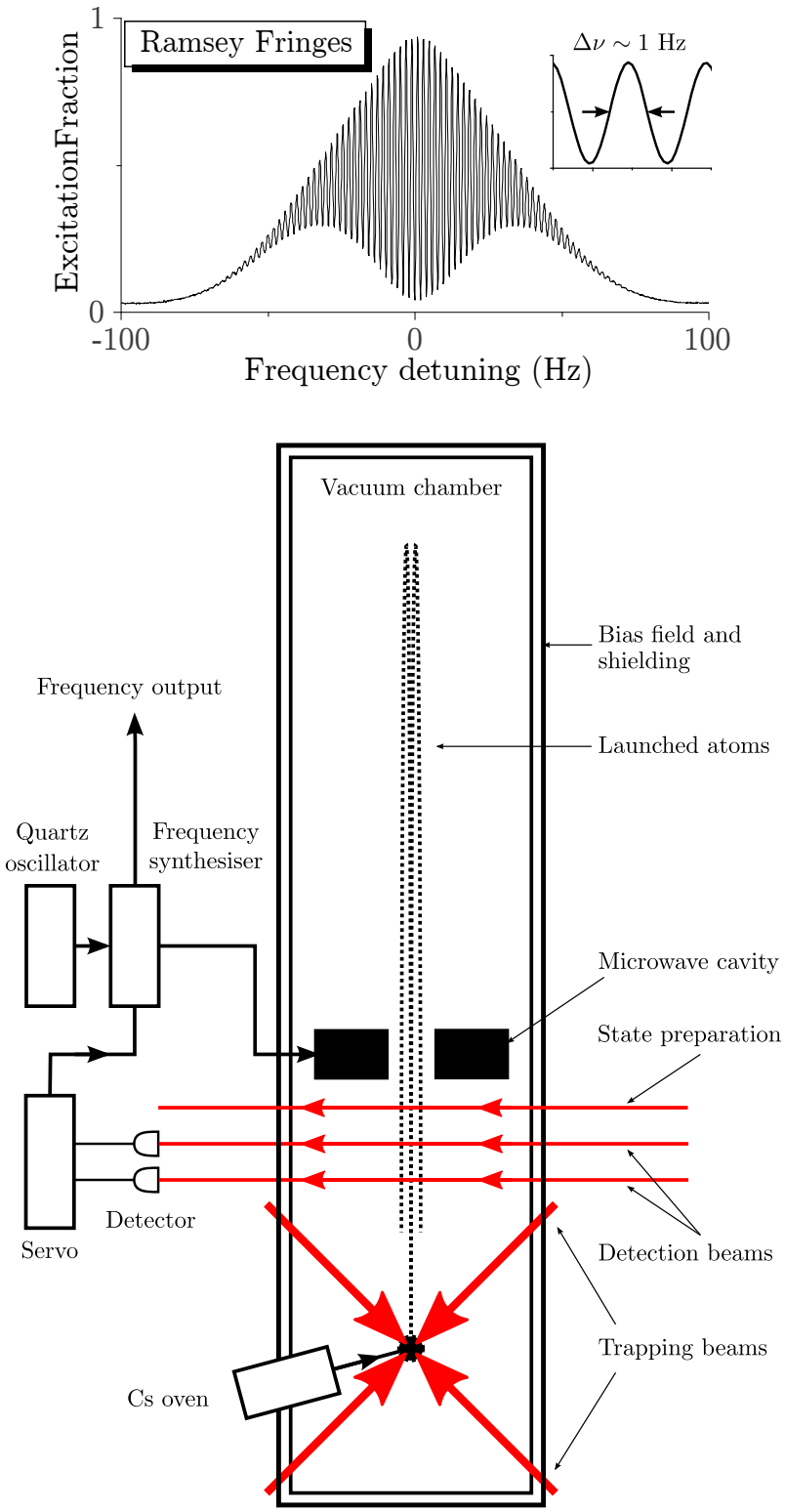


Figure 1.2: **Atomic fountain apparatus** - (Top) Ramsey fringes as measured for the Rb fountain at NPL. The central fringe is blown up (inset) and has linewidth of ∼1 Hz. (Bottom) Schematic of laser cooled atom fountain microwave frequency standard.

was accepted by the BIPM [41]. Dual species fountains, operating Cs and Rb in the same apparatus, have been used to explore variation, as suggested by some cosmological observations, of the fine-structure constant, α. by measuring the relative hyperfine transition frequencies over a period of five years [40]. Although no statistically significant variation was recorded the data allowed an upper limit to be placed on the possible size of the variation, albeit not the most stringent one.

Once a comparatively small effect, the black body radiation (BBR) shift in Cs (and to a similar extent in Rb) also accounts for a significant portion of the uncertainty budget. At a meeting of the CIPM in 1997 the definition of the second was amended to clarify that the hyperfine transition frequency corresponds to an atom at rest at a temperature of 0 K. A correction due to the BBR induced shift of the atoms at room temperature (~ 300 K) must then be applied. As the BBR shift (to the lowest order) scales with temperature to the fourth power as,

$$\frac{\Delta\nu_{BB}}{\nu_0} \approx \beta \left(\frac{T}{T_0}\right)^4 \tag{1.1}$$

where T_0 is usually given as 300 K, cryogenic cooling (down to $T \sim 90$ K) of the fountain flight chamber would decrease the BBR shift by a factor of ~ 100 to the 1 part in 10^{16} level, with a corresponding reduction in the uncertainty of the shift. For a given desired uncertainty the constraint on the exact knowledge of the temperature is then relaxed, with an uncertainty of ~ 3 parts in 10^{17} relating to 90 ± 4 K, in contrast to a room temperature apparatus for which the temperature must be known and controlled to within ± 0.1 K; not an easy task. Additionally, the coefficient β (-1.711×10^{-14} for Cs [42]) must preferably be known sufficiently so as not to limit determination of the shift. Much work, both theoretical and experimental, has been carried out to this end. Implementation of this cryogenic arrangement is currently being evaluated in the NIST-F2 and INRIM IT-CsF2 fountains [43].

Steady improvements over the last 50 years or so have led to current microwave primary frequency standards demonstrating inaccuracies into the 10^{-16} range [44] and quantum-limited[1] instabilities at the level 10^{-14} at 1 s [47]. The total uncertainties of the NIST-F1 and SYRTE-FO2, two of the best fountains in operation, are evaluated at near 4 parts in 10^{16} and expected to reach 1 part in 10^{16} through better control of the BBR shift [48, 49]. The NPL Cs-F2 fountain was recently evaluated with type-B uncertainties (i.e., those that must be measured or otherwise determined, see Sec. 2.1.1) of 2.3×10^{-16} owing to a better

[1] To reach this limit the short-term instability of the microwave oscillator must be sufficiently low. State-of-the-art quartz crystal oscillator technology typically limits this to ~ 1 part in 10^{13} at 1s. Cryogenic sapphire oscillators (CSO) developed at the University of Western Australia [45] have demonstrated a frequency instability of 3 parts in 10^{15} at 1s. As an alternative, microwave synthesis from a stabilised optical frequency, utilising an optical frequency comb as a transfer oscillator, demonstrated at PTB, currently offers frequency instability of ~ 1 part in 10^{14} [46]

understanding of cavity distributed phase shifts and the effect of cavity lensing[1]. However, like Cs beam standards before, Cs fountains are approaching the limit of their practical implementation and efforts to advance frequency metrology further may be better spent elsewhere. Just as we have moved from pendulums (1 Hz) to quartz (~ 100 kHz) and further again to Cs (~ 10 GHz), each time gaining from an increase in frequency, a better frequency standard can come from operating at higher frequencies again – in the optical domain.

1.2 Clocks in Context

The SI system of units conists of seven base units; the second, metre, kilogram, ampere, kelvin, mole, and candela. The accuracy in which the defined SI second can be realised far surpasses that of any other measurement of a fundamental unit. Currently this is at the level of parts in 10^{16} which to put into real terms corresponds to a clock losing or gaining only 1 second in 300 million years! As a consequence the SI unit of length, the metre, was redefined in terms of the SI second as "...the length of the path travelled by light in a vacuum during a time interval of 1/299 792 458 of a second" [51].

As the precision and accuracy to which we can 'keep time' grows, so do the applications. Many technologies and sciences rely on the accuracy and stability of the modern frequency standard. So, to answer the much asked question, "...why do you need a clock that good?", here are some answers:

- Definition of the SI second (Cs)
- Secondary representations of the SI second (Mircrowave:Rb, H, Optical: Sr Hg)
- Length metrology
- Global navigation satellite systems (GPS, GLONASS, Compass, Galileo)
- Communication synchronisation (the internet)
- Deep space navigation
- Radio telescopes (very long baseline interferometry)
- Geodesy (gravitational red-shift)
- Gravitational wave detection
- Tests of Einstein's equivalence principle
- Tests of special and general relativity

[1] A consequence of microwave-photon recoil. Lensing results from a roughly quadratic microwave field amplitude distribution acting on the atoms wavefunction, in analogy with the optical dipole force [50]

- Extremely high precision probe of ultracold physics

Atomic clocks are no doubt a highlight of atomic physics.

1.3 Thesis Outline

A brief account of the history, development, and role of accurate time measurement has been provided in this introduction. The remainder of this thesis is structured as follows:

- In Chapter 2 I build on the fundamental ideas of precision frequency metrology, discuss the operating principles of optical frequency standards, and compare the merits of the two most prominent approaches: 'ion clocks', which are based on a laser cooled trapped ion, and 'lattice clocks', based on many laser cooled atoms trapped in an optical lattice. The current status of each approach is summarised and consideration given to their current limitations and future prospects.

- In Chapter 3 a Sr optical lattice clock is described. A description of the apparatus and techniques required to laser cool and trap atomic Sr, in preparation for clock spectroscopy, is given. The design and implementation of the NPL experimental apparatus is detailed throughout and where possible experimental data included.

- Chapter 4 explores the design principles of an extended cavity diode laser (ECDL) for high precision spectroscopy and reports on the implementation and characterisation of two designs.

- In Chapter 5, the ac dipole polarisability of each Sr clock state is calculated by summing individual contributions from coupled states, and further to this, an estimation of the blackbody radiation (BBR) shift is provided. Methods to tackle to BBR shift are discussed and an experiment to measure directly the BBR shift proposed. Steps towards realisation of the experimental apparatus are detailed.

Finally, in Chapter 6, I conclude with a brief outlook for the future prospects of the NPL Sr lattice experiment and in a broader sense the challenges and opportunities facing the field of frequency metrology.

2

Optical Frequency Standards

So, we have seen what has been and what is current, but what is next? A continuation of the trend in development of time standards moves us towards clock frequencies in the optical domain. The benefits of optical clocks are no secret but have until recently been sidelined by technical limitations. However, over the last decade, seeing the invention of the femtosecond optical frequency comb and laser linewidths creeping below the Hz level, the promise of clocks with inaccuracies at the level of 1 part in 10^{18} or better is becoming a reality. The following discussion briefly describes some of the prerequisites of precision optical spectroscopy and reviews progress of optical frequency standards to date.

2.1 Better Clocks Q Up

We are all familiar with the measurement of length by means of a ruler. If asked to measure the length of an object precisely we would all choose a ruler with well-defined narrow markings, or ticks, spaced as closely as we could reasonably read (such as ruler C in figure 2.1). Our measure would then involve counting the ticks of the ruler up to the length of the object. A smaller tick interval (or the more frequent they are) means we count more for a given length. Assuming we can count to the nearest tick, the fractional uncertainty in our measurement is $< 1/$(number of ticks counted). By simply having more ticks per unit length, our fractional length uncertainty is reduced. For example, an object close in length to 5 ticks of ruler A when measured with ruler A gives us a fractional length uncertainty of $< 1/5$, but when measured with ruler B this is reduced to $< 1/25$. The width of the tick, ΔL, also factors into our measurement. For rulers A and B the ticks are broad and so we have to estimate the position of the centre. Our estimation might get us close, but there will be some doubt. If we assume we can find the centre of a tick to within 1/10th of its width, regardless of its size, then a narrower tick gives us a lower uncertainty of its exact position. The ticks of ruler C are 1/4 the width of those of rulers A and B. Our uncertainty in the position of the centre of the tick is then reduced by 1/4, which in absolute terms goes from ΔL/10 to ΔL/40. Our original choice of ruler was then

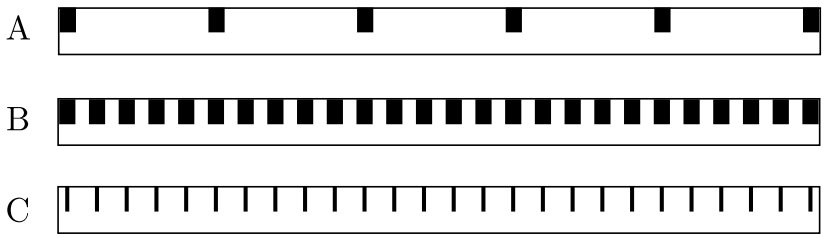


Figure 2.1: **Rulers** - Reducing the measurement uncertainty.

a good one. This principle is key to building better frequency standards. In a quantum frequency standard, our length scale represents an energy scale, related to frequency by $\nu = E/h$. A quantum resonator will absorb energy corresponding to the precise spacing of energy levels. This energy spacing is effectively what we measure, by means of a frequency measurement, in a quantum frequency standard.

We can characterise the ability of a resonator to store energy by the quality-factor or Q. The Q is defined as the ratio of energy stored to energy lost per oscillation cycle, or put another way, the oscillation angular frequency times the exponential decay time of the stored energy. In a two level atom with electronic ground state $|1\rangle$ (energy E_1) and excited state $|2\rangle$ (energy E_2), and populations c_1 and c_2, we may express the dissipation of stored energy as the fraction of population in the excited state as, $c_2(t)/c_2(0) = \exp(-\Gamma\, t)$, where Γ is the exponential decay rate of the excited state population (equivalent to the Einstein A_{21} coefficient) and t is time. The time $t = 1/\Gamma$, for which the population reaches 1/e of its initial value, defines the excited state lifetime. The Q is then given in terms of the resonant frequency $\nu_0 = (E_2 - E_1)/h$ as,

$$Q = \frac{\nu_0}{\gamma} \tag{2.1}$$

where $\gamma = \Gamma/2\pi$ is the natural linewidth of the atomic transition $|1\rangle \leftrightarrow |2\rangle$. We may write this more generally as $Q = \nu_0/\Delta\nu$ where $\Delta\nu$ is the resonator linewidth. High-Q resonators offer a high precision so effort developing frequency standards is spent to increase the Q of the measured resonance. For atomic frequency standards we achieve this by reducing the measured width of the resonance feature or by choosing an atomic transition of higher frequency.

2.1.1 Clock Characteristics

The performance of a clock can be described in the main by the two quantities *accuracy* and *precision*. The (in)accuracy of an atomic clock is determined by the (un)certainty in

which the natural (unperturbed) frequency of the atomic resonance is known. A number of factors contribute to shift the measured clock frequency from that of the unperturbed frequency. How well we know these shifts, so that we can correct for them, determines the final accuracy that we can attribute to the standard. A measure of the standard's absolute frequency brings with it an additional absolute frequency uncertainty. Currently, a primary frequency standard must, by definition, operate with ^{133}Cs to realise the SI second or serve as an absolute frequency reference. The frequency inaccuracy associated with the primary standard, separated into type-A (statistical) and type-B (other, determined primarily by parametric model based predictions and measurement) uncertainties, must be included in the uncertainty budget of the absolute frequency measurement.

The precision is a measure of the repeatability of the observed clock frequency and is more commonly referred to as (in)stability for a given averaging time τ. This instability is characterised by the "Allan variance" or "two-sample variance" denoted $\sigma_y^2(\tau)$ and is usually expressed as the Allan deviation [52], $\sigma_y(\tau) = \sqrt{\sigma_y^2(\tau)}$, which can be written as,

$$\sigma(\tau) \approx \frac{1}{Q(S/N)}\sqrt{\frac{t_c}{\tau}} \tag{2.2}$$

where t_c is the period of the cycle required to correct the oscillator frequency, (S/N) is the signal to noise ratio associated with the frequency measurement, and τ is the averaging time.

It is clear that adopting a clock transition with higher frequency (as $Q = \nu/\Delta\nu$), given all else equal, will improve the frequency stability of the standard. A jump from the microwave ($\sim 10^{10}$ Hz) to the optical regime (on the order of hundreds of terahertz, 10^{14} Hz), offers the potential to greatly reduce the instability by a factor of 10^4 - 10^5! Since many of the frequency shifts that affect accuracy are independent of ν we can also expect to gain similarly here too.

2.1.2 Narrowing the 'Line'

The linewidth of the atomic resonator is fundamentally set by its "natural-linewidth" which is a consequence of the energy-time uncertainty principle, $\Delta E \Delta t \gtrsim \hbar/2$. A "long-lived" excited clock state such that Δt is large then gives us a well defined energy and ergo a natural linewidth which is small. It is not uncommon to find atoms with transitions offering ultra-narrow (∼mHz or less) natural linewidths in the optical domain. Such transitions are typically forbidden by one or more atomic selection rules and termed "weakly allowed" as the chances of exciting one are pretty slim. An extreme example is that of the electric-octupole transition at 467 nm ($^2S_{1/2}, F = 1 \rightarrow {}^2F_{7/2}, F = 0$) in a Ytterbium ion ($^{171}Yb^+$) which has a natural linewidth ∼nHz. That corresponds to an excited state lifetime on the order of 10 years! Ultimately the lifetime of the excited state will limit the coherence time

of the clock spectroscopy but with the availability of ultra-narrow transitions this seems a long way off.

Before we get too carried away with the prospect of ultra-narrow resonance features we must deal with the motion of the atoms. An atom at rest in the laboratory frame will absorb radiation emitted by the interrogating oscillator at frequency $\nu_{osc} = \nu_0$ with maximum probability. Now consider the atom to be moving with velocity v towards the source of radiation. In the rest frame of the atom the frequency of the incoming radiation ν'_{osc} appears higher due to the 'compressing' effect of the atom's motion toward the source. This is known as the Doppler effect and it is simple to show that $\nu'_{osc} = \nu_{osc}/(1 - v/c)$ where c is the speed of light. The energy of the incoming photon as seen by the atom is then shifted away from resonance by $\Delta E = h(\nu'_{osc} - \nu_0)$, known as the Doppler shift, and the probability of absorption by the atom is reduced. The atom will instead prefer to absorb radiation emitted by the source at a frequency $\nu_{osc} = \nu_0(1 - v/c)$. This principle is fundamental to laser cooling (in particular Doppler cooling) as we will see later (section 3.3). For a thermally distributed cloud of atoms obeying Maxwell-Boltzmann statistics the contribution of many Doppler shifted atoms result in a new Doppler broadened linewidth $\Delta\nu_D \propto \nu_0\sqrt{kT/m}$ where k is the Boltzmann constant, T the temperature of the atom cloud, and m the mass of an atom. We can see from this that the Doppler effect is a bigger problem at higher frequencies and is reduced for heavier atoms and lower temperatures.

Ideally, we would like the measured linewidth $\Delta\nu$ to be Fourier-limited such that the linewidths of both the resonator $\Delta\nu_{atom}$ and probing oscillator $\Delta\nu_{osc}$ are less than $\Delta\nu \approx 1/t_{int}$ where t_{int} is the time for which the atoms are interrogated. It is then the aim to maximise the time t_{int} of this interrogation while satisfying the previous condition. It is often the case that the limit to t_{int} is otherwise imposed. In Cs beam and fountain clocks this occurs due to the limited flight time of the atoms through the microwave cavity. Another example is the "ballistic clock", discussed previously (see paragraph three section 1.1.2.2), which also suffers as a result of the motion of atoms. So why not just make the interrogation region MUCH bigger to ensure we interact with the atom for longer? To an extent this is what the development of Cs standards aimed to do, however, the homogeneity of the interrogation must be preserved and this becomes increasingly difficult as the region of interrogation is increased. If we are to do better then we must find a way of confining atoms to a small region where they can be held for the duration of the interrogation.

Thankfully, solutions exist. At present there are two main approaches, both similar in aim, to address the problem of atomic motion for frequency metrology: the ion-trap (section 2.3), and the relatively recent "magic-wavelength" optical lattice trap (section 2.4). The aim in each case is to confine the atom in a well-defined environment and with minimal perturbation to the clock transition. But first, we examine the anatomy of a clock

and the technology required to realise a clock in the optical domain.

2.2 A Clock in Pieces

A high performance clock, broadly speaking, can be broken into three components, depicted in Fig. 2.2:

1. a *short-term-stable local oscillator*, which is disciplined in the long term to
2. a *frequency reference*, and
3. a *counter* to measure the oscillations and output in a usable form

2.2.1 Oscillator: The Clock Laser

An oscillator is required to sustain the time interval, or frequency, of the reference with suitably high short-term-stability. For early standards based on the length of the mean solar day the role of the local oscillator was well served by the humble pendulum. For microwave standards, piezoelectric oscillators provide a microwave signal close to the transition frequency. In the case of optical standards, "cavity-stabilised-lasers" invariably play the role of the local oscillator. From here on in we shall refer to this oscillator as the "clock laser" operating at frequency $\nu_c(t)$.

A laser alone, said to be "free-running", is insufficiently stable to controllably (and coherently) interrogate the atomic reference. Therefore before being stabilised to the atomic reference it must be pre-stabilised to a short-term-stable passive optical resonator – the optical cavity. The simplest stable configuration of an optical cavity is the Fabry-Perot resonator which generally consists of two partially transmissive curved mirrors, of reflectance R, separated by a distance L. Light coupled into the lowest order transverse spatial mode (TEM_{00}) of the optical cavity is transmitted only at resonances defined by $L = n\lambda/2$, where n is an integer, and λ the wavelength of the coupled light, such that a standing wave is formed. The cavity is often characterised by its finesse, given by,

$$\mathcal{F} = \frac{\pi\sqrt{R}}{1-R} \approx \frac{FSR}{\Delta\nu_{cavity}} \tag{2.3}$$

where FSR is the cavity free-spectral-range and $\Delta\nu_{cavity}$ the cavity bandwidth. For clock laser systems, the laser frequency is typically servo locked to a resonance feature of a high-finesse ($\sim$250 000) optical cavity using the Pound-Drever-Hall (PDH) method [55]. Since the frequency of the cavity resonance and therefore the laser, provided a sufficient lock is obtained [56, 57], depends on the length of the cavity's optical path, defined primarily by the mirror and spacer dimensions, measures must be taken to minimise variation of this dimension. For example a variation in optical path length of about 1 fm for a cavity 100 mm long would result in a frequency shift of about 4 Hz for light at 698 nm (the wavelength

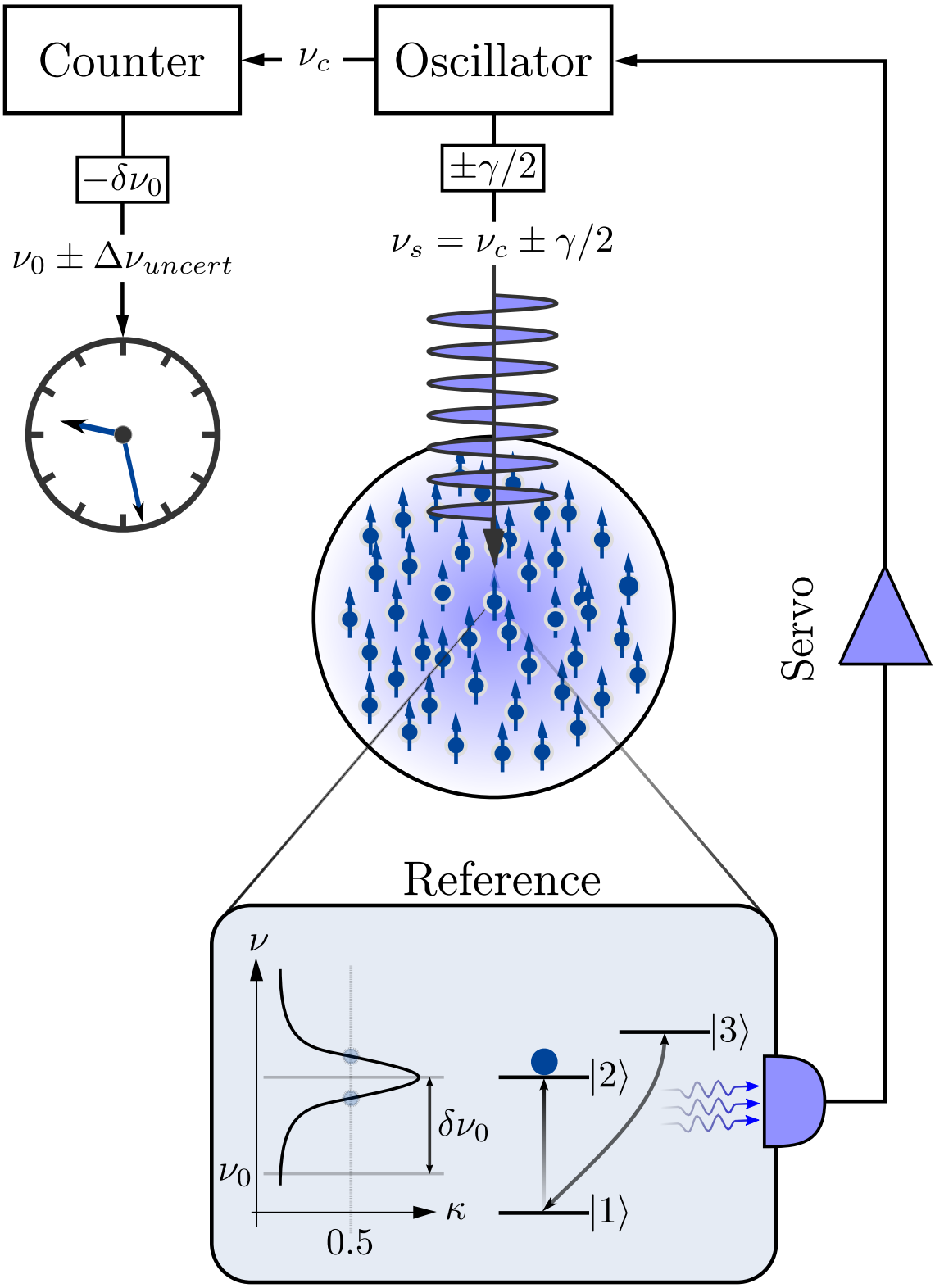


Figure 2.2: **A High-Performance Clock** - Schematic depicting the general operating principle of an atomic clock

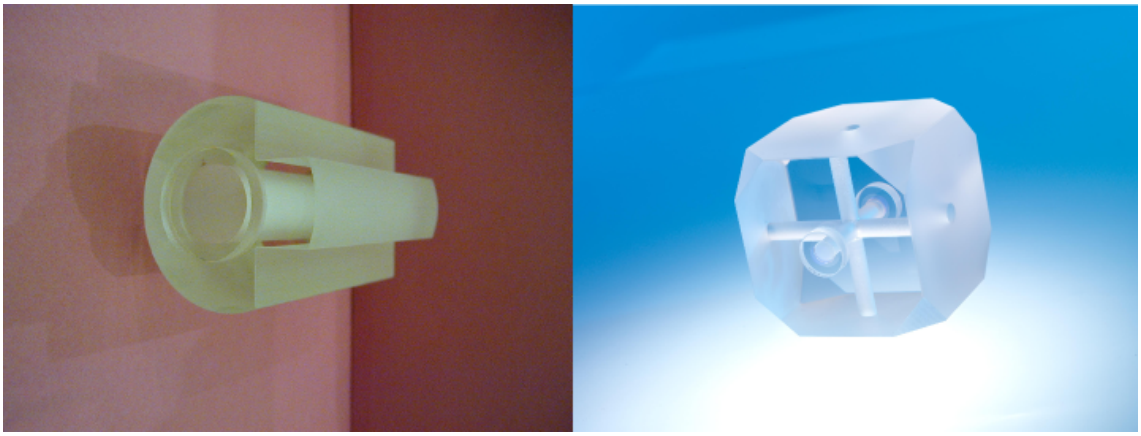


Figure 2.3: **Optical Cavities for Highly-Stabilised Lasers** - Example of vibration insensitive optical cavity spacer designs, courtesy of S. Webster, NPL. Left to right: the "cut-out" cavity [53], and the "omni-g" force insensitive cavity [54], both shown here unmounted.)

of the clock transition in neutral strontium). This corresponds to a change in length of the order of an atomic nuclei, or to put it another way, equivalent to increasing the diameter of the sun by no more than the thickness of a human hair! ULE – a TiO_2 doped fused silica glass – is generally used as the cavity spacer due to its property of ultra-low-expansion at close to room temperature. Various spacer geometries have been explored with a view to reduce acceleration-induced deformation from environmental vibrational and gravitational effects. A reduction by more than a factor of 1000 in the response of a cavity to vertical vibrations – an acceleration sensitivity of about $1 \times 10^{-10}\,\mathrm{g}^{-1}$ – has been demonstrated for cavities operated in the laboratory [53, 58] and later with transportable mountings [59, 60]. Subsequently, driven by the growing interest in spaceborne applications [61], 'field-compatible' cavities have been developed with greater intrinsic insensitivity to acceleration in all directions [54, 62, 63]. Furthermore, active cancellation of vibration-induced phase noise has been demonstrated [64].

Sub-hertz linewidths at several seconds (fractional frequency instability of $\sim 1 \times 10^{-15}$) have been demonstrated for a range of laser systems [58, 65, 66], where further reduction is limited by the fundamental noise limit of the cavity due to thermal-related Brownian motion effects on the mirror substrates and coatings [58, 67]. Reduction of the thermal noise limit is now the primary focus of oscillator development for high performance clocks with the prospect of short-term fractional frequency instabilities $<1 \times 10^{-16}$ in sight [68–70].

2.2.2 Reference

Artefacts. One might consider a reference based on the periodic motion of an electrical or mechanical artefact. For example, the rate at which a pendulum clock 'ticks' relies on

the precise period of the 'swing' of the pendulum which is primarily determined by its length. To build a second clock which 'ticks' at the same rate as the first would require an exact copy of the original pendulum. In practice such reproducibility is not achieved and unintended differences in the manufacture of the second clock result in it ticking at a different rate. In any case the pendulum of each clock will inevitably 'age' producing a gradual change in the period of each 'swing', before eventually wearing out. In the end we are left with two clocks each claiming a different amount of time has passed, so how do we know what time it really is?!

Such a device is suitable to provide a 'flywheel' time-interval (or frequency) reference in the short term, *but* must be regularly calibrated by a superior, repeatable, long-term-stable reference.

Atoms. Quantum frequency standards utilise an internal (generally electronic) transition in an atom to serve as the frequency reference for our clock laser. This "clock transition" has frequency centred at ν_0 given by,

$$\nu_0 = (E_2 - E_1)/h \tag{2.4}$$

where E_1 and E_2 are the quantised energies of the ground $|1\rangle$ and excited $|2\rangle$ states of the transition, and h is the Planck constant. The precise spacing of these energies defines the rate at which the clock 'ticks' and it is this energy gap, free of environmental perturbations, that we aim to measure. In contrast to an artefact reference, an atomic reference is made, by nature, indistinguishable from another of the same type in a given environment, its frequency is constant in time – providing fundamental constants remain constant(!) – and it will not 'wear-out', making it the ideal candidate for a frequency reference.

Referencing the line. It is desirable to use ultra-narrow clock transitions for reasons of precision, however, detecting the occurrence of such a transition directly is difficult. Instead, spectroscopy is generally accomplished with an electron shelving scheme [71], which utilises an auxiliary detection state $|3\rangle$, see Fig. 2.4. Following interrogation by the clock laser, the atom is excited to a superposition quantum state $|\psi\rangle = c_1|1\rangle + c_2|2\rangle$. The excitation probability $p = |c_2|^2$ is measured by projecting state $|\psi\rangle$ onto state $|2\rangle$ by application of a second laser resonant with the $|1\rangle \leftrightarrow |3\rangle$ auxiliary transition. For a single measurement p is either 0 or 1, detected by observing the fluorescence (or lack of) from the auxiliary transition, depending on whether or not the electron was 'shelved' in state $|2\rangle$. Successful shelving of the electron is referred to as a "quantum jump". Fluctuations in the clock readout, termed quantum projection noise (QPN), $\delta p = 1/\sqrt{N}$ for N uncorrelated atoms (improved to $\delta p = 1/N$ for a maximally entangled ensemble), provide a fundamental limit to the clock stability [72]. Clock operation relies on the averaging of many measurements to obtain an accurate representation of p at a given probe

frequency ν_c. To "lock" the clock laser to the atomic reference, see Fig. 2.2, $p = |c_2|^2$ is measured at $\nu_s = \nu_c \pm \gamma/2$ where ν_c is kept to ν_0 by steering the clock laser to maintain $p = 0.5$. The slope of the line shape here is steepest, offering the greatest sensitivity to clock laser drift $\delta\nu_c(t) \approx \kappa\gamma\delta p$, where κ (close to 1) depends on details of the lineshape. An error signal is extracted from the deviation of p from the value 0.5 and corrections are made to the clock laser frequency with a cycle time t_c. The quantum-limited instability is then [73],

$$\sigma(\tau) \approx \frac{\delta\nu_c(t)}{\nu_0} = \frac{\kappa}{Q\sqrt{N}} \tag{2.5}$$

where a total of $N = n_c\tau/t_c$ atoms are measured over an averaging time τ and a number n_c measured per cycle time t_c. Furthermore, $n_c = t_c n_{at}/(t_{int} + t_d)$ where n_{at} is the total number of atoms interrogated in time t_{int} and t_d is the measurement dead-time. For a single atom or ion ($n_{at} = 1$) knowledge of the excitation probability must be accumulated over a sequence of measurements. In contrast, for a many-atom system ($n_{at} \gg 1$) sufficient knowledge can be gained in a single measurement, reducing t_c, and in turn, the instability. However, dead-time can be pronounced in neutral atom systems due to the destructive nature of the measurement, which requires preparation of a new ultracold atomic sample per measurement cycle. This dead-time leads to the phenomenon of the Dick-effect [74–76] in which residual frequency noise inherent in the clock laser is converted to low Fourier frequencies as a consequence of aliasing due to the cyclic nature of the clock interrogation. This effect is reduced for short dead-time periods [77], however, longer t_d can be accommodated providing the local oscillator noise is suitably low.

Frequency shifts. It is generally the case that we do not actually measure ν_0 in the first instance. A number of factors contribute to shift the measured clock frequency from that of the natural unperturbed frequency, such that,

$$\nu_0 = \nu_c - \delta\nu_0 \pm \Delta\nu_{uncert} \tag{2.6}$$

where $\Delta\nu_{uncert}$ is the uncertainty in our determination of ν_0. The origin of these frequency shifts can be broadly grouped into those:

1. intrinsic to physical atomic properties,
2. introduced in the atomic interrogation, and
3. present in the electronic servo scheme.

At the head of these are those intrinsic to the physical atomic properties. Primarily these are field-related shifts, largely a consequence of the Zeeman and Stark effects. The particular sensitivity to these shifts depends critically on the configuration of the atom; the nature of the clock transition and transitions surrounding it. The second point covers,

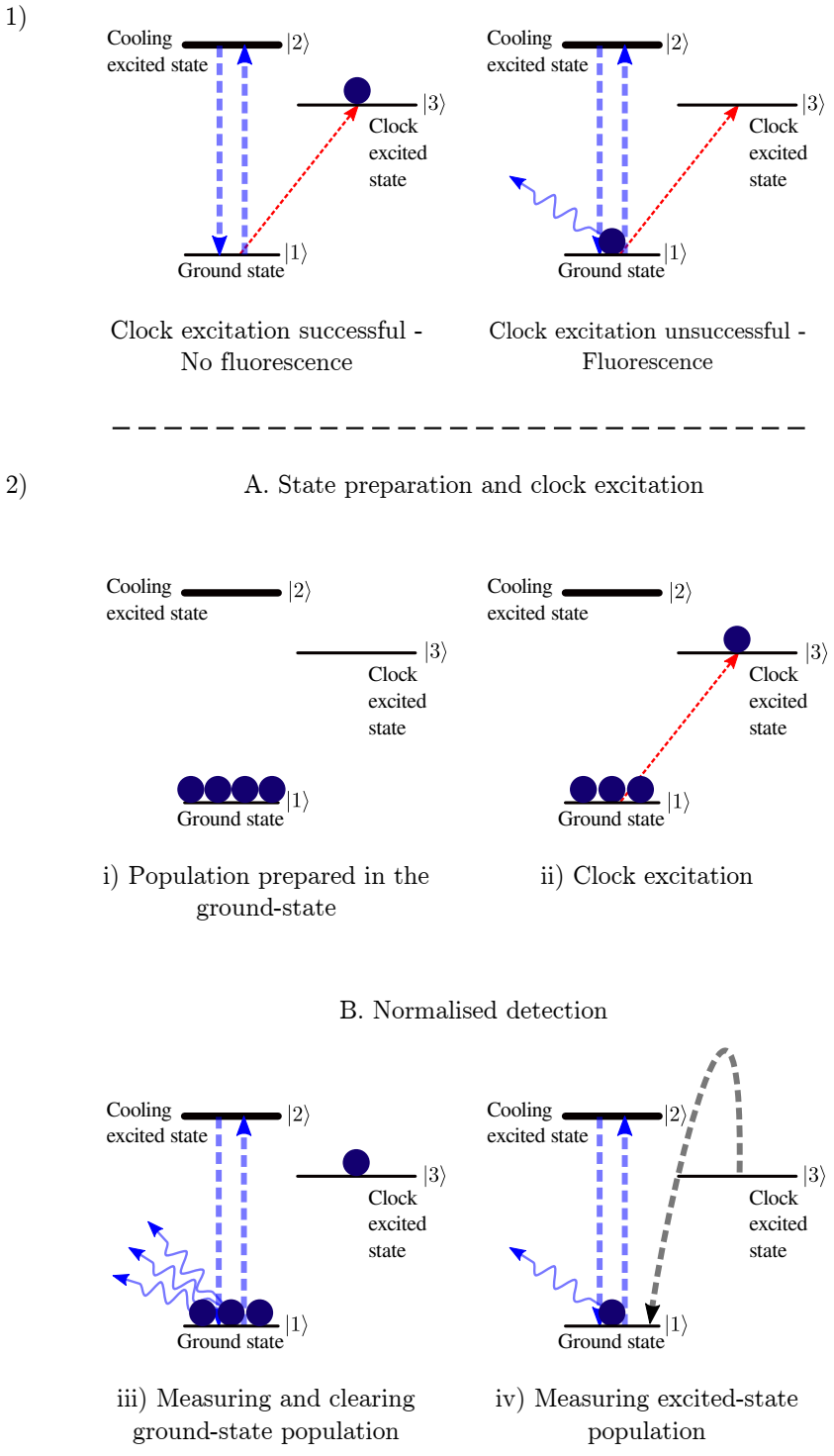


Figure 2.4: **Electron Shelving Detection Scheme** - The clock transition is too weak to observe directly so instead a strong transition, usually the cooling transition, is used to probe the position of the electron. If the clock excitation is a success the electron will be "shelved" in the meta-stable excited clock state. The subsequent probe light will not interact and there will be no fluorescence.

for example, Doppler shifts resulting from motion of the atoms during interrogation, or the effect of inhomogeneity of the probing radiation such as wavefront curvature.

Each known shift, accounted for in an error budget, must be characterised and measured and a correction made to ν_c. Where possible, it is desirable to eliminate the presence of frequency shifts in the first instance. A careful initial choice of atomic reference can yield a clock with favourable performance.

2.2.3 Frequency Counter

Finally, an electronic frequency counter is used to determine the frequency of the oscillator of the standard under measure, by comparison with a reference oscillator, serviced by the SI second. This occurs either directly – for radiation countable within the means of electronic devices (microwave counters extend to $\sim 50\,\mathrm{GHz}$) – or via a 'clockwork' – capable of linking optical frequencies to microwave in some countable way. RF-to-optical frequency chains – notably that developed at PTB; used for the first frequency measurements of the Ca optical frequency standard operating at 456 THz [78] – allowed the measurement and comparison of optical frequencies relative to Cs. However, such frequency chains offered limited measurement accuracy and universality, so the progress of frequency standards based on optical transitions was hampered.

A revolutionary step forward came with the invention of the femtosecond optical frequency comb. Ultrashort ($\sim 10^{-15}\,\mathrm{s}$) pulses from a mode-locked laser, separated in time by $\tau = 1/f_{rep}$ (where f_{rep} is the pulse repetition rate), produce a well-defined broad-band of discrete optical frequencies, or 'comb modes', separated in the frequency domain by f_{rep}. Optical frequencies are measured by down-conversion to the microwave band via beat note generation between the referenced optical oscillator and a nearby referenced comb mode of known frequency. Optical frequency combs provide a convenient, universal 'clockwork' with measurement inaccuracies $\sim 10^{-19}$ [79], clearing the way for development of optical frequency standards (for a detailed description of the femtosecond optical frequency comb see the book edited by J. Ye and S.T. Cundiff [80]).

2.3 Single Ion Clocks: Quality over Quantity

An ion trap exploits the relatively large Lorentz force experienced by a charged particle in the presence of an electromagnetic field. Ideally, we would like our trap to be a static harmonic potential with the minima at zero electric potential but as Earnshaw's theorem tells us this is not possible ($\nabla \cdot E = 0$). Ion traps (in particular the Paul trap) get around this by using both dynamic (ac) and static (dc) electric fields to generate an approximately harmonic trapping quadrupole pseudo-potential. The pseudo-potential can be thought of as a rotating "saddle" potential which on average keeps the ion in the centre of the trap where the field is null (see analogy with ball on rotating saddle under a gravitational

potential). Therefore we can think of the ion as being held in free-space, relatively free of any Stark shift[1], but with the benefits of tight confinement – explained in the following discussion.

2.3.1 Doppler- and Recoil-Free Spectroscopy

Ion traps typically offer very deep conservative trapping potentials, $\sim 1\,\mathrm{eV}$ or $\sim 10^4\,\mathrm{K}$, and will readily capture "hot" ions. If we are to take advantage of the long coherence times offered by ultra-narrow features we must first cool the ion, ideally to the ground state of the trap. As the ion cools and occupies lower motional states the trap better approximates a harmonic potential and the motional states can be described by the well-known quantum harmonic oscillator model with quantised motional energies,

$$E_n = h\nu_z \left(n + \frac{1}{2}\right) \tag{2.7}$$

where ν_z is the vibrational frequency associated with the trapping potential - often used to characterise the trap. The ion can then make two types of transition: carrier transitions, where the ion changes its internal quantum state only, or sideband transitions, where the ion changes both its internal quantum state and external motional (vibrational) state. The extent of the ion's motion in the trap is characterised by the oscillator length $z_0 = \sqrt{\hbar/4\pi m\nu_z}$ and may be parameterised relative to the wavelength of the transition we are probing by the Lamb-Dicke parameter η, which in a 1D harmonic potential along z is,

$$\eta_z = kz_0 = \frac{1}{\lambda_P}\sqrt{\frac{h}{2m\nu_z}} = \sqrt{\frac{\nu_R}{\nu_z}} \tag{2.8}$$

where $k = 2\pi/\lambda_P$ is the wavenumber of the carrier transition, and λ_P is the probe laser wavelength. We can see here that this also parameterises the confinement of motion in terms of the frequency shift due to the atom recoil when absorbing a carrier photon, given by $\nu_R = h/2m\lambda_P^2$, relative to the trap vibrational frequency.

Our Doppler broadened feature can now be thought of as a carrier modulated at frequency ν_z by the quantised atomic motion. The relative strength of sideband transitions to the carrier is determined by η^2 times a factor that depends on whether motional energy is gained or lost. A "blue-detuned" sideband from $n \to n+1$ with frequency $\nu_P + \nu_z$ gains one motional quantum $\Delta n = +1$ and is suppressed by the factor $\eta^2\,(n+1)$. A "red-detuned" sideband from $n \to n-1$ and frequency $\nu_P - \nu_z$ loses one motional quantum $\Delta n = -1$ and is suppressed by the factor $\eta^2 n$. Clearly then at $n = 0$ transitions of $\Delta n = -1$ can no longer take place and the red sideband vanishes indicating we have reached the motional ground state. For confinement on the order of λ_P or less such that the spatial

[1] Transitions in ions with a quadrupole moment experience a shift as a result of an interaction with static electric field gradients, which exist at some level, depending on the trap.

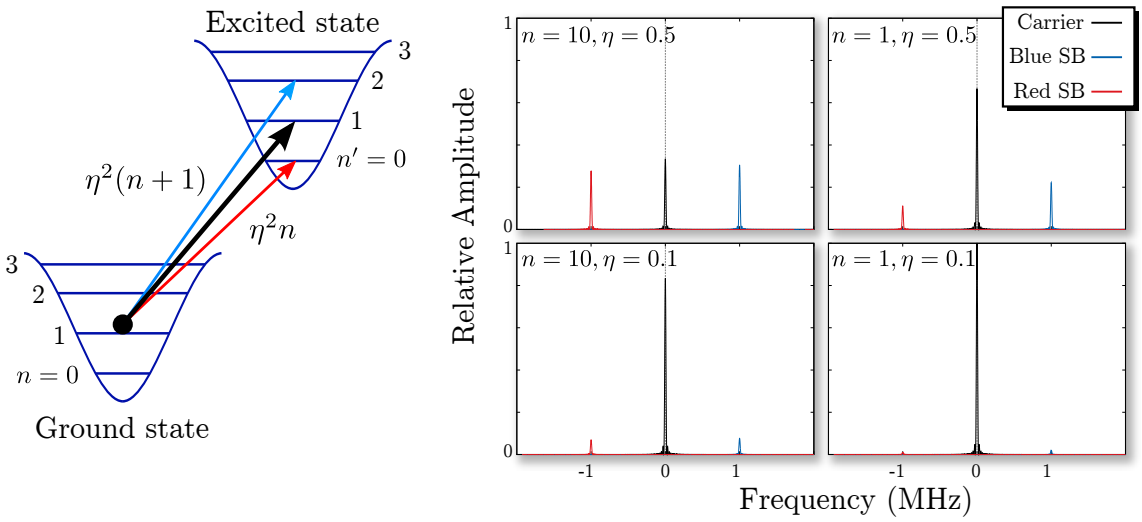


Figure 2.5: **Lamb-Dicke Confinement** - Motional energies in a near harmonic potential.

excursion of the atoms motion is constrained to the order of the relevant clock wavelength $\eta < 1$ (or modulation index < 1) we are said to be in the Lamb-Dicke regime and the carrier amplitude is dominant. For a sufficiently narrow feature or large depth of trap the motional sidebands are resolved from the carrier. The issues resulting from atomic motion present in free-space spectroscopy are now reduced to that of a small potential effect of line pulling between carrier and sidebands. As the carrier does not depend on n we can probe it (almost) free of Doppler and recoil effects [81, 82].

Doppler cooling is typically not sufficient to reach the motional ground state and so additional techniques, namely resolved sideband cooling on narrow transitions [71, 83], and resolved Raman sideband cooling, have been developed.

2.3.2 Current Status of Ion Optical Clocks

The reduction of motional, collisional, and electromagnetic perturbations offered by laser-cooled trapped ions provides a promising environment to operate an optical clock. As $n_{at} = 1$, high clock stability requires the realisation of a high Q resonance feature. A comparison highlighting the potential and achieved Q of several ion optical clock transitions implemented at various laboratories around the world is shown in Table 2.1.

2.3.2.1 Outperforming Cs: Useful for fundamental physics

Systematic frequency uncertainties of optical standards are now, in several cases, estimated as smaller than those of Cs microwave primary standards (see Table 2.2) and in many cases offer greater stability as a result of high-Q. Interest has thus focussed on measuring frequency ratios between optical standards. Sub-hertz level ($\nu_1/\nu_2 = 3.8 \times 10^{-16}$) comparisons between two single-ion frequency standards based on the electric-quadrupole

Table 2.1: Q comparison of ion optical clocks

Species	Transition[a]	λ (nm)	γ_{nat} (Hz)	Q_{theory}	Q_{exp}	Lab(s)
$^{171}Yb^+$	$^2S_{\frac{1}{2}}-^2F_{\frac{7}{2}}$	467	$\sim 10^{-9}$	$\sim 10^{24}$	4.9×10^{13} [84]	NPL, PTB
$^{204}Tl^+$	$^1S_0-^3P_0$	202	<0.01	$>1.5\times10^{17}$	–	–
$^{27}Al^+$	$^1S_0-^3P_0$	267	0.008	1.4×10^{17}	4.2×10^{14} [85]	NIST, PTB
$^{40}Ca^+$	$^2S_{\frac{1}{2}}-^2D_{\frac{5}{2}}$	729	0.2	2.1×10^{15}	–	Innsbruck, NICT
$^{115}In^+$	$^1S_0-^3P_0$	237	0.8	1.6×10^{15}	2.9×10^{13} [86]	MPQ, NICT, PTB
$^{88}Sr^+$	$^2S_{\frac{1}{2}}-^2D_{\frac{5}{2}}$	674	0.4	1.1×10^{15}	–	NPL, NRC
$^{199}Hg^+$	$^2S_{\frac{1}{2}}-^2D_{\frac{5}{2}}$	282	1.9	5.6×10^{14}	1.6×10^{14} [87]	NIST
$^{171}Yb^+$	$^2S_{\frac{1}{2}}-^2D_{\frac{3}{2}}$	436	3.1	2.2×10^{14}	6.8×10^{13} [84]	PTB, NPL

[a]We use here the standard *Russell-Saunders* notation for the term symbol, $^{2S+1}L_J$, where S is the total spin and $2S+1$ the spin multiplicity, L is the total orbital angular momentum, and J is the total angular momentum.

transition in $^{171}Yb^+$, with a natural linewidth of 3.1 Hz, have been demonstrated at PTB [88]. Frequency ratios offer a useful probe into the potential time variation of the fine-structure constant α_f, which determines the splitting scale of atomic fine-structure. By selecting transitions with maximally dissimilar dependence on α_f an increased sensitivity is achieved. One such example is the measurement of the ratio of the $^{171}Yb^+$ quadrupole to the ultra-narrow octupole transition in the same ion [89], being actively pursued at NPL and PTB, which offers a very sensitive measure of possible time variation of α_f in the convenience of a single apparatus. Another example is the frequency ratio of two standards based on trapped $^{27}Al^+$ and $^{199}Hg^+$ single ions which was measured at NIST with a fractional frequency uncertainty of 5.2 parts in 10^{17}, dominated by the statistical uncertainty of 4 parts in 10^{17}. This measurement placed a constraint on the possible variation of α_f of $\dot{\alpha_f}/\alpha_f = -1.6 \pm 2.3 \times 10^{-17}\,\mathrm{yr}^{-1}$ [90].

2.3.2.2 Al^+ QLC: A note worthy performer

Convential ion frequency standards utilise spherical radio-frequency (rf) Paul traps, occupied by a single ion which is laser-cooled and probed directly. This then limits the choice of ion to one that has both an accessible cooling transition and a clock transition with favourable properties. To circumvent this a quantum logic clock scheme has been developed[98] and implemented at NIST [99, 100]. In a linear rf Paul trap a "spectroscopy" ion, which possesses the desired clock transition, is motionally coupled via the Coulomb interaction to an auxiliary "logic" ion. Unlike the spectroscopy ion, the logic ion can be

Table 2.2: Ion optical clock status as of the year 2010

Species	Transition	Inaccuracy $\delta\nu/\nu$ (best reported)	Abs. Uncertainty (best reported)	BBR shift at 300 K (10^{-16})	Quadrupole moment (ea_0^2)[a]
$^{27}Al^+$	$^1S_0$–$^3P_0$	8.6×10^{-18} [91]	–	-0.08	0
$^{199}Hg^+$	$^2S_{\frac{1}{2}}$–$^2D_{\frac{5}{2}}$	1.9×10^{-17} [90]	6.5×10^{-16} [92]	?	-0.51
$^{171}Yb^+$	$^2S_{\frac{1}{2}}$–$^2D_{\frac{3}{2}}$	4.5×10^{-16} [93]	1.1×10^{-15} [93]	-2.4	-0.22
$^{40}Ca^+$	$^2S_{\frac{1}{2}}$–$^2D_{\frac{5}{2}}$	2.0×10^{-15} [94]	2.4×10^{-15} [94]	9.3	1.83
$^{88}Sr^+$	$^2S_{\frac{1}{2}}$–$^2D_{\frac{5}{2}}$	2.5×10^{-15} [95]	3.4×10^{-15} [95]	7.4	2.6
$^{171}Yb^+$	$^2S_{\frac{1}{2}}$–$^2F_{\frac{7}{2}}$	5.5×10^{-16} [96]	1.0×10^{-15} [96]	-5.4	2.08
$^{115}In^+$	$^1S_0$–$^3P_0$	1.4×10^{-14} [86]	1.8×10^{-13} [97]	0.2	0

[a]Expressed in atomic units (a.u.), where e is the elementary charge and a_0 is the bohr radius.

directly laser-cooled, allowing sympathetic cooling and clock readout of the spectroscopy ion in the absence of a suitable cooling/detection transition. A comparison of two $^{27}Al^+$ quantum logic clocks (QLC) at NIST, the first with a $^9Be^+$ logic ion (frequently used in quantum information processing (QIP) experiments at NIST) and to better effect the second with $^{25}Mg^+$, similar in mass to Al, demonstrated a fractional frequency difference of only $\nu_{AlMg}/\nu_{AlBe} = -1.8 \pm 0.7 \times 10^{-17}$ after a series of 56 separate measurements. The systematic fractional frequency uncertainty of the best clock was evaluated at 8.6 parts in 10^{18}, losing 1 second in 3.7 billion years (which is just over a quarter of the age of the universe!), limited predominantly by relativistic time dilation effects from secular and micromotion of the ion held in the trap (enhanced due to the relatively small mass of Al). By deliberately displacing the ion in one of the clocks from the confining quadrupole field null, thereby inducing a well defined harmonic motion (perpendicular to the probe laser wave vector, $\mathbf{k}$) with velocity $v_{rms} = \sqrt{\langle v^2 \rangle}$ ranging from $\sim 1\,\mathrm{m\,s^{-1}}$ to $35\,\mathrm{m\,s^{-1}}$, Chou and co-workers were able to clearly demonstrate the effects of relativistic time dilation (second-order Doppler-shift) at speeds experienced by people on an everyday basis. Furthermore, disparate 'tick' rates due to the effects of gravitational red-shift were observed for a clock height displacement $\Delta h = 33\,\mathrm{cm}$. The resulting fractional frequency shift of $(4.1 \pm 1.6) \times 10^{-17}$ was used to determine a change in height of $37 \pm 15\,\mathrm{cm}$ ($\Delta\nu/\nu = g\Delta h/c$ where $g \simeq 9.8\,\mathrm{m\,s^{-1}}$), in good agreement with the known displacement [85].

2.3.2.3 On the horizon

The success of the Al^+ clock is largely a result of the reduced intrinsic sensitivity of the clock transition to field-related shifts. This is a feature common to group-13 post-

transition metal elements (boron (B), aluminium (Al), gallium (Ga), indium (In), thallium (Tl)), which typically offer high frequency, high-Q clock transitions with zero quadrupole moment and small fractional BBR shift, as first noted by Dehmelt in several proposals [71, 101, 102]. Several groups are now exploring sympathetic cooling of a number of these 'exotic' clock ions in linear Paul traps. For example, some attention (NICT and PTB) is going towards an improved $^{115}In^+$ standard with sympathetic cooling via $^{40}Ca^+$, $^{171}Yb^+$, and $^{115}Cd^+$ being explored. No doubt spurred on by the success of Al^+, new schemes, aside from quantum-logic spectroscopy, are being developed to enable direct readout of 'difficult' clock transitions. For example, vacuum ultra-violet (VUV) spectroscopy using the conventional cooling transition in the clock ion (for $^{115}In^+$, $^1S_0 - ^1P_1$ at 159 nm with $\Gamma/2\pi \simeq 1.1$ GHz), or alternatively using the much weaker but more easily accessed inter-combination line ($^1S_0 - ^3P_1$ at 230 nm with $\Gamma/2\pi \simeq 360$ kHz). The latter will likely result in a reduced photon counting rate which may increase the readout time needed between corrections to the clock laser, and in turn increase the stability requirements of the clock laser. To compensate, we might consider constructing a hybrid clock where the stability of a neutral atom optical clock serves to stabilise the ion clock laser between measurements, thereby achieving the stability of a many-atom clock with the accuracy of a single-ion clock. Such a scheme has been proposed for $^{115}In^+$ utilising a Sr optical lattice clock [103]. It is possible that 'piggybacking' in this way will lead to the best results.

2.4 Optical Lattice Clocks: Quality and Quantity

In addition to high Q, optical neutral many-atom ($n_{at} \gg 1$) standards aim to take advantage of the increased stability offered by the reduced measurement time required of large atom ensembles (Eq. 2.5).

2.4.1 Ballistic Clock

An early such example, developed at NIST [104] and PTB [105], is the "ballistic" clock based on a freely expanding cloud of Ca atoms. Atoms are initially prepared in a magneto-optical-trap (MOT), but in order to avoid large Zeeman and Stark shifts these confining fields must be switched off for the duration of the spectroscopy, leaving the atoms free to move under gravity and by their thermal energy. Due to the scaling of Doppler effects ($\propto \nu$) in the optical domain, traditional two-pulse Ramsey spectroscopy is severly hindered by relatively large distributions of first-order Doppler shifts, which integrate to reduce fringe contrast. To combat this a four-pulse Ramsey-Bordé technique [106] was developed where an additional two pulses probe from the opposing direction giving rise to two distinct interactions; the interaction of interest cancels the initial Doppler de-phasing and the

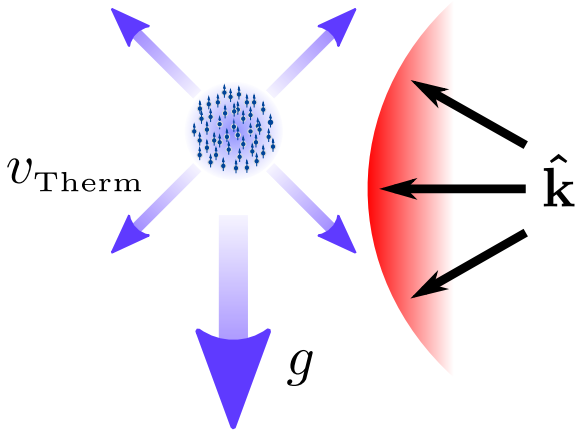


Figure 2.6: **Ballistic Clock Interrogation** - A laser cooled ensemble of Ca atoms are released from the constraints of a MOT for field-free clock interrogation. The residual thermal atomic motion and acceleration due to gravity coupled with the wavefront curvature of the interrogating laser beam, results in a distribution of Doppler shifted atomic resonances.

Ramsey fringe signal is recovered[1]. Owing to the relatively simple operation, a very fast measurement duty cycle (<10 ms) is achieved aiding the stability to better than 4 parts in 10^{15} at 1 s [107]. However, even with the addition of narrow line laser-cooling to sub-recoil temperatures [108], residual Doppler shifts, from thermal and gravitational effects in free-space interrogation, limit the potential accuracy of this approach.

2.4.2 Light-shift cancellation at the "magic-wavelength"

Ideally, we would like to take advantage of the benefits of perturbation-free confinement available to trapped ion standards. We can trap neutral atoms in optical traps utilising the dipole force but this relies on a perturbation of the trapped state. This perturbation is a consequence of the interaction of the atom's charge distribution with an oscillating electric field – referred to as the ac Stark effect. The size of the perturbation is controlled primarily by the intensity $I = \epsilon_0 c\langle|\mathrm{E}|^2\rangle$, and wavelength λ, of the trapping light and varies between states depending on the polarisability $\alpha(\lambda, \hat{\mathbf{e}})$; ϵ_0 is the vacuum permittivity, c the speed of light in a vacuum, and $\hat{\mathbf{e}}$ is the polarisation vector. An expansion of the ac Stark-shift in even powers of electric-field amplitude, where $\mathcal{E} = \langle|\mathrm{E}|\rangle = \mathrm{E}_0/\sqrt{2}$ is the time-averaged electric-field amplitude, can be expressed as a perturbation of state $|a\rangle$ as (see for example [109]),

$$\delta E_a^{Stark}(\lambda, \hat{\mathbf{e}}) = -\frac{1}{2}\alpha_a(\lambda, \hat{\mathbf{e}})\,\mathcal{E}^2 - \frac{1}{16}\gamma_a(\lambda, \hat{\mathbf{e}})\,\mathcal{E}^4 + \ldots \tag{2.9}$$

[1]It should be noted that the maximum theoretical fringe contrast that can be achieved in this way is 0.5, compared to 1 in the two-pulse scheme, as symmetry denotes half the interaction results in doubling of the dephasing.

where $\alpha_a(\lambda, \hat{\mathbf{e}})$ and $\gamma_a(\lambda, \hat{\mathbf{e}})$ are the generalised dynamic polarisability and (second) hyperpolarisability, respectively, of state $|a\rangle$. A transition from state $|a\rangle \rightarrow |b\rangle$ will be shifted in frequency by $\delta\nu$ depending on the residual polarisability $\Delta\alpha = \alpha_a - \alpha_b$ and hyperpolarisability $\Delta\gamma = \gamma_a - \gamma_b$ as,

$$\delta\nu_{ab}^{Stark}(\lambda, \hat{\mathbf{e}}) = -\frac{1}{2h}\Delta\alpha(\lambda, \hat{\mathbf{e}})\,\mathcal{E}^2 - \frac{1}{16h}\Delta\gamma(\lambda, \hat{\mathbf{e}})\,\mathcal{E}^4 + \ldots \tag{2.10}$$

Residual frequency shifts can easily be as large as $\delta\nu \sim$100 kHz, which if uncharacterised lead to an inaccuracy of $\sim 10^{-9}$, placing unrealistic constraints on the trapping laser intensity. Additionally, due to the form of the trapping potential, the shift will be non-uniform across the atomic ensemble.

To negate the effect of the trapping light on the clock transition we require a situation where both the ground and excited clock states of an atom are perturbed equally, regardless of their position in the trap, such that the residual shift cancels. This occurs in the electric dipole approximation for $\Delta\alpha^{E1}(\lambda, \hat{\mathbf{e}}) = 0$, providing higher order effects ($\propto \mathcal{E}^4$) [110] are negligible at the level of interest [111, 112].

At the 6th Symposium on Frequency Standards and Metrology, Hidetoshi Katori, from the university of Tokyo, proposed such a scheme for Sr atoms trapped in a red-detuned ($\alpha(\lambda, \mathbf{e}) > 0$) optical lattice tuned to the "magic-wavelength" ($\lambda = \lambda_m$), allowing effectively Stark-free confinement of atoms, independent, to a good approximation, of the lattice intensity [113]. Furthermore, using a clock transition of $J = 0 \rightarrow J' = 0$ we become sensitive only to the scaler component of the light-shift (see. Sec. 2.4.3). This technique promises to marry the Doppler- and recoil-free spectroscopy of single-ion standards (with sub-wavelength confinement in the Lamb-Dicke regime), with the increased signal-to-noise ratio of conventional neutral atom standards, afforded by sheer atom number. In doing so a moderate number of atoms $n_{at} \sim 10^4$ can potentially decrease the clock instability by a factor of $\sqrt{n_{at}} \sim 100$ in comparison to single-ion standards. Coupled with the realisation of high Q features in optical traps emulating an array of Paul-like traps, we can then aim to reach QPN limited instabilities on the order of $1 \times 10^{-17}/\sqrt{\tau}$ with no expected lattice-imposed limit to clock inaccuracy to the level of $<1 \times 10^{-17}$, depending on trapping parameters [112, 114, 115]. Initial experiments using Sr demonstrated first-order cancellation of the light-induced frequency-shift for magic-wavelength-tuned optical lattices [111, 116, 117]. Subsequently, magic trapping wavelengths have been identified for a number of candidate reference atoms [118–122], summarised in the review article by Derevianko and Katori [123].

Of additional help, for magic wavelengths far from atomic resonances, the sensitivity to lattice frequency detuning is relatively small. For the red-detuned magic wavelength in Sr, $\lambda_m = c/\nu_m \approx 813\,\text{nm}$, $\left|\delta\nu^{Stark}/\delta\nu_m\right| \approx 1 \times 10^{-9}$ for lattice intensity $I_L = 10\,\text{kW cm}^{-2}$. This corresponds to an absolute frequency determination of ν_L to within $\sim$1 MHz to provide a cancellation of $\Delta\alpha^{E1}$ at the level of 1×10^{-18} – not a particularly difficult task for

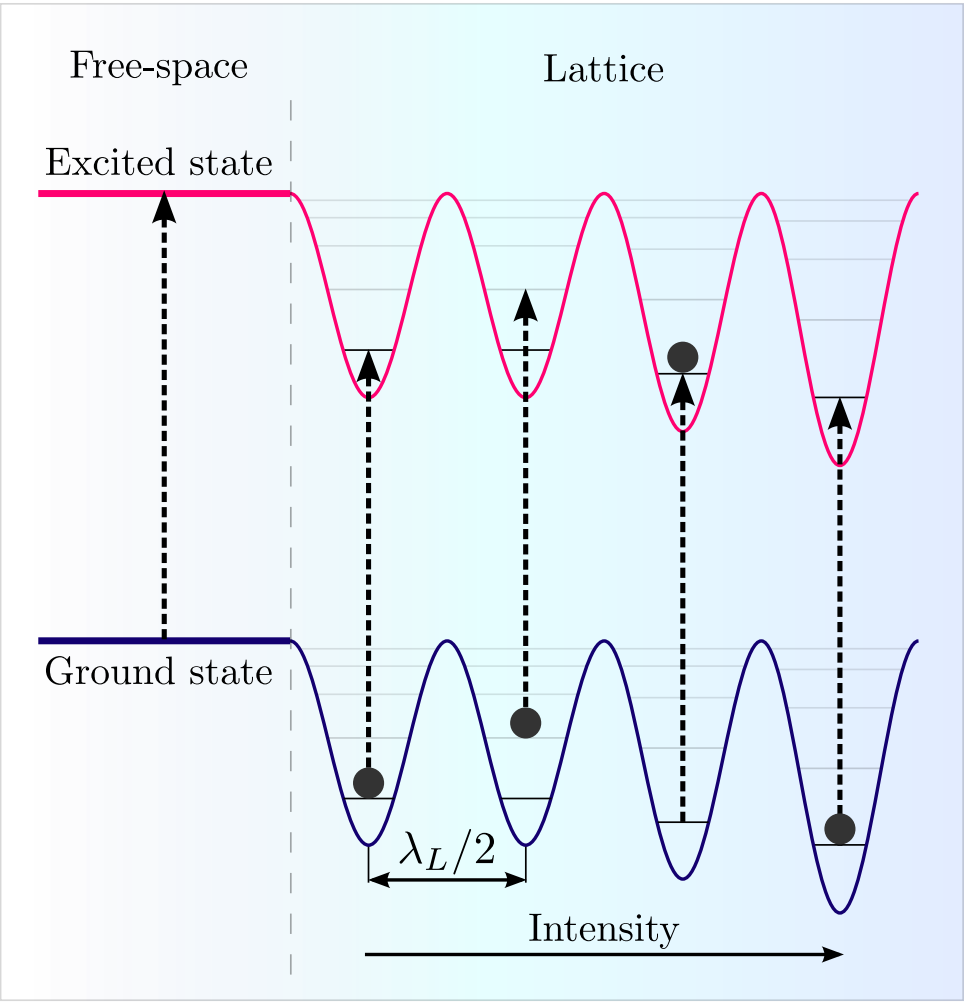


Figure 2.7: **Stark-Free Trapping at the Magic-Wavelength** - A 1D optical lattice potential with Lamb-Dicke confinement. The ground and excited clock states are equally perturbed leading to a cancellation of the Stark-shift.

a frequency metrology lab.

2.4.3 Optical lattice trap and higher order effects

It is my aim here to give the reader an insight into effects of the trapping potential that may intrude on the ultimate accuracy of this technique, with examples given for the case of Sr (for a detailed description see, for example, theses of Boyd [124] and Westergaard [125]). Details of the lattice potential relevant to the following discussion are given in Sec. 3.7.2.

2.4.3.1 Polarisability: Scalar, Vector, Tensor

We can start by considering the higher-order terms of the electric dipole dynamic polarisability. A rigorous application of perturbation theory to second-order (found in Ref. [42]) gives,

$$\alpha_{FM}(\lambda,\hat{\mathbf{e}}) = \underbrace{\alpha_F^S(\lambda)}_{\text{Scalar}} + \underbrace{(\hat{\mathbf{k}}\cdot\hat{\mathbf{B}})\mathcal{A}\frac{M_F}{2F}\alpha_F^V(\lambda)}_{\text{Vector}} + \underbrace{\left(\frac{3|\hat{\mathbf{e}}\cdot\hat{\mathbf{B}}|^2-1}{2}\right)\frac{3M_F^2-F(F+1)}{F(2F-1)}\alpha_F^T(\lambda)}_{\text{Tensor}} \tag{2.11}$$

where $\alpha_F^S(\lambda)$, $\alpha_F^V(\lambda)$, $\alpha_F^T(\lambda)$, are the scalar, vector, and tensor polarisabilities, respectively. $F = I + J$ is the total angular momentum with sub-states M_F (I is the nuclear spin quantum number). The unit vectors $\hat{\mathbf{k}}$ and $\hat{\mathbf{B}}$ represent the lattice wavevector and quantising magnetic field, respectively. $\mathcal{A}$ is the degree of circular polarisation, $\mathcal{A} = \pm 1$ for $\sigma^{\pm}$ circularly polarised light, and zero for linear polarisation.

Clearly, for states with $F = M_F = 0$, the vector and tensor light shifts vanish. This occurs for bosonic isotopes with zero nuclear spin. For fermions of minimal ($I = 1/2$) nuclear spin, such as ^{171}Yb and ^{199}Hg, we see that the tensor contribution vanishes. For other fermions, such as ^{87}Sr and ^{173}Yb, the presence of nuclear spin $> 1/2$ means all terms contribute and the total shift becomes sensitive to polarisation and magnetic field vectors, which must be carefully controlled.

In fermions, due to the hyperfine interaction, the clock transition develops a non-zero differential Landé factor (which is larger in the excited clock state ($\mu_S \gg \mu_I$)) leading to a first order Zeeman-shift. To find the un-shifted transition frequency ν_0, a measurement scheme alternating between stretched $+M_F$ states and $-M_F$ of both ground and excited states is used to average the shift. For example in ^{87}Sr with nuclear spin $I = 9/2$, transitions ν_+ ($M_F = +9/2 \rightarrow M_F' = +9/2$) and ν_- ($M_F = -9/2 \rightarrow M_F' = -9/2$) are measured and ν_0 determined as $\nu_0 = (\nu_+ + \nu_-)/2$. Conveniently, the vector light shift has a similar dependence on M_F and so is absorbed into this field cancellation technique [126].

An added complication comes when considering the size of the polarisabilities them-

selves. For a $J = 0 \rightarrow J' = 0$ transition, where the state is spherically isotropic, α^V and α^T are expected to not contribute [113]. In fermions, the addition of nuclear-spin leads to two effects: 1) hyperfine structure, and 2) state mixing.

To an extent, providing the detuning of the lattice (or coupling) laser is much bigger than the hyperfine splitting, we can approximate the interaction of the lattice as acting on a simplified J system and ignore the hyperfine structure [113]. However, in our quest of making an accurate clock this may not be satisfactory. Since the size of the hyperfine splitting of the excited triplet state $^3\mathrm{S}_1$ (which dominates the shift of the $^3\mathrm{P}_0$ clock state) is much larger than the $^1\mathrm{S}_1$ state (responsible for the ground state shift), we may consider the approximation breaking down first for the $^3\mathrm{P}_0$ clock state and investigate the vector and tensor contributions from this state only as a reasonable estimate of α^V and α^T [124].

Additionally, as a result of the nuclear-spin-induced state mixing, the clock state does not perfectly satisfy $J = 0$. The resulting mixing of the nearby $5s5p\ ^3P_1$ state with the excited $5s5p\ ^3P_0$ clock state has an undesirable effect on vector and tensor polarisabilities, i.e. they increase. In Sr, this effect is most significant for the tensor polarisability which increases dramatically, although it is still orders of magnitude down on the scalar polarisability. In bosonic isotopes utilising the technique of magnetically induced spectroscopy (MIS), which to some extent simulates the effect of nuclear spin, the pure $J = 0$ clock state is mixed with the $J = 1$ triplet P state (see Sec. 3.8.1) resulting in a tensor and vector contribution to the total polarisability. It turns out, however, that the size of the field required in MIS is much lower ($\sim$10 G) than the effective nuclear-spin-induced field ($\sim 10^4$ G) and so we can expect the vector and tensor terms, mediated by the field-dependent mixing coefficients, to be negligible for bosons.

Both effects have been considered for Sr and shown to be manageable [124, 127].

2.4.3.2 Polarisability: M1, E2

The polarisability to a higher-order of multipolar interaction is given by,

$$\alpha^{EM}(\lambda, \hat{\mathbf{e}}) = \alpha^{E1}(\lambda, \hat{\mathbf{e}}) + \alpha^{M1}(\lambda, \hat{\mathbf{e}}) + \alpha^{E2}(\lambda, \hat{\mathbf{e}}) \tag{2.12}$$

So far we have neglected the magnetic dipole α^{M1} and electric quadrupole α^{E2} contributions to the dynamic polarisability as the size relative to α^{E1} is estimated to be $\sim 10^{-7}$ [110]. However, as pointed out in Ref. [128], the multipolar contributions could in fact be significant at the level of 1×10^{-16} fractional frequency due to a spatial mismatch of the lattice potentials . This becomes clear if we consider the field of a 1D optical lattice, which we can describe as a standing wave with electric field amplitude $\mathbf{E} = \mathrm{E}_0 \hat{\mathbf{e}}_y \sin(kz)\cos(\omega t)$. Following Maxwell's equation $\boldsymbol{\nabla} \times \mathbf{E} = -\frac{1}{c}\frac{\partial \mathbf{B}}{\partial t}$, the corresponding magnetic field is given by $\mathbf{B} = -\mathrm{E}_0 \hat{\mathbf{e}}_x \cos(kz)\sin(\omega t)$, which is out of phase with the electric field by $\lambda/4$ (see Fig. 2.8). Since the electric quadrupole (E2) interaction scales with electric field gradient,

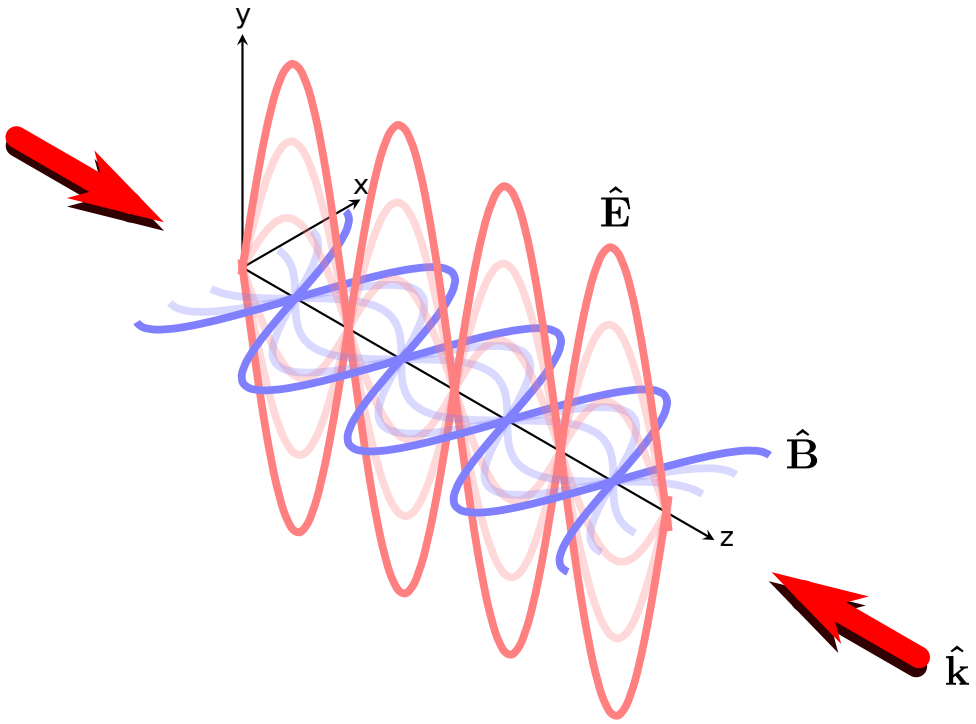


Figure 2.8: **EM Standing Wave** - Depiction of the electric and magnetic fields of a standing wave optical lattice shown to inform consideration of the contribution of magnetic dipole and electric quadrupole interactions.

this is clearly also maximum $\lambda/4$ out from **E** and shares the $\cos(kz)$ spatial dependence of the **B**-field. Scalar multipole clock frequency shifts are therefore dependent on the position of the atom in the trap which is modulated by the atomic motion. The shift is calculated to have a $\sqrt{I}$ dependence so we can not rely on lowering trap depths to moderate the effect. In reply, Katori et al. addressed the potentially problematic shift with an atomic-motion-free definition of the magic wavelength, at the cost of a small but measurable trap dependent offset perturbation $\delta\nu$ [115]. The correction to $\delta\nu$ is found by measuring properties of the trap via the motional sidebands and is expected to be measurable at the 10^{-18} level, with the multipolar interaction effectively removed [115]. Its contribution has been investigated experimentally for ^{87}Sr, but with no resolvable shift at the level of 10^{-17}, even for moderately high trap depths of $150E_R$, the shift is suggested to be much smaller than first expected [112].

2.4.3.3 Hyperpolarisability

To trap neutral atoms requires the application of very large fields ($\sim$ 10 to 100 kW cm^{-2}), especially when compared to trapped ions. We must then consider shifts arising from the interaction of the trapping field with the second order electric susceptibility of an atom, termed hyperpolarisability, $\gamma(\lambda, \hat{\mathbf{e}})$, which scales as I^2 and does not cancel at the

magic wavelength. One contribution to γ is from two-photon transitions, which could be problematic if $\lambda_{2P} \approx \lambda_m$. In Sr, with $\lambda_m \approx 813.43\,\text{nm}$, two such transitions exist; the first order forbidden 5s5p $^3\text{P}_0 \leftrightarrow$ 5s7p $^1\text{P}_1$ transition at $2\times$ 813.36 nm, only 30 GHz away from the magic wavelength, and the fully allowed 5s5p $^3\text{P}_0 \leftrightarrow$ 5s4f $^3\text{F}_2$ at $2\times$ 818.57 nm. The contribution of each to the frequency of the $^1\text{S}_0 \leftrightarrow ^3\text{P}_0$ clock transition has been investigated experimentally for Sr [111]. Trapping intensities about 10 times greater than is normal were used to leverage an enhancement factor of 100 to the measurement sensitivity (since γ contribution $\propto I^2$). Fortunately, for $\lambda_L = \lambda_m$, the residual shift due to two photon transitions was shown to be negligible. A later experiment [112] placed an improved limit of $\delta\nu^{Hyper} = 0.46 \pm 0.18\,\mu\text{Hz}\,(U_0/E_R)^2$ on the size of the shift, demonstrating no impediment to clock performance at the level of $<10^{-17}$ for trap depths $<150\ E_R$, in line with the original estimate of 5×10^{-18} in fractional frequency units for $U_0 = 150$ [110]. A similar investigation has been carried out for Yb [119].

A typical trap depth for Sr operated at the magic wavelength is on the order of $100E_R$ or $\sim$15 µK, corresponding to axial vibrational sidebands at $\pm$68 kHz (compare with ion-traps with $\nu_z \sim \pm 1\,\text{MHz}$). Perhaps naively, one might think to reduce the trap depth to reduce the size of lattice related shifts. This is problematic in two ways: 1) The depth of the trap is already shallow, lowering it further may reduce trap lifetimes through tunnelling loses and necessitate further cooling of the atoms, 2) Tunnelling between lattice sites is increased, leading to a more pronounced Bloch band-structure with an associated frequency broadening and shift. In a uniform lattice potential with degenerate eigenstates across lattice sites, the site-to-site tunnelling follows a resonant process and is therefore strongly enhanced, requiring tight confinement in deep potentials to impede the effect. The key to minimising tunnelling is then in removing the resonance. This occurs for an accelerated lattice, such that each adjacent lattice site is shifted in energy by maz, with m the mass of the atom, a the acceleration, and z the position along the lattice. Such an arrangement can be implemented experimentally by simply orientating the lattice vertically so that gravity provides the acceleration [129]. In doing so trap depths of 5 to 10 E_R should be sufficient to suppress the tunnelling induced shift to the level of 10^{-18} or below [129], with the hyperpolarisability contribution reduced to the level of 1×10^{-19} or less.

It has also been proposed that a "magic-ellipticity" of the lattice field may exist in which the shift vanishes [130].

2.4.3.4 Blue detuned optical lattice

An alternative approach is to use a so-called blue-detuned optical lattice where atoms are trapped in the intensity minima of the lattice field. This occurs for a lattice frequency tuned to the blue side of the dominant interacting dipole transition such that $\alpha(\lambda, \mathbf{e}) < 0$. To confine atoms in three-dimensions (3D) we can no longer rely on the radial intensity

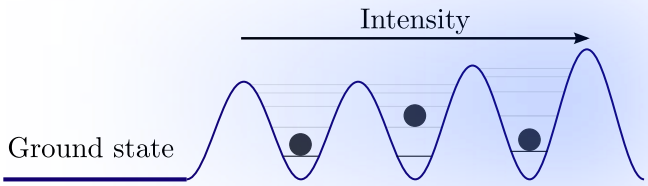


Figure 2.9: **Blue Detuned Lattice Potential** - Atoms are confined at the nodes of the standing wave in regions of low intensity. Successful trapping requires a 3D geometry of optical lattice.

Table 2.3: Neutral-atom optical clocks current status as of mid 2011

Species	Transition	Inaccuracy $\delta\nu/\nu$ (best reported)	Abs. Uncertainty (best reported)	Other Abs. Freq. Measurements
^{87}Sr	$^1S_0$–$^3P_0$	1.4×10^{-16} [131]	8.6×10^{-16} [131]	[132] [117] [126] [131] [133] [134] [135]
^{171}Yb	$^1S_0 \rightarrow ^3P_0$	3.4×10^{-16} [136]	1.4×10^{-15} [136]	[137]
^{174}Yb	$^1S_0 \rightarrow ^3P_0$	1.5×10^{-15} [138]	1.8×10^{-15} [138]	–
^{88}Sr	$^1S_0 \rightarrow ^3P_0$	2.9×10^{-15} [139]	3.0×10^{-15} [139]	[140]
^{40}Ca	$^1S_0 \rightarrow ^3P_1$	6.6×10^{-15} [141]	7.5×10^{-15} [141]	[142]

distribution of a 1D optical lattice and instead adopt a 3D lattice geometry. We also require that a magic wavelength exist for $\alpha(\lambda, \mathbf{e}) < 0$. A quick look at the calculated polarisabilities of states $^1S_0$ and $^3P_0$ (see Sec. 5.1) we see that two such wavelengths exist at $\lambda_{mB1} \approx 390\,\text{nm}$ and $\lambda_{mB2} \approx 360\,\text{nm}$. By measuring the null light shift resulting from the application of a 'blue' laser to atoms trapped in a red-detuned magic wavelength lattice, λ_{mB1} was measured to be $389.889 \pm 0.009\,\text{nm}$ [114]. In such a trap the hyperpolarisability is calculated to be 2×10^{-19} for trap depths of $\sim 60\ E_R$.

2.4.4 Current Status of Neutral Atom Optical Clocks

Since the initial proposals by Katori [110, 113] and first implementation in 2003 [143] optical lattice clock (OLC) development has flourished. By 2006 several absolute frequency

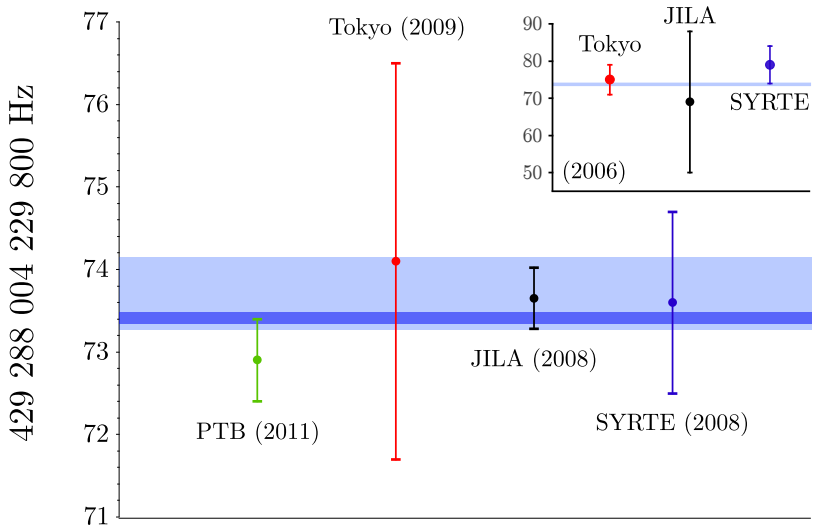


Figure 2.10: **^{87}Sr Clock Frequency Measurement Comparison** - Latest absolute frequency measurements from PTB, Tokyo, JILA, and SYRTE are plotted for ^{87}Sr and weighted mean with standard error shown (thin blue bar). Large (light-blue) bar shows CIPM recommended value of 429 288 004 229 873.7 Hz with associated uncertainty 1×10^{-15}, from initial measurements in 2006 (inset).

measurements of ^{87}Sr had been reported by labs around the world [117, 126, 132] (Fig. 2.10 inset) culminating in the acceptance of the clock frequency 429 288 004 229 873.7 Hz, with a fractional uncertainty of 1×10^{-15}, as a secondary representation of the SI second [144]. Measurements of the bosonic isotopes ^{174}Yb [138] and ^{88}Sr [140] soon followed. The last four measurements of ^{87}Sr (Fig. 2.10) agree to 2.8×10^{-15} – within the combined error bars, which are largely imposed by the reference to Cs. As a result of the lattice clock technique, record level quality-factors where achieved [145], although recently pipped by the Al^+ ion standard (see Table 2.1). Competitive measurements of ^{171}Yb have also been made [136, 137]. A summary of lattice clock accuracy evaluation is given in Table 2.3.

2.4.4.1 Current Limitation: Black-body radiation shift

Black-body radiation (BBR) shifts currently dominate OLC uncertainty budgets (see for example Sr [131, 135] and Yb [136]). At room temperatures (∼300 K) the fractional frequency shifts of Sr and Yb are $\sim 10^{-15}$ with uncertainty $\sim 1 \times 10^{-16}$ (see Table 2.5) which is comparable to the best uncertainty evaluations (see Table 2.3).

The BBR shift arises from an unmatched perturbation of the ground and excited clock states when bathed in thermal radiation of temperature T_{env}, described by Planck's Law with radiation energy density u_{BBR}, related to the square of the time-averaged electric field

Table 2.4: Q comparison of neutral atom optical clock candidates

Species	I	Transition	λ_{clk} (nm)	γ_{nat} (mHz)	Q_{theory}	Q_{exp}	Lab(s)
^{87}Sr	9/2	$^1S_0 \rightarrow ^3P_0$	698	1.2[a]	3.5×10^{17}	2.4×10^{14} [145]	JILA, Tokyo, SYRTE, PTB, NIM, LENS, NPL
^{88}Sr	0	$^1S_0 \rightarrow ^3P_0$	698	–	–	1.7×10^{14} [73]	
^{171}Yb	1/2	$^1S_0 \rightarrow ^3P_0$	578	6.9[a]	7.5×10^{16}		NIST, NMIJ, KRISS, INRIM, Duesseldorf
^{173}Yb	5/2	$^1S_0 \rightarrow ^3P_0$	578	6.1[a]	8.5×10^{16}		
^{174}Yb	0	$^1S_0 \rightarrow ^3P_0$	578	–	–	1.3×10^{14} [147]	
^{199}Hg	1/2	$^1S_0 \rightarrow ^3P_0$	265.6	99[b]	1.1×10^{16}	2.7×10^{11} [149]	SYRTE, Tokyo
^{201}Hg	3/2	$^1S_0 \rightarrow ^3P_0$	265.6	66[b]	1.7×10^{16}	–	
^{25}Mg	5/2	$^1S_0 \rightarrow ^3P_0$	457	0.07[a]	9.2×10^{18}	–	Hannover
^{24}Mg	0	$^1S_0 \rightarrow ^3P_0$	457	–	–	–	
^{43}Ca	7/2	$^1S_0 \rightarrow ^3P_0$	659	0.35[a]	1.3×10^{18}	–	Western Australia
^{40}Ca	0	$^1S_0 \rightarrow ^3P_1$	657	470 000	9.7×10^{11}	2.3×10^{12}[c]	NIST, PTB
^{67}Zn	5/2	$^1S_0 \rightarrow ^3P_0$	309.5	2.5[d]	3.9×10^{17}	–	–

[a] Ref. [146]
[b] Ref. [148] - Avg. of theory and experiment.
[c] A 200 Hz fringe width is reported (NIST) using the Ramsey-Bordé technique.
[d] Ref. [150]

by,

$$\mathcal{E}^2_{\mathrm{BBR}} = \frac{u_{\mathrm{BBR}}(T_{\mathrm{env}})}{\epsilon_0} = \frac{8\pi h}{\epsilon_0 c^3}\int_0^\infty \frac{\nu^3}{\exp(h\nu/k_{\mathrm{B}}T_{\mathrm{env}})-1}\,\epsilon(\nu)\,\mathrm{d}\nu = \underbrace{\frac{8\pi^5 k_{\mathrm{B}}^4}{15\epsilon_0 h^3 c^3}}_{c_1}\cdot T^4_{\mathrm{env}} \tag{2.13}$$

where $\epsilon(\nu)$ is a frequency dependent factor which is unity everywhere for a perfect blackbody. In atomic units ($k_{\mathrm{B}} = \hbar = \frac{1}{4\pi\epsilon_0} = 1$, and $c = 1/\alpha_f$), as is often written in the literature, the attenuation factor $c_1 = \frac{4}{15}(\pi\alpha_f)^3$, which is related to the Stefan-Boltzmann constant, σ, by $\sigma = c_1\epsilon_0 c/4$. At room temperature (300 K) the radiation peaks at around 10 µm. This is much longer than the relevant transitions which couple to the $|^1\mathrm{S}_0\rangle$ and $|^3\mathrm{P}_0\rangle$ states (see Sec. 5.2) and so we can treat the perturbation as quasi-static, using the static polarisability $\alpha(0)$, with a small dynamic correction η_j. The shift of state $|j\rangle$ is then calculated in the usual way as,

$$\delta\nu_{\mathrm{BBR}}\,|j\rangle = -\frac{1}{2h}\alpha_{|j\rangle}(0)\,\mathcal{E}^2_{\mathrm{BBR}}\,[1+\eta_j] = -\frac{c_1}{2h}\alpha_{|j\rangle}(0)\,T^4_{env}\,[1+\eta_j] \tag{2.14}$$

with the differential shift of the clock transition as,

$$\delta\nu_{\mathrm{BBR}} = \delta\nu_{\mathrm{BBR}}\,|^3\mathrm{P}_0\rangle - \delta\nu_{\mathrm{BBR}}\,|^1\mathrm{S}_0\rangle \tag{2.15}$$

Due to the isotropy of the field, the vector and tensor contributions average out and we consider only the scalar polarisability term, which is dominated by electric-dipole (E1) transitions. For Sr, the BBR-induced shift of the ground and excited clock states in the E1 approximation are [151],

$$\delta\nu^{\mathrm{E1}}_{\mathrm{BBR}}\,|^1\mathrm{S}_0\rangle = -1.698 \pm 0.002\,\mathrm{Hz} \tag{2.16}$$

$$\delta\nu^{\mathrm{E1}}_{\mathrm{BBR}}\,|^3\mathrm{P}_0\rangle = -4.052 \pm 0.032\,\mathrm{Hz} \tag{2.17}$$

and the differential shift of the clock transition is,

$$\delta\nu_{\mathrm{BBR}} = -2.354 \pm 0.032\,\mathrm{Hz} \tag{2.18}$$

The 1.4% error, which encroaches at the 7.5×10^{-17} level, is dominated by the uncertainty in the calculated excited state polarisability [151, 152]. Around 97 % of the ground state shift arises from the E1 interaction with the $^1\mathrm{P}_1$ state which is well-characterised, leading to an uncertainty at the level of 0.1 % [152]. The dynamic contribution is neglected in the ground state but contributes 2.7 % to the excited state shift (or 5 % of the total shift), primarily as a result of coupling to the 5s4d $^3\mathrm{D}_1$ state in the infra-red (at 2.6 µm, see Fig. 3.1) [151].

For completeness, we should briefly mention here the contribution of higher order multipole terms, in particular the magnetic-dipole (M1) and electric-quadrupole (E2) terms

which follow the electric-dipole term (E1) in the decay rate expansion of $e^{i(\mathbf{k}\cdot\mathbf{r})}$. It is noted by Porsev [151] that multipolar terms (EJ, MJ) scale as (in atomic units) $\alpha_f^{2J+1}\, T_{env}^{2J+2}$, providing the relevant transition energies are much greater than the thermal radiation energy (see for example Eq. (2.13) cast in the E1 approximation). The M1 interaction, in comparison to E1, is anyway suppressed by a factor of $\alpha_f^2 \sim 10^{-4}$. The E2 term is suppressed by $\alpha_f^2 \left(\frac{k_B T_{env}}{E_h}\right)^2 \sim 10^{-10}$, where E_h is the Hartree energy (the atomic unit of energy), as noted. For the Sr ground state and $T_{env} = 300\,\mathrm{K}$ the E2 term is negligible and can be ignored, however, the M1 term contributes at the level $\delta\nu_{\mathrm{BBR}}^{M1}\left|{}^1\mathrm{S}_0\right\rangle \approx 2\times10^{-4}\,\mathrm{Hz}$ or 5×10^{-19} in fractional units. We need not worry about this for the time being but keep in mind that it may eventually require consideration at the projected OLC inaccuracy of 1×10^{-18} [116].

Dealing with the excited state is complicated by the existence of transitions between states of the ${}^3\mathrm{P_J}$ fine-structure manifold which have wavelengths in the region of thermal wavelengths – the M1 allowed ${}^3\mathrm{P}_0 \rightarrow {}^3\mathrm{P}_1$ transition at 53.5 µm and E2 allowed ${}^3\mathrm{P}_0 \rightarrow {}^3\mathrm{P}_2$ transition at 17.2 µm – so we may expect a large contribution. However, owing to the broad thermal radiation distribution their contribution is washed out and they are further attenuated by powers of the coupling constant α_f. The shifts have been calculated as $\delta\nu_g^{\mathrm{M1}} = 2.4\times10^{-5}\,\mathrm{Hz}$ and $\delta\nu_g^{\mathrm{E2}} = 2.5\times10^{-8}\,\mathrm{Hz}$ and can be completely neglected [151].

For convenience, the fractional BBR shift is often written in the form,

$$\frac{\delta\nu_{\mathrm{BBR}}}{\nu_0} \approx \beta\left(\frac{T_{\mathrm{env}}}{T_0}\right)^4 \tag{2.19}$$

where β is the dimensionless BBR static shift coefficient, defined in terms of the scalar Stark coefficient k_s as,

$$\beta = c_1 \cdot \frac{T_0^4}{\nu_0}\, k_s\ ; \qquad\qquad k_s = -\frac{1}{2}\left[\alpha_e^S(0) - \alpha_g^S(0)\right] = -\frac{1}{2}\Delta\alpha(0) \tag{2.20}$$

Values of $\delta\nu_{\mathrm{BBR}}/\nu_0$ at 300 K ($\approx \beta$ for $\eta \ll 1$) for several divalent atoms are listed in Table 2.5.

Clearly, knowledge of the shift coefficient is only half the story and we must also concern ourselves with measurement of the black-body environment surrounding the atoms. Modifying Eqn. 2.14 to include the temperature uncertainty ΔT_{env}, the BBR shift uncertainty can be written as,

$$\Delta\left|\delta\nu_{\mathrm{BBR}}\left|j\right\rangle\right| = \left|\frac{c_1}{2h}\alpha_{|j\rangle}(0)\, T_{env}^3\left[1+\eta_j\right]\right| \Delta T_{env} \tag{2.21}$$

For example, for Sr, a ΔT_{env} of 1 K around 300 K corresponds to a fractional uncertainty of 7.3×10^{-17}. When added in quadrature with the uncertainty in the shift coefficient, the total BBR related uncertainty is at the level of 1×10^{-16}. This imposes the limit to

Table 2.5: Comparison of BBR-induced shifts of the $^1S_0 \rightarrow {}^3P_0$ clock transition in neutral atom optical clocks.

		BBR Shift @ 300 K		
Species	ν_0 ($\times 10^{14}$ Hz)	$\delta\nu_{\mathrm{BBR}}$ (Hz)	$\delta\nu_{\mathrm{BBR}}/\nu_0$ ($\times 10^{-16}$)	Ref.
Sr	4.29	-2.354 ± 0.032	-55.0 ± 0.7	[151]
Ca	4.54	-1.171 ± 0.017	-26.0 ± 0.4	[151]
Yb	5.18	-1.25 ± 0.13	-24 ± 3	[151]
Mg	6.55	-0.258 ± 0.007	-3.9 ± 0.1	[151]
Hg	11.3	-0.181	-1.6	[120]

the current inaccuracy evaluation of Sr OLCs, as previously mentioned.

The black-body environment surrounding the atomic sample in a typical apparatus can be difficult to characterise for a number of reasons. Firstly, many atomic species considered here (Ca, Sr, Yb, Mg) have low vapour pressures at room temperature and therefore must be heated to obtain a sufficient atom flux in the trapping region. For Sr, an oven source (see Sec. 3.2) operating at $T_{oven} \sim 900\,\mathrm{K}$ is typical. The corresponding BBR shift depends on the exposure of the atomic sample to the oven radiation which is primarily determined by considering the direct line-of-sight radiation seen by the atoms in a solid angle Θ, given as,

$$\delta\nu_{\mathrm{BBR}}\,|j\rangle = \frac{\Theta}{4\pi}\left(-\frac{c_1}{2h}\alpha_{|j\rangle}(0)\,T_{oven}^4\,[1+\eta_j]\right) = \frac{\Theta}{4\pi}\,\delta\nu_{\mathrm{BBR}}^{oven}\,|j\rangle \tag{2.22}$$

For radiation at 900 K the BBR shift in Sr is around 180 Hz ($= \delta\nu_{\mathrm{BBR}}^{oven}\,|j\rangle$). While this is potentially highly problematic, by designing the vacuum system to minimise Θ it is feasible to reduce the contribution of shift to the level of 1×10^{-19} (for example a 1 mm aperture placed half a metre from the atomic sample in line with the oven).

In addition, there will be an influence by indirect radiation from the oven which is channelled down the vacuum apparatus interior walls. Again, this may be reduced by introducing apertures between the oven and atomic sample but only to the limit of the required atomic beam diameter. To further reduce the channelling the relevant vacuum chamber interior walls may be treated with 'black' (IR absorptive) coatings, although it is often undesirable to introduce additional substances into the vacuum. An alternative is to introduce a baffle structure to prevent grazing incidence guiding of radiation; perhaps most simply this can be achieved by threading the interior of the atomic beam tube. Of course, if we could block the atomic beam and therefore oven radiation during the interrogation period we could quite reasonably neglect all influence of the oven, except perhaps conductive heating of the vacuum system which may produce a temperature

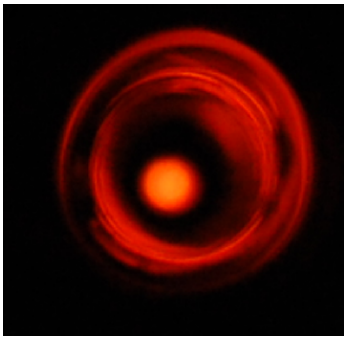


Figure 2.11: **Looking into the oven** - A photograph showing the black-body radiation visible in the optical domain emitted from a hot oven (∼900 K). Photograph taken through end viewport ∼1 m downstream of oven. Centre dot is direct emission and the surrounding halo indirect as channelled by the stainless steel DN16 atomic beam tube.

gradient in the interrogation region of the vacuum system (this, however, is unlikely to be significant, especially in oven designs where the heaters are appropriately shielded and at best are inside the vacuum system). To effect this a mechanical shutter could be introduced into the vacuum system, although this brings with it added complexity and operational risk. Perhaps a more satisfying solution is to deflect or transport atoms out of the line-of-sight of the oven by exploiting optical forces acting on the atomic sample.

The next difficulty comes in defining the majority environment (most of the 4π steradian) seen by the atoms. The surrounding vacuum system is largely composed of stainless steel and quartz-glass (fused silica is common) windows. The emissivity of these surfaces differs and complicates the evaluation of the BBR field.

To address the influence of the BBR shift, we can consider two approaches: **i)** characterisation and control, and **ii)** minimisation.

Characterisation and control. At the projected inaccuracy level of 1×10^{-18}, the room temperature BBR shift of Sr must be known to approximately 0.02 %. This requires sufficient knowledge of both the shift coefficient, and the blackbody environment of the atoms, which must be controlled to the level of 0.02 K for an inaccuracy approaching 1×10^{-18}. The shift coefficient can be calculated from the atomic polarisabilities of the clock states, much like in the determination of the magic wavelength, only here we must consider the coupling of states across a broad BBR spectrum. This requires a precise knowledge of the frequencies and oscillator strengths of the transitions dominating the shift (see Sec. 5.2), which can be measured experimentally [152].

Alternatively, we may aim to measure the shift directly by varying the temperature of a well-defined blackbody environment, or BBR chamber, which surrounds the atoms during clock interrogation. Atoms may be moved into such a chamber using a moving lattice arrangement [153, 154]. The coefficient can then be determined by a fit to the function in Eq. 2.19. The BBR chamber can also serve in normal clock operation to ensure the

BBR environment remains well-defined, with the hope of achieving 0.02 K temperature uncertainty (for our ultimate accuracy goal). This is of course very challenging and it is more realistic to expect a 0.1 K temperature uncertainty, stemming from temperature gradients and instabilities, and measurement inaccuracies, which corresponds to a fractional uncertainty of 7.3×10^{-18}.

Minimisation. Another approach is to reduce the temperature of the environment seen by the atoms with a cryogenic apparatus [154]. Operation at 77 K (with liquid nitrogen) reduces the shift to approximately 10 mHz or 2.4×10^{-17} in fractional units and the associated uncertainty is 3.0×10^{-19}. In doing so the constraint on knowledge of the temperature is relaxed to 1 K for an uncertainty of 1.2×10^{-18}.

To tackle the shift from the other side, an optical clock based on Hg has been proposed [120]. The room temperature shift is -0.181 Hz which, coupled with the high clock frequency of $\sim 1.13 \times 10^{15}$ Hz, gives a fractional shift of 1.6×10^{-16}. A temperature uncertainty of 1 K around room temperature provides a 2.1×10^{-18} factional uncertainty, without the added complexities of a cryogenic apparatus. Furthermore, if we did want to go to cryogenic temperatures the shift is reduced to $\sim 7 \times 10^{-19}$ and the uncertainty is relaxed to plus $\sim$20 K – the contribution of the BBR shift is well and truly minimised.

The relevant transitions in Hg (in the UV) are in most part out of range of semiconductor laser systems, requiring more complex and sizable laser apparatus. In contrast, Sr OLC operation can utilise all-semiconductor laser technology, yielding a much simpler apparatus. So, we will stick with Sr for now and explore some of the techniques discussed to manage the BBR shift.

2.5 Conclusion

To summarise, the hyperpolarisability contribution should not pose a limitation to the accuracy of lattice clocks any time soon and can be suppressed to the level of 10^{-19} [112, 114] or even removed [130] depending on trapping parameters. The multipole spatially dependent shift [128] has not been observed at the level of 1×10^{-17} [112] and a situation has been identified in which the spatial dependence is removed at the cost of a small shift which should be measurable at the level of 1×10^{-18} [115]. The vector polarisability is absorbed into the field cancellation measurement technique between stretched spin states [126] and the tensor shift (not present for $F = 1/2$ states) is minimised for the appropriate field geometries (and can be absorbed into the evaluation of the magic wavelength). Satisfied that the magic wavelength lattice trapping technique promises an accurate clock we can go ahead and build one of our own.

3

A Strontium Optical Lattice Clock

3.1 Electronic atomic structure

The periodic table orders and groups elements according to their electronic configuration. Group-1 elements, known as the alkali metals, contain only one valence electron (like hydrogen) and are therefore an attractive starting point for studies in theoretical and experimental atomic physics. The spin 1/2 electron gives rise to a structure of spin doublet states. A well-known example of these is the $^2\mathrm{S}_{1/2}$ ground state which splits via the hyperfine interaction to provide the Cs (and Rb) microwave clock transition. Several strong dipole transitions are allowed from the $L = 0$ ground state to higher lying $L = 1$ states. These $S \rightarrow P$ transitions have been exploited in many laser cooling experiments over the years, including use in the first demonstrations of laser cooling and trapping neutral atoms [155, 156], and as a crucial step towards the realisation of the first Bose-Einstein-Condensate (BEC) [157, 158]. However, the lack of a suitable clock transition in the optical domain turns our attention elsewhere.

Next in the periodic table is the group-2 alkaline-earth metals, which contain two valence electrons. The two-electron pairing gives rise to spin singlet ($S = 0$) and spin triplet ($S = 1$) states, for anti-parallel and parallel spin pairings, respectively. Similarly to alkali metals, broad (almost) closed electric-dipole (E1) transitions suitable for initial manipulation of atomic motion (slowing, cooling, trapping) exist from $S \rightarrow P$, here from the $^1\mathrm{S}_0$ ground state to the $^1\mathrm{P}_1$ states. The simplicity of the spin singlet $J = 0$ ground state removes the complications of ground state optical pumping and the model of the 2-level atom is nearly ideally realised. However, the number one attraction for optical frequency standards comes courtesy of the lowest lying excited triplet states of the $^3\mathrm{P}_\mathrm{J}$ manifold.

On first sight, transitions between the spin singlet ground state and triplet P_J manifold appear to be strictly forbidden by the selection rule $\Delta S = 0$, which holds in the Russell-Saunders (spin-orbit) LS-coupling regime, with $J = L + S$. However, for heavier atoms the LS-coupling progressively breaks down and in the extreme case J is better described

Table 3.1: Sr transition properties.

Transition	Wavelength (nm)	Transition rate Γ (10^6 s^{-1})
1	460.86	190.01
2	293.27	1.87
3	689.45	0.0469
4	698.4	–
5	707.21	39.73
6	688.02	25.89
7	679.29	8.97
8	496.93	12.8
9	483.34	34.35
10	474.33	41.67
11	2603.1	0.2712
12	6.5×10^3	3.9×10^{-3}
13	1.8×10^3	2.2×10^{-3}
14	1.9×10^3	1.1×10^{-3}
15	717	9

by the sum of each individual angular momentum vector, j_1 and j_2, as $J = j_1 + j_2$, where we are said to be in the jj-coupling regime, and $j = l + s$ uses the individual electron spin and orbital angular momentum. Here, the spin triplet states are mixed with the corresponding singlet states and thus $\Delta S = 1$ transitions, commonly referred to as intercombination lines, acquire an E1 transition moment, although typically much smaller than their $\Delta S = 0$ counterpart. In the case of the $^1S_0 \leftrightarrow {}^3P_1$ spin forbidden transition, the coupling results in the $^3P_1$ state acquiring a small admixture of the $^1P_1$ wavefunction and with it a weak electric-dipole moment. Comparing the rates of this transition in Table 3.3 (later in the text) it is clear that the effect is enhanced for heavier atoms). The $^1S_0 \leftrightarrow {}^3P_1$ transition has only one decay route back to the ground state and as a result of its narrow linewidth is well suited to narrow-line Doppler cooling.

For the clock transition we can benefit from violating even more rules. The $^1S_0 \rightarrow {}^3P_0$ ($\Delta S = 1$, $J = 0 \rightarrow J = 0$) transition is doubly forbidden, by both spin and angular momentum. As a consequence the natural linewidth is pretty much zero in bosonic isotopes (although we can change this with external fields), and $\ll 1$ Hz in fermions, courtesy of the nuclear-spin-induced hyperfine interaction. The hyperfine quenched transition linewidth

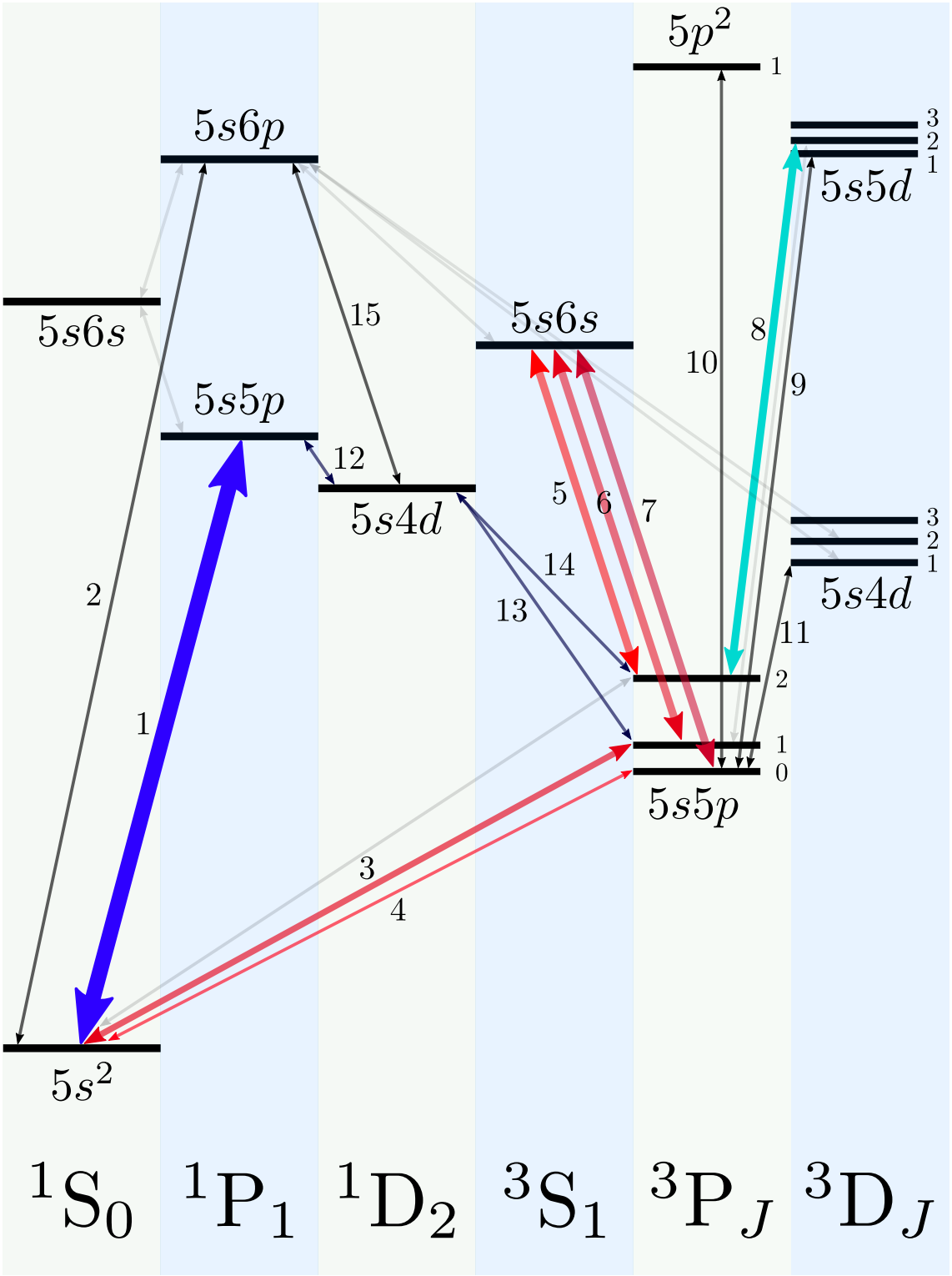


Figure 3.1: **Strontium Energy Level Scheme** - Relevant energy levels for Sr (hyperfine structure not shown). Transition properties are listed in Tab. 3.1.

for a selection of candidate reference atoms is given in Table 2.4. The $J = 0 \rightarrow J = 0$ transition is ideally suited to clock use, as discussed in section 2.4.3.1.

The electronic structure described here for group-2 atoms is typical of divalent atoms and is well-suited for implementation as a frequency standard in the optical domain. Candidate reference atoms for optical lattice clock (OLC) use include group-2 alkaline-earth elements Mg, Ca, Sr, and Ba, group-12 transition metal elements Zn, Cd, and Hg, and Yb from the lanthanide series, although much of the focus to date has been on Sr (as first proposed) [116, 117, 126, 131–135], Yb [136, 147, 159, 160], and recently Hg [120, 149].

3.1.1 Strontium

Table 3.2: Stable isotopes of Sr and their natural abundance.

Atomic mass number	Nuclear spin	Natural abundance (%)
88	0	82.58
87	9/2	7.00
86	0	9.86
84	0	0.56

Strontium, atomic number $Z = 38$, has four stable, naturally occurring isotopes with atomic mass numbers 84, 86, 87, and 88, shown in Table 3.2. Generally, for isotopes of even atomic number and atomic mass number the spin pairing of nucleons results in a total nuclear spin $I = 0$. This follows for three of the Sr isotopes, ^{84}Sr, ^{86}Sr, and ^{88}Sr, each bosonic with nuclear spin $I = 0$. The remaining odd isotope is fermionic with nuclear spin $I = 9/2$, which brings with it hyperfine structure and an intrinsic non-zero clock transition linewidth $\sim$1 mHz. Sr has a ground state electronic configuration [Kr] $5s^2$ and electronic structure as shown in Figure 3.1.

3.2 A Strontium Source

The first challenge we face in making our clock is producing a vapour in vacuum that we can work with. For this we require knowledge of the vapour pressure of the atomic species at a given temperature. This can be modelled by the Antoine equation, which is an adaptation of the Clausius-Clapeyron relation, as [161],

$$\log_{10} P = A + \frac{B}{T} + C \log_{10} T + DT + ET^2, \tag{3.1}$$

where P is the vapour pressure in units of mmHg and T is the temperature in kelvin. The Antoine equation arises from an empirical fit to experimental data and fits well over

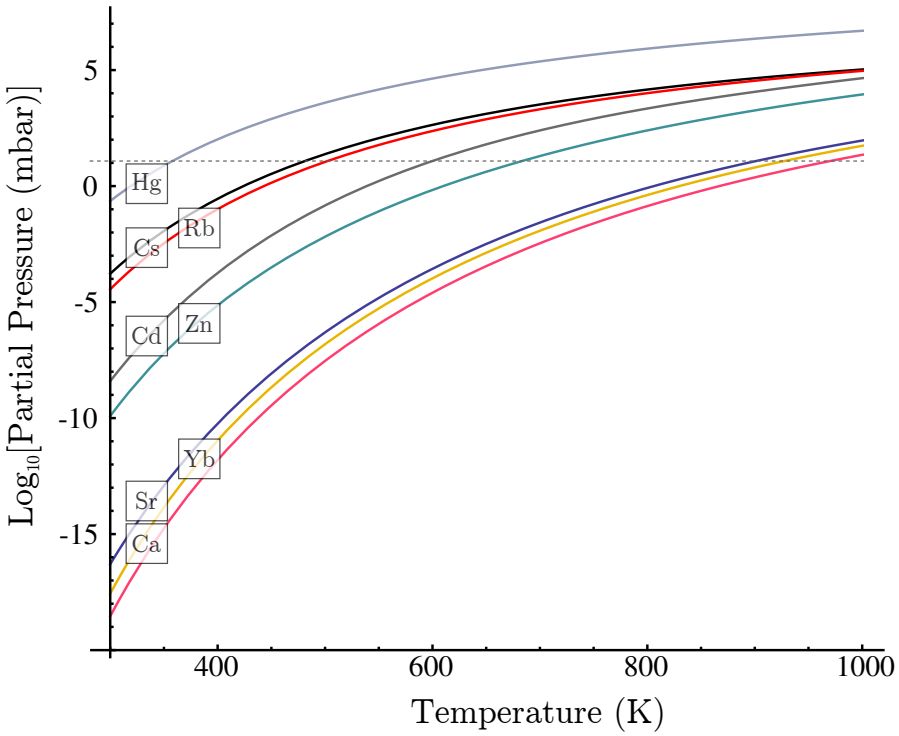


Figure 3.2: **Vapour Pressures** - A comparison of vapour pressures for a selection of atomic species of interest to quantum frequency metrology. Data is taken from Chemical Properties Handbook [161] and has been extrapolated out of specified temperature ranges for approximate comparison only.

a given range of temperatures. A, B, C, D, and E are the fit parameters, determined for each atomic species. For comparison, vapour pressure versus temperature for a number of relevant atomic species including Sr are plotted in Figure 3.2.

3.2.1 Vapour source

The first disadvantage of Sr (also Ca, and Yb) relative to alkali metals Cs and Rb is the reduced (by around 2 orders of magnitude) room temperature vapour pressure. To reach similar vapour pressures, and therefore atomic densities n (following the ideal gas equation, $n = P/k_{\mathrm{B}}T$), Sr must be heated to around 600 K. In a volume of gas in thermal equilibrium (here the atomic vapour), the probability distribution of particle speeds is described by the Maxwell speed distribution,

$$f(v) = \frac{4}{\sqrt{\pi}} \frac{1}{\beta^3} v^2 \exp(-v^2/\beta^2) \tag{3.2}$$

where v is the particle velocity,

$$\beta = \sqrt{(2k_{\mathrm{B}}T/m)} \tag{3.3}$$

is the most probable velocity, and

$$\tilde{v} = (2/\sqrt{\pi})\beta \tag{3.4}$$

is the mean (rms) particle velocity. In a heated sample we have a broader distribution of particle speeds with a larger mean thermal energy, in contrast to our ultimate aim.

3.2.1.1 Vapour cell

Conveniently, Cs and Rb vapour can be manufactured into simple vapour filled glass cells suitable for use in simple spectroscopy experiments. A similar cell for strontium is not straightforward. Alkaline-earth metals are highly corrosive and at elevated temperatures the reaction with silicates in glass is problematic. Additional constraints are also placed on vacuum component materials; copper gaskets and brazes, often used in ultra-high vacuum (UHV) systems, are at risk of corrosion. A number of pursuits into alkaline-earth metal vapour cells making use of sapphire, which is highly resistant to corrosion and does not react with Sr (at least at moderate temperatures $< 900\,\mathrm{K}$ [162]), have been executed with reasonable success [162, 163]. Notably, an alumina[1] ceramic cell with sapphire viewports was constructed at JILA and used in Sr narrow-line cooling experiments [163]. To achieve a resilient vacuum tight seal between the viewports and ceramic block a method of glass frit sealing [162] was adopted. The cell was operated at $\sim 650\,\mathrm{K}$ reaching atomic densities on the order of $10^9\,\mathrm{cm}^{-3}$, sufficient for loading a MOT. Because sapphire is a uniaxial birefringent crystal, care must be taken to use the proper crystal axis orientation to avoid unwanted polarisation changes of transmitted light. For this we require the optic or extraordinary axis, which in sapphire is the "fast" axis (also c-axis), perpendicular to the window face or at the "zero angle", often referred to as c-cut or z-cut. Sapphire also has a relatively high refractive index ($n \approx 1.76$) which leads to a surface reflectivity $R \approx 7.6\,\%$ ($R = [(n_0 - n_1)/(n_0 + n_1)]^2$) which is about twice that of uncoated glass. An anti-reflection (AR) coating may be applied to the outer surface but the interior must be kept clear of corrodible substances.

3.2.1.2 Heat pipe

Another approach is the heat pipe [164, 165]. Although designs usually offer limited optical access, heat pipes can be useful for simple spectroscopy, for example, in locking lasers to atomic absorption lines. An example is the Sr heat pipe developed for spectroscopy of the $^1\mathrm{S}_0 \leftrightarrow {}^3\mathrm{P}_1$ intercombination line for the purpose of long term stabilisation of a laser used in narrow line cooling [166]. Again, sapphire provides a window to the Sr vapour, however, to avoid the difficulties of vacuum sealing viewports at high temperatures, a buffer zone, in which a clean vacuum is maintained, exists at either end of the pipe. Standard viewports

[1] A polycrystalline form of sapphire also known as polycrystalline alumina (PCA).

(water-cooled as a precaution) are used to vacuum seal the pipe and the Sr vapour is nominally contained in the central, sapphire and stainless steel enclosed, region, or cell. Heat is delivered to the cell in close proximity to the sapphire windows to encourage Sr to deposit elsewhere of the optics. Due to the small oscillator strength of the intercombination line, a high optical absorption path length is required to provide adequate signal. The Sr heat pipe described here has an optical path length of 60 mm, requiring an atomic density of $10^{12}\,\mathrm{cm}^{-3}$, which is achieved at a cell temperature of $\sim 675\,\mathrm{K}$.

3.2.1.3 Benefits and Issues

It is important to maintain a low residual gas pressure, $< 10^{-8}\,\mathrm{mbar}$, in the vacuum to minimise background gas collisions which are detrimental to trap lifetimes [167]. Typically an ion pump services this requirement. Of course, we aim not to remove the atomic vapour so will have to tolerate collisions from this background. The vacuum is helped also by the gettering properties of Sr. Evaporated Sr deposited on the vacuum system walls can, over time, form a very effective so-called evaporated getter film, which serves in the sorption of many atmospheric gasses [168, 169]. Generally, due to the recycling nature of vapour cells and heat pipes we should expect long operational lifetimes, without replenishment of the sample reservoir, limited only by chemical losses of the atomic sample and of course that which is sorbed by the vacuum pump. Ultimately, the high temperature environments and relatively large background pressures are not appropriate for high precision spectroscopy. In particular, for shallow trap depths, such as the dipole lattice traps used in OLCs, trap losses from background collisions are essential in determining trap lifetime [170] and can severely limit clock interrogation times, and therefore achieved Q.

An obvious drawback for clock spectroscopy is the large BBR shift of the clock transition, which is $> 50\,\mathrm{Hz}$ at 650 K and is difficult to control over a large volume, especially where different materials are present. A more subtle consequence of the elevated temperature is BBR quenching of metastable states; a problem which was observed for the magnetically trapped $^3\mathrm{P}_2$ metastable state in Sr [171] and studied in determination of the $^3\mathrm{P}_2$ state lifetime [172]. The quenching results from BBR driven excitation to states of the nearby $5s4d\,^3\mathrm{D}$ manifold (transitions in the infra-red) which can decay to the ground state via the $^3\mathrm{P}_1$ state ($^3\mathrm{P}_1$ state lifetime $\sim 21\,\mu\mathrm{s}$). For the clock transition in Sr the expected hyperfine induced $^3\mathrm{P}_0$ state lifetime is $\sim 132\,\mathrm{s}$. At temperatures of just 340 K the BBR quenching rate begins to dominate and at 600 K the state lifetime is severely quenched to $\sim$100 ms (see section 3.8.2).

3.2.2 Atomic beam apparatus

An alternative method, commonly used in atomic physics experiments, is the atomic beam apparatus. The beam is formed by a controlled expansion of gas into a region of low pressure (typically UHV, residual gas pressure, P_{chmbr}, $< 10^{-9}\,\mathrm{mbar}$) from a heated source

at pressure P. At low source pressures, the geometry of the beam is defined primarily by the dimensions of the aperture, or nozzle, which connects the heated source to the experimental chamber. In this way, a highly collimated and intense flux of atoms may be delivered to the experimental chamber, with the issues surrounding the hot source (3.2.1.3) far removed.

3.2.2.1 Velocity distribution

For an effusive source with beam exiting along z and Maxwellian source distribution, the longitudinal velocity distribution (to direction of major flow) is [173],

$$I(v_z) = \frac{2I_0}{\beta^4} v_z^3 \exp(-v_z^2/\beta^2) \tag{3.5}$$

where $I(v_z)\,\mathrm{d}v_z$ is the beam intensity in a velocity interval $\mathrm{d}v_z$ in units of atoms $\mathrm{s}^{-1}\,\mathrm{m}^{-2}$, such that the total intensity $I_0 = \int_0^\infty I(v_z)\,\mathrm{d}v_z$. Characteristic velocities are:

- Most probable velocity: $v_{mp} = \beta\sqrt{(3/2)}$
- Average velocity: $v_{av} = (3/4)\beta\sqrt{\pi}$
- RMS velocity: $v_{\mathrm{RMS}} = \beta\sqrt{2}$

The additional dependence on v in Eq. 19, compared to Eq. 3.2, is apparent from a consideration of the probability of a particle escaping the source (a fast atom has many more attempts at finding an accepted escape trajectory, per unit time, than a slow atom). The transverse velocity distribution is defined by the nozzle geometry, which constrains the allowed escape trajectories from the source, and is dependent on the longitudinal velocity. Further details of the atomic beam flow characteristics are given in Appendix A.

3.2.2.2 Sr oven construction

The atomic beam source typically consists of a heated crucible, filled with the atomic sample ($\sim$ few grams), and a channel nozzle, often heated to temperatures above the crucible to avoid blockages by deposition. For simplicity, heaters can be outside the vacuum, although it is preferable for reasons of efficiency and thermal isolation to mount them internally. For some applications it may be preferable to use a commercially available dispenser[1] source which benefits from its ease of implementation. A Sr dispenser spectroscopy cell, used for laser stabilisation, has been built and operated at Durham University [174], where they are also pursuing a compact Sr dispenser fed pyramid MOT [175] apparatus [176]. Such dispensers offer a simple solution to atomic beam source production but with only crudely collimated beams much of the sample may be wasted if further apertures

[1] For example, ALVASOURCES from Alvatec, available for a number of alkali and alkaline-earth metals, including Cs, Rb, Sr, Yb, Ca, and Mg.

are required to collimate the output. Such a dispenser may be useful for loading of a 2D MOT which can capture and compress a relatively large atomic distribution to form a well collimated atomic beam source (see for example the Sr optical lattice clock project at the University of Birmingham).

The NPL Sr oven (version 1 - designed by Y. Ovchinnikov) is shown in Fig. 3.3. At the core of the oven is a heated stainless steel crucible, with capacity for roughly 4 g of dendritic Sr, and a separately heated nozzle arranged inside two layers of stainless steel radiation shielding. The crucible and nozzle are press fit into copper surroundings around which mineral insulated steel sheathed heater wire is wound, enclosed by a stainless steel outer casing. K-type thermocouples insulated by 2 hole ceramic beads are attached at points close to the nozzle and crucible and monitored with the aim of keeping the nozzle temperature above the crucible by >50 K to prevent blockages. The oven assembly is mounted to a 4.5″CF stainless steel flange by a central stainless steel shaft. In operation, with the oven heated to 900 K, heat conduction to the flange results in external temperatures of only ∼330 K, and radiative heat transfer to the surrounding vacuum walls is small.

We have tested two nozzle configurations: one multichannel, and one single channel. The multichannel nozzle consists of around 50 stainless steel tubes, dimensions 200 µm diameter, 10 mm length, packed into a 2 mm diameter stainless steel sleeve which is press fit into a copper cylinder for heating. The oven ran successfully for an equivalent period of several continuous months of operation. Inspection of the oven after complete expulsion of the first Sr load revealed excessive corrosion to the nozzle copper surrounding (Fig 3.3 image d)) and consequently the nozzle was partially blocked. Unfortunately damage was incurred during retrieval of the nozzle from the copper and a replacement multichannel nozzle unavailable. Due in part to time constraints, a simplified replacement nozzle was pursued consisting of a single channel, dimensions 1 mm diameter, 11 mm length, machined in the centre of a stainless steel cylinder. The additional nozzle heater was removed and the nozzle block fixed into the end of the crucible. For such a design the peaking factor is somewhat reduced (see Appendix A) and the centre line beam intensity, which is sampled downstream by a collimating aperture, begins to saturate, and much of the initial beam is wasted. A comparison of nozzle dimensions can be made to the average inter-atomic collisional mean free path to gain insight into the nature of the atomic flow. Details of the expected flow characteristics and dependence on nozzle geometry are given in Appendix A. In practice, we are often forced to work in the regime $Kn < 1$ to achieve sufficient beam intensity at the experiment chamber (where Kn is the Knudsen number used to characterise the nature of the flow [see Appendix A]). The collisional mean free path for ^{88}Sr-^{88}Sr collisions is on the order of 100 µm at source temperatures ∼900 K (Appendix A). Under typical conditions we generally operate in the opaque flow regime for the multichannel nozzle and in continuum flow for the comparatively large dimension

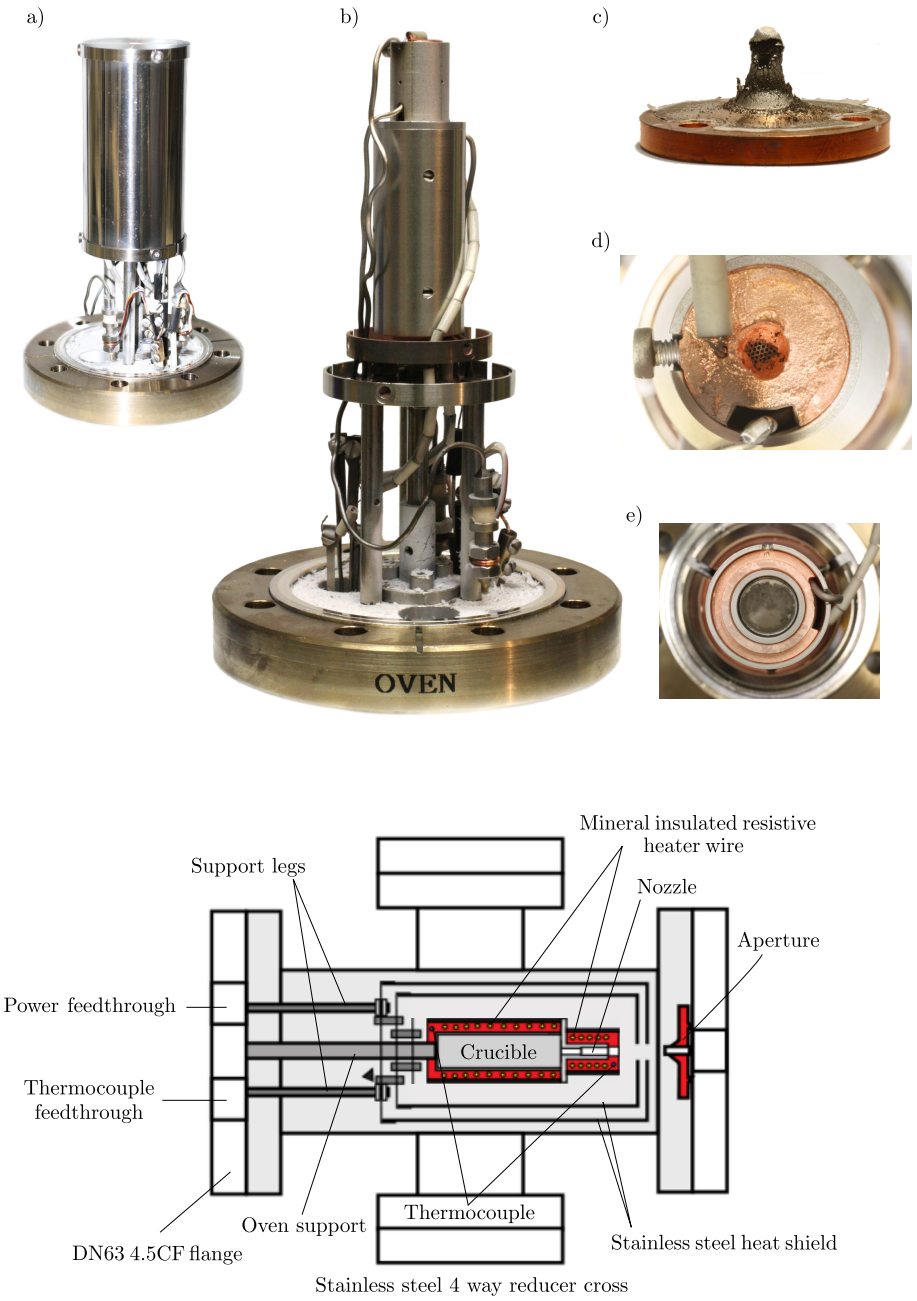


Figure 3.3: **NPL Sr oven** - (Top) Photographs of the NPL Sr oven showing a) fully assembled oven with thermal radiation shielding, b) oven with shielding removed showing separate crucible and nozzle heating sections, c) copper aperture with large Sr deposit built up over period of one full oven discharge, d) multi channel nozzle after use, copper has been corroded by Sr, showing attached thermocouple in ceramic bead insulation, and damaged heater wire (bottom), e) inside the crucible with nozzle section removed. (Bottom) Schematic of oven.

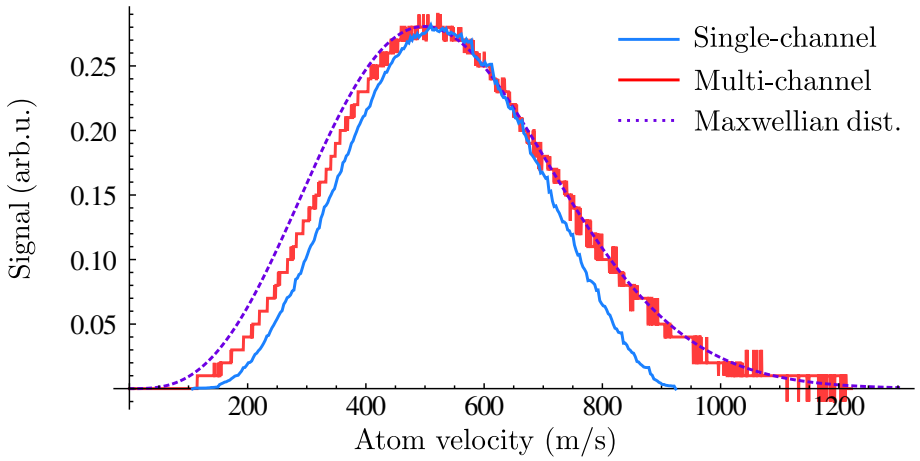


Figure 3.4: **Atomic beam velocity distribution** - Longitudinal velocity distributions taken by fluorescence detection of beam formed by single channel and multi channel nozzles as described in the text. Source temperature measured as 873 K and corresponding Maxwellian distribution added for comparison. Slow atoms are lost in the case of each nozzle, however, fast atoms are additionally absent from the resulting flow of the large single channel nozzle (note: distribution amplitudes have been scaled to coincide at the peak).

single channel nozzle. The subsequent longitudinal velocity distribution has been measured (by fluorescence detection) for each nozzle and shows characteristic properties of each associated flow regime, with a loss of slow atoms in each case in comparison to a Maxwellian distribution of an effusive source, and an additional loss of fast atoms in the continuum flow regime (Appendix A). A preferable nozzle design would have a high multiple of channels with channel diameter well below the collisional mean free path length, and channel length sufficient to operate at the transition threshold from transparent flow to opaque flow to ensure maximal collimation for minimal channel length. Limitations to this ideal are usually presented at the manufacturing stage. Multi channel nozzles can be made by compiling lengths of cut hypodermic needle tubing, although this is typically limited to inner diameters $\sim$100 µm with wall thickness of $\sim$50 % inner diameter. Other methods include stacking micro corrugated stainless steel sheets to form multiple, albeit somewhat irregular, channels or perhaps more costly precision machining methods such as electric discharge machining (EDM) or micro drilling could offer precision machined nozzles with ideal properties.

The atomic beam flux was measured by absorption spectroscopy on the strong $^1S_0 \rightarrow {}^1P_1$ transition for the single channel nozzle at a distance of 9 cm downstream (centre of spectroscopy/transverse cooling cross, see Sec 3.5.4.1 for details of UHV apparatus) and 69 cm downstream in the centre of the MOT region in the experimental chamber. A 1 mm diameter collimating aperture is positioned 10 cm downstream of oven nozzle exit and samples the centreline beam flux. Absorption spectroscopy relies on the fact that

photons in the spectroscopy beam are scattered out of the beam into random directions by spontaneous emission diminishing the photon flux in the direction of the spectroscopy beam. By scanning over an atomic resonance and observing the transmitted beam power on a photo-detector an absorption feature is observed with amplitude related to the optical density of the atomic vapour, which for a known average velocity can be interpreted as a measurement of atomic flux. Following Beer's law, the absorbed power can be expressed as,

$$P(x) = P_0 \exp(-\sigma_{eg} n x) \tag{3.6}$$

where x is the absorption length, n the atomic density, and P_0 the incident power in the spectroscopy beam. The atomic absorption cross section, σ_{eg}, is given by,

$$\sigma_{eg} = \frac{3\lambda^2}{2\pi} \underbrace{\frac{1}{1+s}}_{g(s)} \tag{3.7}$$

where $g(s)$ is the power broadened transition linewidth, and λ the transition wavelength. The atomic column density is found by rearranging Eq. (3.6) and the flux found by,

$$F = n v_{av} \pi r^2 \tag{3.8}$$

where v_{av} is the average atomic velocity (see Appendix A), and r is the atomic beam radius.

Results of the atomic beam flux measurements are presented in Fig. 3.5 alongside estimated beam fluxes calculated for an effusive source. The measured total flux in the cross region is significantly lower than estimated. Some of the difference can be accounted for by a more complete interpretation of the absorption feature. As the atomic beam here is highly divergent and the absorption feature Doppler broadened by several γ, to γ_D, the peak amplitude does not represent well the total flux and a single transverse velocity class approximation is no longer valid. The approximate correction provides a factor of $\sim \gamma_D/\gamma$ increase, however, the calculated flux remains many times higher. An explanation for this discrepancy requires further investigation and is not necessary for the advancement of this work. On the other hand, the flux measured downstream of the collimating aperture is within order of magnitude agreement with calculation. The saturation of the measured flux with temperature is proposed to be due to saturation of the centre line beam intensity, which forms the apertured beam, in comparison to the total beam flux and is characterised by a diminishing peaking factor and broadening of the beam angular distribution. The atomic beam spatial distribution was measured at the chamber centre by fluorescence imaging with a "light sheet" resonant with the ${}^1S_0 \rightarrow {}^1P_1$ transition and imaged through the end viewport. The image was also used to align the atomic beam by manipulating

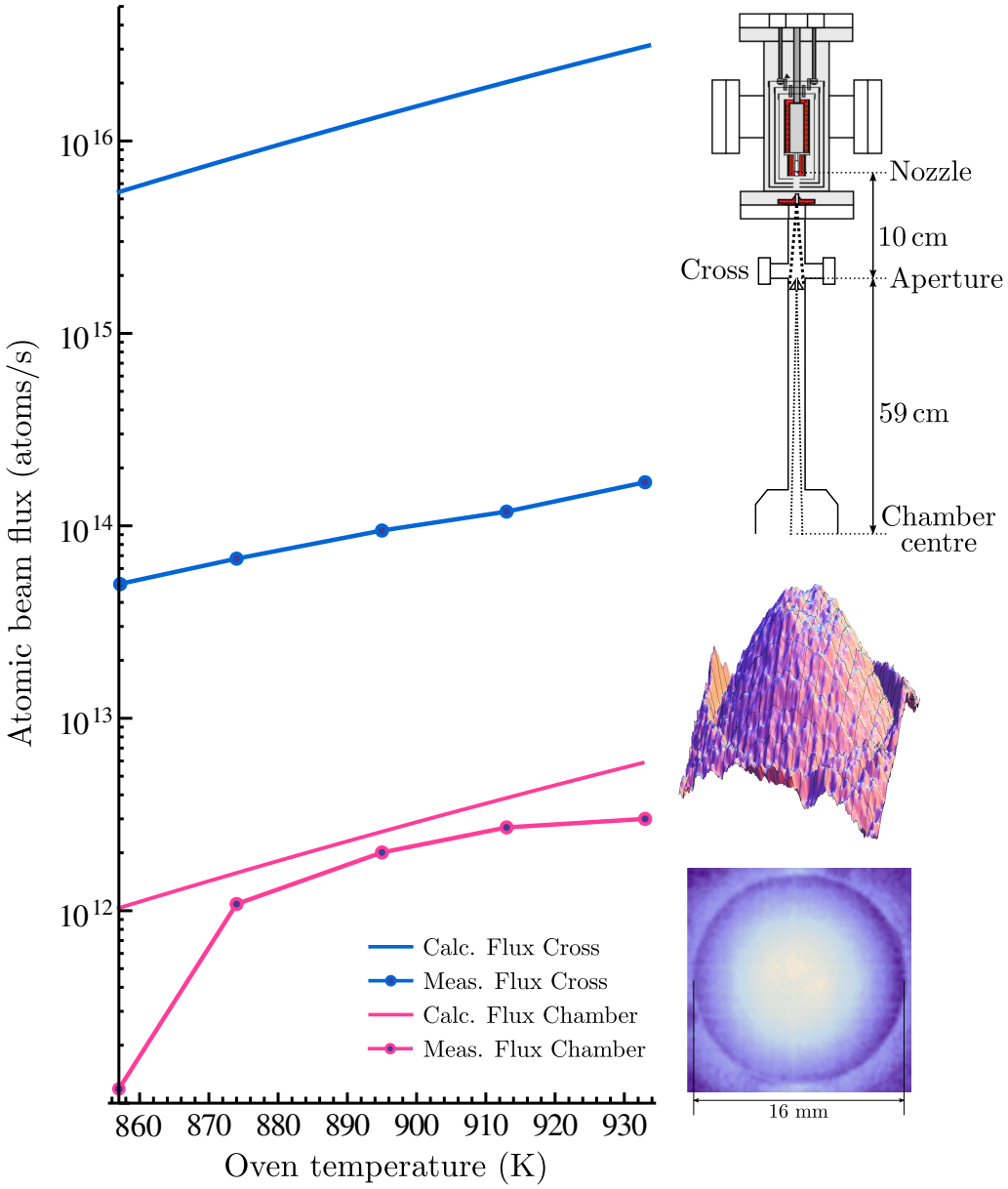


Figure 3.5: **Atomic beam flux** - Measured and calculated atomic beam flux for single channel nozzle (described in the text) at positions before (cross) and after (chamber) a collimating aperture. Arrangement of atomic beam apparatus with positions of the "cross" and "chamber" labelled (top right). Plots of the spatial distribution of atomic beam as measured in the chamber centre by fluorescence imaging.

the position of the oven relative to the main chamber; there is a surprising amount of give in the UHV joints without compromising vacuum (although bellows are often used to provide this freedom).

The advantages of a beam source are numerous. Removal of the hot source from the experiment chamber significantly reduces BBR related effects (discussed previously). As the residual atomic vapour outside the beam is minimal, the vacuum system can be constructed with standard materials with minimal risk of corrosion, including the use of AR-coated quartz glass viewports. Out-gassing of vacuum components is also reduced at lower temperatures making pressures $\lesssim 10^{-10}$ mbar easy to service with differential pumping schemes. Furthermore, mechanical or optical "shutters" can be implemented to chop delivery of the atomic beam to the experiment region during sensitive measurement or shallow trap loading, for example, following completion of initial trap loading in each measurement cycle. This all adds up to longer trap lifetimes. However, atomic beam apparatus are typically rather large and inefficient and require slowing of the atomic beam. An interesting alternative method could utilise laser ablation of a Sr target. The target could lie within close proximity to the MOT, leading to smaller apparatus and efficient loading, and benefit from being switched rapidly on demand.

3.3 Laser Cooling Neutral Atoms

We previously discussed the need for cold atoms in reducing the atomic motion, crucial for high-Q spectroscopy. Additionally for neutral atoms, the confining force experienced by a neutral atom in a dipole trap is much weaker (typically by a factor $\sim 10^8$) than that of trapped ions, resulting in trap depths, U_0, of only a few tens of $\mu\mathrm{K}(\times k_\mathrm{B})$, even at relatively high optical intensities of $\sim 10\,\mathrm{kW\,cm^{-2}}$. We therefore require preparation of ultra-cold atomic samples before trapping in a lattice. The following describes techniques of laser cooling relevant to slowing and trapping on the $^1\mathrm{S}_0 \leftrightarrow {}^1\mathrm{P}_1$ and $^1\mathrm{S}_0 \leftrightarrow {}^3\mathrm{P}_1$ transitions in Sr.

3.3.1 Atom-Light Interaction: The Basics

The development of techniques to laser cool and trap neutral atoms is well documented [177]. Here we focus on a few of the basic concepts of light's interaction with matter, leading to its mechanical action on matter, and discuss some of the important results.

Light displays properties of both particles and waves. A single particle of light (photon) has, like matter, energy ($E_{ph} = \hbar\omega$) and momentum ($\mathbf{p}_{ph} = \hbar\mathbf{k}$), where the wavevector $\mathbf{k}$ is related to the wavelength of the light, λ, by $|\mathbf{k}| = k = 2\pi/\lambda$. When an atom, with momentum $\mathbf{p}_{at} = m\mathbf{v}$, absorbs a photon of frequency ω_{abs}, exciting it from the ground to the excited internal state, it receives a momentum impulse $\hbar\mathbf{k}$ and its momentum becomes $\mathbf{p}_{at} = m\mathbf{v} + \hbar\mathbf{k}$. If the atoms velocity and light wavevector are anti-parallel then the atoms

motion is reduced by the recoil velocity,

$$v_r = \frac{\hbar k}{m} \tag{3.9}$$

At some time later, determined by the excited state lifetime, $\tau = 1/\Gamma$ (during which the atom does not absorb further radiation), the internal state relaxes back to the ground state and the absorbed energy is released into a random (ignoring stimulated emission) direction θ_j (to the light wavevector) as a photon with frequency,

$$\omega_{emit} = \omega_0 + \mathbf{k}' \cdot \mathbf{v}' - \frac{\hbar k^2}{2m} \tag{3.10}$$

where $\mathbf{k}\cdot\mathbf{v}$ is the Doppler shift (Sec. 2.1.2) due to the atoms velocity. The atom recoil in the direction of the wavevector is thus $\hbar k \cos\theta_j$. Importantly, the emission is spatially isotropic (not always, but the principle generally applies) and the net impulse tends towards zero for a large number, N_{sc}, of photon emission events, such that,

$$\Delta p_{at} = \sum_{j}^{N_{sc}} \hbar k \left(1 - \cos\theta_j\right) \cong N_{sc}\hbar k \tag{3.11}$$

We are left then with the change in momentum only from the direction of absorption and in this way we may reduce the atom's motion and thus cool it. For the two cooling transitions in Sr, at 461 nm and 689 nm, the recoil velocity is $v_r = 9.8\,\mathrm{mm\,s^{-1}}$ and $v_r = 6.6\,\mathrm{mm\,s^{-1}}$, respectively. Although this is small, by using "fast" optical transitions (with $\Gamma \sim 1 \times 10^7\,\mathrm{s^{-1}}$) and scattering many photons, it is possible to slow atoms from several hundreds of $\mathrm{m\,s^{-1}}$ to an approximate stand still in fractions of a second.

3.3.2 Velocity dependent scattering force

Due to the Doppler shift, $\mathbf{k}\cdot\mathbf{v}$, atoms initially resonant with the laser field, when slowed, move out of resonance and the slowing process diminishes. For an atom moving in opposition to the light field wavevector, the frequency of the absorbed photon, ω_{abs}, in the laboratory rest frame, is given by,

$$\omega_{abs} = \omega_0 + \mathbf{k}\cdot\mathbf{v} + \frac{\hbar k^2}{2m} \tag{3.12}$$

such that the effective detuning of the light field is,

$$\Delta_{\text{eff}} = \omega_L - \omega_{abs} = \omega_L - (\omega_0 + \mathbf{k}\cdot\mathbf{v} + \omega_r) = \Delta - \mathbf{k}\cdot\mathbf{v} - \omega_r \tag{3.13}$$

where ω_L is the frequency of the interacting light field, ω_r the recoil frequency, and $\Delta = \omega_L - \omega_0$ is the laser detuning from resonance. The resulting velocity dependent "scattering"

force can be found by considering the rate, $R_{sc} = \dot{N}_{sc}$, at which momentum is transferred from the laser light to the atom, where each scattering event corresponds to one photon absorption and re-emission cycle. Including saturation effects of the scattering process we have,

$$\mathbf{F}_{sc} = \hbar \mathbf{k} R_{sc} = \hbar \mathbf{k} \Gamma \underbrace{\frac{1}{2} \frac{s_0}{1 + s_0 + (2\Delta_{\text{eff}}/\Gamma)^2}}_{\rho_e} \tag{3.14}$$

where ρ_e is the excited state fraction, $s_0 = I/I_{sat}$ is the on resonance saturation parameter for the light-atom interaction with saturation intensity,

$$I_{sat} = \frac{2\pi^2 \hbar c \Gamma}{3\lambda_0^3} \tag{3.15}$$

and λ_0 the transition wavelength. We may also write s_0 in terms of Rabi frequency $\Omega = E_0 d/\hbar$, where d represents the dipole matrix (see Sec. 3.7.1), as,

$$s_0 = 2\frac{\Omega^2}{\Gamma^2} \tag{3.16}$$

3.3.3 Optical Molasses

We may now consider cooling in one-dimension by two identical counter-propagating laser beams, as depicted in Fig. 3.6. The force experienced by the atom is,

$$\mathbf{F}_{1\text{D}} = \frac{\hbar \mathbf{k} \Gamma s_0}{2} \left(\frac{1}{1 + s_0 + (2\Delta_1/\Gamma)^2} - \frac{1}{1 + s_0 + (2\Delta_2/\Gamma)^2} \right) \tag{3.17}$$

where, neglecting recoil effects (these are later included as a heating process),

$$\Delta_1 = \Delta - kv \tag{3.18}$$

$$\Delta_2 = \Delta + kv \tag{3.19}$$

The cooling light in each case is red detuned ($\Delta < 0$) such that the Doppler shift due to opposing motion brings the light into resonance. The atom then preferentially scatters photons from the opposing light field and experiences a viscous force or "friction" which scales with velocity, acting to reduce the atom's motion. In analogy to the viscous "honey-like" by-product of sugar production, this configuration is named (by Chu and co-workers) optical molasses. This principle can be exploited to cool atoms in three dimensions and is the key idea behind Doppler cooling. The force is plotted in Fig. 3.6 for $\Delta = -\Gamma/2$ and $s_0 \ll 1$, which corresponds to the detuning required to achieve the minimum atomic temperature. The two Lorentzians from the force due to each light field, offset by $\pm\Delta$, are also shown (dashed). For small velocities ($v \ll |\Delta|/k$) we may expand Eq. 3.17 to the

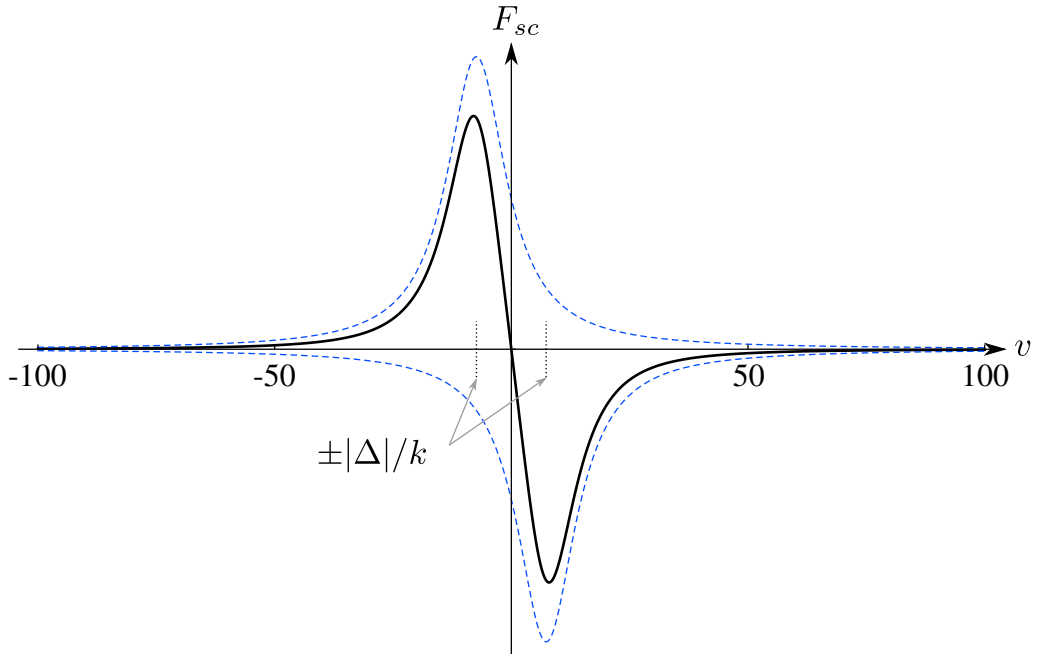


Figure 3.6: **Optical Molasses** - Velocity dependent scattering force for a 1D optical molasses

lowest order in $\mathbf{v}$ to obtain the viscous damping force,

$$\mathbf{F}_{\text{OM}} \cong \frac{8\hbar k^2}{\Gamma} \frac{s_0 \Delta}{(1 + s_0 + (2\Delta/\Gamma)^2)^2} \mathbf{v} \equiv -\beta \mathbf{v} \tag{3.20}$$

Assuming the light field is made up of monochromatic laser light, such that the linewidth of the laser $\Delta\nu_L \ll \gamma$, the velocity capture range, v_c, for which atoms are likely to be substantially cooled, is on the order of,

$$\pm\frac{|\Delta| + \Gamma/2}{k} \sim \pm\frac{\Gamma}{k} = \pm\frac{\Gamma\lambda}{2\pi} = \pm\gamma\lambda \tag{3.21}$$

For the two cooling transitions in Sr, at 461 nm with $\gamma = 30.2\,\text{MHz}$ and 689 nm with $\gamma = 7.6\,\text{kHz}$, this gives a v_c of approximately $14\,\text{m}\,\text{s}^{-1}$ and $5\,\text{mm}\,\text{s}^{-1}$ respectively. Clearly, the broad 461 nm transition offers a substantially greater capture range (and is thus used for first-stage cooling) although still relatively small compared to the most probable velocity typical of a Sr thermal beam ($\sim$400 $\text{m}\,\text{s}^{-1}$ to $500\,\text{m}\,\text{s}^{-1}$).

To obtain the limit of this cooling process we must include heating effects resulting from the discrete photon recoil. Taking a closer look at the photon emission process we can see the atom in fact undergoes a random walk of length N_{sc} in momentum space, with step size $\hbar k$, constituting a heating process. The average frequency of each absorbed (emitted) photon (Doppler shifts cancel) is given by $\omega_{abs} = \omega_0 + \omega_r$ ($\omega_{emit} = \omega_0 - \omega_r$). The average change in kinetic energy of the atom per photon scattering event is thus

$\hbar(\omega_{abs} - \omega_{emit}) = 2\hbar\omega_r$. For our two beam configuration we scatter photons in to a random direction at a rate $2R_{sc}$ (assuming the laser fields are uncorrelated and saturation effects can be ignored ($s_0 \ll 1$)), corresponding to a heating rate of $4R_{sc}\hbar\omega_r$. Equating with the cooling rate, $\mathbf{F}_{\mathrm{OM}} \cdot \mathbf{v}$, and invoking the equipartition theorem in one dimension, as $\frac{1}{2}k_{\mathrm{B}}T_r = \frac{1}{2}m\langle v^2\rangle$, we get the steady state solution,

$$k_{\mathrm{B}}T_{\mathrm{D}} = \frac{\hbar\Gamma}{4}\frac{(1 + (2\Delta/\Gamma)^2)}{-2\Delta/\Gamma} \tag{3.22}$$

which has a minimum value at $\Delta = -\Gamma/2$ of,

$$k_{\mathrm{B}}T_{\mathrm{D}(limit)} = \frac{\hbar\Gamma}{2} = \frac{h\gamma}{2} \tag{3.23}$$

which is the well known Doppler cooling limit, valid for a simple two level system. For atoms with degenerate sub-levels an additional cooling mechanism, known as Sisyphus cooling, allows sub-Doppler temperatures to be reached. It is instructive here to consider the recoil limited temperature, T_r, resulting from the kinetic energy gained by a single photon emission event, $E_r = \frac{\hbar^2k^2}{2m}$, leading to,

$$k_{\mathrm{B}}T_r = \frac{\hbar^2k^2}{m} \tag{3.24}$$

This sets the lower limit for laser cooling where a radiative interaction of the atom with the light persists, although optical techniques to cool beyond this limit do exist [178, 179].

3.3.4 Compensation of the Doppler shift

As previously discussed, the Doppler shift results in a velocity dependent force which limits the range over which a laser field of fixed detuning is effective. To slow an atom in an atomic beam from $500\,\mathrm{m\,s^{-1}}$ to an approximate standstill requires the frequency detuning of the counter-propagating slowing light to be adjusted over a range of $\sim$1 GHz.

Chirp Cooling

One solution is to sweep the laser frequency in synch with the slowing process such that the Doppler shift is continuously compensated and a constant slowing force is experienced by the atoms [180]. In a thermally distributed atomic beam, atoms are 'picked up' throughout the slowing process and slowed to a final velocity, dependent on the final laser detuning. This results in a compression of the velocity distribution to a lower speed, such that both the mean and variance of the velocity is reduced, accounting for both slowing and cooling processes. The sweep time can be estimated from the number of photon kicks required to stop the atom, as $N_{sc} = v_0/v_r$. The maximum rate at which an atom scatters photons is $\Gamma/2$ ($= 1/2\tau$) and for stable deceleration, a, we choose $a < a_{max}$. Thus to slow a Sr

atom from $500\,\mathrm{m\,s^{-1}}$ to a stand sill (using the 461 nm transition) requires $N_{sc} = 50833$, with a sweep time of $2\tau N_{sc} a_{max}/a \sim 1$ ms. This technique is known as chirp cooling and is effective in producing a high flux pulsed source of slow atoms [181]. However, as it relies on a temporally tuned interaction, many atoms are not slowed, and the slowing efficiency in continuous operation is limited by the chirp duty cycle.

Spectrally Broadened Light Source

An alternative method is to use a spectrally broadened laser (SBL) source, covering the band $\omega < \omega_f$, where ω_f is the detuning required for a final velocity $v_f = (\omega_o - \omega_f)/k$, counter-propagating to the atomic beam. The broadened spectrum need not be continuous but may consist of a series of discrete frequencies, providing the separation is less than the homogeneous linewidth of the atomic transition. A problem with this method arises due to the non-resonant scattering force at the tail of the Lorentzian, which continues to slow atoms beyond v_f. As the force has no spatial (or temporal) dependence along the beam axis, v_f is reached for different atoms at different points along the length of the interaction region. Thus atoms experience differing amounts of "post-cooling" (referring to the cooling after v_f is reached), leading to a reduction in the velocity compression. To counter this, in a technique proposed by Hoffnagle [182], a co-propagating monochromatic beam with frequency ω_0 is added to balance the non-resonant light pressure on the slow atoms, and create a force resembling a 1D molasses. This technique was demonstrated by Zhu and co-workers [183], and extended to use two SBL sources in a 1D molasses configuration, combining both acceleration and deceleration of the thermal source to form a narrow velocity peak at higher velocities. The idea can be extended to a 3D molasses configuration with an increased capture velocity, and is exploited in the initial stage of narrow line cooling in Sr optical lattice clocks (see Sec. 3.6).

Zeeman Slower

The final method exploits not a change in the cooling light frequency but a change in the atomic level spacing experienced by an atom in a magnetic field, $\mathbf{B}$ as a result of the Zeeman effect. The effective detuning, as in Eq. 3.25, is modified to include this frequency shift as,

$$\Delta_{\text{eff}} = \Delta - \mathbf{k}\cdot\mathbf{v} - \mu'\mathbf{B}/\hbar \tag{3.25}$$

where $\mu' = (g_e M_e - g_g M_g)\mu_B$ is the transition magnetic moment, $g_{g,e}$ the Landé g-factors of the ground and excited states, $M_{g,e}$ the magnetic quantum number, and $\mu_B = \frac{e\hbar}{2m_e}$ is the Bohr magneton, where m_e is the electron mass. By appropriate tuning of the $\mathbf{B}$-field, and thus the Zeeman shift, along the length of the atomic beam, the Doppler shift may be continuously compensated, for a fixed slowing light detuning, as atoms slow and progress

through the slower. The apparatus to accomplish this is thus known as a Zeeman slower and was first proposed [184] and demonstrated [155] by Phillips and co-workers. Much like the chirp cooling method, atoms at velocities less than the initial capture velocity are picked up later in the slowing process, however, because we rely here on a spatial compensation and not a temporal one, this process, and the production of slow atoms, is continuous. The capture and escape velocities of atoms traversing the Zeeman slower depend on the details of the slowing light detuning and size of **B**-field.

If we are to capture atoms with an initial velocity v_i, travelling along x, and slow to a final velocity v_f, assuming a constant acceleration, a, the length of slower required is by simple kinematics,

$$L_0 = \frac{v_f^2 - v_i^2}{2a} \approx -\frac{v_i^2}{2a} \tag{3.26}$$

where a is negative for deceleration, and the velocity at position x is,

$$v(x) = v_i \sqrt{\left(1 - \frac{x}{L_0}\right)} \tag{3.27}$$

The required field profile to constantly offset the Doppler shift is thus,

$$B(x) = B_0 \sqrt{\left(1 - \frac{x}{L_0}\right)} + B_{\text{bias}} \tag{3.28}$$

where B_0 is total change in magnetic field over $0 \leq x \leq L_0$ and $B_{\text{bias}} \approx \Delta/\mu'$ is the bias magnetic field used to offset the overall field profile.

Often, the deceleration is not constant; as for a convergent slowing beam geometry with increasing saturation parameter, $s_0(x)$, towards the entrance of the slower, or for a non ideal profile of the magnetic field. Instead, the desired field profile is found by considering the local deceleration over the slower length and solving numerically for a single atom trajectory. The local deceleration considered here is below the local maximum, given by,

$$a_{\max}(x) = \frac{\hbar \mathbf{k} \Gamma}{2m} \frac{s_0(x)}{1 + s_0(x)} \tag{3.29}$$

for the given local laser intensity, which provides stability of slowing and increased velocity compression of the slowed atom flux. The extent to which the deceleration is diminished is characterised by the parameter ϵ such that,

$$a(x) = \epsilon \, a_{\max}(x) \tag{3.30}$$

The profile of the magnetic field is then designed to provide slowing with constant ϵ. The length of the slower is then set by capture and exit velocities, and ϵ parameter, which is

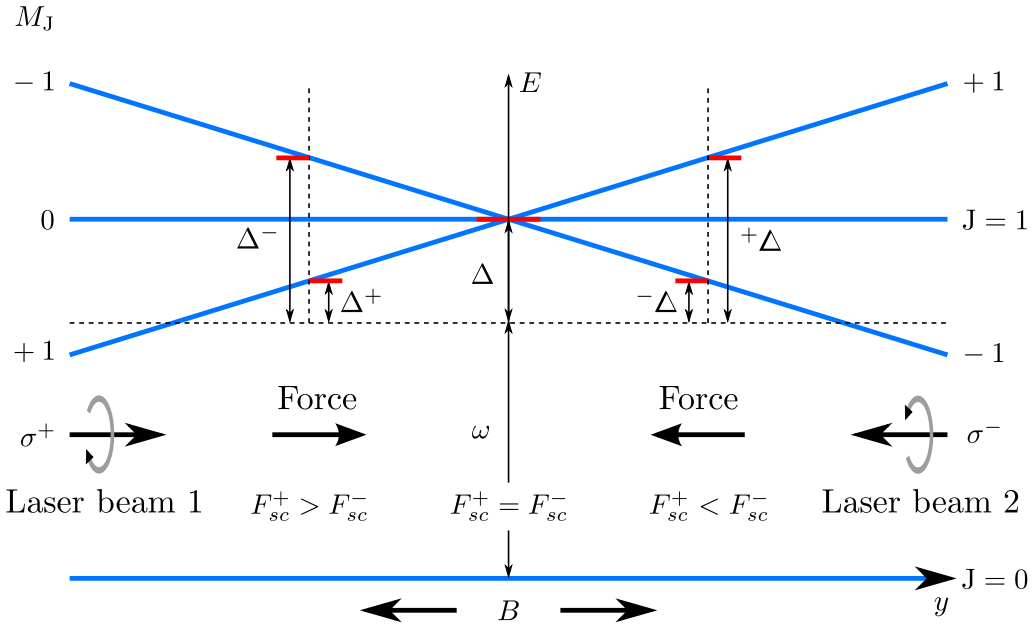


Figure 3.7: **Mechanism of a magneto-optical trap** - The operating principle of a MOT shown for the 1D case for a simple $J = 0$ to $J = 1$ system. Key to operation are the angular momentum selection rules which serve to ensure the magnetic sub-states M_J interact with the corresponding light field, $\sigma^{\pm}$ for $M_J = \pm 1$, only, such that angular momentum is conserved. Coupled with appropriate magnetic field gradient, this ensures the force always points towards the centre, at which the forces are balanced and the atom is trapped.

constrained by the available slowing beam power. For further details see Refs.[185–187].

3.3.5 Magneto-optical trap (MOT)

A magneto-optical trap combines the radiative scattering force, as used in an optical molasses, and the frequency shift due to a magnetic field to produce a robust trap for neutral atoms. The velocity dependent force of an optical molasses serves to cool atoms, however, the atoms are free to diffuse out of the light field as there is no position dependence to the force. The addition of an inhomogeneous magnetic field, together with a particular polarisation of light, introduces a restoring force which leads to compression of atoms towards the field minimum where atoms are trapped.

The trapping force is derived as in Eq. 3.17, but here the effective detuning of each MOT beam includes the field related shift as,

$$\Delta_1 = \Delta^+ = \Delta - kv + \mu' B/\hbar \tag{3.31}$$

$$\Delta_2 = \Delta^- = \Delta + kv - \mu' B/\hbar \tag{3.32}$$

where B is a linear function of position y with gradient A, such that $B(y) = Ay$. Expanding

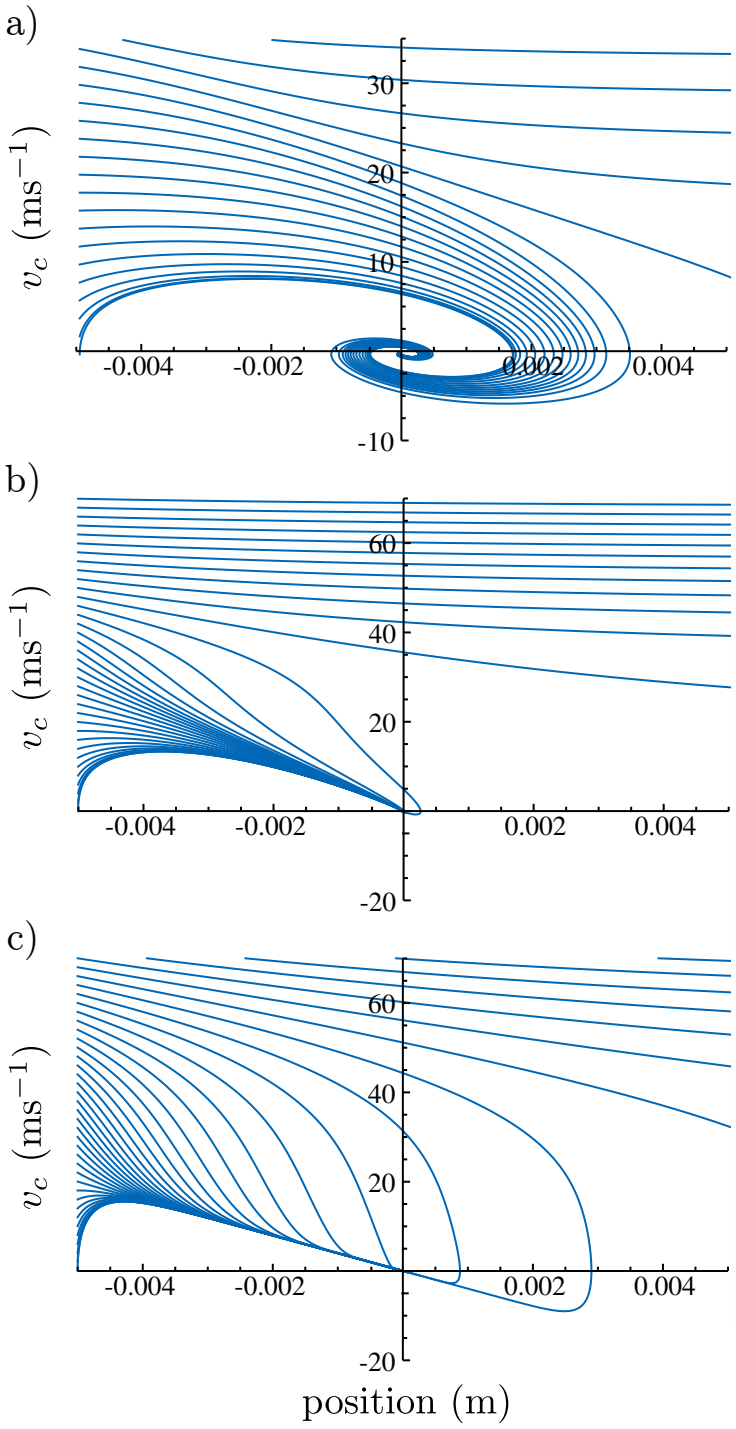


Figure 3.8: **Particle trajectories in 1D MOT** - Calculated for parameters: magnetic field gradient 55 G cm^{-1}, detuning $-1.3\,\Gamma$ and s_0 (power for 461 nm MOT with 1 cm beam diameter) a) 0.06 (1 mW), b) 0.60 (10 mW), and c) 6.0 (100 mW). Position is relative to trap centre.

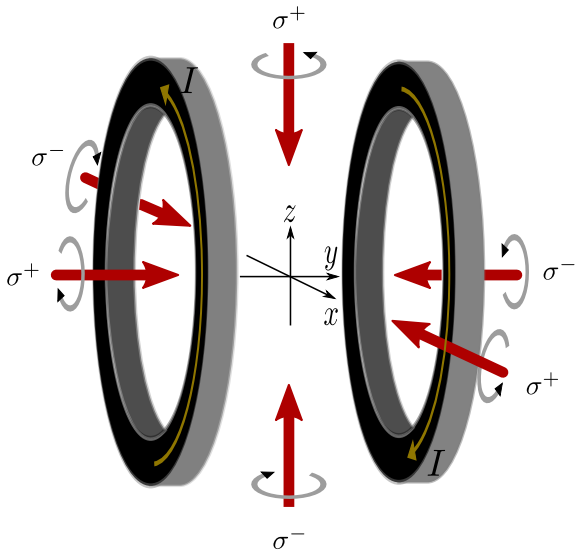


Figure 3.9: **3D MOT configuration** -

Eq. 3.17 for small Doppler and Zeeman shifts, the force can be written as,

$$F_{\text{MOT}} \cong -\beta v - \kappa y \tag{3.33}$$

where the first term on the right, as previously defined for the optical molasses, provides a viscous force, and the second term,

$$\kappa = \frac{\mu' A}{\hbar k}\beta \tag{3.34}$$

is the restoring force. Atoms entering the MOT within the velocity capture range then experience a damped harmonic motion as,

$$\ddot{y} + \frac{\beta}{m}\dot{y} + \frac{\kappa}{m}y = 0 \tag{3.35}$$

The principle of operation is depicted in Fig. 3.7 for the 1D case and is easily extended to 3D (Fig. 3.9), where a quadrupole **B**-field, generally produced using an (approximately) anti-Helmholtz coil pair, generates the required field gradients. It is worth noting that the magnetic field gradient on axis of the coil centres is twice as large as those off axis, such that,

$$\frac{\partial B_z}{\partial z} = \frac{\partial B_x}{\partial x} = -\frac{1}{2}\frac{\partial B_y}{\partial y} \tag{3.36}$$

and is often quoted in the literature for the axial case only.

The capture velocity of a MOT is increased in comparison to a simple molasses. A simple estimate may be gained by considering the maximum velocity of an atom which is

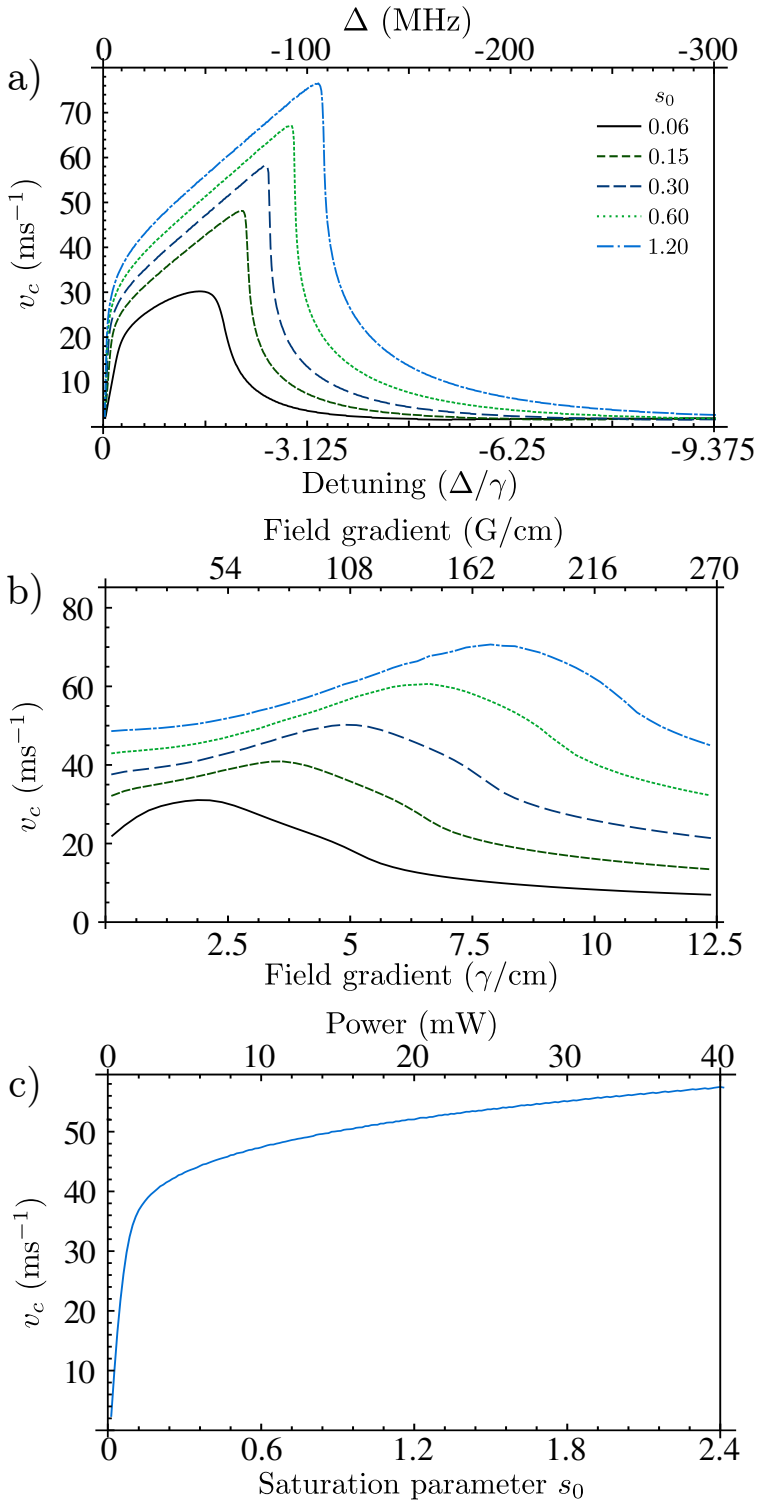


Figure 3.10: **Capture velocity for various MOT parameters** - Numerical results of the equations of motion for particles entering a 1D MOT. Axes are labelled for the general case (bottom) and for the 461 nm "blue" Sr MOT (top). Plots show capture velocity versus: a) trapping beam detuning for a range of intensities at field gradient $2.5\gamma\,\mathrm{cm}^{-1}$ ($55\,\mathrm{G\,cm}^{-1}$ for blue MOT). b) magnetic field gradient for detuning -1.25γ (-40 MHz). c) trapping beam intensity for detuning -1.25γ and field gradient $2.5\,\gamma\,\mathrm{cm}^{-1}$ ($55\,\mathrm{G\,cm}^{-1}$). MOT beam diameter of 1 cm is used throughout.

slowed to zero within the dimensions of the MOT laser beams. Using Eq 3.26 the MOT capture velocity is,

$$v_c = 2\sqrt{ar_c} \tag{3.37}$$

where r_c is the capture radius, generally given by the radius of the trapping beam, and a is the maximum acceleration realised by the given field gradient and MOT beam power. A numerical simulation of the atom trajectories within the MOT trapping region has been carried out and used to calculate the expected capture velocity for various MOT parameters. The results are presented in Fig. 3.10.

It is preferable to have large MOT capture velocity to load the trap at high rate. When loading from vapours which are thermally distributed according to Maxwellian statistics the benefit is obvious. When loading from a Zeeman slowed source, with slow peak that can be arbitrarily tuned, we may expect the importance of a large v_c to diminish. However, as atoms are slowed, the ratio of transverse to longitudinal velocity increases and the atomic beam increasingly diverges, reducing the density of slow atoms entering the MOT region. It is then preferable to keep v_c and v_f relatively large, with $v_f < v_c$.

3.4 Laser Cooling Divalent Atoms

As discussed in section 3.1 there are two transitions we can employ to produce our ultracold sample. A comparison of these cooling transitions for a number of candidate reference atoms can be found in Table 3.3. Typically, the broad ($\Gamma/2\pi \sim 10's$ MHz) electric-dipole allowed transition between the $^1S_0$ ground-state and the singlet $^1P_1$ excited-state is cycled in a first stage of cooling to Doppler limited temperatures ∼mK. A second stage of cooling is then carried out on the spin-forbidden narrow ($\Gamma/2\pi \sim$ sub kHz to MHz) intercombination line to the triplet $^3P_1$ excite-state where much lower temperatures ∼μK suitable for trapping in the lattice are reached. Further cooling to the motional ground state of the trap can be carried out using resolved sideband cooling on the $^1S_0 \leftrightarrow {}^3P_1$ line. For odd isotopes, the presence of nuclear-spin induced magnetic degeneracy in the ground-state offers the possibility of Sisyphus sub-Doppler cooling; explored in Sr [188] and Yb, [189] and used to good effect in Hg where the intercombination line is relatively broad [190].

3.5 $^1S_0 - {}^1P_1$: Initial cooling and trapping Sr

3.5.1 Blue MOT

The first stage of cooling Sr uses the 461 nm "blue" transition which is capable of cycling photons at a rate $1.9 \times 10^8\,\mathrm{s}^{-1}$, corresponding to a maximum deceleration of $\sim 5 \times 10^5\,\mathrm{m\,s}^{-2}$.

Table 3.3: Properties of Sr cooling transitions for divalent neutral atoms.

		$^1P_1$		$^3P_1$		
Species	Atomic number, Z	λ (nm)	$\Gamma/2\pi$ (MHz)	λ (nm)	$\Gamma/2\pi$ (kHz)	Ref.[a]
Mg	12	285.3	79.6	457.1	0.031	
Ca	20	422.6	34	657.2	0.47	
Sr	38	460.7	30.2	689.4	7.5	[191, 192]
Ba	56	553.7	18.9	791.4	47.6	
Zn	30	213.9	112	307.7	4.71	[150]
Cd	48	228.8	91	326	70	[193]
Hg	80	184.9[b]	119	254	1300	
Yb	70	398.9	28	556	182	

[a] Data is taken from the NIST Atomic Spectra Database unless otherwise specified.

[b] In the case of Hg the broad cooling transition is not easily accessible with current laser technology, however, the inter-combination line is suitable for single-stage sub-Doppler cooling (in odd isotopes) where temperatures $\sim$2 µK have been demonstrated [190].

Table 3.4: Laser cooling properties for first and second stage cooling transitions in Sr.

Parameter	First stage	Second stage
λ	461 nm	689 nm
ω_r	$6.7 \times 10^4\,\mathrm{s}^{-1}$	$3.0 \times 10^4\,\mathrm{s}^{-1}$
I_{sat}	$42.7\,\mathrm{mW\,cm}^{-2}$	$10.1\,\mu\mathrm{W\,cm}^{-2}$
a_{max}	$9.34 \times 10^5\,\mathrm{m\,s}^{-2}$	$157.2\,\mathrm{m\,s}^{-2}$
v_r	$9.8\,\mathrm{mm\,s}^{-1}$	$6.6\,\mathrm{mm\,s}^{-1}$
v_D	$261\,\mathrm{mm\,s}^{-1}$	$17.2\,\mu\mathrm{m\,s}^{-1}$
T_r	1.02 µK	458 nK
T_D	725 µK	182 nK
v_c	$13.9\,\mathrm{m\,s}^{-1}$	$5.2\,\mathrm{mm\,s}^{-1}$

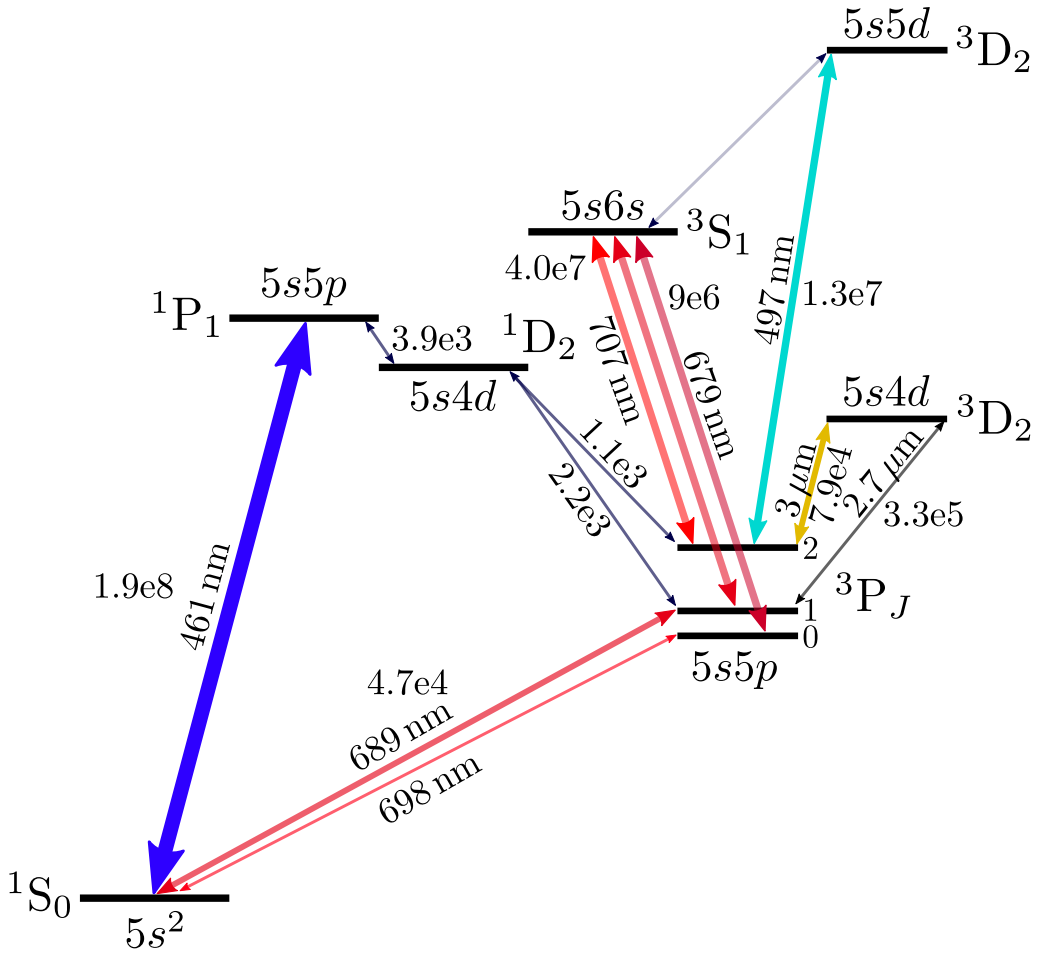


Figure 3.11: **Reduced Sr energy level scheme** - Transitions relevant to cooling and trapping atomic Sr.

This makes it possible to slow atoms from very high velocities $\sim$400 m s^{-1} to a relative stand still in <20 cm. Once slowed the atoms are trapped in a 3D MOT where, under optimal conditions, further cooling to the Doppler limit of 261 mm s^{-1} or 725 μK may be reached (see Tab. 3.4). Often this limit is not reached, as may be predicted from the MOT parameters used (e.g., see Eq. (3.22)), or because additional heating processes are present, such as the absorption of spontaneous emission and two-body cold collisions, which are enhanced in a dense MOT. The dependencies for a range of MOT parameters versus MOT capture velocity have been modelled and are presented in Fig. 3.10. In typical operation, a large MOT capture velocity $\sim$50 m s^{-1} is expected. The parameters have a handle on a range of MOT properties which must be considered depending on the subsequent application of the trapped atoms. For two-stage cooling it is expected a high degree of compression, relying on high magnetic field gradients, will be required to aid efficient transfer to the smaller capture volume of the second stage MOT. The large linewidth of the $^1S_0 \rightarrow {}^1P_1$ transition, $\gamma = 30.2$ MHz, demands large field gradients, several γ over the trapping region, and typically >40 G cm^{-1} is used [188].

Additional complications arise from a slight breakdown of the ideal two-level system assumed thus far. The $^1S_0 \leftrightarrow {}^1P_1$ transition is not fully closed and a weak decay channel exists from the $^1P_1$ state to the $^1D_2$ state with rate $\Gamma = 3.9 \times 10^3$ s^{-1} (branching ratio of about 1 in 50 000). Decay continues from the $^1D_2$ state to both the $^3P_1$ and $^3P_2$ states with branching ratio of 2/3 and 1/3 respectively. Atoms in the $^3P_1$ state decay back to the ground state in around 21 μs and (assuming sufficiently large MOT capture volume [163]) re-enter the cooling cycle, however, those in the $^3P_2$ metastable state (lifetime $\sim$120 s at room temperature) are shelved and lost from the MOT. The steady-state MOT atom number N_{MOT} is dictated by the loading rate L compared to the loss rate Γ_{loss} as,

$$N_{\mathrm{MOT}} = L/\Gamma_{loss} \tag{3.38}$$

The total loss rate is a combination of shelving losses, rate Γ_s, and losses due to background gas collisions, rate Γ_{bg}, as $\Gamma_{loss} = \Gamma_s + \Gamma_{bg}$, with trap lifetime $1/\Gamma_{loss}$. The shelving rate is determined by the decay rate of the $^1P_1$ excited state fraction to the $5s5p\,{}^3P_2$ state. The shelving loss rate need not include the $5s4d\,{}^1D_2$ decay rate (as the fraction destined to reach the $5s5p\,{}^3P_2$ state are effectively lost from the cooling cycle by the time they reach the $5s4d\,{}^1D_2$ state) and may be written as,

$$\Gamma_s = \rho_e\, b(^1D_2 \rightarrow {}^3P_2)\, \Gamma(^1P_1 \rightarrow {}^1D_2) \tag{3.39}$$

where b is the branching ratio (= 1/3) and ρ_e is the excited state fraction (as in Eq. (3.14)). Assuming the loss rate is dominated by shelving losses and neglecting the background collision losses, for typical MOT parameters ($\Delta = -40$ MHz and $s_0 \sim 6 \times 0.5$, where the factor 6 accounts for the total number of MOT beams) the estimated trap lifetime

is ∼2 ms. For typical loading rates $\sim 10^9\,\mathrm{s}^{-1}$ the steady state MOT number is estimated as $N_{\mathrm{MOT}} = 2 \times 10^6$ atoms. Since the loss rate is relatively small the MOT can operate without additional repumping lasers to clear out the metastable states, nevertheless, the MOT atom number and trap lifetime are significantly increased when they are used.

3.5.2 Repumping schemes

3.5.2.1 Repumping from the $5s4d\,^1D_2$ state

The first repumping strategy one might consider is to drive atoms out of the $5s4d\,^1D_2$ state before they further decay to the $5s5p\,^3P_{1,2}$ states. A possible route is to excite to the $5s6p\,^1P_1$ state which decays directly to the ground state at a rate $1.87\,\mathrm{s}^{-1}$ and to the $5s5p\,^1P_1$ state via the $5s6s\,^1S_0$ state at a similar rate. Other decay routes involve intercombination transitions to the $5s6s\,^3P_1$ and $5s4d\,^3D_{1,2}$ states for which the transition rates are not well known, and some of which branch into metastable states where the atom is shelved and lost. Regardless, this method has been explored by Vogel [163] and in other work by Kurosu [194] but with disappointing results, showing an improvement of around only a factor of two in steady state MOT number.

3.5.2.2 Repumping from the $5s5p\,^3P_2$ state

Failing effective repumping from the $5s4d\,^1D_2$ state we consider driving atoms out of the $5s5p\,^3P_2$ state. As shown in Fig. 3.11 there are three possible routes; to the $5s6s\,^3S_1$ at 707 nm, the $5s5d\,^3D_2$ state at 497 nm, or the $5s4d\,^3D_2$ state at 3 µm. Historically, the 707 nm transition has been preferentially used due to the difficulty in realising laser light at 497 nm and 3 µm and we consider this scheme first. The $5s6s\,^3S_1$ state decays to all states of the $5s5p\,^3P$ multiplet with 25 % of the atoms pumped out of the $5s5p\,^3P_2$ state being shelved in the $5s5p\,^3P_0$ state. Modifying the branching term in Eq. (3.39) to account for 1/4 loss ($b = 1/3 \times 1/4$) we gain a factor of 4 increase in steady state MOT number. We can then apply light at 679 nm to clear out the $5s5p\,^3P_0$ state and recover all atoms to the MOT, providing residual atomic motion does not carry atoms outside the MOT capture volume in this time. We may then expect only losses due to background gas collisions, however, as the MOT number increases and high atom densities are reached two-body cold collision losses emerge dominant and limit the steady state MOT number [163], which is typically enhanced by a factor of >10 [195].

An alternative is to clear out the $5s5p\,^3P_2$ state via the $5s5d\,^3D_2$ state which decays almost completely to the $5s5p\,^3P_{2,1}$ states with only a small fraction, <0.3 %, escaping to the $5s6p\,^3P$ multiplet [196]. The decay to the $5s5p\,^3P_1$ is around four times that of the $5s5p\,^3P_2$ providing efficient repumping within only a few 497 nm driven cycles. The drawback comes in generating light at this wavelength for which diode lasers (to the author's knowledge) are not readily available. Light can be generated by second-harmonic

Table 3.5: Isotope shifts of the $5s^2\,{}^1S_0 \rightarrow 5s5p\,{}^1P_1$ transition

Isotope	Lower Level	Upper Level	Rel. strength	Isotope shift[a] (MHz)
^{88}Sr	$5s^2\,{}^1S_0$	$5s5p\,{}^1P_1$	1	0
^{87}Sr	$5s^2\,{}^1S_0$ F=9/2	$5s5p\,{}^1P_1$ F=7/2	4/15	-12.2
	$5s^2\,{}^1S_0$ F=9/2	$5s5p\,{}^1P_1$ F=11/2	6/15	-55.2
	$5s^2\,{}^1S_0$ F=9/2	$5s5p\,{}^1P_1$ F=9/2	5/15	-72.2
^{86}Sr	$5s^2\,{}^1S_0$	$5s5p\,{}^1P_1$	1	-124.5
^{84}Sr	$5s^2\,{}^1S_0$	$5s5p\,{}^1P_1$	1	-270.6

[a] [188, 200]

generation (SHG) in non linear crystals (often $KNbO_3$) of a 994 nm extended cavity diode laser (ECDL) but this provides extra complication and expense. A third method, employed by Mickelson et al. [197], utilises the lower lying $5s4d\,{}^3D_2$ state which decays only to the $5s5p\,{}^3P_{2,1}$ states, with preference to the $5s5p\,{}^3P_1$ state. Again, the difficulty arises in realising the required wavelength of light, at 3.01 µm. This can be achieved with seeded optical parametric oscillators (OPOs), perhaps using fibre lasers to seed, but with greater expense and complexity in comparison to diode laser based systems. Ultimately, the results of these repump methods are similar to the 707 nm plus 679 nm method [197, 198] and the additional laser at 679 nm is anyway required to clear out the $^3P_0$ clock state during the readout process (see Fig. 2.4). Both 707 nm and 679 nm wavelengths are easily generated, and with ample power, with use of simple ECDLs.

Worthy of note here is the potential value of the $^1P_1 \rightarrow {}^1D_2 \rightarrow {}^3P_2$ MOT drain which serves to continuously load cold atoms into the $5s5p\,{}^3P_2$ metastable state which are magnetically trapped by the MOT quadrupole field. One use is in the formation of a Bose-Einstein condensate of ^{88}Sr through sympathetic cooling with ^{87}Sr where the magnetically trapped metastable state serves to store one isotope for extended time periods during collection and cooling of the other [199].

3.5.3 Experimental details: Laser sources

3.5.3.1 461 nm light source

The 461 nm light is generated by a commercial master-oscillator laser plus optical power-amplifier (MOPA) and ring cavity enhanced SHG system by Toptica. A Littrow configuration ECDL operated at 922 nm seeds a tapered amplifier which outputs ~850 mW of optical power used to pump a non-critically phase matched $KNbO_3$ crystal, held at ~312 K, in a bow-tie cavity. Up to 400 mW of blue light at 461 nm has been generated

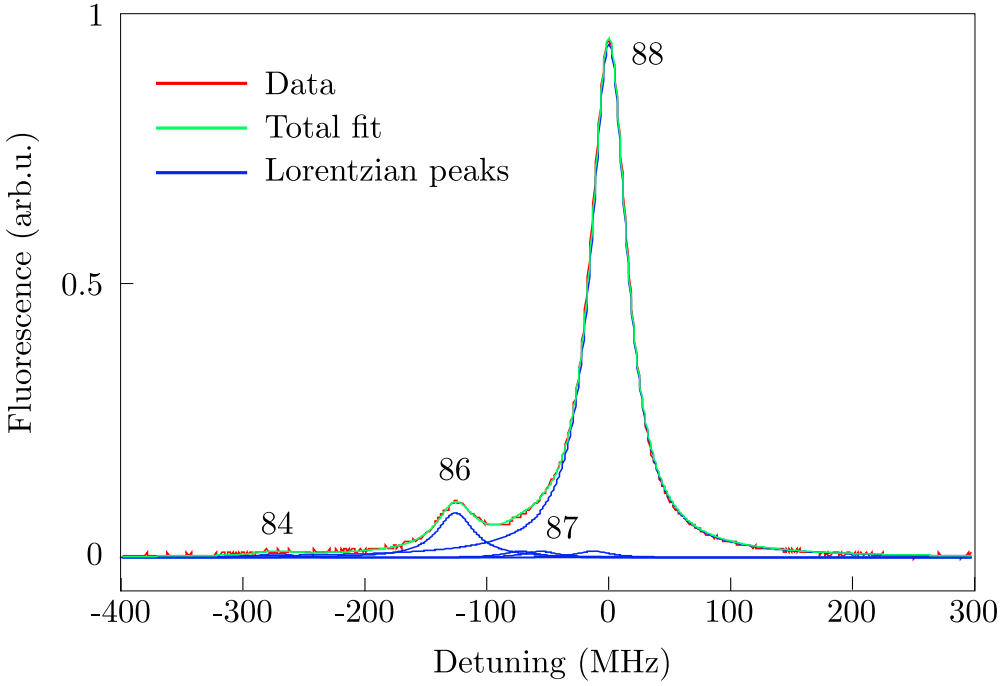


Figure 3.12: **Fluorescence of $5s^2\,{}^1S_0 \rightarrow 5s5p\,{}^1P_1$ line measured in a well-collimated Sr atomic beam** - A fit of Lorentzian peaks for isotopes 88, 87 (three components), 86, and 84 has been made. The estimated relative abundances are 88 %, 3.3 %, 8 %, and 0.7 % respectively, in some agreement with the expected values (Tab. 3.2). ^{87}Sr appears reduced which may be due to the altered spatial radiation profile. The FWHM of the ^{88}Sr peak is found to be ∼34 MHz, close to the natural linewidth of γ =30.2 MHz.

with 350 mW typical. The beam quality is however quite poor in both spatial mode and pointing stability, thought in part to be from thermal lensing occurring in the doubling crystal. We correct the laser output astigmatism and circularise the beam with a single cylindrical lens between two spherical lenses of a telescope. The SHG cavity, which is tunable by a piezoelectric transducer (PZT) on one of the cavity mirrors, is locked by the Pound-Drever-Hall (PDH) method to the master oscillator. This is in turn stabilised to a low-drift tunable optical cavity by the PDH method, with feedback to the laser current and PZT, to provide medium term stability of the cooling light (∼MHz per day). The cavity is formed of a cylindrical Zerodur spacer with two curved mirrors on fused silica substrates attached at each end, one fixed and optically contacted and the other tunable over several 10s of GHz, with cavity length 92 mm. The cavity is operated under vacuum (held at around 1×10^{-7} mbar with a Varian Miniature VacIon pump) to minimise air density fluctuations and isolate from lab temperature fluctuations, which otherwise dynamically vary the effective cavity length. The vacuum chamber is actively temperature controlled and held just above room temperature with instability not exceeding 1 mK per day typical.

The light at 461 nm is divided between Zeeman slowing (80 mW, −600 MHz), MOT (30 mW, −40 MHz), probe (10 mW, 0 MHz), and transverse cooling (10 mW, −15 MHz) applications, which are frequency shifted to the required detuning with acousto-optic modulators (AOM) and optical power distributed and tuned with $\lambda/2$ waveplates and polarising beam splitter (PBS) cubes. We choose to fibre couple, with polarisation maintaining fibre, the probe and MOT beams to the vacuum chamber to both clean the beam spatial mode and address beam pointing instability issues. These issues make it necessary to intensity stabilise the light at the output of the fibres, which we achieve in the standard way by servoing the AOM RF drive power, thereby dynamically altering the diffraction efficiency and optical power in each diffraction order. For this we use a Minicircuits voltage controlled RF attenuator, which is effectively a double balanced mixer circuit, placed between a voltage controlled oscillator (VCO) and RF power amplifier. The control voltage is derived from the output of a simple integrator circuit which is fed an error signal from a comparison of a set-point voltage and measurement photo-diode signal. Due to the poor mode quality at the fibre input we achieve only 60 % coupling efficiency.

Three AOMs, from IntraAction Corp., with tellurium dioxide acousto-optic material and centre frequency 200 MHz, and another, glass and 60 MHz, are used to produce all required frequencies (as shown in Fig. 3.13) and (for the former) can be operated over the range 150 MHz to 280 MHz (provided diffraction angle is compensated). The laser frequency is set at −450 MHz and a single or double pass (depending on Zeeman Slower final field configuration) through the glass material AOM, taking the −1 diffraction orders, provides the required slowing beam detuning. The MOT and probe detunings are achieved by doubling passing AOMs at drive frequencies 205 MHz and 225 MHz respectively. We

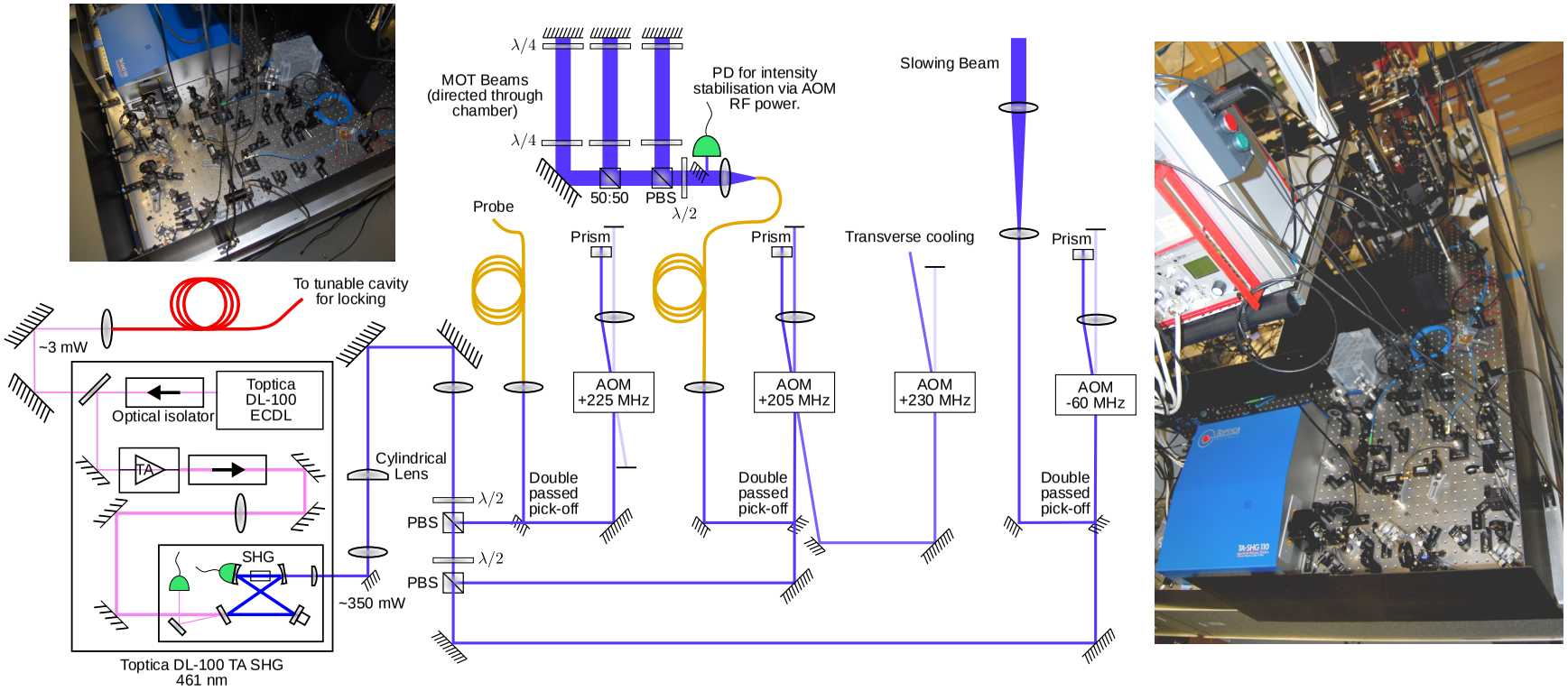


Figure 3.13: **461 nm light source** - Schematic of optical components involved in 461 nm "blue" system including: Toptica DL-100 TA SHG laser source, beam correction optics, and double pass AOM frequency shifting scheme.

achieve up to 97 % diffraction efficiency in single pass at high optical powers and note a high sensitivity to beam waist and degree of collimation, with greatest efficiency achieved for large (∼1 mm waist) well-collimated beams, and only a small (negligible) sensitivity to polarisation is observed. We double pass using the spatially separated beams method with retro-reflection and spatial offset provided by a right angled prism and lens positioned at the focal length from the AOM crystal centre and prism centre and achieve a double pass efficiencies of ∼80 %. This method is adopted in preference to the polarisation extraction method partly for cost reasons but primarily as it provides higher extinction of the light when switched as there is no reliance on the quality of anti-reflection coatings and purity of polarisation as is otherwise the case. An in-situ (i.e., no angular correction to compensate diffraction angle) frequency tuning range of ∼70 % of that for single pass is achieved for the double passed beam. This comparison was made by measuring the diffraction efficiency in single pass and double pass versus AOM RF drive frequency over a full range (such that the diffraction efficiency goes from zero to maximum and back to zero) and compare the tuning range of each pass, taking 50 % diffraction efficiency as a cut-off. To recycle the power lost in the zeroth order of the second pass of the MOT AOM we pick off this light to a second AOM operated in single pass with drive frequency 230 MHz and take the +1 order to generate light at −15 MHz for transverse cooling. Although power efficient, the dependency of this method on the MOT AOM drive frequency is potentially problematic and an alternative route would be to setup the transverse cooling light AOM in double pass at drive frequency 217.5 MHz with a direct feed from the laser. To provide experimental control the VCOs and RF attenuators are interfaced with Labview via PXI hardware allowing software control of drive frequency and power. In addition, a TTL controlled RF switch provides high extinction of the AOM RF drive power for high extinction of the non-zero AOM diffraction orders, and used together with a mechanical shutter eliminates direct laser light leakage delivered to the vacuum chamber during frequency measurement that would otherwise cause large dynamic stark shifts of the clock transition.

It is worth noting here that (ZnSe or GaN based [201, 202]) laser diodes capable of operating at 461 nm are now becoming available, driven no doubt by the demand for "true-blue" production in the laser projector market. Such a development potentially offers a greatly simplified and reduced cost laser apparatus for future Sr experiments.

3.5.3.2 Repump lasers

The repump transitions at 679 nm and 707 nm have natural linewidths $\gamma = 1.4$ MHz and $\gamma = 6.4$ MHz, respectively. For cold atoms in the MOT centre broadening effects will be small and we preferably require power spectral density of the laser source within the natural transition linewidth. To this end, the repump light at 679 nm and 707 nm is provided by two in-house built Littrow ECDLs with anti-reflection (AR) coated laser diodes from Laser2000, model SAL-685-25 and SAL-0705-20, respectively. The diodes are available un-

coated relatively cheaply and are manufactured by Opnext, models HL6750MG-A (centre frequency 685 nm) and HL7001MG-A (centre frequency 705 nm) respectively. The coating, although not absolutely necessary, certainly makes tuning to the correct wavelength far easier and in some cases essential. The ECDL design is based on a Newport SL25.4BD gimbal optical mount with micrometer adjusters and an adapter piece made to hold the grating at the approximate Littrow angle, which mounts via a piezoelectric tube. Plane holographic gratings of 1800 lines mm^{-1} are used with Littrow angles of 37.67° for 679 nm and 39.52° for 707 nm light. The mount with grating is assembled in a machined Dural block which forms an end-plate of the ECDL. The laser diode is mounted in a cylindrical brass block which is screwed, using nylon inserts to isolate the metal screw from the brass (in preference to nylon, or similarly thermally insulating, screws) to another Dural end-plate with a ring peltier thermo-electric module sandwiched between. The end-plate acts as the heat-sink to the peltier module which is used to temperature stabilise the laser diode at the desired temperature with an in-house built temperature controller (see Ch. 4 for details of temperature control). A lens mount is fixed over the laser diode mounting end-plate in which an achromatic lens in a cylindrical casing is inserted, adjusted to optimally collimate the beam, and fixed in place with a grub screw. The two ends of the ECDL are connected by an aluminium tube which can be cut to an arbitrary length to produce the desired cavity length. These ECDLs were based on an existing design and originally intended for use as clock lasers but due to many drawbacks in the design an alternative ECDL was designed for use in the lab (see Ch. 4). An initial cavity length of a relatively long 10 cm was implemented with the intention of reducing the fractional length change of the cavity for a given mechanical perturbation and aid passive frequency stability. In practice the length makes operation quite tricky as a consequence of a reduced external cavity mode spacing (∼1.5 GHz) and additional sensitivity to alignment of the grating, in particular in the non-dispersive, here vertical, plane of the diffraction grating, and so we plan to reduce the cavity length in the future. The grating is typically used in the transverse electric (TE) mode with light polarisation (diode polarised along long or "slow" axis of diode laser facet (the short transverse beam axis in far field)) parallel to the grating lines (referred to as P-plane polarised). The configuration ensures optimum resolving power of the grating as the long transverse beam axis covers the maximum number of grating lines. The gratings are nominally 20 % efficient in the 1st order (fed back to the laser) which is often sufficient to pull the diode wavelength, however we had some difficulty reaching 707 nm with some diodes, aided by rotating the diode in its mounting, and hence polarisation relative to the grating, to increase feedback by partial use of the more efficient transverse magnetic (TM) mode. It is expected the 685 nm diode must be cooled to operate at 679 nm and the 705 nm diode heated to reach 707 nm although no significant benefit was observed either way over a range of approximately ±5 K about room temperature (20 °C).

The PZT driver and diode current source are in-house designs with the latter adapted from the design of K.G. Libbrecht and J. Hall [203] by Christopher Edwards. For temperature control we have tested the Maxim MAX1978 EV integrated PID temperature controller with PWM (500 kHz) H-bridge output topology providing up to ±3 A output current with high efficiency, which is intended for communications laser diode modules. Unfortunately, as a consequence of electromagnetic interference, the switching topology leads to a non-negligible modulation of the laser diode current at the switching frequency, and in turn the light acquires noise sidebands at ±500 kHz. No real effort was made to minimise this effect as noise critical applications are better served with a linear output topology controller. The result, although not ideal, should be adequate for operation of the repump lasers.

3.5.3.3 Multiple wavelength frequency stabilisation to an optical cavity

ECDLs, exploiting wavelength selective optical elements and extended cavity lengths, successfully act to reduce the linewidth of a bare laser diode (upwards of a few 10s of MHz) to ∼100 kHz or below, often limited by current noise of the driving current source which tunes the laser frequency through charge carrier density driven refractive index changes in the diode gain medium. However, their medium to long term frequency stability, arising from thermal and mechanical creep, is generally inadequate for unmonitored spectroscopic use. To address this, here, the laser frequency is stabilised to a resonance feature of a low-drift optical cavity. By extracting the derivative of the cavity resonant line feature a frequency discriminant is obtained from which corrections to the laser frequency may be instructed (see Ch. 4 for details). Through the action of the laser diode current ("fast" acting, bandwidth ∼1 MHz) and grating position ("slow" acting, bandwidth several kHz), the ECDL effective cavity length is compensated to maintain a steady frequency at line centre of the cavity resonance.

For the Sr lattice experiment there are several optical wavelengths that require stabilisation. Here, we propose the locking of four discrete optical wavelengths (922 nm, 679 nm, 707 nm, and 813 nm) to a single low-drift tunable optical cavity using the Pound-Drever-Hall (PDH) locking method and wavelength separation by optical filters. The optical cavity is described in Sec. 3.5.3.1 and the proposed locking scheme depicted in Fig. 3.14. From the cavity mirror coating reflectance data and Eq. (2.3) we can estimate a cavity finesse of 450 at 922 nm, 2100 at 679 nm, 3100 at 707 nm, and 2500 at 813 nm which are in a useful range for robust frequency stabilisation. Conveniently, suitable dichroic and short/long pass filters are available from Thorlabs, and with reference to Fig. 3.14 these are, D1: DMLP900 dichroic; transmits above 920 nm, D2: DMLP605 dichroic; transmits below 720 nm, F1: FES0700 shortpass; >80 % transmission at 679 nm and ∼0 % at 707 nm, F2: FEL0700 longpass; >80 % transmission at 707 nm and ∼0 % at 679 nm. Furthermore, by using a range of optical modulation frequencies the PDH locking signal prior

to demodulation may be electronically filtered for more robust wavelength isolation. In operation, each wavelength may be tuned to the correct cavity mode with the aid of an optical wavemeter before locking, and the difference between the nearest cavity mode and required atomic frequency bridged with an AOM. Other than its reduced cost and use of resources in comparison to duplicating an independent cavity stabilisation scheme for each wavelength, this scheme intrinsically relates the long term frequency drift of a single optical cavity to all wavelengths and therefore allows simple multiple simultaneous correction. By referencing the cavity, quickly and simply, to the 461 nm fluorescence signal, long term stability of all four wavelengths is achieved.

3.5.4 Experimental details: Apparatus

3.5.4.1 Ultra-High Vacuum (UHV) apparatus

The vacuum apparatus consists of a Sr oven (Sec. 3.2.2), a small spectroscopy cell intended for transverse cooling, an atomic beam delivery tube allowing space for Zeeman Slowing, and an experimental chamber. The system is differentially pumped with a $40\,\mathrm{l\,s^{-1}}$ ion pump (Varian VacIon Plus 40 StarCell) servicing the "high-pressure" oven side of the vacuum system (pressure $1 \times 10^{-7}\,\mathrm{mbar}$ typical with oven running), and a $20\,\mathrm{l\,s^{-1}}$ ion pump (Varian VacIon Plus 20 StarCell) aided by a non-evapourable getter (NEG) (SAES Getters CapaciTorr CF 35 base flange and C 400-2 DSK cartridge and heater) pumping the experimental chamber (pressure $\sim 1 \times 10^{-10}\,\mathrm{mbar}$). The NEG efficiently pumps hydrogen gas, which accounts for the majority of vacuum residual gas content (checked with residual gas analyser (RGA)), at a specified rate $\sim 100\,\mathrm{l\,s^{-1}}$. A 1 mm aperture on axis of the atomic beam, and immediately downstream of the spectroscopy cell (10 cm from oven nozzle exit), separates the two sides. This is closely followed by a manually operated viton sealing gate valve, placed to shutter the atomic beam and allow servicing of the oven without breaking vacuum to the experimental chamber. All-metal valves (copper seal and bonnet) are included on each side of the vacuum system to allow initial pumping from air (we use a Varian Mini Task turbomolecular vacuum pump). The experimental chamber comes from Kimball Physics and is the 8″ diameter extended spherical octagon, model MCF800-ExtOct-G2C8A16 in 316LN (non-magnetic) stainless steel. All vacuum components are connected in the usual way (for UHV) with CF type flanges and copper gaskets. To aid serviceability, by preventing corrosion, silver plated copper gaskets are used in the vicinity of the oven. For the viewports we use the softer annealed copper gaskets with the aim of reducing the required sealing force (derived from the applied tightening tension required to complete the seal) to minimise stress on the viewport, which may otherwise lead to unwanted birefringence in the glass. The viewports are from Torr Scientific Ltd and are a fused silica glass (surface quality 20/10 scratch/dig, flatness $< 8\lambda$) with a non-magnetic tantalum brazed seal to a 316LN stainless steel CF flange, and may be baked to

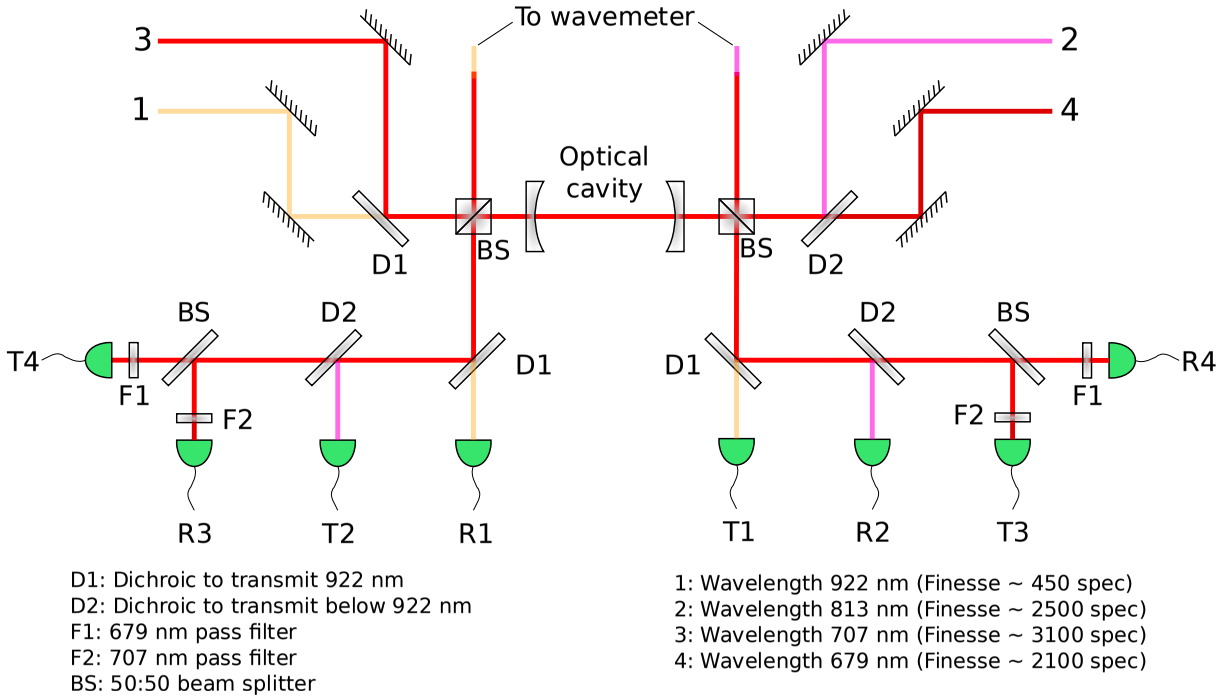
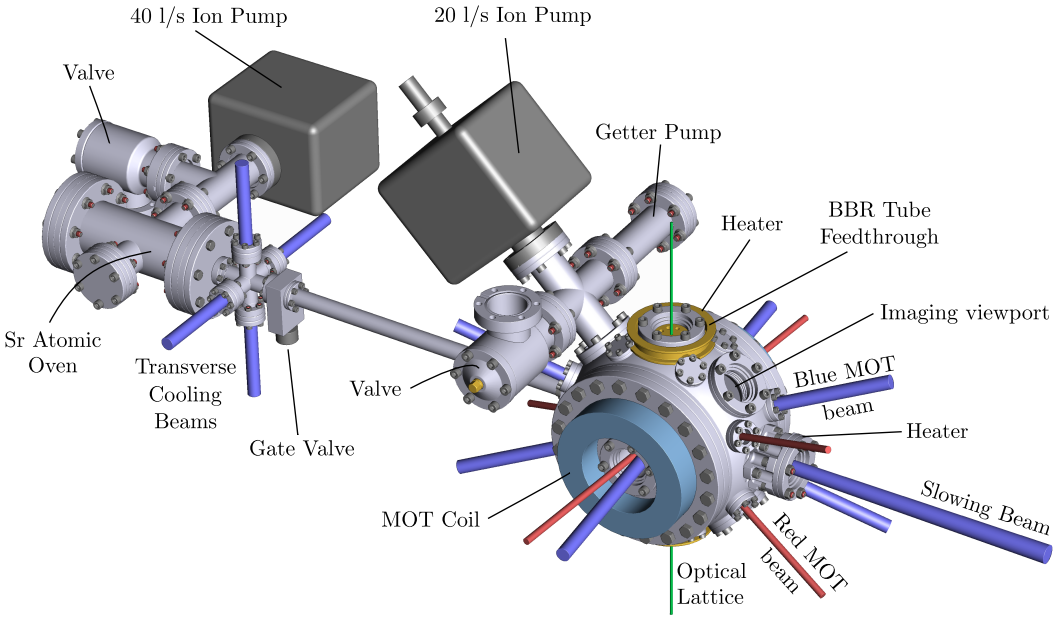


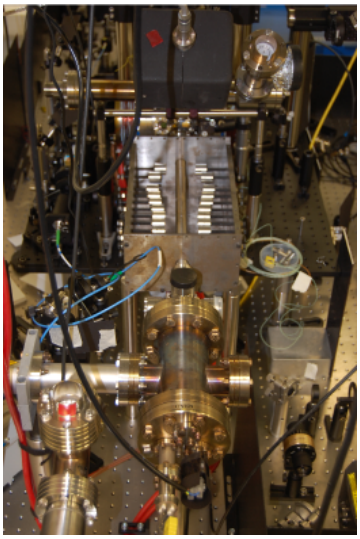
Figure 3.14: **Four wavelength locking scheme** - Schematic of the proposed locking scheme. T# and R# label the detected cavity transmitted and reflected signals of wavelength number label #.

~470 K. Each is AR coated for the relevant wavelengths and for the lattice viewports this includes 813 nm, 698 nm, and 532 nm (however, the coating would not stretch to include 461 nm in addition to these). Viewports for blue and red MOT beams are coated for single wavelengths only). For the lattice viewports, where birefringence is highly undesirable, low stress mounting options were considered. Indium wire is often used to mechanically seal glass viewports to metal vacuum chambers by virtue of its high malleability and ability to wet glass (will cold weld to glass so does not require clamping once the seal is made), but is constrained to low temperature operation (and bake out) by limit of its relatively low melting point (~430 K). An alternative is to use lead solder in place of indium which may be baked at temperatures exceeding 525 K. However, lead solder lacks the cold welding properties of indium and sealing requires a permanent clamp (see for example [204, 205]). The force applied to this clamp however can be less than that required to seal a CF flange and can be carefully applied uniformly across the viewport to minimise strain. Such a sealing method may be adopted in future revisions of the apparatus. The slowing beam viewport, which faces the atomic beam, is of z-cut sapphire and AR coated on the outer surface only to present a corrosion resistant surface to the Sr atomic beam (see Sec. 3.2.1.1 for details). A Kimball Physics close coupler provides clearance around the viewport for heater access in aid of clearing Sr deposits from the Sapphire. All vacuum components are cleaned for UHV and following assembly baked to a minimum of 470 K (limited by viewports) for several days under vacuum to encourage out-gassing of surface contaminants. The complete apparatus including optical configuration is shown in Fig. 3.15.

3.5.4.2 Optical access and MOT coils

To allow space for lattice optics the whole system is mounted at a raised height with chamber centre ~38.5 cm above the optical table. Blue and red MOT beams are delivered independently (3 retro-reflected beams for each MOT) with access given by 8 1.33″CF (DN16) ports and the two 8″CF side flanges (reduced to 2.75″CF (DN40) viewports), which limits the MOT beam size to ~1 cm. It is noted that in the current configuration the MOT beams are not fully orthogonal and are reduced to a 45° angle in the transverse (to coil axis) magnetic field direction on axis of the atomic beam. The confinement in a usual MOT is anyway twice weaker in the transverse directions compared to the longitudinal (on axis) direction as a result of the shape of the quadrupole field produced by the anti-helmholtz coil pair. Here we have an additional asymmetry between transverse beams and the projected restoring force in the vertical direction is reduced to about 70 % of usual but should not pose any difficulties. A six-way DN16 cross provides 4-axis optical access immediately following the oven (centre of cross 9 cm downstream of oven) which may be used for laser spectroscopy or transverse cooling, although with limited length of interaction. A 1 mm collimating aperture is secured in the furthest leg of the cross (away





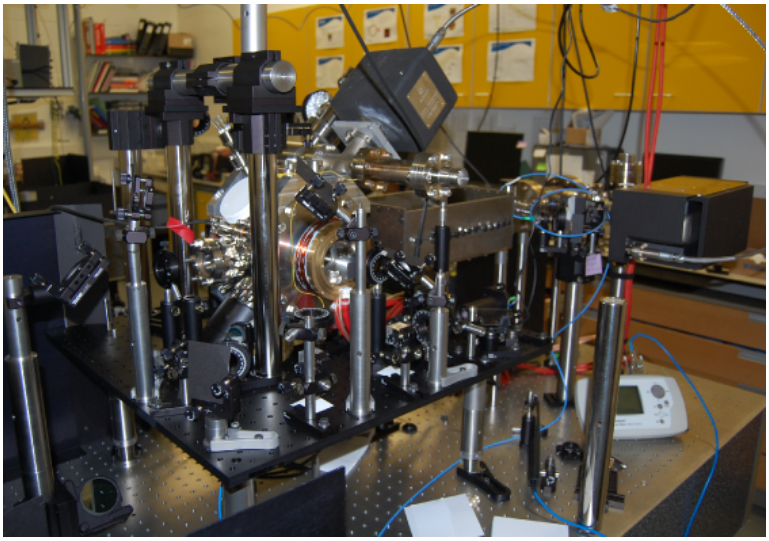


Figure 3.15: **Vacuum Apparatus** - (Top) Render of a 3D drawing of the vacuum apparatus as it exists in the lab. Drawing assembled in VariCad (for Linux) using (largely) component manufacturer provided STEP files). (Bottom right) Photograph of the assembled vacuum system and surrounding MOT optics. (Bottom left) View along the oven and permanent magnet Zeeman slower.

from oven) 10 cm downstream of the oven nozzle.

The MOT coils must produce large field gradients >40 G cm^{-1} and allow rapid (∼10 ms) switching of the field to ∼1 G for the second stage of cooling. They must also be suited to providing a uniform field ∼10 G when switched to helmholtz configuration for magnetic induced spectroscopy (see Sec. 3.21). Given the external dimensions of the vacuum chamber, coils made to fit externally and to this specification present a moderate challenge. For coils mounted inside the vacuum (see for example the Sr apparatus of PTB or Durham) a small separation of coils is possible, allowing high field gradients to be reached with relatively small peak fields. However, having additional pieces inside the vacuum system brings with it additional complications. Another option is to manufacture non-standard side flanges which mount the coils within a recess, positioned inside the chamber, to achieve a shorter coil separation (see, for example, the transportable apparatus of the Florence group [206]. Alternatively, a large coil with a hefty current supply and efficient water cooling can be used. A suitable coil may be 15 cm diameter, with 90 turns producing 0.66 G cm^{-1} A^{-1}, wound with copper tubing to allow efficient water cooling. However, currently, we are utilising MOT coils intended for a 2D MOT, which were to operate continuously around a small chamber. They have 500 turns of 0.9 mm polyester enamelled copper wire wound around an unbroken (no cut to minimise eddy currents) aluminium former of diameter 95 mm, which is mated to a brass cooling ring through which cold water is pumped. The coils produce an axial gradient 2.4 G cm^{-1} A^{-1} requiring 17 A to produce 40 G cm^{-1}. However, heating is already a problem at 10 A corresponding to an axial field gradient 24 G cm^{-1} (coils have dc resistance, R ∼4 Ω, power dissipated ∼400 W [almost 3 times this at 40 G cm^{-1}]), and with relatively high inductance (estimated L ∼30 mH) the circuit time constant, L/R, is ∼7.5 ms with corresponding switching time (to fully off) estimated to be ∼40 ms. Subsequent measurements of the field decay of the coils when switched confirm this estimate. The coils are currently mounted directly to the 2.75″CF viewports on each side flange. A 5 kW power supply (model EA-PS 8200-70 by Elecktro-Automatik) is used to power the coils.

3.5.5 Experimental results of the first cooling stage

Initial cooling and trapping has be carried out on the $^1S_0 \leftrightarrow {}^1P_1$ transition with the MOT loaded from a slow atom flux exiting a novel permanent magnet Zeeman slower [185]. The slower consists of a 2D array of permanent neodymium disc magnets with field arranged transverse to the atomic beam direction [185]. The capture and exit velocities are approximately 420 m s^{-1} and 25 m s^{-1} with slowing length ∼25 cm and is designed to operate with 70 mW of optical power in the slowing beam, which is convergent towards the oven source. Note, due to the transverse field arrangement linearly polarised light is required, perpendicular to the magnetic field direction, of which only half is resonant with the spatially tuned magnetic sublevel. For optimum parameters of the slower, we

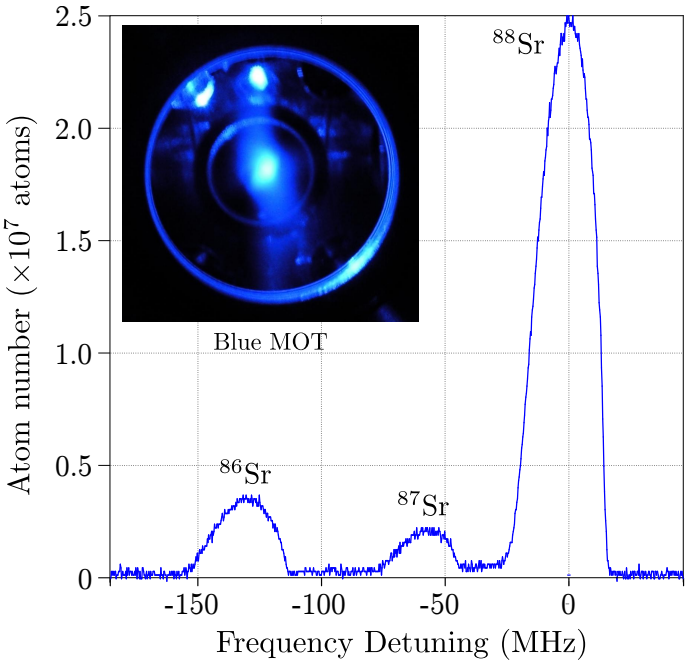


Figure 3.16: **MOT Isotope Scan** - MOT parameters: Axial field gradient $\sim$20 G cm^{-1} and individual MOT beam power $\sim$4 mW with waist $\sim$5 mm. Note, the frequency detuning is relative to that for maximum loading of the ^{88}Sr MOT.

measure a slow atom flux of $\sim 3.5 \times 10^9$ atoms s^{-1} centred at $\sim$30 m s^{-1} for ^{88}Sr, from an atomic beam of total flux 1×10^{11} atoms s^{-1}, and load $\sim 2.5 \times 10^7$ atoms in to a MOT operating the same $^1S_0 \leftrightarrow {}^1P_1$ transition. Further details of the slower can be found in Refs. [186, 187], which includes full characterisation of the slower by measurements of the longitudinal velocity distribution at the slower exit and MOT loading rates for various slower operating parameters. An enhancement in MOT number of around 17 is achieved with the addition of repump lasers at 707 nm and 679 nm, as previously discussed, with loading time $\sim$0.5 s.

To validate the slowing and capture of atomic Sr the 1st stage cooling laser frequency (slowing beam and MOT beams together) was scanned over isotopes ^{86}Sr, ^{86}Sr, and ^{86}Sr by tuning the length of the optical cavity to which the master laser at 922 nm is stabilised. The MOT fluorescence is collected on a home-built large area photodetector (using Hamamatsu S3590-18 Si PIN photodiode) and the measured signal presented in Fig. 3.16. The relative atom number between isotopes is in good agreement with expectation from natural abundances.

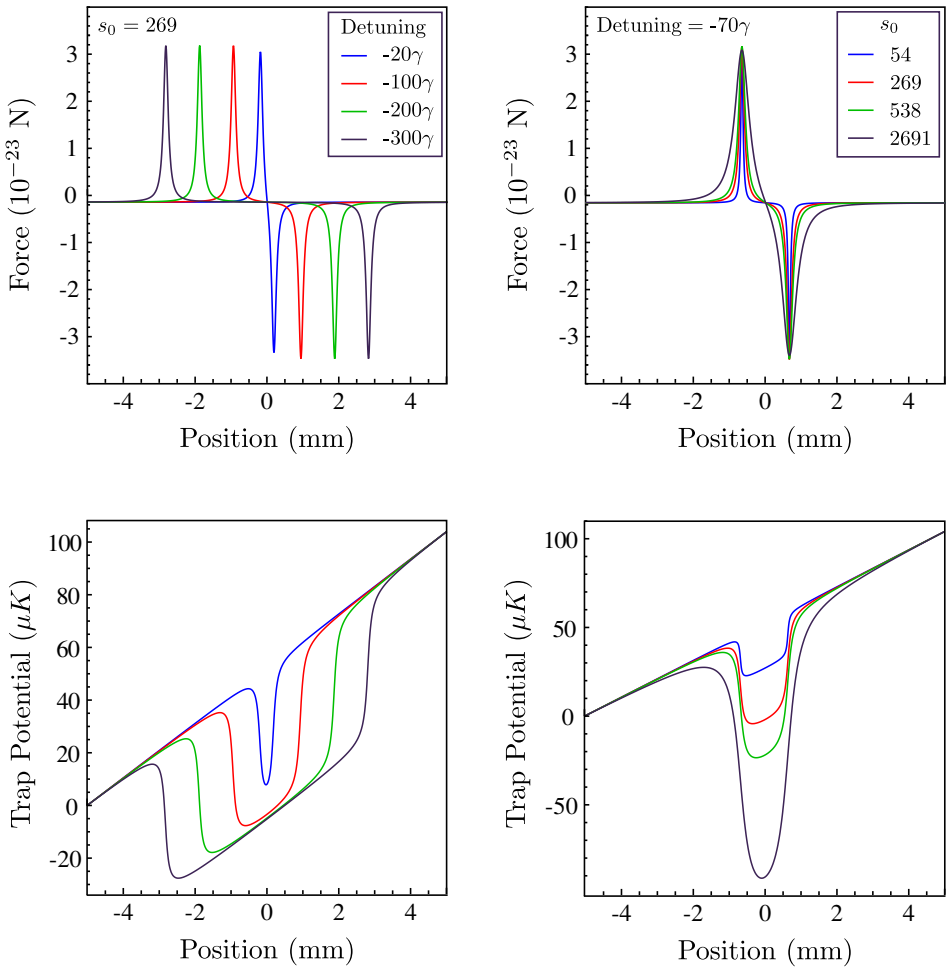


Figure 3.17: **Second-Stage Cooling** - (Top) Semiclassical radiative force versus position for the 689 nm MOT along z, with gravity included. (Bottom) The corresponding trap potential in temperature. An axial magnetic field gradient of 5 G is used throughout (2.5 G along z). Here, the transition linewidth γ is 7.4 kHz and s_0 (which is for each MOT beam) is calculated for beam waist $w_0 = 2$ mm (beam power ranges from 50 µW to 500 µW.)

3.6 $^1S_0 - {}^3P_1$: Second-stage cooling Sr

3.6.1 Red MOT

Following cooling and trapping on the $^1S_0$ – $^1P_1$ transition described above, atoms are loaded into a red MOT operating on the narrow (∼7 kHz) $^1S_0$ – $^3P_1$ transition at 689 nm, allowing Doppler cooling to recoil limited temperatures ∼1 μK suitable for efficient loading into weak conservative potentials. In contrast to the first stage of cooling, which has $\Gamma/\omega_r \sim 3 \times 10^3$, the narrow cooling line is characterised by $\Gamma/\omega_r \sim 1.6$ and the cooling forces are comparable to the local gravity with $a_{max}/g = 16$ (see Fig. 3.17) and requires only moderate magnetic field gradients (1 G cm^{-1} to 10 G cm^{-1}). As a consequence the atoms find equilibrium below centre of the MOT and appear to sag under the influence of gravity. Such a system provides an opportunity to investigate both semiclassical and quantum mechanical cooling processes, the dynamics of which have been exhaustively studied elsewhere in previous works [207–209]. We reserve the following discussion for detailing the apparatus required to realise such a narrow line MOT in extension to the initial cooling.

3.6.2 Experimental details: 689 nm light source

To take advantage of the cold temperatures offered by narrow line Doppler cooling we require a light source with similar (or better) spectral property. We must also be able to spectrally broaden this source to cover the extent of the Doppler profile arising from the residual atomic motion following first-stage cooling. Assuming a temperature of ∼mK a bandwidth of 0.5 MHz to 1 MHz ($\Delta\nu = \sqrt{Tk_B/m}$) directed to higher detunings should be sufficient.

The 689 nm cooling light is generated by an in-house ECDL which is locked using the PDH method to a high-finesse optical cavity. The PDH locking method is a form of FM spectroscopy applied to detecting an optical cavity resonance and providing feedback to the laser frequency to maintain resonance. Details of the PDH locking method will not be given here, however, the interested reader is referred to the thesis of T. Day [210] and the original paper by Drever et al. [55]. Additionally, and of particular use to the experimenter tasked with stabilising diode lasers, the chapter produced by R. Fox et al. for "Cavity-Enhanced Spectroscopies" [211] provides a very useful manual.

The optical cavity (which previously served as the clock cavity for the NPL Sr ion project) consists of a horizontally mounted 10 cm cylindrical ULE spacer with two curved mirrors on a ULE substrate optically bonded at either end and a ventilation hole drilled transversely to centre. The cavity finesse was measured to be ∼65 000 by cavity ring-down spectroscopy, corresponding to a cavity bandwidth (FWHM of resonance feature) of ∼23 kHz and a mirror reflectance of 99.995 % at 689 nm. Typically, cavity mirrors exhibit losses due to imperfections on or within the mirror coating, which may be caused simply

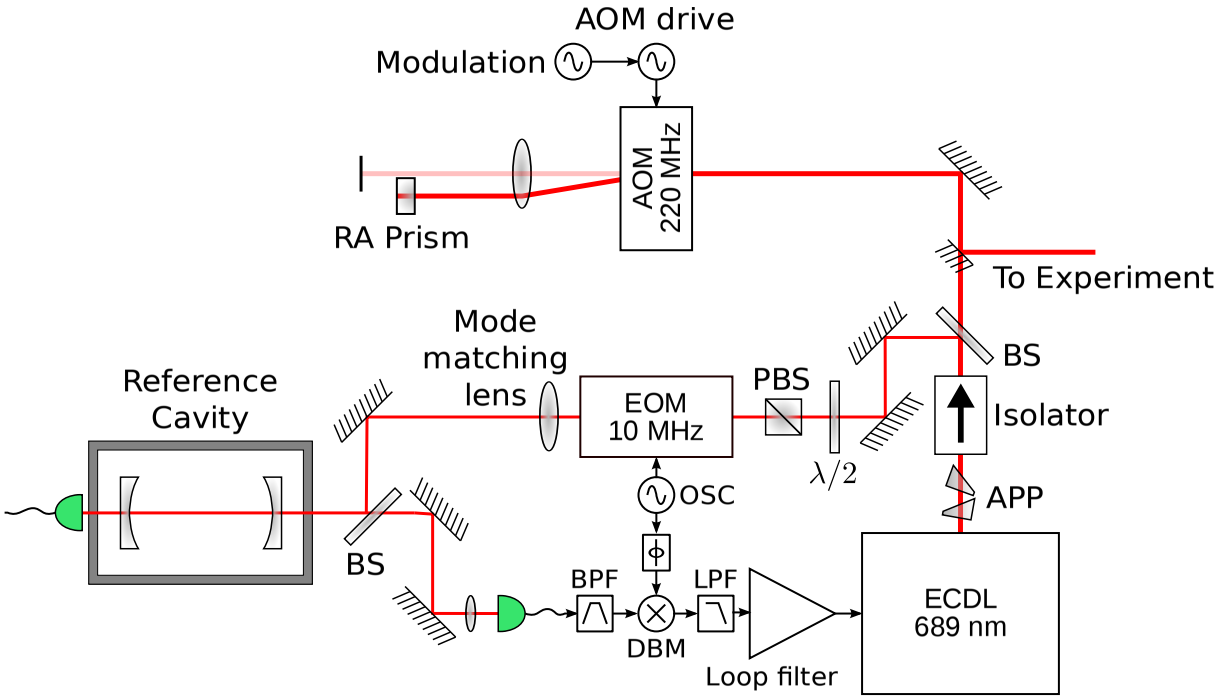


Figure 3.18: **689 nm Light Source** - Schematic of the optical setup for the cavity-stabilised second-stage cooling laser. PBS is polarising beam splitting cube, APP – anamorphic prism pair, RA – right angled, BS – beam splitter, BPF – bandpass filter, LPF – low pass filter, and DBM – double balanced mixer.

by surface contaminants that may be removed with cleaning. The combined scattering and absorption losses, characterised by L, may be determined by a measure of the cavity finesse together with the cavity transmission, used to determine the mirror transmittance, T, where $R + T + L = 1$. The cavity finesse may then be determined approximately according to $(L + T)^{-1}$. Typical losses of the 'best' available mirrors are in the region of a few ppm, which is consistent with the results here.

The cavity is operated under vacuum (held at around 1×10^{-7} mbar with a Varian VacIon $2\,\mathrm{l\,s^{-1}}$ pump) to minimise air density fluctuations and isolate from lab temperature fluctuations, which otherwise dynamically vary the effective cavity length. For example, consider the refractivity $(n - 1)$, where n is the local refractive index of air at room temperature along the optical path length as a function of pressure [212],

$$n - 1 \approx 2.5 \times 10^{-7} P(\mathrm{mbar}) \tag{3.40}$$

where P is the pressure in units of mbar. The effective cavity length determines the cavity free spectral range as $\nu_{\mathrm{FSR}} = \frac{c}{2Ln}$ and the relative frequency shift of the cavity resonance is,

$$\frac{\delta\nu_P}{\nu} = (1 - 1/n) \approx 2.5 \times 10^{-7} P(\mathrm{mbar}) \tag{3.41}$$

For a frequency stability $\sim$1 kHz (fractional frequency instability $\sim 2.3 \times 10^{-12}$) a cavity operated at atmospheric pressure ($\sim$1 bar) requires a fractional pressure stability of 1×10^{-5}, which is unrealistic. At a pressure of 1×10^{-7} mbar this is relaxed significantly accommodating fluctuations as large as 10 000 % (for the clock laser where a fractional frequency instability $\sim 1 \times 10^{-15}$ or better is required, the constraint on pressure fluctuation here is at the 10 % level which is likely achieved in most vacuum apparatus operating in a well-defined steady state environment).

The vacuum chamber is wrapped with Constantan heater wire and actively temperature stabilised at just above room temperature with instability not exceeding 1 mK per day typical (lab temperature stability ± 0.1 K typical). This is aided by a layer of rubber thermal insulation which is wraps around the cavity vacuum chamber and also lines an aluminium sheet box which sits over the vacuum chamber. At room temperature the ULE linear coefficient of thermal expansion (CTE) is $\alpha_L \sim 1 \times 10^{-8}\,\mathrm{K^{-1}}$. It is then necessary that the cavity sees temperature fluctuations no bigger than 100 µK if we are to maintain a frequency instability of $\sim$1 kHz. As the cavity is somewhat isolated from conductive and convective heat transfer mechanisms we expect a reduced response to environmental fluctuations with a thermal time constant dominated by radiative heat transfer. One approach then is to apply substantial radiative shielding to the inner chamber using very low emissivity materials (i.e., highly reflective surfaces, such as polished aluminium or gold [chemically stable]). Here we rely on the shielding of the machined stainless steel vacuum

chamber (emissivity ∼0.14). Finally, a decreased temperature sensitivity may be achieved by stabilising the temperature of the cavity to correspond to the minima of the ULE CTE, which is targeted at room temperature but often falls several degrees off depending on the ULE batch. Such a measurement is easily made (providing one has a second system for beat note comparison or an optical frequency comb handy) by (very) slowly ramping the cavity temperature and measuring the locked laser frequency, which should turn around at the CTE minima. Such a measurement has not yet been made for this optical cavity but is expected to be below room temperature, requiring a redesign of the cavity vacuum chamber thermal control.

In addition to environmental temperature perturbations, the energy supplied by the laser to the cavity mirrors can result in noticeable heating effects. Given a finesse of 130 000 with power enhancement factor $N = \mathcal{F}/\pi$ the intracavity power is $P_{intra} = 4 \times 10^4 P_{inc}$, which even for a small input power of 10 µW (coupled into the cavity) results in a significant circulating power of 0.41 W. Calculating the shift due to this heating is not straightforward and depends on the physical properties of the mirror substrate and coating. Some experimental investigation carried out with a similar cavity [213] (finesse ∼400 000) reports a dependency of 15 Hz µW^{-1} of coupled light. We typically use ∼10 µW incident to the cavity (set by increasing the light level just above the locking system's electronic noise floor to ensure optical limited noise near the shot noise limit) with a free-running stability of <1 %, and as such poses no threat to the laser's frequency stability at the required level.

Fig. 3.18 shows the schematic of the locking setup. The ECDL is of Littrow design (see Ch. 4) and generates about 10 mW of optical power at 689 nm. The output beam is first circularised with an anamorphic prism pair (APP) and passes through an optical isolator (∼40 dB) to prevent unwanted optical feedback to the laser diode. The majority of light is sent to the experiment via a double passed AOM which bridges the gap from the nearest optical cavity mode and atomic resonance (measured with an optical frequency comb to be 440 MHz) and allows frequency modulation necessary for efficient cooling, described above. A small amount of light is picked off for the cavity lock. This light is first polarised, here with a standard polarising beam splitting cube (extinction ratio T_P/T_S 10^4:1 in transmission; Glan-Thompson polariser can be used if higher extinction required), before entering the electro-optic modulator (EOM) (Leysop EM200A-PM) driven by a high-voltage FET oscillator (serving as the local oscillator [LO]) for phase modulation (PM). It is important to set the polarisation correctly for pure PM, i.e., with the light linearly polarised along the extraordinary crystal axis (z-axis or optical axis), as rotation of the polarisation (resulting from a polarisation which samples the crystal birefringence) will lead to an unwanted amplitude modulation (AM) following subsequent polarising optics. This AM produces in-phase blue and red sidebands (in contrast to anti-phase PM sidebands) at the EOM modulation frequency which do not cancel when mixed on the in-loop optical detector. When this signal is demodulated to baseband in a step to

produce the locking error signal this AM results in an offset (known as the optical offset) in the frequency of the lock point. The offset can be compensated with an electrical offset, however, dynamic variation of the AM will result in an instability of the laser frequency. Here it is sufficient to ensure proper alignment through the EOM to minimise AM, however, in more demanding situations it may be necessary to introduce a scheme for active correction of the residual AM [214, 215]. Care must also be taken to avoid additional etalons in the optical path which act to modulate the relative amplitudes of the PM sidebands, leading to further offsets of the error signal which vary with frequency of the laser. Such etalons are generally formed between surfaces of optics in beam path normal to the laser wavevector and the cavity mirrors, and vary with changing beam path distances resulting from air currents and temperature fluctuations. Generally, choosing a low modulation frequency minimises the influence of such parasites but is traded for reduced lock capture range and is usually solved by careful arrangement of optics.

Following the EOM, light is directed into the TEM00 spatial cavity mode with a pair of steering mirrors (the second is in fact a glass plate) and mode matching lens (for details of mode matching see, for example, Ref. [216]). The glass plate allows the reflected cavity signal to be extracted for locking and is used in preference to a $\lambda/4$ waveplate plus PBS (typically used) to minimise the aforementioned AM. The cavity transmission is viewed with a CCD camera during alignment to monitor the cavity mode and subsequently with a silicon PIN photodiode. The reflected signal is focussed onto a small area avalanche photodiode (APD) which is AC coupled and amplified. The detected signal contains a measure of the laser frequency noise as a pedastal of noise sidebands around a central beat at the modulation frequency, f. This signal is bandpass filtered to eliminate frequencies near DC, $2f$ and higher and mixed with the LO signal in a double balanced mixer (DBM). It is important to eliminate common signals at multiples > 1 of f as these will demodulate to cause spurious DC offsets to the error signal. The baseband signal is extracted with a low pass filter ($f_0 \ll f$) and fed to the laser current and PZT via the loop filter (see Ch. 4). A locking bandwidth of $\sim$400 kHz is achieved and a sub kHz laser linewidth is estimated.

3.7 One-Dimensional Optical Lattice Trap

3.7.1 Dipole force

We previously considered the radiative force experienced by a two level atom for an atom-light interaction where detuning, Δ, is small ($\Delta \ll \Omega$). We now turn our attention to the case for large detuning, $|\Delta| \gg \Omega$, in which the influence of photon scattering is substantially reduced. Instead, we are concerned with the perturbation of energy levels by the presence of the laser field, such that we may create conservative trapping potentials by exploiting laser field intensity gradients. We start by considering the atom as a simple

oscillator in a classical radiation field [217].

Classically, an atom placed in an oscillating electric field $\mathbf{E}(\mathbf{r},t) = \hat{\mathbf{e}}\, E_0(\mathbf{r}) \exp(-i\omega t) + c.c.$ experiences an oscillating induced dipole moment $\mathbf{p}(\mathbf{r},t) = \hat{\mathbf{e}}\, p(\mathbf{r}) \exp(-i\omega t) + c.c.$, related by the frequency dependent complex polarisability α as,

$$\mathbf{p} = \alpha \mathbf{E} \tag{3.42}$$

The interaction potential, U_{dip}, between the electric field and the induced dipole moment is given by the time average of the instantaneous electrostatic interaction energy, V_{int}, as,

$$U_{dip} = \langle V_{int} \rangle = \int_0^{\langle \mathbf{E} \rangle} -\mathbf{d}(\mathbf{E}) \cdot \mathrm{d}\mathbf{E} = -\frac{1}{2}\langle \mathbf{pE} \rangle = -\frac{1}{2}\mathrm{Re}(\alpha)\, \langle \mathbf{E}^2 \rangle \tag{3.43}$$

which differs from that of a permanent dipole moment by the factor $1/2$. Substituting for intensity, I, using the relation $I = \epsilon_0 c \langle \mathbf{E}^2 \rangle$, we have,

$$U_{dip} = -\frac{1}{2\epsilon_0 c}\mathrm{Re}(\alpha)\, I \tag{3.44}$$

This accounts for the dispersive interaction concerned with the real part of the polarisability, which arises from the in-phase component of the dipole oscillation. In a non-uniform electric field the atom experiences a force, known as the dipole force, given by,

$$F_{dip}(\mathbf{r}) = -\boldsymbol{\nabla} U_{dip}(\mathbf{r}) = -\frac{1}{2\epsilon_0 c}\mathrm{Re}(\alpha)\, \boldsymbol{\nabla} I \tag{3.45}$$

The idea of using this force to trap particles was first proposed by Letokhov [218] (and later by Ashkin [219]). The imaginary part of the polarisability, which describes the out-of-phase component of the dipole oscillation, accounts for absorption of the field. The power absorbed is given by [217],

$$P_{abs} = \langle \dot{\mathbf{p}} \mathbf{E} \rangle = \frac{\omega}{\epsilon_0 c}\mathrm{Im}(\alpha)\, I \tag{3.46}$$

and is later re-emitted as dipole radiation. Assuming a quantised field with photon energy $\hbar\omega$ and neglecting saturation effects, we may consider the discrete absorption and re-emission of power as a photon scattering event with corresponding rate given by,

$$R_{sc} = \frac{P_{abs}}{\hbar\omega} = \frac{1}{\hbar\epsilon_0 c}\mathrm{Im}(\alpha)\, I \tag{3.47}$$

Adopting the Lorentz model of a classical oscillator we may find the form of the polarisability. Here, we consider an electron at position r with elementary charge e, and mass m_e, elastically bound to the core of the atom and undergoing harmonic motion with oscillation eigenfrequency ω_0 (in analogy to a mass on a spring). The electron's motion is damped

as a result of energy lost by dipole radiation (the classical analogue to spontaneous emission), as described by the well-known Larmor equation concerning the power radiated by an accelerated charge. The equation of motion for a driven oscillation of the electron is thus,

$$\ddot{\mathbf{r}} + \Gamma\dot{\mathbf{r}} + \omega_0^2\mathbf{r} = -\frac{e}{m_e}E(t) \tag{3.48}$$

Assuming the solution has the same form as the oscillating field, such that $r(t) = \hat{\mathbf{e}}r_0\exp(-i\omega t)$, we arrive at the expression for the polarisability,

$$\alpha = \frac{e^2}{m_e}\frac{1}{\omega^2 - \omega_0^2 + i\omega\Gamma_\omega} \tag{3.49}$$

where we have used the relation $\mathbf{p} = -e\mathbf{r} = \alpha\mathbf{E}$, and the classical damping rate,

$$\Gamma_\omega = \frac{e^2\omega^2}{6\pi\epsilon_0 m_e c^3} \tag{3.50}$$

Introducing the on resonance damping rate $\Gamma \equiv \Gamma_{\omega_0} = (\omega_0/\omega)^2\Gamma_\omega$, the polarisability can be written as,

$$\alpha = 6\pi\epsilon_0 c^3\frac{\Gamma/\omega_0^2}{\omega^2 - \omega_0^2 + i(\omega^3/\omega_0^2)\Gamma} \tag{3.51}$$

A semi-classical approach, where we consider a two-level quantum system interacting with a classical electric field, yields the same result for α but with a modification to the radiative decay rate, given by,

$$\Gamma = \frac{2\omega_0^3}{6\pi\epsilon_0\hbar c^3}\left|d\right|^2 \tag{3.52}$$

where d represents the dipole matrix element $\langle e|\,\mathbf{d}\,|g\rangle$, for the the dipole moment operator $\mathbf{d} = -e\mathbf{r}$, and Γ is equivalent to the Einstein A_{21} coefficient. Invoking the rotating wave approximation (RWA), valid for $|\Delta| \ll \omega_0$, such that $\omega/\omega_0 \approx 1$ (but not valid for $\omega = \omega_0$), and $\Delta = \omega - \omega_0$, where ω is the frequency of the interacting light field, the dipole potential can be written as,

$$U_{dip}(r) = \frac{3\pi c^2}{2\omega_0^3}\frac{\Gamma}{\Delta}I(r) \tag{3.53}$$

and scattering rate,

$$R_{sc}(r) = \frac{3\pi c^2}{2\hbar\omega_0^3}\left(\frac{\Gamma}{\Delta}\right)^2 I(r) \tag{3.54}$$

and are related by,

$$R_{sc} = \frac{\Gamma}{\hbar\Delta} U_{dip} \tag{3.55}$$

We can conclude two general results that will help us in designing our trap.

- **Sign of detuning:** As mentioned in Sec. 2.4 we can build traps with $\Delta < 0$ ($\Delta > 0$), where we are said to be red (blue) detuned, and trap atoms in the intensity maxima (minima) of the light field. Due to the intensity profile of a Gaussian beam, it is simple to construct a trap in 3D using a single focussed Gaussian beam for the red detuned case. Trap geometries for the blue detuned case are less simple although benefit from the reduction in intensity experienced by the trapped atom (see for example hyperpolarisability 2.4.3.3, also note the reduced scattering rate which manifests in a reduced trap heating rate).

- **Trap depth: Δ vs I:**

$$U_{dip} \propto I/\Delta \tag{3.56}$$

$$R_{sc} \propto I/\Delta^2 \tag{3.57}$$

  It is then generally the goal to operate at large detunings and high intensities to minimise the scattering rate for a given potential depth. Of course, for our magic wavelength lattice we do not have this freedom of choice.

3.7.2 Lattice Potential

The simplest lattice configuration, and one first considered for frequency metrology [113], is that of a one-dimensional (1D) red-detuned optical lattice trap formed of a retro-reflected tightly focussed gaussian laser beam (waist w_0 $\sim$50 µm is typical) with wavelength λ_L. We may construct the electric field amplitude of our 1D optical lattice as a superposition of two counter-propagating Gaussian beams. Starting with one beam propagating along z we have the real part of the electric field as,

$$\mathbf{E}(r,z,t) = \frac{w_0}{w(z)} e^{-(r/w(z))^2} E_0\, \hat{\mathbf{e}}\, \cos(kz - \omega t), \tag{3.58}$$

where $k = 2\pi/\lambda$ is the wave vector along the z-axis, r is the radial coordinate in the transverse direction, $\omega = 2\pi c/\lambda$ is the oscillation angular frequency, and t is time. The beam waist is given by $w(z) = w_0(1 + (z_R/z)^2)$ with Rayleigh length $z_R = \pi w_0^2/\lambda$ (the distance along z in which $w(z) = \sqrt{2}w_0$, with w_0 at $z = 0$). The longitudinal or Gouy phase $\xi(z) = -\arctan(z/z_R)$, and wavefront curvature $R(z) = z(1+(z_R/z)^2)$, are not important here and have been neglected. Our superposition of two identical counter-propagating

waves is then,

$$\mathbf{E}_L(r,z,t) = \mathbf{E}_1(r,z,t) + \mathbf{E}_2(r,z,t) = 2\frac{w_0}{w(z)}e^{-(r/w(z))^2}E(t)\,\hat{\mathbf{e}}_L\,\cos(k_L z) \tag{3.59}$$

where the oscillating electric field amplitude $E(t) = E_0\cos(\omega t)$, and we have used the conditions,

$$\omega_1 = \omega_2 \equiv \omega_L, \quad \mathbf{e}_1 = \mathbf{e}_2 \equiv \mathbf{e}_L, \quad k_1 = -k_2 \equiv k_L, \quad w_1 = w_2 \equiv w_0, \quad E_1 = E_2 = E_0 \equiv \frac{E_L}{2},$$

Taking the intensity $I_L = \varepsilon_0 c\,\langle \mathbf{E}^2 \rangle$, where the angle brackets indicate a time average, ε_0 is the permittivity of free space, and c is the speed of light, and the unit polarisation vector has the property $\hat{\mathbf{e}}^* \cdot \hat{\mathbf{e}} = 1$, we have,

$$I_L(r,z) = \underbrace{2\varepsilon_0 c\,|E_0|^2}_{4I_0}\left(\frac{w_0}{w(z)}\right)^2 e^{-2(r/w(z))^2}\,\cos^2(k_L z). \tag{3.60}$$

The field is typically described as a *standing wave* or 1D optical lattice. The trapping potential energy $U_L(r,z)$ corresponding to a state $|a\rangle$ is determined by the ac Stark shift δE_a^{Stark} such that,

$$U_L(r,t) = U_0\left(\frac{w_0}{w(z)}\right)^2 e^{-2(r/w(z))^2}\,\cos^2(k_L z) \tag{3.61}$$

where,

$$U_0 = \delta E_a^{Stark} = -\frac{1}{2}\alpha_a\langle \mathbf{E}^2\rangle = -\alpha_a\frac{4P}{\varepsilon_0 c\pi w_0^2}. \tag{3.62}$$

Here, P is the total optical power in one of the incident beams, and α_a is the polarisability of state $|a\rangle$ calculated in Sec. 5.1. In a retro-reflected 1D optical lattice configuration, P is the total power input to form the lattice. It is often useful to express the peak trap depth as a temperatue, given by $T_{trap} = U_0/k_{\mathrm{B}}$, where k_{B} is the Boltzmann constant. Atoms in the centre of the potential with temperature $T_{at} < T_{trap}$ will remain trapped.

For $\alpha_a > 0$, which occurs for a lattice frequency tuned to the red side of the dominant interacting dipole transition, atoms are confined at the intensity maxima of the lattice-field, resulting in a $\sin^2(k_L z)$ spatially modulated trapping potential. Each lattice site is separated by half the lattice wavelength, $\lambda_L/2$, and is roughly "pancake" shaped, described by the radial and axial characteristic trap frequencies ν_r and ν_z, respectively. For small displacements of z and r from the trapping centres, such that $\sin^2(k_L z) \approx k_L z$, the axial and radial harmonic-like components of the potential are $U_L(z) \approx U_0(k_L z)^2$ and $U(r) = U_0[-2(r/w_0)^2]$. Equating to a harmonic oscillator potential $U_{ho} = \frac{1}{2}m\omega_0^2 x^2$, where m is the atomic mass, and replacing the characteristic oscillator angular frequency ω_0 with $2\pi\nu_r$

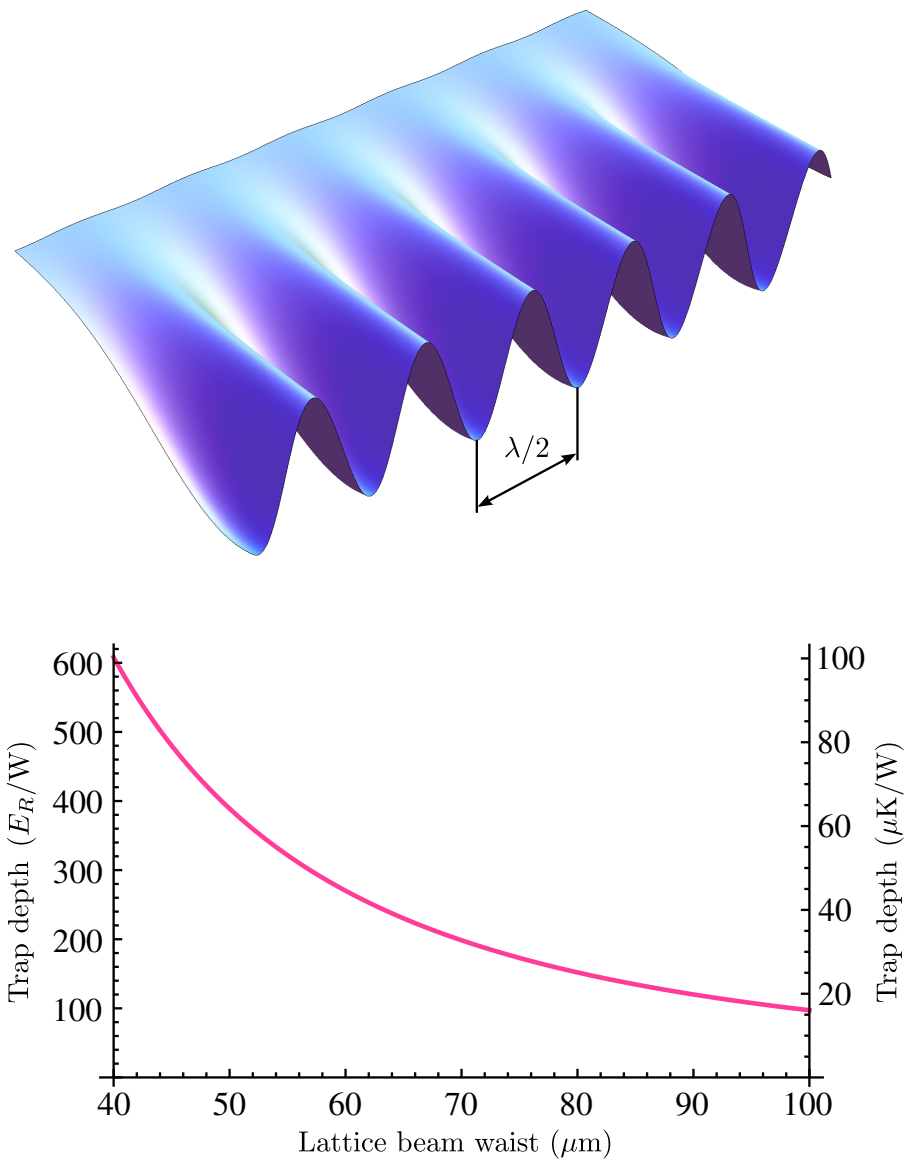


Figure 3.19: **1D Optical Lattice Potential** - A cross section of the lattice potential showing tight axial confinement and weaker radial confinement (top), and the peak trap depth versus lattice waist per watt of one way optical power (bottom).

and $2\pi\nu_r$, the trap frequencies are determined as,

$$\nu_r = \sqrt{4U_0/m\,(2\pi w_0)^2} \tag{3.63}$$

$$\nu_z = \sqrt{2U_0/m\lambda_L^2} \tag{3.64}$$

The radial confinement is relatively weak with trap frequencies typically on the order of 100 Hz. The axial confinement is much tighter, 100 or so times higher than in the radial direction, offering Lamb-Dicke confinement in 1D, accessed when probed collinear with the lattice beam.

The peak trap depth, U_0 is typically described in terms of the recoil energy associated with the absorption of a lattice photon, $E_R = p^2/2m = h^2/2m\lambda_L^2$ and axial trap frequency ν_z (which can be measured by observing the resolved motional sidebands), as,

$$U_0 = \nu_z^2 \frac{m^2\lambda_L^4}{h^2} E_R \tag{3.65}$$

A typical trap depth for Sr operated at the magic wavelength $\lambda_m \approx 813\,\text{nm}$, is on the order of $100E_R$, corresponding to axial sidebands at $\pm 68\,\text{kHz}$ (compare with ion-traps with $\nu_z \sim \pm 1\,\text{MHz}$). Finally, comparing the radial and axial trapping frequencies,

$$\frac{\nu_z}{\nu_r} = \frac{\sqrt{2}\pi w_0}{\lambda_L} \tag{3.66}$$

gives us a spectroscopic measure of the beam waist, useful for characterising the trapping conditions seen by the atoms.

3.7.3 Spectroscopic effects of the trapping potential

In reality our optical lattice trap only approximates a harmonic potential close to the motional (vibrational) ground state. The $\sin^2(kz)$ potential becomes increasingly anharmonic, deviating from the infinitely deep harmonic potential ($U_{ho} = \frac{1}{2}m\omega^2 z^2$), as we move from the trap zero-energy. As a result, ν_z decreases for higher levels of n and transitions between vibrational states at different levels of n generates a sideband spectrum with broken degeneracy. As required, our carrier is unaffected, providing the criteria for Lamb-Dicke confinement is satisfied ($\eta \ll 1$, see Sec. 2.3.1).

Another effect concerning the 1D trap is due to motion in the weakly confined radial direction. This is largely responsible for the asymmetric line shape observed in trap sideband spectra and results from the changing trapping potential experienced by an atom oscillating in the radial direction around trap centre. The atom 'sees' a lower intensity at the trap extremities leading to a reduced trap frequency, and the sideband is 'washed-out' to lower frequencies (see Fig. 3.20). As the atomic motion depends on the temperature of the atomic sample, the sideband lineshape may be used as a measure of the sample

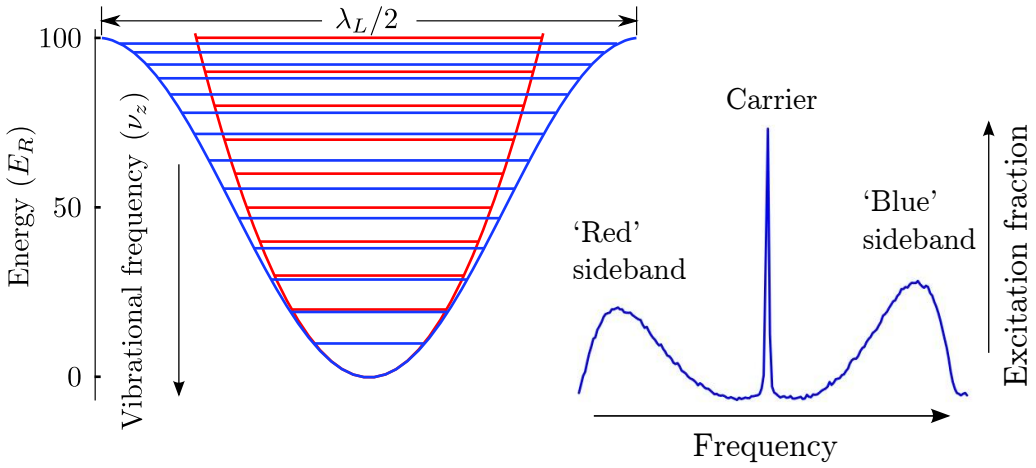


Figure 3.20: **Trap Anharmonicity** - (Left) Comparison of harmonic trapping potential with eigenvalues versus the $\sin^2 z$ lattice potential (for illustration only). (Right) Typical spectrum showing resolved motional sidebands in an optical lattice potential (courtesy of NIST).

temperature.

The atomic motion also implicates the Rabi frequency and peak clock excitation fraction achievable, which is covered in some detail in the thesis of Boyd [124].

3.7.4 813 nm laser source

An ECDL (developed as part of this work, see Ch. 4) operated at 813 nm (laser diode from Eagleyard, model: EYP-RWE-0840-06010-1500-SOT02-0000) is used to seed a commercial tapered amplifier (Toptica BOOSTA) to provide 500 mW of optical power for lattice use (it is noted that 1 W modules are now available). We expect to operate with a 50 µm lattice waist with approximately 300 mW available for trapping, producing a trap depth of $\sim$120 E_{R} or $\sim$20 µK.

3.8 The $^1\mathrm{S}_0 - {}^3\mathrm{P}_0$ Clock Transition: Allowing the forbidden

The clock excitation takes place on the spin- and angular-momentum-forbidden intercombination line from the $^1\mathrm{S}_0$ to the $^3\mathrm{P}_0$ excited-state. In odd isotopes the clock transition is weakly allowed via inherent hyperfine state mixing, providing a permanent natural linewidth of a few mHz which is directly accessible with a single tuned laser. Details of the hyperfine quenching leading to this transition rate can be found, for example, in Refs. [125, 146, 220].

3.8.1 Magnetically Induced Spectroscopy

The clock transition in even-isotopes, possessing zero nuclear spin, could be considered metrologically superior to that of odd-isotopes due to an increased insensitivity to lattice polarisation and the absence of a first-order Zeeman shift. However, the lack of hyperfine structure, while greatly simplifying level structure, presents a clock transition of (near enough not to matter) zero linewidth, forbidding direct optical excitation. Several techniques, including electromagnetically induced transparency and multi-photon excitation, have been proposed [221] but often require complex phase locked laser systems with precise control of several laser intensities and are not straightforward to implement. Perhaps a more attractive scheme is a field-induced state mixing technique (known as magnetically induced spectroscopy, or MIS) in which a non-zero linewidth can be engineered, enabling direct optical excitation of the forbidden clock transition [222]. First demonstrated in ^{174}Yb [159], the technique is simple employing only an additional uniform magnetic field and can be easily implemented in existing optical lattice clock experiments as demonstrated in ^{88}Sr [140].

3.8.1.1 Magnetic state mixing

To gain insight into the field parameters required to implement MIS in our experiment we first consider the atom-field interaction, following the treatment given in Refs. [128, 147]. We start by writing the modified Hamiltonian as,

$$H_{tot} = H_a + H_{mag} \tag{3.67}$$

where H_a is the unperturbed atomic Hamiltonian and the magnetic interaction $H_{mag} = -\boldsymbol{\mu} \cdot \mathbf{B}$. The magnetic moment, in the absence of nuclear spin, is given by $\boldsymbol{\mu} = \mu_{\mathrm{B}}(g_L \mathbf{L} + g_S \mathbf{S})$, with $g_L = 1$ and $g_S \approx 2$. As a result of the magnetic interaction, the upper clock state acquires a small admixture of states ψ, and its wavefunction is modified according to first order perturbation theory as,

$$\left|{}^3P_0'\right\rangle = \left|{}^3P_0\right\rangle + \sum_{\psi \neq {}^3P_0} \frac{\langle \psi | \boldsymbol{\mu} \cdot \mathbf{B} \left|{}^3P_0\right\rangle}{\hbar \Delta_\psi} |\psi\rangle \tag{3.68}$$

which sums over all relevant states of ψ with frequency detuning Δ_ψ from the $^3P_0$ state. As the interaction is dominated by the contribution of the $|{}^3P_1, M_J = 0\rangle$ state we may truncate our sum to include only this state and consider a simple 3-level model, as shown in Fig. 3.21, such that we may write Eq. (3.68) as,

$$\left|2'\right\rangle = |2\rangle + \frac{\langle 3 | \boldsymbol{\mu} \cdot \mathbf{B} |2\rangle}{\hbar \Delta_{32}} |3\rangle = |2\rangle + \frac{\Omega_B}{\Delta_{32}} |3\rangle \tag{3.69}$$

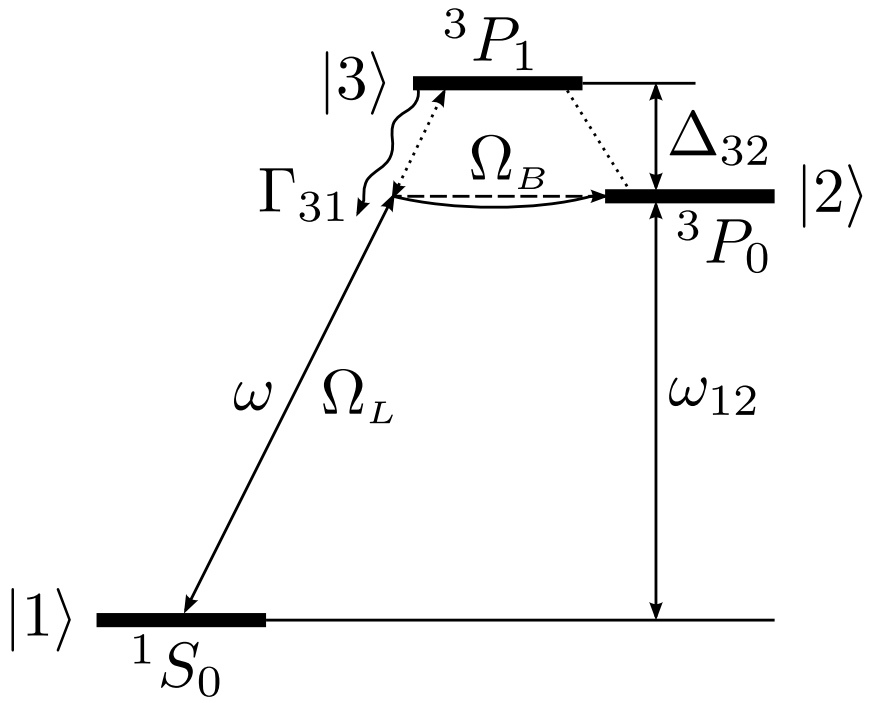


Figure 3.21: **State mixing** - Parameters relevant to the MIS technique. Diagram reproduced from Ref. [147].

where $\Omega_B = \langle 3| \boldsymbol{\mu} \cdot \mathbf{B} |2\rangle / \hbar$ is the Rabi frequency resulting from the magnetic coupling interaction. The normalisation factor, N, of the mixed state $|2'\rangle$ may be written as $N = \left(1 + \frac{\Omega_B}{\Delta_{32}}\right)^{-1/2}$, such that $|2'\rangle = N\left(|2\rangle + \frac{\Omega_B}{\Delta_{32}} |3\rangle\right)$. However, for the small field perturbations considered here, N is close to unity and can be neglected. For the states here represented by $|2\rangle$ and $|3\rangle$ it can be shown that $\Omega_B \approx \sqrt{2/3}\, \mu_B |B| / \hbar$, [147]. A weak transition may now occur between clock states $|1\rangle$ and $|2'\rangle$ with Rabi frequency,

$$\Omega_{12} = \langle 1| \mathbf{d} \cdot \mathbf{E} |2'\rangle / \hbar \approx \frac{\Omega_B}{\Delta_{32}} \langle 1| \mathbf{d} \cdot \mathbf{E} |3\rangle / \hbar = \frac{\Omega_L \Omega_B}{\Delta_{32}} \tag{3.70}$$

where $\Omega_L = \langle 1| \mathbf{d} \cdot \mathbf{E} |3\rangle / \hbar$ is the Rabi frequency resulting from the coupling of states $|1\rangle$ and $|3\rangle$ by the applied oscillating electric field $\mathbf{E}$ at frequency $\omega \approx \omega_{12}$. Here, this corresponds to the intercombination transition $^1S_0 \rightarrow {}^3P_1$ which is weakly dipole allowed via the intercombination interaction (Sec. 3.1) with decay rate Γ_{31}. We may interpret the result of Eq. (3.70) in the picture of a two-photon transition, with Ω_{12} the on-resonance two-photon Rabi frequency. The first photon is detuned by Δ_{32} from the $|1\rangle \rightarrow |3\rangle$ one-photon resonance and the magnetic coupling of states $|2\rangle$ and $|3\rangle$ corresponds to a second photon of zero frequency such that the two-photon resonance satisfies $\omega = \omega_{12}$. The decay

rate of the upper clock state then becomes [128],

$$\Gamma_{21} \approx \Gamma_{31} \frac{\Omega_B^2 + \Omega_L^2}{\Delta_{32}^2} \tag{3.71}$$

We may write Eq. (3.70) in terms of fields **E** and **B** as,

$$\Omega_{12} = \frac{\langle||d||\rangle\langle||\mu||\rangle(\mathbf{E}\cdot\mathbf{B})}{\hbar^2\Delta_{32}} = \alpha\sqrt{I}B\cos\theta \tag{3.72}$$

where $\langle||\mu||\rangle$ and $\langle||d||\rangle$ are the reduced magnetic and electric dipole matrix elements corresponding to transitions ${}^3P_0 \rightarrow {}^3P_1$ and ${}^1S_0 \rightarrow {}^3P_1$ respectively, I is the probe light intensity, B is the magnetic field amplitude, and θ is the angle between a linearly-polarised **E**-field and **B**-field. The coefficient α contains all other quantities, including the evaluation of the transition matrix elements.

3.8.1.2 Field related clock shifts

The necessary application of these fields presents two of the largest shifts in even-isotope clocks that must be evaluated; namely that of the second-order Zeeman shift arising from the applied magnetic field, and probe light induced ac Stark shift as a result of off-resonant interactions. Keeping for now to our three level model, the perturbation to the clock states caused by the magnetic field interaction is, according to second-order perturbation theory,

$$\Delta_B^{(2)} = -\frac{|\langle 3|\,\boldsymbol{\mu}\cdot\mathbf{B}\,|2\rangle|^2}{\hbar^2\Delta_{32}} = -\frac{\Omega_B^2}{\Delta_{32}} \tag{3.73}$$

and the ac Stark shift resulting from the light field interaction is,

$$\Delta_L = \frac{\Omega_L^2}{4\Delta_{32}} \tag{3.74}$$

We may rewrite Eq. (3.70) in terms of field related shifts (for a light field linearly polarised in the direction of **B**) as,

$$\Omega_{12} = 2\sqrt{|\Delta_L\Delta_B|} \tag{3.75}$$

The quadratic Zeeman shift is sufficiently estimated within this three level model and using the previously given result of the matrix element we may evaluate Eq. (3.73) to give,

$$\beta = \frac{\Delta_B}{B^2} = 2\pi \times -23.3\,\mathrm{Hz\,mT^{-2}} \tag{3.76}$$

where we have used the value $\Delta_{32} = 5.60\,\mathrm{THz}$ for the fine structure splitting [223]. This is in agreement with the value measured in Ref. [134]. Evaluation of the probe light induced

clock shift, which arises due to the differential polarisability of the clock states, requires a multilevel treatment for sufficient estimation. Using the values $\alpha(^1S_0) = 343.75$ a.u. and $\alpha(^3P_0) = 946.90$ a.u. obtained from the polarisability calculations for $\lambda = 698.4\,\text{nm}$ (see Sec. 5.1, Tab. 5.2), we get,

$$\kappa = \frac{\Delta_L}{I} = 2\pi \times -28.2\,\text{Hz/W cm}^{-2} \tag{3.77}$$

which is in good agreement with the experimental and theoretical values quoted in Ref. [152]. This differs from the approximate value $\kappa = 2\pi \times -18\,\text{Hz/W cm}^{-2}$ given in Ref. [128], although this may be obtained by truncating the polarisability calculation to include only coupling of states $5s5p\,^1P_1$ and $5s6s\,^3S_1$ to the ground and excited clock states respectively, as is alluded to in the text of Ref. [128].

Estimation of the induced Rabi frequency Ω_{12} as given by Eq. (3.72), may be written as [128],

$$\Omega_{12} = \xi\sqrt{|\Delta_L \Delta_B|}\,\cos\theta \tag{3.78}$$

where the dimensionless factor $\xi \equiv \alpha/\sqrt{\beta\kappa}$ accounts for the fact that not all of the field coupled states contributing to shift the clock states contribute to enhance the induced transition rate, e.g., for the simple 3 level model, where only the light shift of the ground state to the $^3P_1$ state contributes, $\xi = 1$. Including only coupling to the $^3P_1$ state, we find $\alpha(^1S_0) = 8.94$ a.u. for 698.4 nm probe light, corresponding to $\Delta_L = 2\pi \times 0.417\,\text{Hz/W cm}^{-2}$. Using Eqs. (3.72) and (3.75) and our estimated shifts for the 3 level system we arrive at a value for $\alpha/2\pi = 197.1\,\text{Hz/T}\sqrt{\text{mW cm}^{-2}}$, in agreement with Refs. [128, 147] (note a factor of 2 discrepancy in Ref. [128] resulting from a differing definition of field used in determination of the light shift). It is then easy to find $\xi = 0.237$ and we may proceed to calculate the field parameters required to induce a suitable clock transition rate. Assuming sub-hertz laser linewidths, we can expect to achieve coherence times $\sim$1 s so a Rabi frequency of $\sim$1 Hz should be sufficient. Table 3.6 lists field parameters required to induce a 1 Hz Rabi frequency with fields set to minimise the overall frequency measurement uncertainty. The associated shifts and expected achievable experimental uncertainties are given. With our best uncertainty estimate the MIS technique should not limit the measurement uncertainty at the level 1×10^{-17}.

3.8.2 BBR Quenching

As discussed in Sec. 2.4.4.1 one way to measure the effect of BBR is to heat the environment surrounding the atoms and measure the resulting frequency shift. A potential problem arises due to quenching of the excited clock state by thermal radiation. This issue was first encountered in Sr for magnetic trapping of the $^3P_2$ metastable state, following loading in a vapour cell MOT [188]. The elevated temperatures necessary to the vapour cell operation

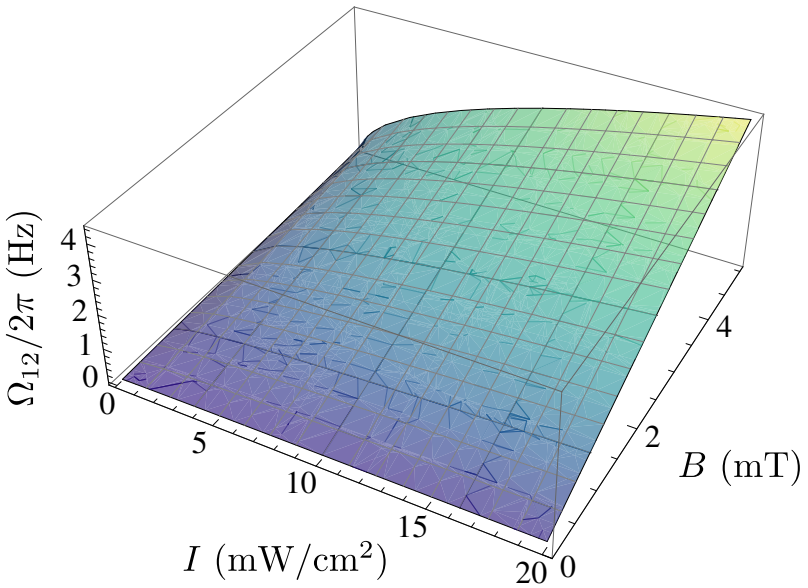


Figure 3.22: **Magnetic induced spectroscopy** - Field-induced Rabi frequency for the ${}^1S_0 \rightarrow {}^3P_0$ clock transition in Sr.

Table 3.6: MIS example parameters for Rabi frequency $\Omega_{12}/2\pi \approx 1\,\mathrm{Hz}$ ($\Gamma_{12} \sim 10^{-6}\,\mathrm{s}^{-1}$).

B (mT)	I (mW cm^{-2})	$\Delta_B/2\pi$	$\Delta_L/2\pi$	ΔB	ΔI	$\delta\nu/\nu$
14.0	1.4	-45.69	-0.41	10^{-3}	10^{-1}	1.4×10^{-16}
5.0	2.5	-145.63	-0.15	10^{-4}	10^{-1}	4.8×10^{-17}
14.0	1.4	-45.69	-0.41	10^{-4}	10^{-2}	1.4×10^{-17}

Table 3.7: Branching terms of relevant to the BBR quenching of metastable states. Frequency is in units $1 \times 10^{15}\,\mathrm{rad\,s^{-1}}$.

Initial state, a	Final state, k	λ (nm)	ω_{ak}	$\Gamma_{L_k L_a}$ ($10^5\,\mathrm{s^{-1}}$)	b_{ak}
$5s5p\,^3P_2$	$5s4d\,^3D_1$	3067.02	0.6142	3.45	1/36
$5s5p\,^3P_2$	$5s4d\,^3D_2$	3011.83	0.6254		9/36
$5s5p\,^3P_2$	$5s4d\,^3D_3$	2923.36	0.6443		1
$5s5p\,^3P_0$	$5s4d\,^3D_1$	2603.13	0.7236	3.45	20/36
$5s5p\,^3P_0$	$5s4d\,^3D_2$	2563.26	0.7349		0
$5s5p\,^3P_0$	$5s4d\,^3D_3$	2498.90	0.7538		0
$5s4d\,^3D_1$	$5s4d\,^3P_1$	–	–	3.45	9/36
$5s4d\,^3D_2$	$5s4d\,^3P_1$	–	–		27/36
$5s4d\,^3D_3$	$5s4d\,^3P_1$	–	–		0
$5s5p\,^3P_1$	$5s^2\,^1S_0$	–	–	0.469	1

result in a BBR driven excitation to states of the nearby $5s4d\,^3$D manifold (transitions in the infra-red) which may then decay to the ground state via the $^3P_1$ state (^{3}P$_1$ state lifetime $\sim 21\,\mu$s). An estimation of this quenching in relation to observed trap lifetime is given in Ref. [188] and was subsequently measured by Yasuda et al. [172].

A simple estimate of the BBR-induced relaxation rate R_{BBR} can be obtained using [172],

$$R_{\mathrm{BBR}} = \sum_{akg} b_{akg} \Gamma_{L_a L_k} \underbrace{\left[\exp\left(\frac{\hbar\,\omega_{ak}}{k_{\mathrm{B}} T_{env}}\right) - 1\right]^{-1}}_{\bar{n}} \tag{3.79}$$

where $\Gamma_{L_a L_k}$ is the transition rate from states of an initial term L_a to final term L_k, ω_{ak} is the angular frequency of the $|a\rangle \leftrightarrow |k\rangle$ BBR driven transition, and $\bar{n}$ is the photon occupation number corresponding to a BBR field with characteristic temperature T_{env}, as seen by the atoms. The branching term b_{akg} is determined for each possible excitation and decay route as the product of branching terms b_{ak} (as in Sec. 5.8) from the metastable state to the ground state, including all intermediate states.

The $^3P_2$ metastable state has an expected natural lifetime of 1050 s [220] and was measured in ^{88}Sr as 520^{+320}_{-140} s [172]. The BBR quenched lifetime is found by considering the possible quenching routes, as shown in Fig 3.23, and there associated branching terms

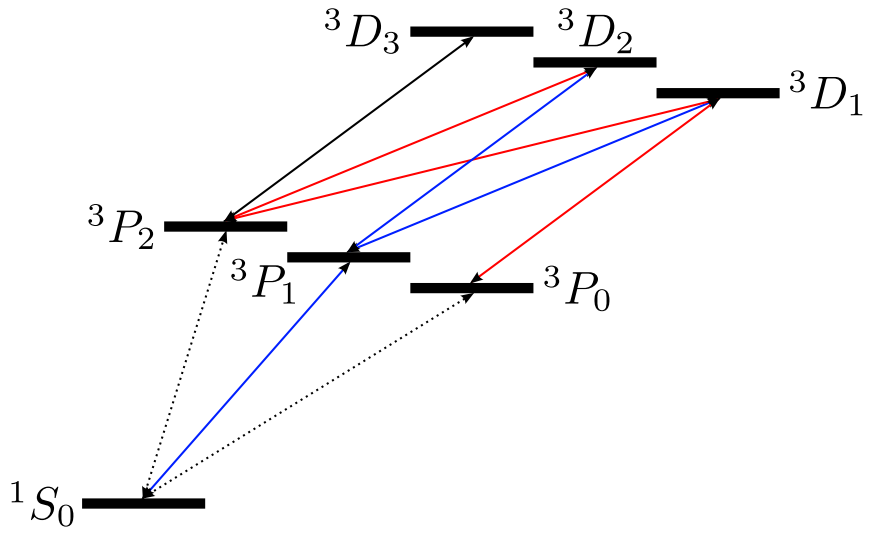


Figure 3.23: **BBR quenching of metastable states** - The levels involved in BBR quenching with excitation (red) and decay routes (blue) shown.

as,

$$^3P_2 \rightarrow {}^3D_1 \rightarrow {}^3P_1 \rightarrow {}^1S_0 \qquad b_{ag} = 9/36^2 \tag{3.80}$$

$$^3P_2 \rightarrow {}^3D_2 \rightarrow {}^3P_1 \rightarrow {}^1S_0 \qquad b_{ag} = 243/36^2 \tag{3.81}$$

Adopting $\lambda = 3.01\,\mu$m for each excitation, the sum over akg may be evaluated and the total branching term $b_{akg} = 7/36$ used, as in Ref. [172]. Decay to the ground state is relatively rapid and may be neglected here. The room temperature BBR quenched $^3P_2$ lifetime is then reduced to $\sim$120 s (at 300 K) and falls off exponentially with temperature. For the clock transition in Sr the expected hyperfine quenched ^{3}P$_0$ state lifetime is $\sim$ 132 s [146]. Only one quenching route is allowed,

$$^3P_0 \rightarrow {}^3D_1 \rightarrow {}^3P_1 \rightarrow {}^1S_0 \qquad b_{ag} = 5/36 \tag{3.82}$$

Due to the shorter wavelength, $\lambda = 2.6\,\mu$m, of the $^3P_0 \rightarrow {}^3D_1$ excitation the quenching rate is significantly reduced in comparison to the $^3P_2$ state. For example, at 300 K the BBR quenched lifetime is $\sim$2000 s, which does not effect that due to the hyperfine interaction. However, if we plan to expose our Sr sample to BBR fields of T_{env} in the range of 400 to 500 K then our expected lifetime is reduced to 20 s down to 1 s, respectively, at which point we'd expect to suffer decoherence effects.

4

Diode Lasers for Precision Spectroscopy

4.1 Extended Cavity Diode Lasers

An extended cavity diode laser (or ECDL) is a semiconductor based laser formed of a laser diode chip with output coupler (here, the diode laser front facet) replaced by an external optic, often with frequency selective properties. While other approaches exist [224], the most common employ the dispersive property of a diffraction grating to provide frequency selective feedback to the laser diode; arranged in either Littrow [225] or Littman-Metcalf [226] configurations, as shown in Fig. 4.1. The apparent simplest arrangement is Littrow, which consists of a diffraction grating set such that the 1st diffraction order is reflected back to the diode laser and the zero order (or specular reflection) coupled out. Tuning is accomplished by rotating the angle of the grating and by translating the grating position to vary the cavity length in the horizontal plane (assuming grating is oriented with rulings running along the vertical direction), both of which vary the output beam position. In addition, the effective cavity length is tuned by varying the diode laser current which acts to adjust the refractive index of the laser chip by charge carrier density. In Littman-Metcalf configuration the grating position is fixed at near grazing incidence and the zero order coupled out. The 1st diffraction order, however, is not coupled directly back to the diode but is retroreflected by an adjustable mirror and the 1st diffraction order of this light is coupled back to the diode. As a result the laser frequency can be tuned by adjusting the position of the mirror without affecting the output beam direction. The twice diffracted optical feedback provides superior frequency selection in comparison to the Littrow configuration, but with the additional loss of the zero order on the second diffraction, applications sensitive to the available optical power could be disadvantaged. Littman-Metcalf designs also benefit from the ability to self correct for misalignment of the cavity optics in the vertical plane by using a prism reflector in place of the mirror

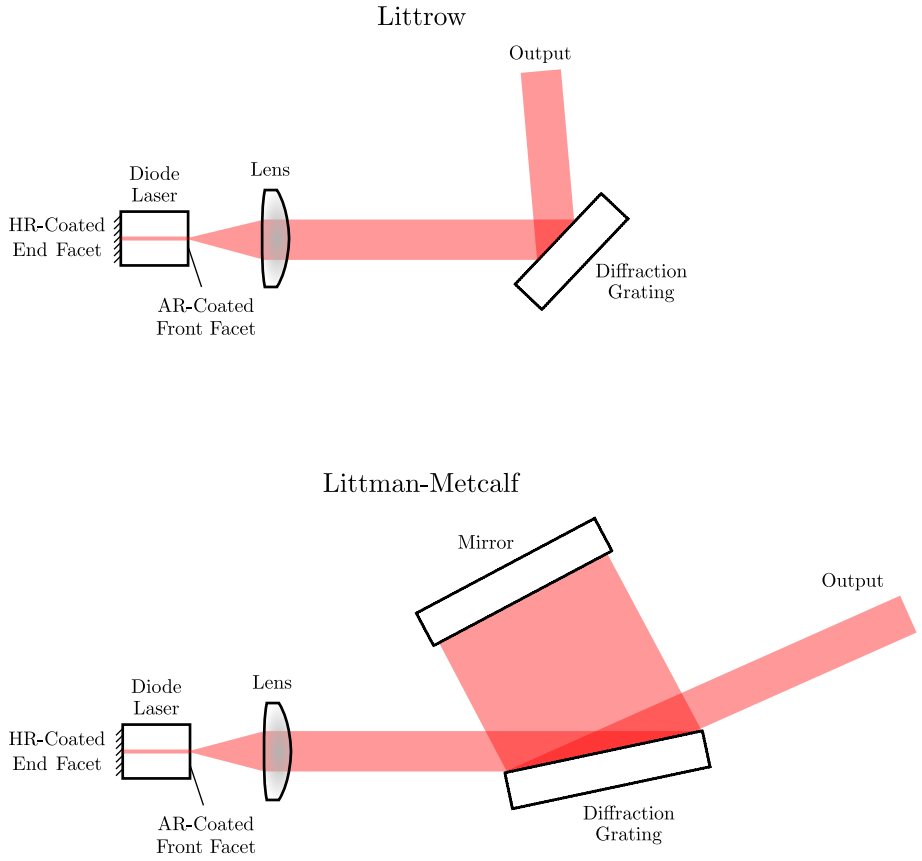


Figure 4.1: **Littrow and Littman ECDL configurations** -

[227]. The requirement for adjustment in the vertical plane is thus removed aiding robust operation and simplifying the construction.

As part of this work, Littrow configuration ECDLs, with the benefit of higher optical output power, to operate at wavelengths centred around 813 nm and 698 nm have been designed and built. One of the major drawbacks of the Littrow design is in the steering of the output beam when the grating angle is tuned. To overcome this, a compensating output mirror is added, fixed to track parallel to the grating, and the beam steering is reduced to a small lateral shift proportional to the grating-mirror separation distance [228]. Furthermore, if so desired, this residual lateral shift can be essentially eliminated with use of a triangular prism in place of the mirror [229].

4.1.1 Littrow Grating Configuration

A ray of light incident on a diffraction grating at angle i (to the grating normal) is diffracted at angle r according to the grating equation [225],

$$m\lambda = d(\sin i + \sin r) \tag{4.1}$$

where m is the diffraction order, d the grating period, and λ the wavelength. Of interest here are angles where the laser diode 'sees' itself in the grating, i.e., for $i = r$ and we are now have,

$$m_L\lambda_L = 2d\sin i \tag{4.2}$$

where the label L refers to the Littrow configuration and the grating serves as a Littrow reflector for a given wavelength λ_L. To ensure a high performance operation of the ECDL we proceed with the following design goals:

- optimise wavelength selectivity
- minimise optical losses

To begin, we set $\lambda = \lambda_L$ in Eq. (4.1) and substitute λ_L from Eq. (4.2) to give,

$$\frac{2m}{m_L} - 1 = \frac{\sin r}{\sin i} \tag{4.3}$$

Diffracted orders, or modes, are arranged in symmetric pairs about the grating normal, with value

$$\left|\frac{2m}{m_L} - 1\right| \tag{4.4}$$

For example, for 1st Littrow order, $m_L = 1$, $\sin i$ is fixed and we have,

$$m = 0 \quad \Rightarrow \quad -1 = \frac{\sin r}{\sin i} \quad \Rightarrow \quad r = -i \tag{4.5}$$

$$m = 1 \quad \Rightarrow \quad 1 = \frac{\sin r}{\sin i} \quad \Rightarrow \quad r = i \tag{4.6}$$

$$m = 2 \quad \Rightarrow \quad 3 = \frac{\sin r}{\sin i} \quad \Rightarrow \quad r > i \tag{4.7}$$

Modes are classified as either 'inner' or 'outer' depending on whether they lie inside or outside of the angular range of the Littrow and zeroth orders. Inner pairs are simply eliminated by choosing $m_L = 1$, while outer pairs are eliminated according to the following criteria [225],

$$\frac{1}{2}\lambda_L < d < \frac{3}{2}\lambda_L \tag{4.8}$$

To further reduce losses at $\lambda \neq \lambda_L$, we now consider minimising the half-width of the Littrow reflection,

$$\Delta\lambda = \frac{\lambda_L}{p} \tag{4.9}$$

where p is the total optical path difference across the illuminated area of the grating. A high angle of incidence increases p. From Eq. (4.2) we therefore require a small grating period, d, to maximise p and thus minimise $\Delta\lambda$. In addition, maximising the spectral angular dispersion [225],

$$\frac{\mathrm{d}r}{\mathrm{d}\lambda_L} = \frac{m_L}{d\cos r} = \left[\left(\frac{d}{m_L}\right)^2 - \left(\frac{\lambda_L}{2}\right)^2\right]^{-\frac{1}{2}} \tag{4.10}$$

improves the wavelength selectivity, and is achieved for d approaching the limit $\lambda_L/2$. The grating resolving power is given by,

$$R = \frac{\lambda}{\Delta\lambda} = mN \tag{4.11}$$

where N is the number of illuminated diffraction 'slits' and is also increased for decreasing d and increasing apparent beam size.

In summary, we aim to satisfy the following criteria,

1. Eliminate all diffraction orders other than the 1st and zeroth to reduce unnecessary losses by satisfying,

   $\frac{1}{2}\lambda_L < d < \frac{3}{2}\lambda_L$

2. Increase number of illuminated grating 'slits'

   - Increase beam spot size

   - Decrease grating period

3. Increase wavelength selectivity by increasing dispersion

   - Decrease $d \to \lambda_L/2$

4.1.2 Synchronous Tuning of the Extended Cavity

We consider here the effects of translation and rotation of the diffraction grating and the case of an optimum pivot point which provides the appropriate amount of each to achieve a wide continuous tuning range without mode-hop.

I begin by pointing the reader to Fig. 1 in Ref. [230] where the two modes of grating translation and one of rotation are depicted together with corresponding tuning profiles.

1. **Longitudinal translation.** The standing wave inside the cavity is stretched leading to a continuous change in wavelength. However, this also changes the diffraction angle from the grating. Eventually, a longitudinal mode with one more $\lambda/2$ periods will be directed into the laser, with the lower losses, and a mode hop back in frequency will occur.

2. **Transverse translation.** The distance between each grating period and laser diode is unchanged, therefore λ remain the same even though the cavity length effectively increases.

3. **Rotation around central vertical axis.** By changing the angle of the grating the Littrow wavelength is changed. A mode hop to a new wavelength occurs when the next mode has lower losses.

4. **Rotation and translation.** For each 'slit' along the grating length (in direction of increasing y) an additional $\lambda/2$ period is accommodated by the cavity. In case a), due to the varying cavity length across the beam, a longitudinal translation of the cavity produces a fractionally different wavelength shift across the beam. So, to ensure mode hop free tuning over an extended range we aim here to elongate all $\lambda/2$ periods equally by combining both rotation and translation in the correct proportions simultaneously.

4.1.2.1 Optimum Grating Pivot Point

We now consider a simple geometry to satisfy item 4) of the above discussion and follow the geometric framework as set out by Nilse et al. [231]. In a Littrow configuration with beam striking the grating at an angle i, tuned by an angle α, the on axis cavity length L_α, as depicted in Fig. 4.2, is determined simply as,

$$L_\alpha = x - y\tan(i-\alpha) \tag{4.12}$$

and the Littrow reflection wavelength is,

$$\lambda_L = 2d\sin(i-\alpha) = \lambda_0\frac{\sin(i-\alpha)}{\sin i} \tag{4.13}$$

The cavity standing wave criteria requires,

$$L_m = m_\alpha\frac{\lambda_L}{2} \tag{4.14}$$

where m is the principal cavity mode number. For mode-hop-free tuning to occur we require the Littrow reflection wavelength to tune synchronously with the principal cavity mode. While we might expect the mode number to remain constant for mode-hop-free

operation, the act of pivoting the grating results in a transverse translation and the axial mode number is changed by ± 1 for each grating period that passes the x axis. The total change in mode number for the geometry pictured (Fig. 4.2), as a continuous function of α (providing $L_\alpha \gg \lambda_m$), is given by [231],

$$\Delta m_\alpha = \frac{y/\cos i - y/\cos(i-\alpha)}{d} \tag{4.15}$$

and we have,

$$m_\alpha = m_0 + \Delta m_\alpha = \frac{2L_0}{\lambda_0} + \frac{2y\sin i}{\lambda_0}\left[\frac{1}{\cos i} - \frac{1}{\cos(i-\alpha)}\right] \tag{4.16}$$

$$= \frac{2}{\lambda_0}\left(x - \frac{y\sin i}{\cos(i-\alpha)}\right) \tag{4.17}$$

Substituting for L_α and m_α we arrive at an expression for the principal cavity mode wavelength,

$$\lambda_m = \lambda_0 \frac{x - y\tan(i-\alpha)}{x - y\sin i/\cos(i-\alpha)} \tag{4.18}$$

which has a solution equivalent to the Littrow reflection wavelength for $x = 0$. We may conclude that a infinite tuning range is achieved for a grating pivot at position $x = 0$ and $y = -L_\alpha \cot(i-\alpha)$. To validate this result and calculate the positional tolerance of the pivot required to satisfy a large tuning range we require calculation of the frequency tuning range, $\Delta\nu$, as a function of pivot point position. We consider the limit of continuous tuning, and therefore the point at which a mode-hop occurs, to occur when the frequency corresponding to the principal cavity mode, ν_m, differs from the Littrow reflection frequency, ν_L, by greater than half of the cavity free-spectral-range (FSR) as,

$$|\nu_L - \nu_m| = \frac{1}{2}\frac{c}{2L_\alpha} \tag{4.19}$$

The tuning range is thus given by,

$$\Delta\nu = |\nu_m(\alpha_+) - \nu_m(\alpha_-)| \tag{4.20}$$

For further details of this calculation refer to the paper by Nilse et al. [231]. In practice, attaching the pivot at the point $x = 0$ in the plane of the grating, as determined above, places heavy constraints on the mechanical design. A further investigation considering a more general geometry, which includes an offset of the grating plane relative to the pivot, is carried out, again by Nilse et al., and it is found that a high mode-hop-free tuning range is achieved for a band of values along $y = -\cot i$ for $x < L_0$. Additionally, it is perhaps preferable to work away from the "optimum" pivot point at $x = 0$. While this

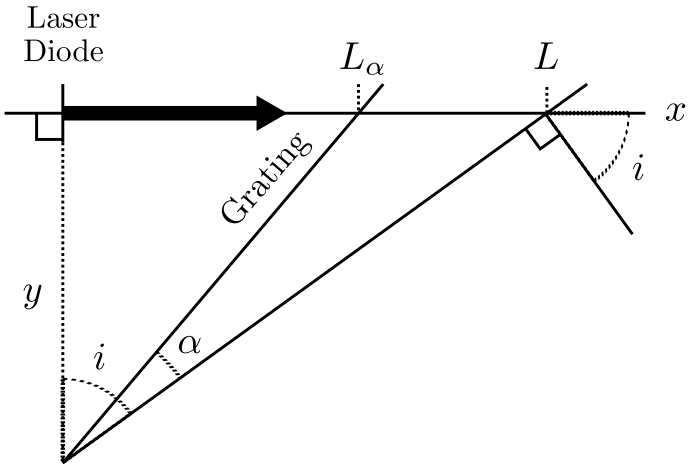


Figure 4.2: **Simplified Littrow geometry** - Grating, at initial angle i and cavity length L, is tuned by angle α to cavity length L_α.

compromises the ultimate mode-hope-free tuning range, the positional tolerance is relaxed with increasing x (see Fig. 4 Ref. [231]) and also allows for a more compact geometry. For a correct design of pivot we would expect a mode-hop-free tuning range $\sim$100 GHz.

4.1.3 Extended Cavity Opto-Mechanical Design

4.1.3.1 Design of the Grating Pivot Mechanism

In realising the ECDL mechanics we are faced with a design choice concerning the nature of the grating pivot mechanism. A flexure hinge element offers a simple lubrication-free sprung pivot, without friction and with limited hysteresis, and is highly suitable to opto-mechanical design. Some investigation into a flexure grating pivot mechanism was carried out, however, due to the limited experience of the author and constraints on time, a conventional 3-point (cone, flat, and 'v'-groove) sprung kinematic mount was chosen to position the grating. Such a mechanism also provides a large range of tunability allowing the cavity to accommodate a reasonable range of wavelengths (typically $> \pm 20$ nm for a given grating) around its central design wavelength.

The movable kinematic frame which houses the grating and compensation mirror (here referred to as the grating arm) is machined from a single piece of aluminium (see Fig. 4.5), and while not an ideal material (moderately high thermal expansion coefficient and low density) it has been chosen in a first instance for its economy of machining. The 'v'-groove on the grating arm is formed by two parallel hardened steel dowels fitted in slots machined vertically at the top horizontal pivot location. This provides constraint in the horizontal direction while allowing freedom of motion in the vertical direction for actuation of the vertical pivot). The common kinematic pivot point is located by a simple hole (typically a cone or trihedral cut out) in which the end ball of the actuator sits, undersized in comparison to the actuator ball diameter. The 'flat' is provided by the end of a ce-

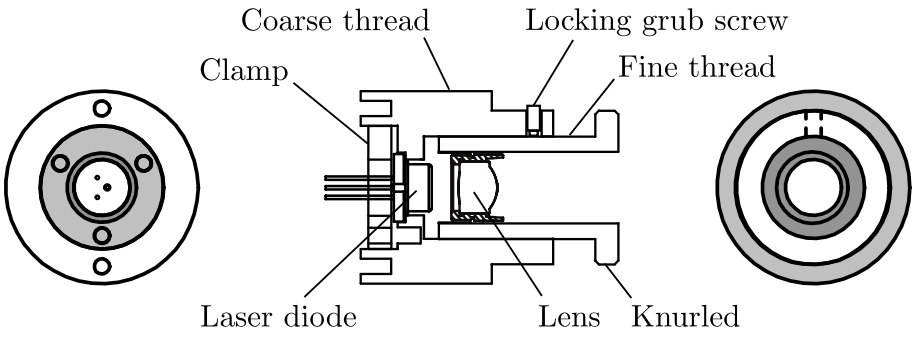


Figure 4.3: **The collimator assembly.** - End and cross-section views of the laser diode collimator assembly. The lens holder is internally threaded to accept a Thorlabs C110TME aspheric lens. On the outer an ultra-fine thread is machined, with its counterpart on the inner of the diode mounting tube, and a nylon-tipped grub screw secures the lens holder in place following adjustment. The diode is clamped into a recess in the tube end with a brass ring secured by three M2 screws. The completed assembly screws into a cut-out in the laser cavity housing.

ramic piezoelectric (PZT) stack (Thorlabs part: AE0203D04F, range: 4.6 µm over 150 V) which is glued into a recess in the grating arm. The actuators used to manipulate the kinematic mount are from Fine Adjustment and boast 170 TPI, or equivalently a 150 µm translation per turn. The material is brass and the outer bushing is interference fit (and on occasion secured with bearing glue) into the aluminium fixed frame mount. The fixed frame mounting forms part of the cavity housing, which includes a threaded hole in which the diode and collimator assembly is secured (Sec. 4.1.3.2). The arm is held in place with two steel coiled extension springs (from Lee Spring Ltd) which are secured under tension with retaining dowel pins, located in grooves in the cavity housing and grating arm. The grating arm and cavity housing are both hard anodised.

The grating (dimensions 12.7 × 12.7 × 6 mm) is glued to the grating arm on top of a piezoelectric disc (Piezomechanik part: Pch150/7x7/2), which provides up to 2 µm (over 150 V range) of linear translation of the grating, and is used for ultra-fine tuning of the cavity length, and therefore laser wavelength, both manually, and as one of the actuators in a wavelength stabilisation servo scheme. The PZT stack on the grating arm provides a secondary electro-mechanical actuator for fine tuning and long term cavity drift correction. The compensating mirror is of the same dimensions as the grating and is glued to the mirror support on the grating arm.

4.1.3.2 Design of the Collimator

The laser diode output beam can be characterised by its divergence from the short (long) output facet dimension, known as the fast (slow) axis, of typically 30° (10°). In the far-field (which is anything greater than about a few hundred microns), this produces a beam of elliptical profile with approximately 3:1 major:minor axis ratio. The beam is shortest along

the long axis of the diode end fact, which is the direction in which the light is polarised. As previously discussed (Sec. 4.1.1) it is desirable to maximise the number of diffraction lines covered, and so we choose to operate the laser oriented with its short axis (or long axis of the beam) in the horizontal direction with the grating lines vertically oriented. The polarisation is thus parallel to the grating lines (said to be P-plane polarisaed) and the grating is operated in transverse electric (TE) mode. The collimation is chosen to provide the desired beam dimensions at the laser output, and in addition to maximise, but not exceed, coverage of the grating. The nominal beam diameter, as determined by the marginal ray, is given by,

$$\text{Beam Diameter} = 2 \cdot EFL \cdot NA \tag{4.21}$$

where EFL is the effective focal length of the collimating lens, $NA = \sin\theta$ is the numerical aperture of the source, and θ is the divergence half angle. Here, collimation is achieved with an aspheric lens (Thorlabs part: C110TME-B) which has $EFL = 6.24\,\text{mm}$ and $NA = 0.40$ (maximum NA of diode is typically ~ 0.26). Positioning of the lens within the extended cavity is critical to providing optimum lasing performance of the ECDL and must be positioned to provide optimum beam collimation. The mechanical design of the ECDL must therefore provide a means of adjustment for the position of the lens relative to the laser diode. It is decided here that fine adjustment of the transverse lens position relative to the laser diode centre is not necessary (manufacturing tolerances of diode and lens allowing) and it is sufficient to consider adjustment of only the axial distance of the lens from the laser diode. Such a simple linear translation of the lens is achieved by mounting it in a finely threaded tube, which may be screwed in to and out of a fixed complementary part. The "collimation tube" is machined from brass, which has a self-lubricating property, as a result of its lead content, and provides a low friction interface for the fine threads to move smoothly. A long, large diameter thread is used to minimise the effect of unwanted play. The final position of the lens is secured by a locking nylon tipped grub screw which clamps the thread of the collimation tube in place (see Fig. 4.3). In practice, due to a small eccentricity of the lens and laser diode, a small, but tolerable, steering of the emerging collimated beam is experienced during positioning of the lens. Alternatively, and to eliminate this problem, the lens may be (approximately) linearly translated by a simple flexure mechanism, but as previously discussed this approach was not pursued here. The complete collimator assembly is screwed, with a coarse thread, in to the cavity housing up to a shoulder on the inner side. The position of the collimator may be tuned with the insertion of a spacer ring, stacked on to the housing shoulder, to provide adjustment of the laser diode position relative to the grating pivot point. This allows for optimisation of the pivot location for a range of operating wavelengths to provide a large mode-hop-free tuning range. The diode is clamped into a recess in the back end of the collimator, designed to accept 9 mm diodes and 5.6 mm diodes with the addition of an

adapter ring.

4.1.3.3 Design Parameters of the ECDLs

The design parameters of the 813 nm 'lattice' ECDL and 698 nm 'clock' ECDL are listed in Tab. 4.1. The ECDLs are intended to provide a high level of tunability around the design wavelength while maintaining high mechanical stability and minimal displacement of the output beam. The geometry is configured to provide a large mode-hop-free tuning range. To achieve a narrow linewidth of the ECDL a long cavity length is preferable, however, the extent to which the cavity is extended must be balanced with the achievable mechanical stability of the cavity and the desired frequency tuning range, both of which suffer with increased cavity length. The clock ECDL, in particular, has been optimised to achieve a narrow linewidth and a generous cavity length of ∼6 cm is here chosen. The longer wavelength lattice ECDL has a ∼4 cm cavity length, which corresponds to a cavity mode number of almost half that of the clock ECDL. Perhaps more key to narrowing the ECDL linewidth is suppression of neighbouring laser diode cavity modes whose competition is expected to provide a line broadening mechanism [232]. Investigations have shown a greater dependence of the ECDL linewidth on the grating resolution than both the cavity length and cavity finesse [232], and so here we use a 2400 lines mm^{-1} grating for the clock ECDL. The number of grating lines covered is further enhanced as a result of the increased corresponding Littrow angle, of ∼57°, which increases the projected area of the laser beam on the grating.

4.1.4 Environmental Considerations

In its exposed form the extended cavity is sensitive to air currents and barometric variations in the lab environment which translate directly to variations in the effective cavity length and thus the operating wavelength of the ECDL. In addition, the laser diode is tuned by temperature and therefore we require a means to control and stabilise diode temperature. We also require the diode casing (ground), which is electrically coupled to the ECDL housing, to be electrically isolated from the optical table earth.

An aluminium box, which includes an o-ring sealed lid, is machined to house the ECDL cavity and provide a hermetic environment for the ECDL to operate. An AR-coated window, 25.4 mm in diameter and 5 mm thick, is glued at the beam exit of the box and is positioned at a sufficient angle to prevent back reflections from coupling back into the laser cavity and also to prevent self interference of the beam.

4.1.4.1 Temperature Control

The cavity housing is secured on top of a 4 cm square Peltier module (RS part: 618-730), positioned with its cold face to the ECDL cavity and the hot side to the box, which serves

Table 4.1: ECDL parameters

Parameter	ECDL Centre Wavelength (nm)		Unit
	813.4	698.4	
Gating Frequency	1800	2400	$\mathrm{lines\,mm^{-1}}$
Littrow Angle	47.07	56.87	$^\circ$
Cavity Length	41	59	mm
Cavity FSR	3.66	2.54	GHz
Lens EFL	6.24	6.24	mm
Beam Size (long axis)	$\sim$3	$\sim$3	mm
Grating Coverage	7928	13174	lines
Screw Actuator (est.)	535	464	$\mathrm{GHz\,turn^{-1}}$
PZT Stack (est.)	110	95	$\mathrm{MHz\,V^{-1}}$
PZT Disc (est.)	81	53	$\mathrm{MHz\,V^{-1}}$
Grating Feedback	$\sim$20	$\sim$10	%
Grating Mirror Separation	6.5	6.5	mm
Output Beam Displacement (est.)	26	72	$\mathrm{\mu m\,nm^{-1}}$

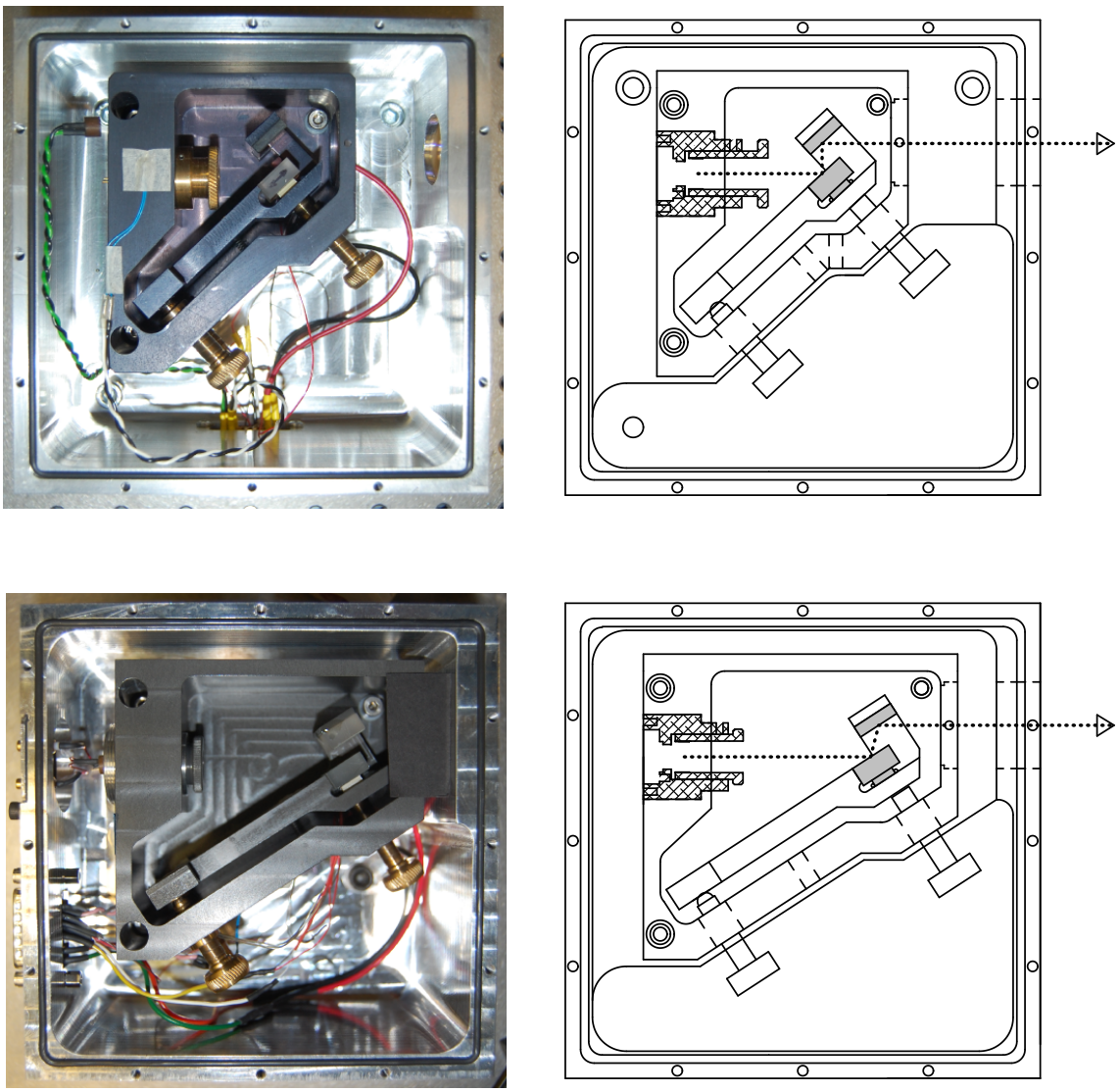


Figure 4.4: **Pictures of Assembled ECDLs** - Photographs and scale drawing of the assembled lattice (top) and clock (bottom) ECDLs. Cavities are enclosed in an aluminium box which provides the opportunity for hermetic sealing, and serves as a heat sink for the cavity Peltier module.

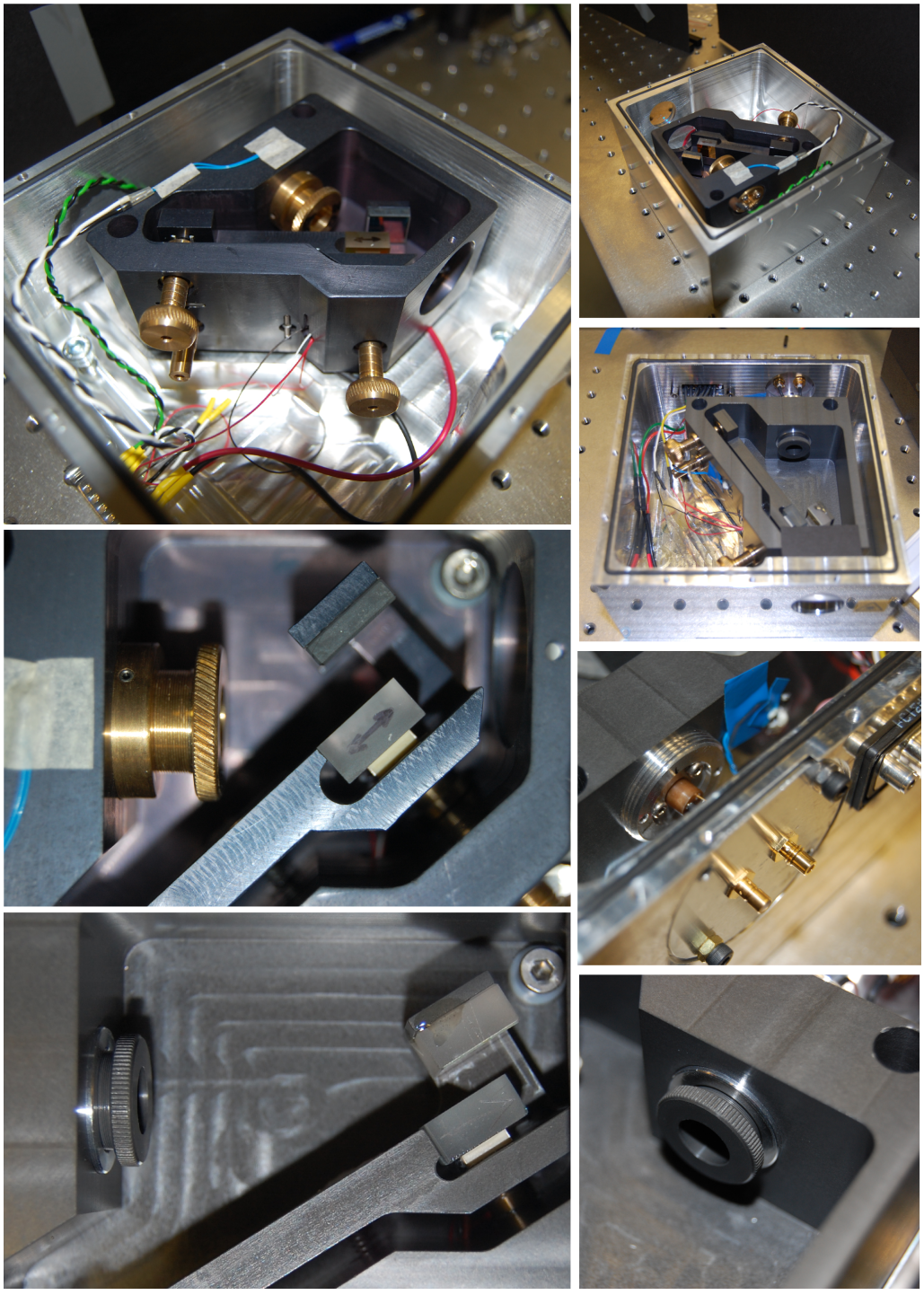


Figure 4.5: **ECDLs** - Various views of the 813 nm and 698 nm ECDLs.

as the heat sink for the thermoelectric heat pump. To provide electrical and thermal isolation of the diode and cavity housing to the box and outside system, nylon inserts are used in the bolt holes of the ECDL cavity mounting. The laser diode temperature is then controlled through the cavity housing to which it is thermally coupled. A PID control loop is implemented to stabilise the cavity temperature to typically within 5 mK over a day. The temperature controller is home built and is based on a single op-amp implementation of a PID control loop filter, which is typical of those used throughout this work. The control loop error signal is formed of the amplified output of a Wheatstone measurement bridge containing a single NTC thermistor (10 kΩ at 25 °C) in one leg of the bridge. The thermistor is glued to the ECDL cavity housing in close proximity to the laser diode. The bridge output is amplified by a two op-amp instrumentation amplifier circuit. The loop filter output signal controls a simple transconductance amplifier which drives the Peltier module.

4.1.4.2 Tuning the PID Controller

Critical to a high performance of the temperature controller is the correct tuning of the PID parameters of the loop filter. Several heuristic methods exist to estimate the required values of the proportional, integral, and differential gains. We have experimented with two such popular methods, Ziegler-Nichols [233] and Tyreus-Luyben (modified Ziegler-Nichols) [234], but with mixed success. The methods require determination of the so-called ultimate gain and ultimate period, which correspond to the minimum proportional gain required to produce sustained oscillations of the control loop output and the period thereof. It is noted that this ultimate gain can be very time consuming to reach, given the long time constant typical of a thermal system, and may even be unobtainable if the thermoelectric actuator or drive circuitry has insufficient capability.

We opt instead to measure the relevant portion of the thermal transfer function of the plant and adjust the loop filter accordingly to provide stable control. The process requires measurement of the plant response, both the amplitude and phase, to a series of driven sinusoidal perturbations. To achieve this, the loop filter is removed from the control loop and the loop filter output replaced by a sine wave of required frequency, with amplitude sufficient to measure a system response at the output of the amplified measurement bridge. The system response is measured for a range of discrete frequencies and logged together with the input signal, here using LabView. A comparison of the measured output to the input allows determination of the system transfer function. Bode plots of the measured system amplitude and phase response for the lattice ECDL, which includes the response of the amplified measurement bridge, are shown in Fig. 4.8, labelled 'System'.

The loop filter, or PID controller (or sometimes lead-lag network), is used to provide the correct in-loop compensation to ensure stable control of the system. The aim is to provide an optimised control bandwidth while avoiding overall positive feedback (phase

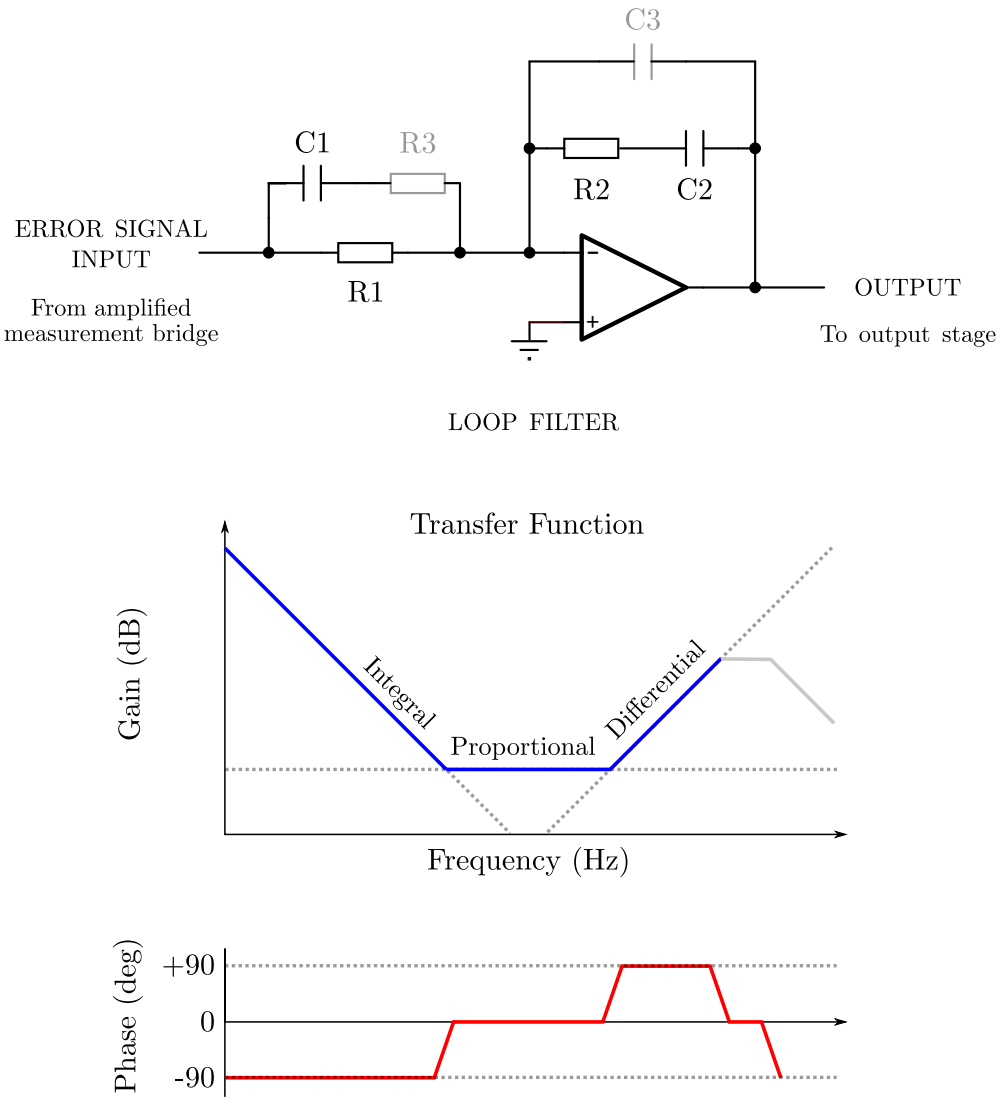


Figure 4.6: **The loop filter** - A single op-amp implementation of a PID controller. Amplitude and phase response bode plots are sketched for clarity.

$\sim -180°$) above unity gain which will result in system oscillations. We use here a single op-amp (OPA277 is suggested) PID controller, see Fig. 4.6, with the integrator gain set by R1 and C2 and the gain of the differentiator by C1 and R2. R3, which is typically small, is set to limit the high frequency gain of the differentiator, and C3, also small, rolls off the gain of the amplifier at high frequencies. The proportional gain is set by the ratio of R2 to R1, however changing this also adjusts the zero corner frequencies of the integrator and differentiator, as does adjusting the integrator and differentiator gains by C2 and C1 respectively. It is often useful to picture the gain transfer function of the PID controller as three lines of gradient -1, 0, and +1 corresponding to the integral, proportional, and derivative gains, as shown in Fig. 4.6. It then becomes evident how adjusting the gain of each component interacts with the controller zero corner frequencies. The integrator provides a 90° phase lag, and the differentiator a 90° phase lead, and transitions by +90° around each zero when heading towards higher frequencies. The loop filter response is simple to calculate with an elementary consideration of the complex impedance of the amplifiers extraneous components, and has amplitude and phase response, ignoring components R3 and C3 (not relevant to the PID operation), given by,

$$|\text{Gain}| = \left[\left(\frac{\text{C1}}{\text{C2}} + \frac{\text{R2}}{\text{R1}}\right)^2 + \left(2\pi f \text{C1}\,\text{R2} - \frac{1}{2\pi f \text{C2}\,\text{R1}}\right)^2\right]^{1/2} \tag{4.22}$$

$$\phi = \tan^{-1}\left[\frac{\left(2\pi f \text{C1}\,\text{R2} - \frac{1}{2\pi f \text{C2}\,\text{R1}}\right)}{\left(\frac{C1}{C2} + \frac{R2}{R1}\right)}\right] \tag{4.23}$$

The loop filter response is plotted, see 'Loop filter' Fig. 4.8, for appropriate component values to produce the desired overall control loop response, see 'Total' Fig. 4.8. We aim to achieve a high low-frequency gain to provide 'tight' control towards the set point temperature. The loop filter differential stage acts to compensate the roll off of the system gain and phase to extend the control bandwidth. The system gain is $\sim$45 dB at DC and rolls off with slope -6 dB per octave, as is expected of a first order low pass filter (the integrator), down to the system 'zero' at around unity gain where the gain flattens out. For stability, a phase margin of around 45° at unity gain and a gain margin greater than 6 dB at phase $-180°$ is targeted.

The error signal of the stabilised system was measured over a $\sim$24 h period, and Allan deviation plotted in Fig. 4.7. A control loop instability of $\sim$250 µK at 10 000 s is demonstrated (no independent temperature measurement is reported here). The method described here has proven to be reliable in providing robust control parameters of the PID controller, and removes the guess work from the tuning process. We apply this technique to tuning of all temperature control loops used throughout this work.

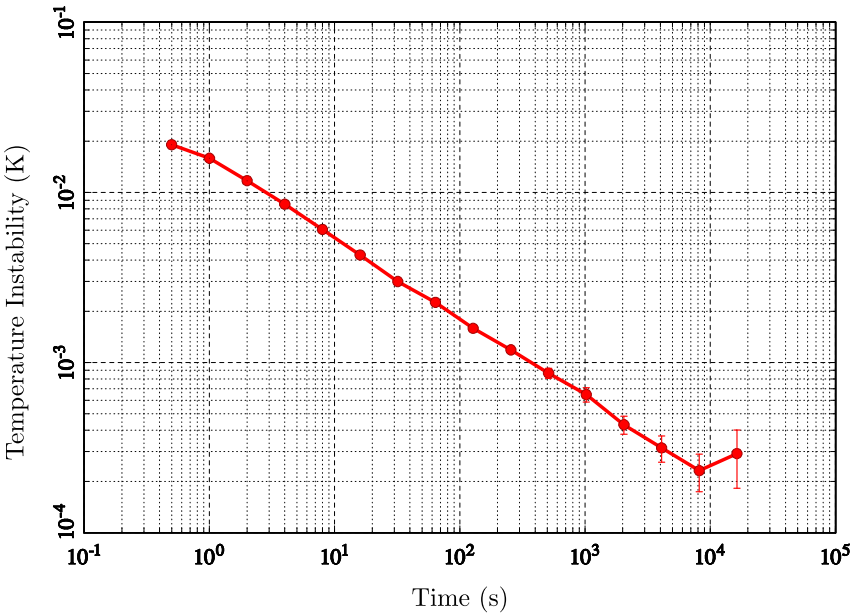


Figure 4.7: **In-Loop Temperature Instability** - Allan deviation of in-loop temperature controller error signal measured over ∼10 000 s. A noise floor corresponding to ∼250 µK fluctuations is achieved at 8000 s.

4.1.5 Characterisation of the ECDL

The clock laser ECDLs are to be stabilised to a high finesse optical cavity by the PDH method, with the aim of reaching sub-hertz laser linewidths at 1 second. To aid diagnostics, two identical clock ECDLs were constructed to allow for beat note comparison of the laser linewidths. The characterisation of each ECDL towards this goal is reported in the following text. Characterisation of the lattice ECDL is not reported.

4.1.5.1 Tuning range

To measure the tuning range of the ECDL the laser light is aligned into a scanning confocal Fabry-Perot interferometer (TekOptics SA2) which is continuously scanned over at least one cavity free spectral range (here FSR = 2 GHz). The resulting cavity fringes are viewed on an oscilloscope and the time axis of the scope calibrated to frequency. The laser frequency can then be tuned and the extent measured. The measured tuning properties of the PZT disc, PZT stack, and screw actuator (required to measure full extent of mode-hop-free tuning range) are provided in Tab. 4.2.

Measured values are in good agreement with the design parameters estimated in Tab. 4.1. The mode-hop-free tuning range is comparable to leading commercial designs, although no effort was made to optimise it. It is anticipated that fine adjustment of the pivot point, by either offsetting the grating arm with actuator adjustment, or by shim-

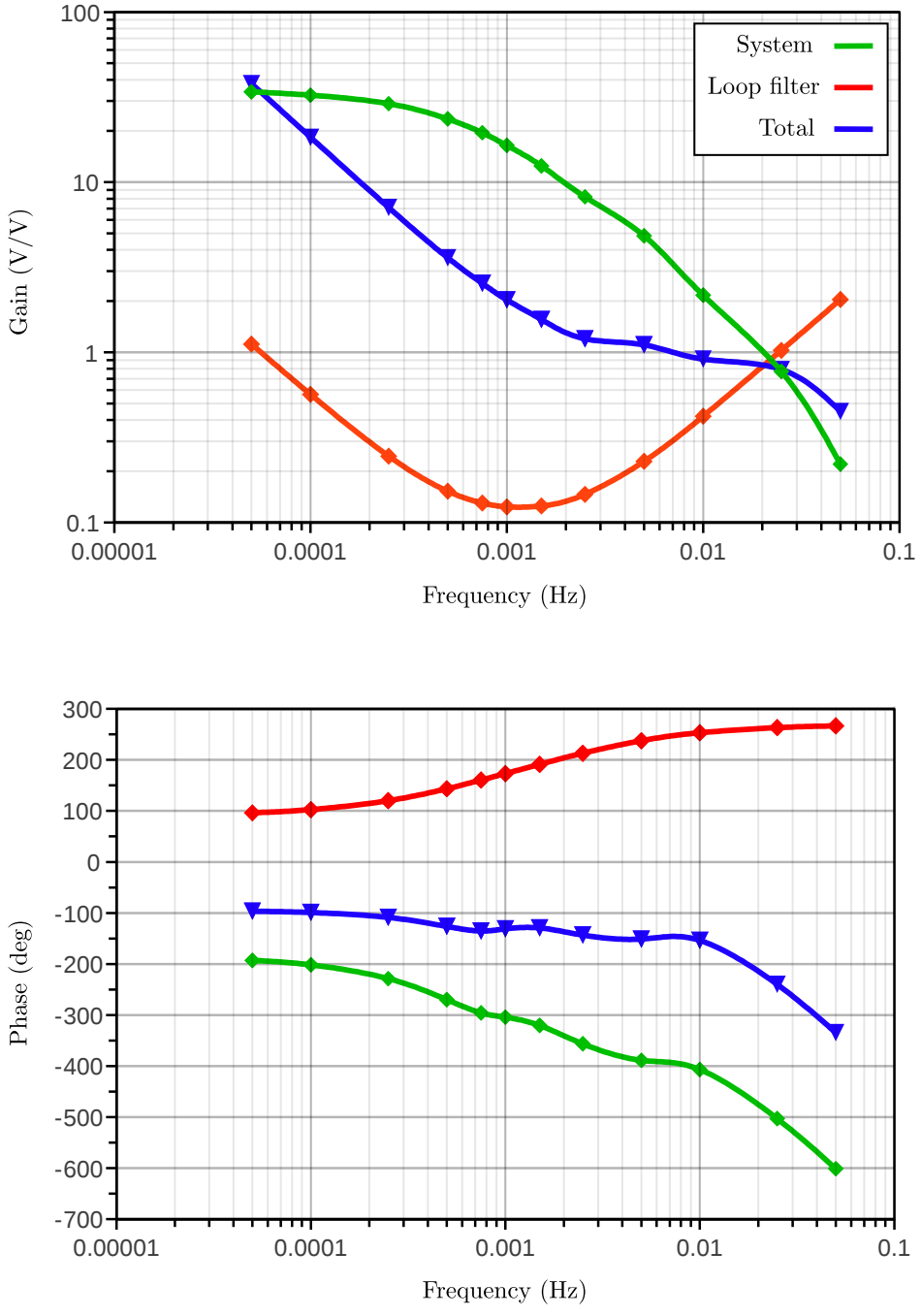


Figure 4.8: **Compensating the system response.** - Bode plots showing the amplitude (top) and phase (bottom) response for the measured the thermal system (green), the calculated loop filter (red), and the result of the two combined (blue).

Table 4.2: ECDL tuning range

Parameter	Clock ECDL	Unit
Mode-hop-free	49	GHz
PZT Stack	100	MHz V^{-1}
PZT Disc	30	MHz V^{-1}

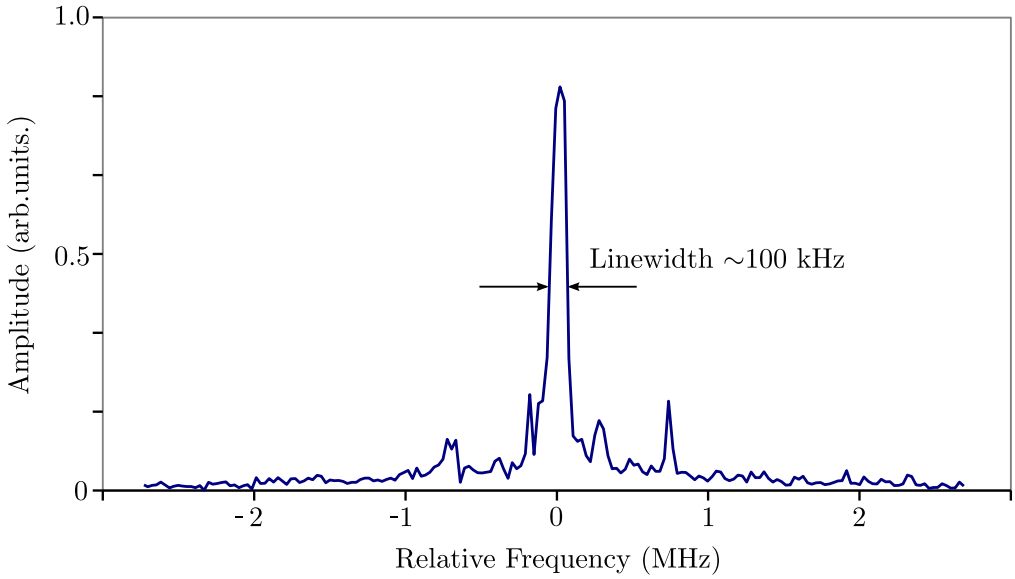


Figure 4.9: **Determination of the clock ECDL linewidth** - The beat signal resulting from the frequency mixing of two identical free-running clock ECDLs.

ming the collimator spacer ring, could further improve the mode-hop-free tuning range. Although not important here, the mode-hop-free tuning range can be enhanced further by complementary tuning of the laser diode current, in a feed-forward scheme, as is standard in several commercial systems. Ultimately, we expect the limit to come from cross talk between the horizontal and vertical degrees of freedom in the grating arm, requiring realignment of the vertical direction over a large tuning range.

4.1.5.2 Free-running instantaneous ECDL linewidth

Characterisation of the clock ECDL linewidth is aided by the availability of an identical second system. The free-running laser linewidth is determined by combining the output of each laser onto a high bandwidth avalanche-photo-diode (APD) and measuring the linewidth of the resulting beat. Making the assumption that each ECDL has a similar linewidth we can deconvolve the measured linewidth to give an estimate of the individual laser linewidth. A typical beat signal is shown in Fig. 4.9 and has a linewidth of ~100 kHz,

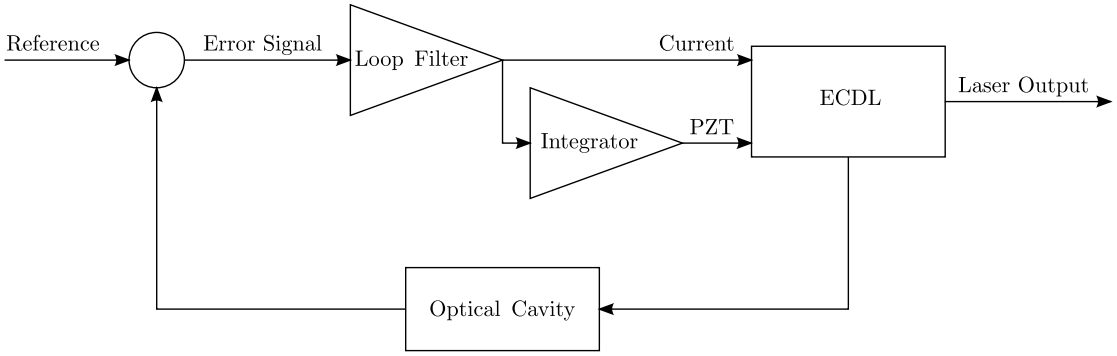


Figure 4.10: **Laser Stabilisation Scheme** - Schematic of the control loop for frequency stabilisation of the ECDL.

which corresponds to an ECDL linewidth of ∼70 kHz. The ECDL tunes by 160 Hz nA^{-1} and it is anticipated that the laser linewidth is limited by noise present on the laser diode current source.

4.1.5.3 Frequency stabilisation

To stabilise the frequency of the ECDL we require a means to measure fluctuations of the laser frequency, compared to the point to which we aim to stabilise, and provide suitable feedback to the ECDL to correct for the frequency deviations. The PDH locking method is one such approach and utilises the reflected signal from an optical cavity (containing both the cavity reflected field and cavity leakage field) to measure optical frequency information below the cavity resonance bandwidth, $\Delta\nu_{cavity}$, and optical phase information above $\Delta\nu_{cavity}$. The PDH error signal is derived from mixing of the cavity sampled laser carrier and the applied modulation sidebands, which have optical powers P_c and P_s respectively. Because detection is shifted to a high modulation frequency, where the laser intensity noise is small (technical noise typically <100 kHz) and can approach the shot noise limit, PDH locking provides a high measurement S/N ratio and is relatively insensitive to intensity fluctuations. The demodulated error signal is dispersion shaped and has an approximately linear slope between minimum and maximum amplitude, known as the frequency discriminator, and is given by [210],

$$D = \frac{8\sqrt{P_c P_s}}{\Delta\nu_{cavity}} \tag{4.24}$$

We may measure this simply as the peak to peak height of the error signal divided by the cavity bandwidth (which may be determined by cavity ring down spectroscopy).

To correct frequency fluctuations, the error signal is fed back to the ECDL drive current

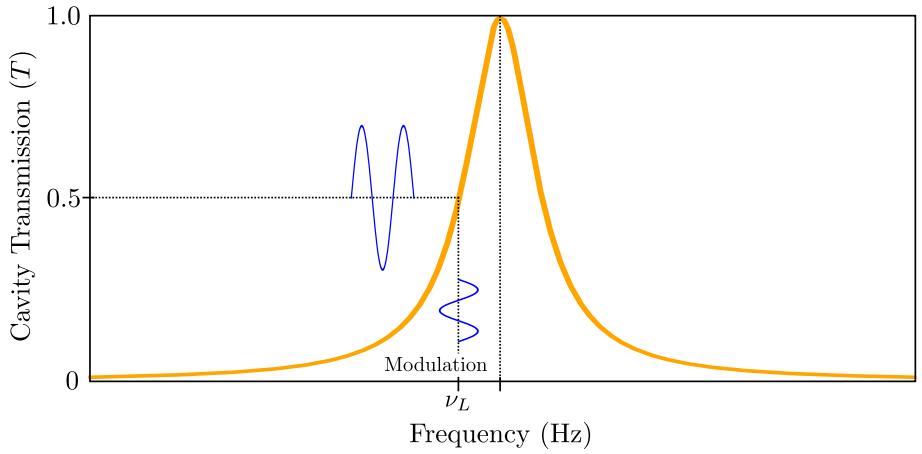


Figure 4.11: **Cavity Transmission Fringe** - Depiction of a side-of-fringe frequency discriminator used for characterisation of the laser current modulation frequency tuning transfer function.

and piezo tuning mechanisms. Similarly to the temperature control loop, stable control requires implementation of a loop filter which provides the required in-loop compensation between error signal and system. The system response may be decomposed into the cavity transfer function and the ECDL current modulation transfer function, which we may characterise in isolation. The cavity response may be dealt with simply and modelled as a first-order low pass filter with corner frequency given by the cavity bandwidth. Determination of the ECDL current modulation transfer function requires a measurement system similar to that which the control loop error signal is derived to provide a suitable frequency discriminant. We use here the 'side' of a cavity transmission, T, fringe of a low finesse optical cavity (finesse ∼100; the cavity and detector bandwidth must be greater than the anticipated ECDL modulation bandwidth ∼MHz). The side-of-fringe discriminator slope, pictured in Fig. 4.11, is given by [210],

$$\frac{\mathrm{d}T}{\mathrm{d}\nu_L} = \frac{T}{\Delta\nu_{cavity}} \tag{4.25}$$

where $\mathrm{d}\nu_L$ is the change in laser frequency around the point $T/2$, and $\mathrm{d}T$ is the corresponding change in cavity transmission. A low finesse of optical cavity provides a relatively low discriminator slope to which the action of the free-running laser noise is small in comparison to the applied modulation response.

The ECDL current modulation amplitude and phase response is measured over a range of modulation frequencies and the transfer function is constructed, see Fig. 4.12. With knowledge of the discriminator slope of the measurement cavity we can characterise the amplitude response of the ECDL in terms of the frequency change for a given modulation signal amplitude, which is applied to the ECDL current source with sensitivity $1\,\mathrm{mA\,V^{-1}}$. The cavity response, also see Fig. 4.12, is modelled as a first order low pass filter and scaled

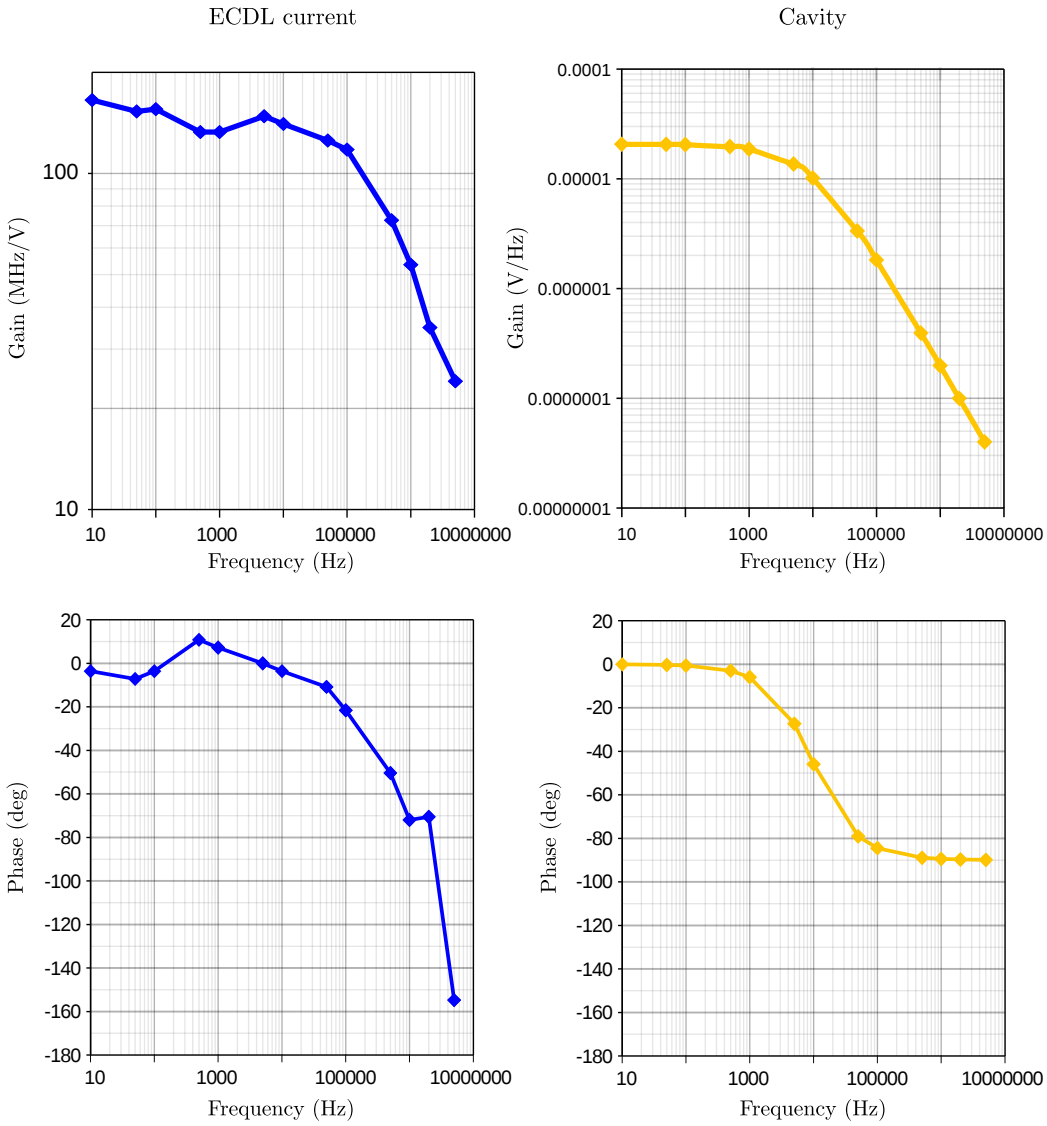


Figure 4.12: **ECDL and Cavity Transfer Functions** - Bode plots of the measured amplitude and phase response of the ECDL current modulation (left top and bottom respectively) and the calculated cavity response (right top and bottom).

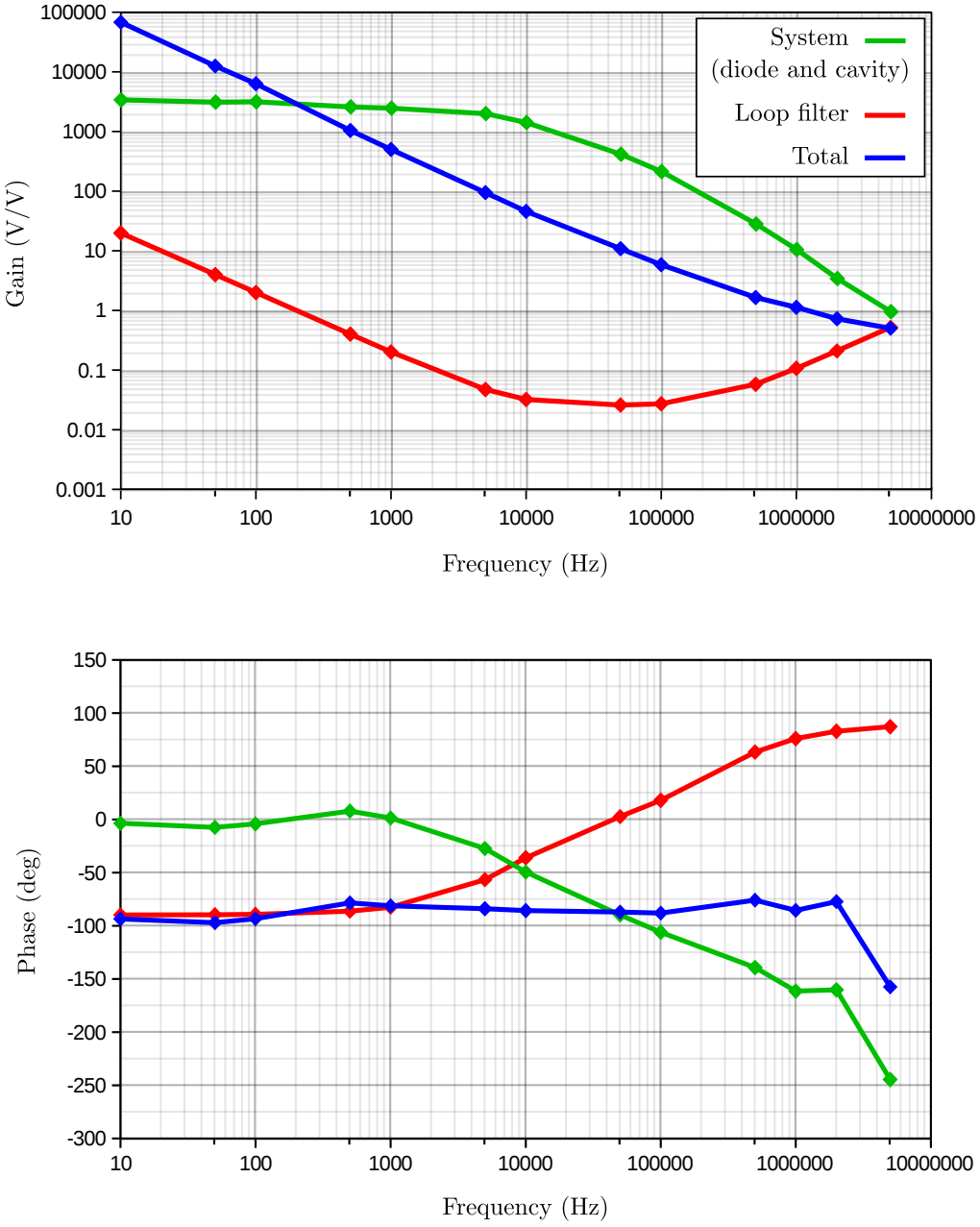


Figure 4.13: **System, Loop Filter, and Total Transfer Functions** - The loop filter filter transfer function is adjusted to compensate the measured response of the system. The 'Total' response is that of the compensated system and provides stable control.

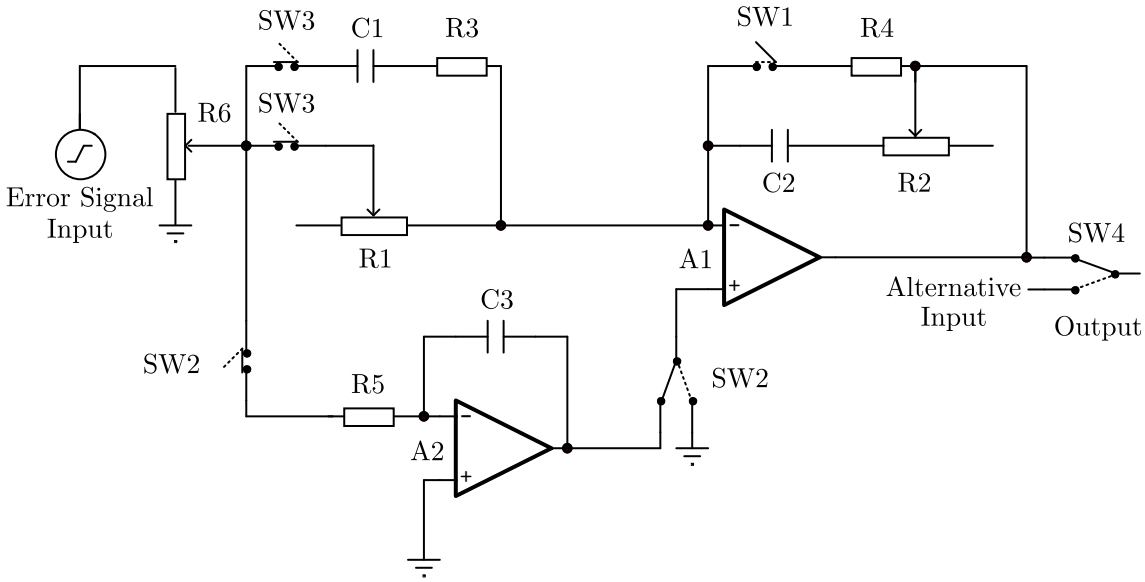


Figure 4.14: **Laser Stabilisation Loop Filter** - Circuit schematic of the signal critical components of the laser stabilisation scheme loop filter.

according to the measured frequency discriminator of the PDH error signal. The clock optical cavity used for stabilisation of the clock laser is a high-finesse ULE spacer cavity of length 7.75 cm and has a vertically oriented mounting to provide an increased vibration insensitivity [58, 235]. For the cavity bandwidth of $\Delta\nu_{cavity} \sim 10\,\text{kHz}$ and the measured error signal peak-to-peak amplitude of 200 mV, for typical optical powers $P_c \sim 10\,\mu\text{W}$, the discriminator slope is $\sim 20\,\mu\text{V}\,\text{Hz}^{-1}$. Note, changing the optical power has the effect of changing the total gain of the system and may be compensated simply with an overall gain control placed before the loop filter (potentiometer R6 Fig. 4.14).

Compensation of the system response is achieved with a loop filter, Fig. 4.14, of similar form to that in Fig. 4.6, and is tuned as previously described, but differs in several ways. Switch SW1, positioned in series with R4 and across the integrating capacitor, is effectively the lock switch and is used to 'reset' the integrator and prevent integrator 'windup' during acquisition of the lock. When closed, the low frequency gain is set according to the ratio of R4/R1 and the corner frequency of the capped integrator provided by the RC network formed of R4, C2, and R2. The option of a second integrator stage is included to provide enhanced gain at low frequencies and may be switched in and out of the system with switch SW2. With SW2 'open' (second integrator switched 'out') the circuit behaves as a simple PID controller. The error signal is compared to the systems electrical ground and the difference nulled by the action of the loop filter. However, the error signal often contains a small DC offset (due in part to residual amplitude modulation) which must be cancelled to ensure locking to the centre of the cavity fringe. To compensate, a precision 5 V reference (Analog Devices AD586L) is implemented to provide a tunable stable offset (which must be stable to $<20\,\mu\text{V}$ for $<1\,\text{Hz}$ frequency stability of the laser)) of range $\sim 100\,\text{mV}$ about

electrical ground and is applied to the error signal via a unity gain inverting amplifier stage. The loop filter output is fed to modulation inputs of both the ECDL current and, via an additional integrator, to the ECDL PZT disc. The additional integrator on the PZT channel acts to cancel the output of the loop filter over the bandwidth of the PZT disc actuator. A servo bandwidth of $\sim$1 MHz is anticipated for current tuning and the PZT disc has a measured bandwidth $\sim$1 kHz (limited by the drive electronics). It is preferable to have a high bandwidth of the PZT channel as corrections made here do not produce amplitude modulation (or very little) of the laser light, which otherwise occurs as a direct consequence of current tuning.

The loop filter is designed with remote operation in mind, as the clock laser system is intended to operate in a remote 'quiet house' where disturbances should be kept to a minimum, and therefore all switches (labelled SW1, SW2, SW3, and SW4) are TTL operated (Vishay DG411HS and 70803 are used). This also enables rapid reconfiguration of the controller, including isolation from the control loop, intended to allow implementation of several useful schemes. One such scheme, although not yet carried out, is the rapid loss and recapture of the lock which provides the opportunity for repeated cavity ring down spectroscopy. This is achieved by operating switch SW3 to isolate and loop filter input and hold the integrator value while the output is switched to the alternative input by SW4 where a perturbing signal is configured to rapidly servo the laser frequency away from resonance. When returned to the original state the integrator value should retain the correct lock point and the lock rapidly reacquired.

Using the method described above the clock ECDL frequency is stabilised to $<$1 kHz and is expected to be improved further to the hertz level with careful optimisation of the loop filter parameters.

5

Atomic Polarisability: Magic wavelengths, probe light shifts, and the BBR shift

5.1 Calculation of the ac Dipole Polarisability

To estimate our optical trap depth and identify the possible "magic" wavelengths we must first calculate the dipole polarisability. From Eq. (3.51) and Eq. (3.52) we may write the polarisability of the lower state, indexed by a, of a transition with frequency ω_0 as,

$$\alpha_a = \frac{2}{\hbar} |d|^2 \frac{\omega_0}{\omega_0^2 - \omega_L^2} \tag{5.1}$$

where ω_L is the frequency of the interacting light field with amplitude E_0, and d is the transition matrix element. In a multilevel system, several levels, of label k, contribute to the shift the energy of the level a, with total shift given by the sum over all levels of k. We may then write a general expression for the dynamic polarisability as,

$$\alpha_a = \frac{2}{\hbar} \sum_k |d_{ak}|^2 \frac{\omega_{ak}}{\omega_{ak}^2 - \omega_L^2} \tag{5.2}$$

Using the relation,

$$\delta\omega_a = -\frac{1}{2\hbar}\alpha_a \langle \mathbf{E}^2 \rangle = -\frac{1}{4\hbar}\alpha_a E_0^2 \tag{5.3}$$

we may calculate the corresponding frequency shift by,

$$\delta\omega_a = \frac{E_0^2}{4\hbar} \left(\frac{2\,|d_{ak}|^2}{\hbar} \frac{\omega_0}{\omega_L^2 - \omega_0^2} \right) \tag{5.4}$$

We now need to know the dipole matrix element d_{ak} for each contributing transition, which is related to the $|a\rangle \rightarrow |k\rangle$ transition rate as in Eq.(3.52). A slight complication arises due to the available data for transition rates. The literature tends to give total decay rates, $\Gamma(^{2S_k+1}L_k \rightarrow {}^{2S_a+1}L_a)$, corresponding to the transition rate from one LS multiplet to another, or equivalently as state lifetime $\tau = 1/\Gamma$ (providing no other significant decay path), but we require the transition rate from a specific sublevel, that of the clock state. The total transition rate must be subdivided according to fine, magnetic, and hyperfine substructure. The problem is a geometric one concerned with angular momentum selection rules and requires use of the well-known Wigner 6-j and 3-j symbols.

We start by considering the line strength, $\mathcal{S}_{J_a J_k}$, for a transition from a lower level $|L_a S_a J_a\rangle$ to an upper level $|L_k S_k J_k\rangle$ between LS multiplets (see for example Ch.9.2 Ref. [236]) which is related to the transition probability Γ_{ak} as,

$$\Gamma_{ak} = \frac{4\omega_{ak}^3}{3\hbar c^3}\frac{g_a}{g_k}\mathcal{S}_{ak} = \frac{2\omega_{ak}^2 e^2}{mc^3} f_{ak} \tag{5.5}$$

where g_a and g_k are the state degeneracy factors.. Also included here is the relation to the oscillator strength, f_{ak}, which will be useful later in determining the completeness of our calculation. To calculate the relative dipole branching between states $|L_a S_a J_a\rangle$ and $|L_k S_k J_k\rangle$, we use the relation [195],

$$X_{ak} = \frac{|\langle L_a S_a J_a||\mathbf{d}||L_k S_k J_k\rangle|^2}{|\langle L_a S_a||\mathbf{d}||L_k S_k\rangle|^2} = (2J_a+1)(2J_k+1)\begin{Bmatrix} L_a & J_a & S_a \\ J_k & L_k & 1 \end{Bmatrix}^2 \tag{5.6}$$

where the terms in the curly bracket represent the Wigner 6-j symbols (which are easily calculated with standard available codes [237]), and index a refers to the initial (lower) state of interest and k the final (upper) state. The double vertical lines, $\|$, enclosing the dipole moment operator, indicate the reduced dipole matrix element, which is independent of magnetic substates M_J, and squared is equal to the $J_a \rightarrow J_k$ line strength, $\mathcal{S}_{J_a,J_k}$. Note, this gives only a *relative* branching ratio between levels. To gain an absolute line strength we consider the decay from the upper level to all levels of the lower multiplet as a fraction of the total decay rate of the upper multiplet to the lower one. As state J_k can potentially decay to all J_a states within the $L_a S_a$ multiplet, we must normalise with respect to the sum of X_{ak} over all J_a states to obtain the absolute decay fraction to the state of interest. Using the following sum rule [195],

$$\sum_{J_a}(2J_a+1)(2J_k+1)\begin{Bmatrix} L_a & J_a & S_a \\ J_k & L_k & 1 \end{Bmatrix}^2 = \frac{2J_k+1}{2L_k+1} \tag{5.7}$$

we may write the branching ratio for the transition rates between fine structure states

$|L_a S_a J_a\rangle$ and $|L_k S_k J_k\rangle$ as,

$$b_{J_a J_k} = \frac{X_{ak}}{\sum_{J_a} X_{ak}} = (2J_a+1)(2L_k+1) \begin{Bmatrix} L_a & J_a & S_a \\ J_k & L_k & 1 \end{Bmatrix}^2 \tag{5.8}$$

which is valid in the LS-coupling approximation and,

$$\Gamma_{J_a J_k} = b_{J_a J_k} \Gamma_{L_a L_k}; \qquad \Gamma_{L_a L_k} = \sum_{J_k} \sum_{J_a} \Gamma_{J_a J_k} \tag{5.9}$$

where $\Gamma_{L_a L_k}$ is the transition rate from the lower $L_a S_a$ multiplet to the upper $L_k S_k$ multiplet. Due to the frequency dependence of the transition rate (see Eq. (3.52)) and the non-degeneracy of the fine structure states within each LS manifold, the branching ratio determined by Eq. (5.8) requires a slight modification to account for the deviation of the transition frequency away from the weighted average, $\omega_{L_a L_k} = (\overline{E_{L_k J_k}} - \overline{E_{L_a J_a}})/\hbar$, to which $\Gamma_{L_a L_k}$ corresponds. For example, consider the decay of the $5p^2\,{}^3\mathrm{P}_1$ state to the states of the $5s5p\,{}^3\mathrm{P}_J$ manifold, which contains the clock transition. The total decay rate from the state $5p^2\,{}^3\mathrm{P}_1$ is split amongst states of the lower manifold as,

$$\Gamma_{J_k L_a} = \Gamma_{{}^3\mathrm{P}_0} + \Gamma_{{}^3\mathrm{P}_1} + \Gamma_{{}^3\mathrm{P}_2} = \frac{2}{6\pi\epsilon_0 \hbar c^3} \underbrace{\left(\omega_{{}^3\mathrm{P}_0} \frac{12}{36} |d_{ak}|^2 + \omega_{{}^3\mathrm{P}_1} \frac{9}{36} |d_{ak}|^2 + \omega_{{}^3\mathrm{P}_2} \frac{15}{36} |d_{ak}|^2 \right)}_{\omega_{cm}^3 |d_{L_a L_k}|^2} \tag{5.10}$$

where the fractions 12/36, 9/36, and 15/36 are the branching ratios, and ω_{cm} is the centre-of-mass frequency, given by an average of the individual transition frequencies weighted by their branching ratio as,

$$\omega_{cm}^3 = \sum_{J_a} b_{J_a J_k} \omega_{J_a J_k}^3 \tag{5.11}$$

We must also consider the coupling strengths between specific magnetic components. This requires use of the well-known Wigner-Eckart theorem which relates the dipole matrix element of a transition between particular M_J components to the reduced dipole matrix element of the $J_a \to J_k$ transition times a coefficient determined by the Wigner 3-j symbol,

$$|\langle L_a S_a J_a M_a | \, d_{\mathcal{A}} \, | L_k S_k J_k M_k \rangle|^2 = \begin{pmatrix} J_a & 1 & J_k \\ -M_a & \mathcal{A} & M_k \end{pmatrix}^2 |\langle L_a S_a J_a || \mathbf{d} || L_k S_k J_k \rangle|^2 \tag{5.12}$$

where the degree of polarisation $\mathcal{A}$ is, as before, zero for linear and ± 1 for $\sigma^{\pm}$ circular polarisations respectively. We require the coupling strength of a particular M_a component to all M_k components of the parent J_k level. Again, the relative branching ratios must be normalised with respect to the total decay rate of each upper component divided amongst

each M_a component. Using the sum rule,

$$\sum_{M_a,\mathcal{A}} \begin{pmatrix} J_a & 1 & J_k \\ -M_a & \mathcal{A} & M_k \end{pmatrix}^2 = \frac{1}{2J_k+1} \tag{5.13}$$

we have the normalised magnetic branching ratio,

$$b_{M_a M_k} = \sum_{M_k,\mathcal{A}} (2J_k+1) \begin{pmatrix} J_a & 1 & J_k \\ -M_a & \mathcal{A} & M_k \end{pmatrix}^2 \tag{5.14}$$

We may now write a general expression for calculation of the dynamic polarisability as,

$$\alpha_a(\omega) = 6\pi\epsilon_0 c^3 \frac{\omega_{J_a J_k}}{\omega_{cm}^3(\omega_{J_a J_k}^2 - \omega_L^2)} b_{J_a J_k} b_{M_a M_k} \Gamma_{L_a L_k} \tag{5.15}$$

which is expressed in atomic units by multiplying through by the factor $1/(4\pi\epsilon_0 a_0^3)$. The static polarisability, $\alpha(0)$, can be found using Eq. (5.15) with $\omega_L = 0$. Before proceeding to calculate the clock state polarisabilities induced by our trapping field we make the following simplification. Our clock states are $J = 0$ with $M_J = 0$ and as discussed in Sec. 2.4.3.1 we require a linearly polarised (or π-polarised) light field. For these conditions the magnetic branching term evaluates to unity for all transitions and we may subsequently ignore it. To calculate the polarisabilities of the ground and excited clock states we first identify the main dipole transitions to which they couple (see Fig 3.1). The $5s^2\,{}^1\mathrm{S}_0$ ground clock state couples to all higher lying $5snp\,{}^1P_1$ states. The $5s5d\,{}^3P_0$ excited clock state involves levels of several terms, coupling to $5snd\,{}^3D_1$ and $5snd\,{}^3S_1$ states, and the doubly excited $4d^2\,{}^3P_1$ and $5p^2\,{}^3P_1$ states. Table. 5.1 contains details of the even parity states (clock state has odd parity, transition requires parity inversion) included in our polarisability calculation.

The ground state polarisability is dominated by the $5s^2\,{}^1S_0 \rightarrow 5s5p\,{}^1P_1$ transition which contributes at the 97 % level to the total static polarisability. Experimental work by Yasuda et al. [191] of photoassociation spectroscopy provides a value for the $5s5p\,{}^1P_1$ state lifetime of 5.263 ± 0.004 ns corresponding to an uncertainty 0.076 %. The remaining ${}^1P_1$ transition rates are less well known. Here we use the values determined by the work of Parkinson et al. as given in Ref. [223] which have stated uncertainties in the region of 10 % to 15 %. The $5s5p\,{}^3P_1$ state also contributes at a similar level to the higher lying ${}^1P_1$ states. The state lifetime has been measured in an atomic beam apparatus by directly observing fluorescence decay, providing a value of 21.3 ± 0.5 µs. An estimate of the total uncertainty of the $5s^2\,{}^1S_0$ polarisability for this calculation is ∼0.5 %.

Many of the transition rates from the $5s5p\,{}^3P_0$ excited clock state to higher lying states are taken from the theoretical work of Ref. [196] and where available experimental values have been included. Considering first the $5snd\,{}^3D_1$ states we start with the lowest lying $5s4d\,{}^3D_1$ state which dominates the static polarisability (and dynamic BBR shift,

$y = 18.43$ at 300 K, see Sec. 5.25). A measurement of the radiative lifetime of the $5s4d\,^3D$ multiplet, which decays only to the $5s5p\,^3P$ multiplet, has been made by Miller et al. as $2.9 \pm 0.2\,\mu s$. A theoretical value of $2.4\,\mu s$ is presented in the work of Porsev et al. [152] and here we adopt the mean value of the two. The $5s5d\,^3D_{1,2,3}$ state lifetimes have been measured by Andrä et al. with $\sim$1 % uncertainty, in close agreement several others measurements (see Table IX Ref. [196]), and the $5s5d\,^3D_1$ state lifetime is given as 16.49 ± 0.10 ns. A small fraction of this $^3D_1$ state decays to the $5s6p\,^3P$ manifold (see Ref. [196]) which is accounted for in the determination of the tabulated (Tab. 5.1) transition rate. Lifetime measurements of the higher lying ^3D states are available at the $\sim$5 % level but are complicated by the additional branching to higher lying ^3P states. Instead, the theoretical values of Werij et al. have been here used (Table IX Ref. [196]).

We next consider the $5sns\,^3S_1$ states. The transition to the first $5s6s\,^3S_1$ state dominates the dynamic polarisability induced by the clock probe light and magic wavelength optical lattice (Tab. 5.2) due to its proximity to wavelengths 698.4 nm and 813.4 nm, respectively. However, the spread in measured state lifetime data is large ($\sim$30 %). An estimate of the $5s5p\,^3P \rightarrow 5s6s\,^3S$ transition rate was obtained in Ref. [238] by treating Γ as a free parameter and fitting calculation to the observed Stark shift around the $^1S_0 \rightarrow {}^3P_1$ magic wavelength (at $\sim$914 nm). A transition rate of $85 \times 10^6\,s^{-1}$ was obtained [238], which is within the upper limit of previously reported measurements, although in $\sim$20 % disagreement with theoretical values reported in Ref. [196] and [152]. However, for calculations performed here we use the weighted mean value of experimental data presented in Werij et al. [196]. Several experimental values of the $5s7s\,^3S$ state lifetime are presented in Table VII Ref. [196] with a spread of around 15 %. Here we use the weighted mean state lifetime of 35.0 ns and the theoretical transition rate to the higher lying $5s6p\,^3P$ multiplet to arrive at the $5s5p\,^3P \rightarrow 5s7s\,^3S$ transition rate of $21.6 \times 10^6\,s^{-1}$ which is in good agreement with the theoretical value given in Ref. [152]. For the remaining higher lying $5sns\,^3S$ states we use the theoretical values of Werij et al. [196].

Finally we consider the doubly excited $5p^2\,^3P$ and $4d^2\,^3P$ states. Several experimentally determined lifetimes of the $4d^2\,^3P_{1,2}$ states are presented in Table XI Ref. [196]. The most precise of these is by Andrä et al. with a value of 7.89 ± 0.05 s for the $5p^2\,^3P_2$ state lifetime. Here we use the experimental $5p^2\,^3P$ state lifetime of 8.3 ns from Corliss and Bozman (presented in Ref. [196]). The rate for the $5s5p\,^3P_0 \rightarrow 4d^2\,^3P_1$ transition is taken as that listed in Ref. [223].

The results of the calculation are presented in Fig. 5.1 and in tabulated form in Tab. 5.2 for the individual intermediate state contributions. We find the magic wavelength for the red-detuned optical lattice at 809 nm and those blue-detuned at 389.9 nm and 360.7 nm in line with experimentally determined values [114]. Magic wavelengths also exist at 347 nm 339 nm although their proximity to neighbouring transitions and steep tuning sensitivity makes them undesirable for use.

The probe light induced clock shift can be estimated from the differential polarisability at the wavelength 698.4 nm and is presented in Sec. 3.8.1.2.

As a check of the completeness of the calculation we make use of the corresponding oscillator strengths and the Thomas-Kuhn sum rule which states,

$$\sum_k f_{ak} = N \tag{5.16}$$

where N is the number of valence electrons. The oscillator strength, f_{ak}, is related to the transition rate as,

$$f_{ak} = \frac{g_k}{g_a} \frac{2m_e \pi \epsilon_0 c^3}{e^2} \frac{\omega_{ak} \Gamma_{ak}}{\omega_{cm}^3} \tag{5.17}$$

where g_a and g_k are the degeneracy factors. For the calculation of the ground state polarisability we find $\sum_k f_{ak} = 1.98$, very close to the required $N = 2$, and the excited state $\sum_k f_{ak} = 1.57$. We may make the assumption that much of the remaining oscillator strength is due to the higher lying states heading into the continuum. In a crude approximation we lump these states at the first ionisation threshold and calculate the transition rate for the residual oscillator strength. Inclusion of this contribution moves the red-detuned magic wavelength by 42 nm to 853 nm. In a similar treatment to that carried out by Ido et al. described above, we can adjust Γ for the $5s5p\,^3P \rightarrow 5s6s\,^3S$ transition to obtain $\Delta\alpha(813.4\text{ nm}) = 0$ and estimate the $5s5p\,^3P \rightarrow 5s6s\,^3S$ transition rate to be $\sim 62 \times 10^6\,\text{s}^{-1}$, in some agreement with the measurement of Jönsson et al. [239]. In reality, however, the error may lie elsewhere, for example in an over estimate of the $5s4d\,^3D$ state lifetime, which if addressed would result in the magic wavelength being pulled towards lower wavelengths, strengthened by the reduced contribution at the ionisation threshold.

5.2 The Dynamic Stark Shift in a BBR Field

We may also estimate the BBR shift from our polarisability calculation. For this we consider the shift due to the dynamic polarisability induced by a component of the BBR-field, $\text{d}\langle \mathbf{E}^2 \rangle$, at angular frequency ω, and integrate over the entire spectrum as,

$$\delta\omega_a = -\frac{1}{2\hbar} \int_0^\infty \alpha(\omega) \text{d}\langle \mathbf{E}^2 \rangle \tag{5.18}$$

and with Eq. (5.2) this becomes,

$$\delta\omega_a = -\frac{1}{2\hbar} \frac{2}{\hbar} \sum_k |d_{ak}|^2 \int_0^\infty \frac{\omega_{ak}}{\omega_{ak}^2 - \omega^2} \text{d}\langle \mathbf{E}^2 \rangle \tag{5.19}$$

Table 5.1: Parameters for calculation of the clock state polarisabilities. Frequencies are in units of 10^{15} rad s^{-1}. All wavelengths are for in vacuum and derived from energy level data in Ref. [223]. Starred values, '*', are for $\Gamma_{J_a J_k}$ which includes the branching term (we set $b_{J_a J_k} = 1$ and $\omega_{cm} = \omega_{ak}$ in all calculations). Values with ω_{cm} inside parenthesis are for J_k to L_a and therefore require the branching term but $\omega_{cm} = \omega_{ak}$. Transition rates to the ionisation threshold are calculated from the residual oscillator strengths and are representative only of the remaining higher lying Rydberg states into the continuum (discussed in the text).

Clock state	Level	λ (nm)	ω_{ak}	$\Gamma_{L_a L_k}$ (10^6 s^{-1})	$b_{J_a J_k}$	ω_{cm}
$5s^2\,{}^1\mathrm{S}_0$	$5s5p\,{}^1\mathrm{P}_1$	460.862	4.087	190.0[a]	1	4.087
	$5s6p\,{}^1\mathrm{P}_1$	293.269	6.423	1.87[b]		6.423
	$5s7p\,{}^1\mathrm{P}_1$	257.024	7.329	5.3[c]		7.329
	$4d5p\,{}^1\mathrm{P}_1$	242.883	7.755	17[c]		7.755
	$5s8p\,{}^1\mathrm{P}_1$	235.504	7.998	18[c]		7.998
	$5s9p\,{}^1\mathrm{P}_1$	230.797	8.162	11.5[c]		8.162
	$5s10p\,{}^1\mathrm{P}_1$	227.592	8.276	6.6[c]		8.276
	$5s11p\,{}^1\mathrm{P}_1$	225.396	8.357	3.7[c]		8.357
$5s^2\,{}^1\mathrm{S}_0$	$5s5p\,{}^3\mathrm{P}_1$	689.449	2.732	0.0469*[d]	–	–
$5s^2\,{}^1\mathrm{S}_0$	1st ionisation	217.712	8.652	10.6	1	8.652
$5s5p\,{}^3\mathrm{P}_0$	$5s6s\,{}^3\mathrm{S}_1$	679.289	2.773	74.58[e]	1/9	2.701
	$5s7s\,{}^3\mathrm{S}_1$	432.766	4.353	21.6[f]		4.280
	$5s8s\,{}^3\mathrm{S}_1$	378.160	4.981	8.22[f]		4.909
	$5s9s\,{}^3\mathrm{S}_1$	355.446	5.299	4.53[f]		5.227
	$5s10s\,{}^3\mathrm{S}_1$	343.525	5.453	2.77[f]		5.411
$5s5p\,{}^3\mathrm{P}_0$	$5s4d\,{}^3\mathrm{D}_1$	2603.13	0.7236	0.381[g]	5/9	0.666
	$5s5d\,{}^3\mathrm{D}_1$	483.339	3.897	61'[h]		3.880
	$5s6d\,{}^3\mathrm{D}_1$	394.192	4.779	26.7[f]		4.761
	$5s7d\,{}^3\mathrm{D}_1$	363.018	5.189	14.2[f]		5.171
	$5s8d\,{}^3\mathrm{D}_1$	348.099	5.411	8.51[f]		5.394
	$5s9d\,{}^3\mathrm{D}_1$	339.326	5.551	5.51[f]		5.534
$5s5p\,{}^3\mathrm{P}_0$	$5p^2\,{}^3\mathrm{P}_1$	474.325	3.971	120[i]	1/3	3.917
$5s5p\,{}^3\mathrm{P}_0$	$4d^2\,{}^3\mathrm{P}_1$	330.753	5.703	59*[c]	–	–
$5s5p\,{}^3\mathrm{P}_0$	1st ionisation	316.309	5.955	9.77	1	5.955

[a] Exp. Ref. [191]
[b] Exp. by Parkinson et al. reported in Ref. [152]
[c] Ref. [223]
[d] Exp. Ref. [192]
[e] Weighted Av. of Exp. Ref. [196]
[f] Av. Theory and Exp. Ref. [196]
[g] Av. Exp. Ref. [240] and Theory Ref. [152]
[h] Exp. lifetime measurement Ref. [241]
[i] Exp. Corliss and Bozman presented in Ref. [196]

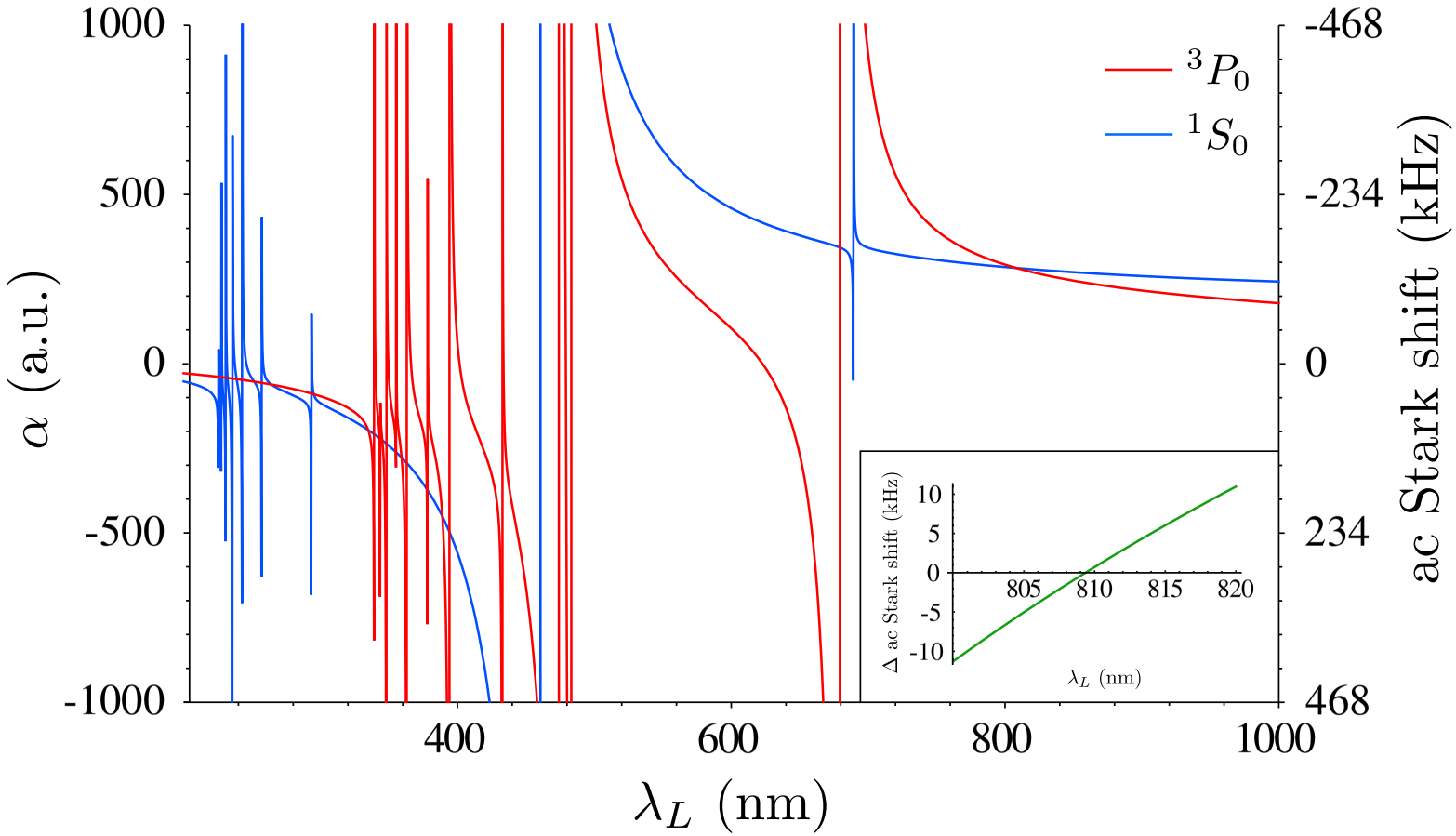


Figure 5.1: **Atomic dynamic polarisabilities** - Plot of the dynamic polarisabilities of ground (blue) and excited (red) clock states. Differential polarisability is shown (inset) for the region around the magic wavelength.

Table 5.2: Individual contributions (ICs) to the ground and excited clock state polarisabilities.. Frequencies are in units of $10^{15}\,\mathrm{rad\,s^{-1}}$. All wavelengths are for in vacuum and derived from energy level data in Ref. [223]. Polarisability due to the the residual oscillator strengths and are calculated at the ionisation threshold and are representative only of the remaining higher lying states into the continuum (discussed in the text).

Clock state	Level	λ (nm)	$\alpha(698.4\,\mathrm{nm})$		$\alpha(813.4\,\mathrm{nm})$		$\alpha(0)$	
			a.u.	%	a.u.	%	a.u.	%
$5s^2\,{}^1\mathrm{S}_0$	$5s5p\,{}^1\mathrm{P}_1$	460.862	329.03	95.72	273.58	97.74	185.74	97.25
	$5s6p\,{}^1\mathrm{P}_1$	293.269	0.36	0.11	0.34	0.12	0.30	0.16
	$5s7p\,{}^1\mathrm{P}_1$	257.024	0.58	0.17	0.56	0.20	0.50	0.26
	$4d5p\,{}^1\mathrm{P}_1$	242.883	1.46	0.42	1.41	0.50	1.28	0.67
	$5s8p\,{}^1\mathrm{P}_1$	235.504	1.35	0.39	1.31	0.47	1.20	0.63
	$5s9p\,{}^1\mathrm{P}_1$	230.797	0.79	0.23	0.77	0.27	0.71	0.37
	$5s10p\,{}^1\mathrm{P}_1$	227.592	0.43	0.12	0.42	0.15	0.38	0.20
	$5s11p\,{}^1\mathrm{P}_1$	225.396	0.23	0.07	0.22	0.08	0.21	0.11
$5s^2\,{}^1\mathrm{S}_0$	$5s5p\,{}^3\mathrm{P}_1$	689.449	9.02	2.62	0.82	0.29	0.23	0.12
$5s^2\,{}^1\mathrm{S}_0$	1st ionisation	217.712	0.49	0.14	0.48	0.17	0.44	0.23
$5s^2\,{}^1\mathrm{S}_0$	All	–	343.75	–	279.89	–	190.99	–
$5s5p\,{}^3\mathrm{P}_0$	$5s6s\,{}^3\mathrm{S}_1$	679.289	766.19	78.44	136.69	45.14	41.36	9.20
	$5s7s\,{}^3\mathrm{S}_1$	432.766	3.11	0.32	2.67	0.88	1.92	0.43
	$5s8s\,{}^3\mathrm{S}_1$	378.160	0.60	0.06	0.54	0.18	0.42	0.09
	$5s9s\,{}^3\mathrm{S}_1$	355.446	0.24	0.03	0.22	0.07	0.18	0.04
	$5s10s\,{}^3\mathrm{S}_1$	343.525	0.13	0.01	0.12	0.04	0.97	0.02
$5s5p\,{}^3\mathrm{P}_0$	$5s4d\,{}^3\mathrm{D}_1$	2603.13	-20.93	2.14	-29.19	9.64	269.79	60.03
	$5s5d\,{}^3\mathrm{D}_1$	483.339	77.95	7.98	62.79	20.73	40.62	9.04
	$5s6d\,{}^3\mathrm{D}_1$	394.192	11.51	1.18	10.25	3.39	7.85	1.75
	$5s7d\,{}^3\mathrm{D}_1$	363.018	4.11	0.42	3.74	1.24	3.00	0.67
	$5s8d\,{}^3\mathrm{D}_1$	348.099	2.02	0.21	1.86	0.61	1.52	0.34
	$5s9d\,{}^3\mathrm{D}_1$	339.326	1.16	0.12	1.07	0.35	0.89	0.20
$5s5p\,{}^3\mathrm{P}_0$	$5p^2\,{}^3\mathrm{P}_1$	474.325	84.82	8.68	69.24	22.87	45.70	10.17
$5s5p\,{}^3\mathrm{P}_0$	$4d^2\,{}^3\mathrm{P}_1$	330.753	19.59	2.01	18.21	6.01	15.21	3.38
$5s5p\,{}^3\mathrm{P}_0$	1st ionisation	316.309	26.26	2.69	24.59	8.12	20.87	4.64
$5s5p\,{}^3\mathrm{P}_0$	All	–	976.89	–	302.81	–	449.41	–

where the sum is over all intermediate states which are coupled to the state of interest by the BBR field. Details of the BBR field are contained within Planck's Radiation Law which describes the spectral radiance as a function of frequency and is related to the time averaged square of the electric field as,

$$\mathrm{d}\langle \mathbf{E}^2 \rangle = \frac{4\pi}{3}\frac{1}{\epsilon_0}\,\mathrm{d}u_{\mathrm{BBR}}(\omega, T_{\mathrm{env}}) = \frac{1}{3}\frac{\hbar}{\epsilon_0 \pi^2 c^3}\,\frac{\omega^3}{\exp\left(\frac{\hbar\omega}{k_{\mathrm{B}}T_{\mathrm{env}}}\right)-1}\mathrm{d}\omega \tag{5.20}$$

where $u_{\mathrm{BBR}}(\omega, T_{\mathrm{env}})$ is the radiation energy density (as in Eq. (2.13)). The factors 4π and $1/3$ account for the integration of the energy density over 4π steradians and the fact that the field is isotropic. The shift of level $|a\rangle$ is then,

$$\delta\omega_a = -\frac{1}{3\hbar\pi^2 c^3 \epsilon_0}\sum_k |d_{ak}|^2 \int_0^\infty \frac{\omega_{ak}}{\omega_{ak}^2-\omega^2}\,\frac{\omega^3}{\exp\left(\frac{\hbar\omega}{k_{\mathrm{B}}T_{env}}\right)-1}\,\mathrm{d}\omega \tag{5.21}$$

which we can write as [242],

$$\delta\omega_a = -\frac{1}{6\hbar\pi^2 c^3 \epsilon_0}\sum_k |d_{ak}|^2 \int_0^\infty \left(\frac{1}{\omega_{ak}+\omega}+\frac{1}{\omega_{ak}-\omega}\right)\frac{\omega^3}{\exp\left(\frac{\hbar\omega}{k_{\mathrm{B}}T_{env}}\right)-1}\,\mathrm{d}\omega \tag{5.22}$$

$$= -\frac{1}{6\hbar\pi^2 c^3 \epsilon_0}\left(\frac{k_{\mathrm{B}}T_{\mathrm{env}}}{\hbar}\right)^3 \sum_k |d_{ak}|^2\, F(y) \tag{5.23}$$

where the function $F(y)$ contains all details of the dynamic Stark shift dependence on the black-body spectral distribution as,

$$F(y) = \int_0^\infty \left(\frac{1}{y+x}+\frac{1}{y-x}\right)\frac{x^3}{\exp(x)-1}\,\mathrm{d}x \underbrace{\approx}_{|y|\gg 1} \frac{2\pi^4}{15y}+\frac{16\pi^6}{63y^3} \tag{5.24}$$

with,

$$y = \frac{\hbar\omega_{ak}}{k_{\mathrm{B}}T_{env}} \qquad\qquad x = \frac{\hbar\omega}{k_{\mathrm{B}}T_{env}} \tag{5.25}$$

The numerical integration of F(y) is presented in Ref. [242] from which the influence of the BBR field in relation to the energy of the transition from the state of interest to the coupled intermediate state can be determined. For low values of y (< 2.616) the function is negative, corresponding to an attraction of the state of interest, i.e., a positive Stark shift. Thereafter the function is positive (the usual region for optical wavelengths) resulting in a negative shift. At the point $y = 2.616$ the net influence of the BBR field results in a zero Stark shift. Substituting the matrix element for the transition rate (using Eq. (3.52)) we

arrive at the expression for the BBR induced frequency shift,

$$\delta\nu_a^{\mathrm{BBR}} = -\frac{3}{4\pi^2}\left(\frac{k_{\mathrm{B}}T_{\mathrm{env}}}{\hbar}\right)^3 \sum_k \frac{b_{J_aJ_k}\Gamma_{L_aL_k}}{\omega_{cm}^3} F(y) \tag{5.26}$$

As the field is unpolarised, containing all components of $\mathcal{A} = 0, \pm 1$, the magnetic branching factor $\sum_k b_{M_aM_k} = 3$ for all considered transitions and has been included in the above expression (this cancels with the previous factor 1/3 included to account for the isotropic nature of the field).

We may separate the BBR shift into static, $\delta\nu_a^{\mathrm{stat}}$, and dynamic, $\delta\nu_a^{\mathrm{dyn}}$, contributions such that,

$$\delta\nu_a^{\mathrm{BBR}} = \delta\nu_a^{\mathrm{stat}} + \delta\nu_a^{\mathrm{dyn}} \tag{5.27}$$

For the static case, setting $\omega = 0$, the value of x vanishes and $F(y) = 2\pi^4/15y$ and we have,

$$\delta\nu_a^{\mathrm{stat}} = -\frac{\pi^2}{10}\left(\frac{k_{\mathrm{B}}T_{\mathrm{env}}}{\hbar}\right)^4 \sum_k \frac{b_{J_aJ_k}\Gamma_{L_aL_k}}{\omega_{cm}^3\omega_{ak}} \tag{5.28}$$

$$= -\frac{1}{2h}\alpha_a(0)c_1T^4 \tag{5.29}$$

where c_1 is as given in Eq. (2.13). The dynamic contribution is then given by the remaining terms for which we replace the function $F(y)$ in Eq. (5.26) with $G(y)$ given by,

$$G(y) = \int_0^\infty \left(\frac{1}{y+x} + \frac{1}{y-x} - \frac{2}{y}\right) \frac{x^3}{\exp(x)-1}\,\mathrm{d}x \underbrace{\approx}_{|y|\gg 1} \frac{16\pi^6}{63y^3} \tag{5.30}$$

For the BBR shift written in the form of Eq. (2.14) we find the parameter η_j as,

$$\eta_j = -\frac{2h}{c_1T^4\alpha_a(0)}\frac{3}{4\pi^2}\left(\frac{k_{\mathrm{B}}T_{\mathrm{env}}}{\hbar}\right)^3 \sum_k \frac{b_{J_aJ_k}\Gamma_{L_aL_k}}{\omega_{cm}^3} G(y) \tag{5.31}$$

$$\approx \frac{120\pi^2}{63}\left(\frac{k_{\mathrm{B}}T_{\mathrm{env}}}{\hbar\omega_{ak}}\right)^2 \tag{5.32}$$

Using the data presented in the previous section, the BBR shift at 300 K has been calculated for the ground and excited clock states. A more complete evaluation should also take into acount the interaction of the core electrons with the radiation field. The polarisability can be divided into two parts as,

$$\alpha(\omega) = \alpha^v(\omega) + \alpha^c(\omega) \tag{5.33}$$

where the superscripts v, and c refer to interactions due to valence electrons, and core

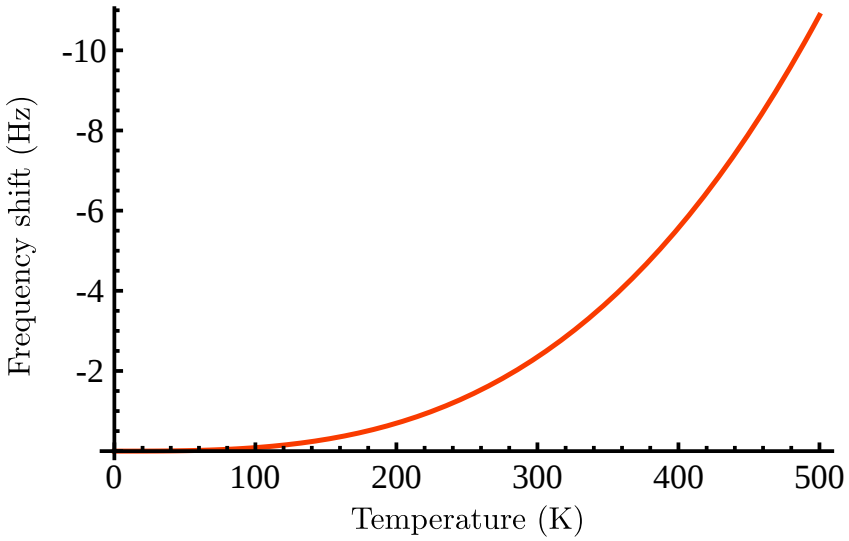


Figure 5.2: **BBR shift.** - Blackbody radiation shift of the $5s^2\,{}^1S_0 \rightarrow 5s5p\,{}^3P_0$ Sr clock transition.

electrons respectively. In Sr this core interaction is evaluated to be 5.4 au and is approximately equal for both ground and excited states [151]. Including this in the BBR shift estimation of the clock transition we find the total dynamic shift of the ground and excited states, at 300 K, to be,

$$\delta\nu_g^{\mathrm{BBR}} = -1.690 \pm 0.008\,\mathrm{Hz} \tag{5.34}$$

$$\delta\nu_e^{\mathrm{BBR}} = -4.039 \pm 0.810\,\mathrm{Hz} \tag{5.35}$$

with overall shift,

$$\delta\nu^{\mathrm{BBR}} = -2.349 \pm 0.818\,\mathrm{Hz} \tag{5.36}$$

in good agreement with results obtained in a rigorous ab initio theoretical treatment by Porsev et al. [151]. Here, we obtain static polarisabilities for the ground and excited clock states of 196.4 a u and 454.8 a u , as tabulated in Tab. 5.3, in good agreement with the accepted literature values of 197.2 a u and 458.3 a u [151]. The corresponding static BBR shift is,

$$\delta\nu_g^{\mathrm{stat}} = -1.687 \pm 0.008\,\mathrm{Hz} \tag{5.37}$$

$$\delta\nu_e^{\mathrm{stat}} = -3.907 \pm 0.810\,\mathrm{Hz} \tag{5.38}$$

with overall shift,

$$\delta\nu^{\mathrm{stat}} = -2.220 \pm 0.818\,\mathrm{Hz} \tag{5.39}$$

Table 5.3: Calculated polarisabilities of key optical wavelengths. Angular frequencies are in units of $10^{15}\,\mathrm{rad\,s^{-1}}$ and polarisabilities are given in atomic units.

λ (nm)	ω	$\alpha(5s^2\,{}^1S_0)$	$\alpha(5s5p\,{}^3P_0)$	Comment
698.4	2.697	343.3	946.9	including continuum
813.4	2.316	279.9	299.8	including continuum
808.8	2.331	281.4	304.7	including continuum
808.8	2.331	280.9	280.9	excluding continuum
848.5	2.222	269.6	269.6	including continuum
–	0	191.0	449.4	sum of ICs[a]
–	0	196.4	454.8	inc. α^c and continuum

[a] 'IC' refers to individual contributions from states listed in Tab. 5.1.

These differ by 0.17 % and 3.26 % from the dynamic terms, respectively, corresponding to dynamic contributions of $-2.795\,\mathrm{mHz}$ and $-131.4\,\mathrm{mHz}$. Due to the high energy of states coupling to the ground state the dynamic contribution is small and approximates well the static polarisability, with the transition to the lowest lying $^1P_1$ state accounting for 99 % of this dynamic term. The quoted uncertainty in the ground state shift is derived from the measurement uncertainties of the transition rates, as discussed above. As is clear from Tab. 5.2 the ground state polarisability is dominated by the lowest lying $^1P_1$ state which contributes at 97 % and has a small measurement uncertainty of <0.1 %. The considered states also form over 99 % of the expected total oscillator strength suggesting the completeness of the calculation is satisfactory.

The story is a little different for the excited state. The relatively low energy transition to the $5s4d\,{}^3D_1$ state at 2.6 µm contributes a significant dynamic component, accounting for ∼97.6 % of the excited state dynamic term. Due to the lack of convincing literature values for several transition rates, the excited state estimated uncertainty is significantly larger. Here, there are four main contributing transitions, as highlighted in Tab. 5.2. Above all, the $5s5p\,{}^3P_0 \rightarrow 5s4d\,{}^3D_1$ transition dominates accounting for around 60 % of the total polarisability. As a rough estimate we have used the spread in the two transition rates used here to obtain an uncertainty of around 20 %. This is deliberately conservative to account for errors arising due to the neccessary calculation of branching ratios and the crude inclusion of the significant remainder (∼21.7 %) of oscillator strength at the ionisation threshold.

To reduce the uncertainty of our calculated BBR shift it seems logical to carry out further experimental work to lower the uncertainty of relevant transition rates. For this, focus

should be first given to the $5s5p\,^3P_0 \rightarrow 5s4d\,^3D_1$ transition as this currently dominates the uncertainty evaluation. Of next importance is determination of the $5s5p\,^3P_0 \rightarrow 5s6s\,^3S_1$ transition rate, as the experimental data currently has a large spread. Perhaps a refinement of this value can be obtained from improved measurements of the probe light induced frequency shift at 698.4 nm, as this state accounts for ∼78 % of the excited state shift here, combined with the constraint of the 813.4 nm magic wavelength. An alternative, or supplementary approach, is to measure directly the atomic polarisability. The static (dc) polarisability can be measured by observing the clock transition frequency shift of atoms when exposed to a strong dc electric field. Many such experiments have been carried out for Cs, amongst others, and work is currently being undertaken at PTB for Sr [154] and at NIST for Yb [243] to determine the static polarisability with a high precision [244]. It is expected that an experimental uncertainty of 7×10^{-4} should be achievable [154] corresponding to a fractional frequency uncertainty of 4×10^{-18} for the static contribution. The uncertainty in the calculated BBR shift arising due to measured transition rates is then reduced to the remaining dynamic contribution, which even for our extremely conservative error estimation corresponds to a fractional frequency uncertainty of 6×10^{-17}. Refinement of the $5s5p\,^3P_0 \rightarrow 5s4d\,^3D_1$ transition rate to an uncertainty of a few percent will then provide a total fractional frequency uncertainty of the BBR shift coefficient below 10^{-17}. Finally, a direct measure of the BBR shift may provide additional confidence in the derived value, as discussed in the following section.

5.3 Measurement of the BBR shift

The T^4 dependence (to first approximation) of the BBR-induced clock frequency shif offers a healthy leverage for determination of the BBR shift coefficient when measured at an elevated temperature. We propose to measure directly this shift in a differential measurement scheme which periodically alternates between "hot" and "cold" BBR environments. The key idea is to employ an optical lattice with long Rayleigh range to provide optical transport of the atomic ensemble into either of two measurement chambers (or BBR tubes) with well-defined but contrasting black-body environments. The delta BBR shift will be directly indicated by the offset observed between clock frequencies measured in each BBR tube, which can be determined without an optical frequency comb by monitoring the clock laser AOM frequency. A similar scheme using a single cryogenic tube (to effectively null the shift) is underway at PTB [154] and a mechanical translation of the magic wavelength optical lattice is achieved. We opt here to use an optical transport system for reasons of superior speed and mechanical simplicity. The vacuum apparatus, including BBR measurement tubes, is shown in Fig. 5.3.

Due to the difficulty in achieving high optical intensities and sufficient Rayleigh range (to ensure sufficient confinement away from beam waist minimum) with laser sources at

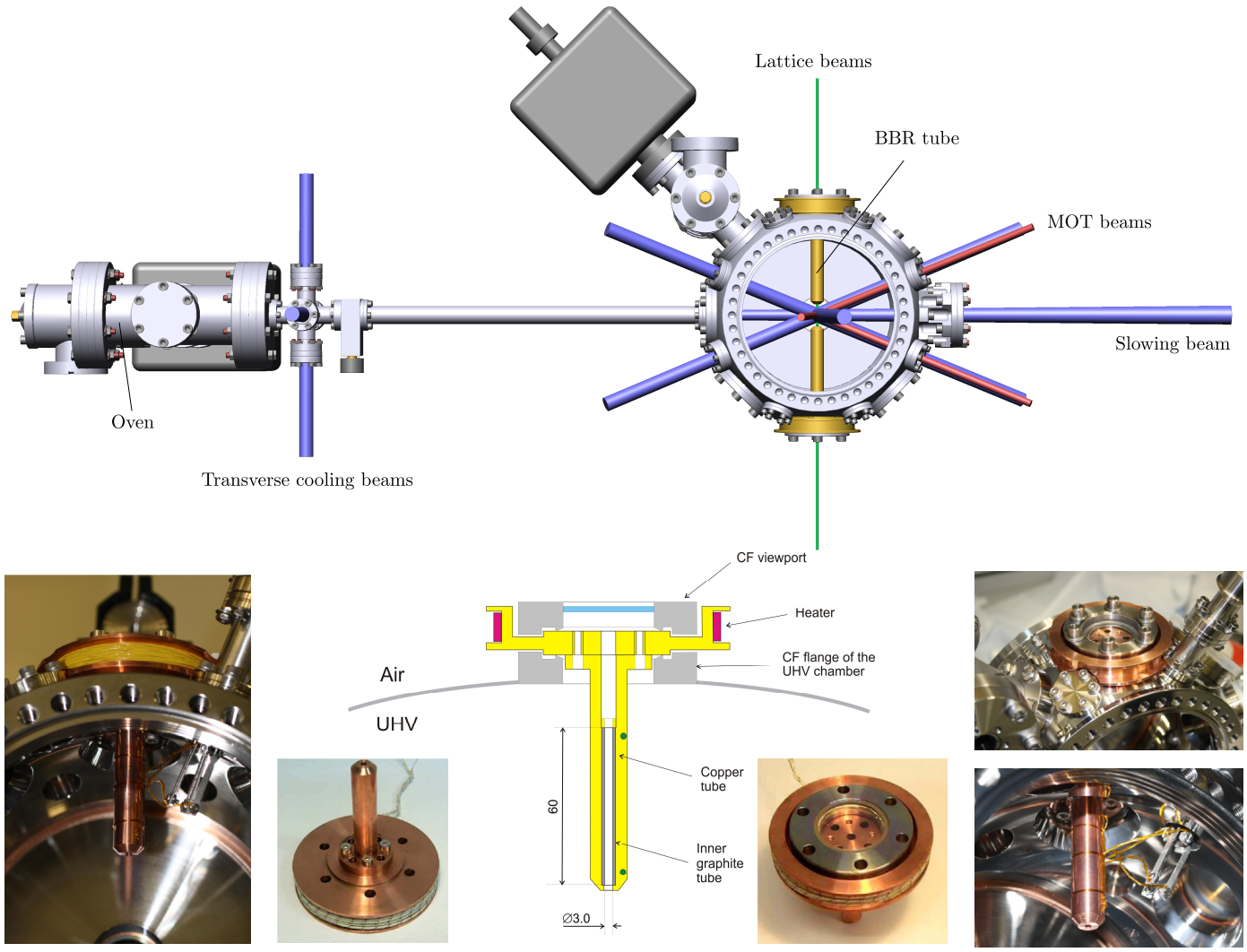


Figure 5.3: **Experiment apparatus for measurement of the BBR shift.** - (Top) A render of the vacuum apparatus with the side flange of the main chamber removed for viewing. (Bottom left/right) Photographs of the assembled BBR tube. (Bottom centre) Schematic of the BBR tube arrangement in cross section.

Table 5.4: Suggested lattice trapping parameters for transport and magic lattices.

λ (nm)	Waist w_0 (μm)	Rayleigh range z_R (cm)	Power P, (W)	State	Trap depth (E_R)	Trap depth (μK)	Scattering rate (s^{-1})
532	200	23.6	3.0	$^1S_0$	84	32	0.51
				$^3P_0$	54	21	0.01
813	50	0.97	0.3	$^1S_0$	117	19	0.03
				$^3P_0$	117	19	0.01

813 nm, we have elected to use a transport optical lattice at 532 nm provided by a 10 W Verdi laser. The decreased detuning of this lattice from the main coupled transitions also leads to an enhancement in trap depth, by factors 2.68 and 1.73 for ground and excited states respectively, in comparison to the 813 nm lattice for equivalent trapping intensity. The clock interrogation must take place with magic trapping and so requires transfer of the transported atoms to the waist of the 813 nm lattice for the duration of the clock interrogation, and then back to be transported out of the tube for clock readout fluorescence imaging. The position of the magic lattice waist must be periodically alternated between BBR measurement tubes, as required, which we aim to achieve with a simple mechanical translation of an optical delay path. The simplified optics schematic is shown in Fig. 5.4. The beam waist of the magic lattice is chosen at 50 μm to provide sufficient trap depth for the available 300 mW one way optical power (without complications of a lattice enhancement cavity). A 200 μm waist is suggested for the transport lattice to give a Rayleigh range of ∼24 cm. These lattice parameters are listed in Tab. 5.4 with corresponding trapping potential and scattering rate for ground and excited clock states.

The lattice is accelerated by imparting a relative frequency shift between opposing lattice beams which is controlled with double passed AOMs and the transport velocity given by,

$$v_{trans} = \frac{\lambda}{2}\Delta\nu \tag{5.40}$$

A linear acceleration of $40\,g$ is suggested, moving the atoms to a peak velocity of $\sim 4\,\mathrm{m\,s^{-1}}$ in 10 ms and back to rest in a further 10 ms over a distance of ∼5 cm. Fig. 5.5 shows the trapping potential modified by a $40\,g$ acceleration.

The operational measurement cycle is:

1. Collect and cool atoms in the chamber centre (blue and red MOTs)
2. Load atoms into 532 nm transport optical lattice
3. Shuttle atoms into BBR measurement tube 1
4. Transfer to 813 nm magic optical lattice

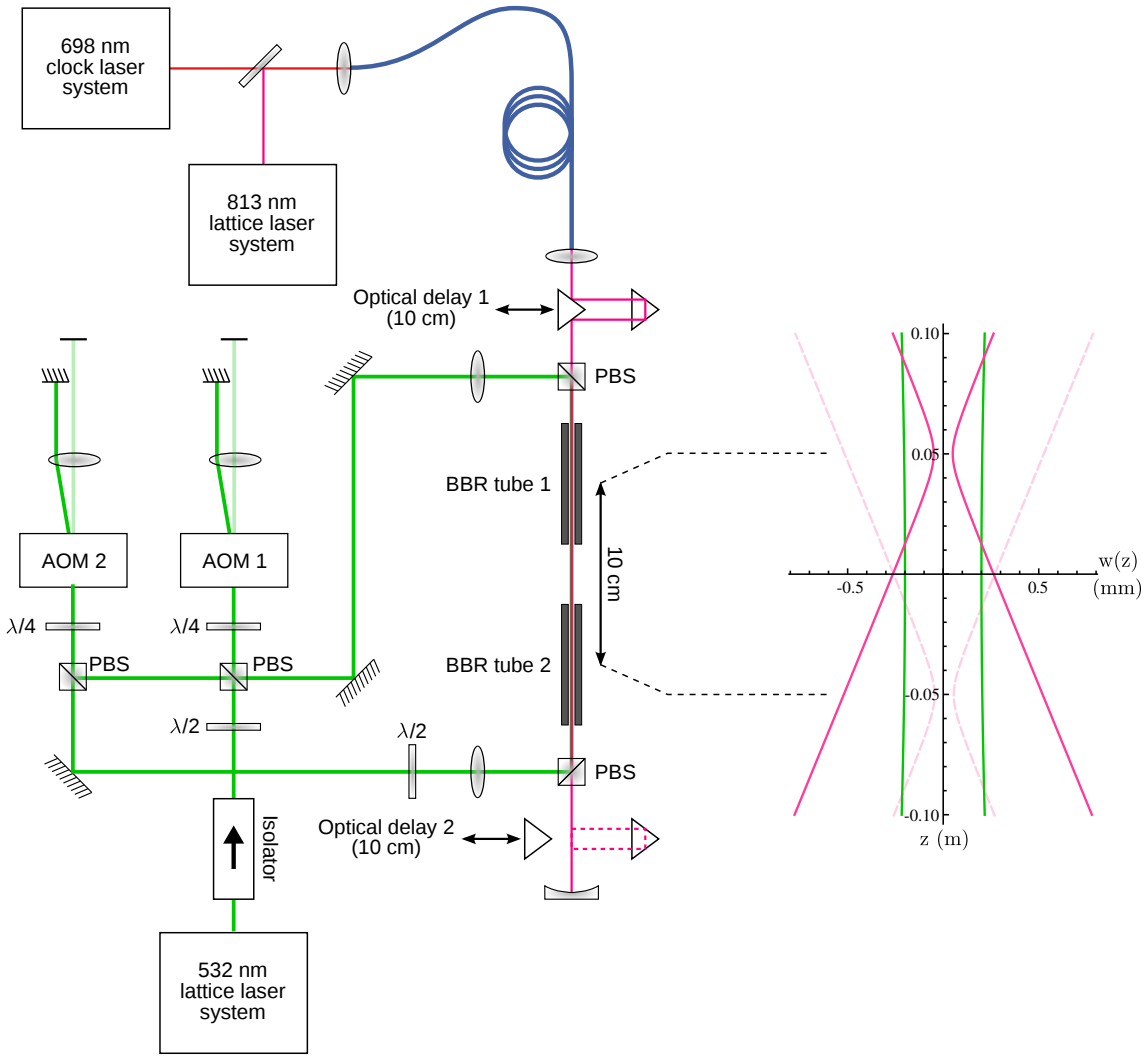


Figure 5.4: **Optics schematic of transport and magic lattices.** - Optical delay paths are mechanically translated to position the waist of the magic lattice and clock laser beams in either of the BBR measurement tubes. Atoms loaded into the transport lattice are shuttled into and out of BBR tubes by controlling (with AOMs 1 and 2) a travelling wave component of the standing wave

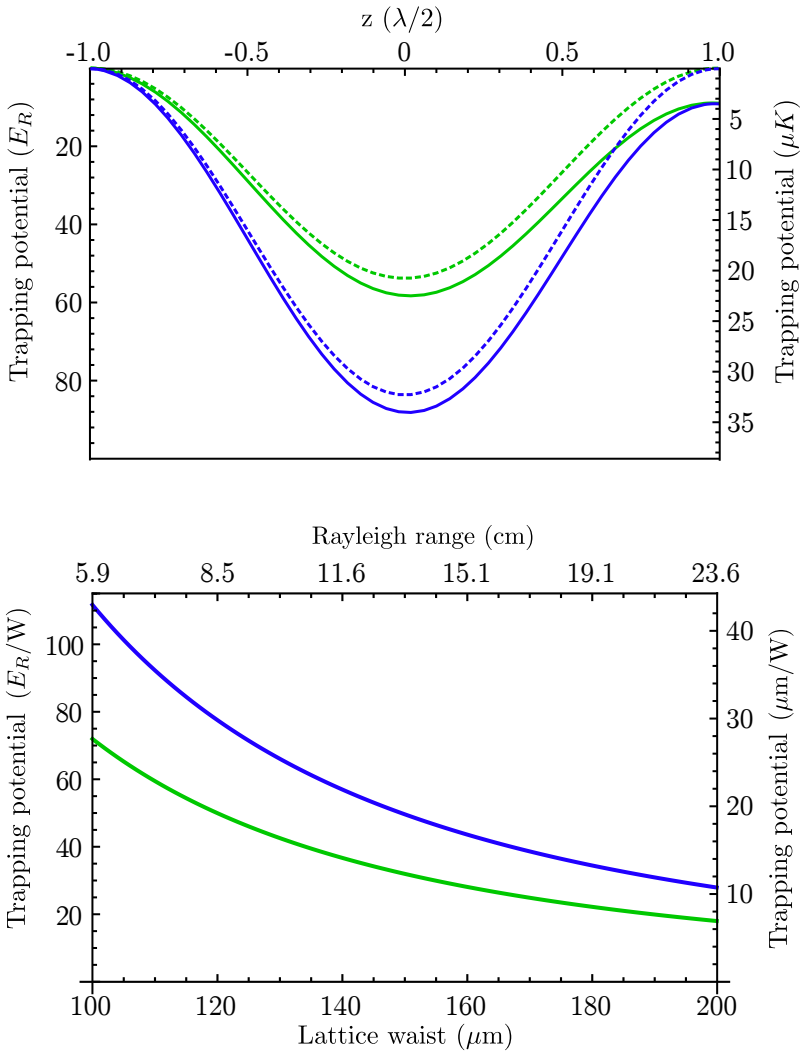


Figure 5.5: **Transport optical lattice potential.** - (Top) Ground and excited clock state trapping potentials of 532 nm optical lattice with 3 W one-way optical power and 200 µm waist; for 40 g accelerated lattice (solid lines), and stationary lattice (dotted lines). (Bottom) Trap depth and Rayleigh range versus beam waist.

5. Interrogate clock transition
6. Transfer back to 532 nm transport optical lattice
7. Shuttle atoms out of BBR tube into to the chamber centre
8. Readout the clock excitation fraction

- After "N" cycles move 813 nm and 698 nm beam waists and transport into BBR measurement tube 2 and carry out the same procedure for another "N" cycles. The number of cycles in each tube, "N", should be adjusted as necessary to provide best results of the two tube comparison.

A possible simplification could arise from using a single zero order Bessel beam optical lattice at 813 nm which has a central radial intensity distribution which does not vary with position along z, allowing sufficient trapping conditions to be maintained over long distances with modest lattice power. Long one-way transport distances of up to 20 cm have been demonstrated for ultra-cold Rb and return-trips distances of 20 cm achieved for a Rb BEC, maintaining a significant condensed fraction on return [245]. A further simplification could come from adopting the non-destructive clock readout technique developed at SYRTE [125, 246]. Here, neither fluorescence or absorption imaging is used, but a phase detection technique which exploits the phase shift experienced by near resonant light interacting with an atom in a particular atomic state (depending on the detection transition used). A weak measurement beam propagating co-linearly with the optical lattice, which forms one leg of a Mach-Zender interferometer, accumulates a phase shift depending on the atomic sample and is mixed with an unshifted local oscillator beam. The optical access requirements allow clock readout to occur without transport back out of the BBR tube. Furthermore, the measurement cycle of subsequent clock interrogation cycles can be improved further if sufficient non-destructive measurement is achieved, such that collection and cooling processes are not required for each cycle and the existing atomic sample can be re-used [246].

The BBR tubes are machined from OHFC copper (which has high thermal conductivity) and are constructed in two parts: 1) the BBR measurement tube, and 2) the heater feedthrough, which are screwed together. A standard 2.75″CF packaged viewport is used for the lattice and is mounted on top of the heater feedthrough which serves as the CF copper gasket. The heater feedthrough/gasket has been repeatedly cycled from room temperature to ∼470 K and back with no detected leak at 1×10^{-11} mbar helium partial pressure, and required no additional tightening. To ensure a good black body it is essential to achieve a high emissivity of the inner tube surface. We opt here to use a graphite tube insert which has emissivity >0.96 depending on surface finish. The graphite was prepared for vacuum by baking under vacuum at ∼670 K for several days to remove contaminants. Type E thermocouples (calibrated to within ±0.1 K absolute) are attached at the tip and base of the BBR tube. At present the experimental chamber contains a

single "test" tube, as the final tube design is yet to be achieved.

Our target measurement inaccuracy is determined as follows. In an asynchronous differential frequency measurement we may expect to reach a relative instability approaching $\sim 1 \times 10^{-16}$ at $\sim 1000\,\mathrm{s}$ [73]. For tubes of temperature 300 K and 400 K the expected BBR shifts are $-2.354\,\mathrm{Hz}$ and $-7.440\,\mathrm{Hz}$, respectively, with differential shift of magnitude $5.086\,\mathrm{Hz}$, or 1.185×10^{-14} in fractional units. The BBR quenching rate at 400 K leads to an estimated excited clock state lifetime of $\sim 20\,\mathrm{s}$, which presents no problem. Assuming the absolute temperature is stable and known to within $\sim 0.1\,\mathrm{K}$ and the tube geometry sufficiently suppresses external influence, the target measurement inaccuracy for the BBR shift coefficient is thus at 2×10^{-17} in fractional units.

6

Conclusions and Outlook

It is the aim of this thesis to describe in general terms the development of a Sr optical lattice clock apparatus, giving consideration to the parameters of operation and required technologies. I report the majority of work completed on the Sr optical lattice clock experiment at the National Physical Laboratory (NPL), to date, since its beginnings in 2007. In this time, the lab has developed from an empty optical table in "Building 3" on the old site of NPL, to the capable mass of equipment it is now, moved into a new lab on the 'new' site of NPL. A highlight of the work to date is a novel permanent magnet Zeeman slower for Sr, which has been designed, constructed, and characterised, and which provides a simple alternative to the conventional solenoid Zeeman slower. The initial Sr experiment vacuum system constructed incorporated a 2D deflection MOT chamber to guide atoms out of the atomic beam into a small measurement chamber. However, due to a change in the plans regarding measurement of the BBR shift this has been abandoned in place of a vacuum system with capability to measure directly the BBR shift. Many hours have been invested in development and construction of multiple laser systems and associated control electronics, required for clock operation, and represents a large chunk of the work carried out so far on the project.

In a broader view, Sr offers an attractive prospect for laser cooling experiments owing to its simple, yet enriched, level structure, which may be accessed in the most part with conventional diode laser technology. In recent years Sr has gained huge popularity throughout the frequency metrology community, and also further afield in studies of ultra-cold gases [247, 248], cold molecules [249], and in studies of Rydberg atoms [250]. Sr optical lattice clocks, operational in laboratories around the world, have demonstrated agreement at the level $<1 \times 10^{-15}$ and are growing in abundance, providing a great chance for further corroboration. A current topic of interest, and some dispute, concerns the investigation of ultra-cold collisions [251]. Recently, atomic interaction sidebands of the clock transition have been observed with high-precision spectroscopy of well-confined ultra-cold ^{87}Sr [252], which highlights the amazing precision of these apparatus. Through further understanding and control of the cold collision shift and knowledge of the BBR shift, Sr

should have no trouble reaching fractional frequency uncertainties at the 10^{-17} level and beyond, which challenges the performance of leading ion optical clocks. A departure from Sr to atoms such as Hg (with reduced intrinsic field-sensitivity) may prove necessary to secure the future of optical lattice clocks. Ultimately, such a standard may be best placed to serve as an intermediate reference for an ion clock of superior accuracy, exploiting the stability of the many-atom lattice clock. However, much work, in particular regarding optical oscillators, still lies ahead to fully realise the exceptional short term stability of the lattice clock. Finally, if one is really keen to make an exceptional clock one might consider pursuing the radio isotope 229-Thorium [253], which possesses a very intriguing nuclear transition in the optical domain (with expected wavelength around 160 nm).

Appendix A

.1 Flow characteristics

.1.1 Beam flux and angular spread

The nature of the flow, defined by collisions within the beam (in particular, in and surrounding the nozzle) can be characterised by the Knudsen number,

$$Kn = \frac{\tilde{\lambda}}{w} \tag{1}$$

where $\tilde{\lambda} = 1/(n\sigma\sqrt{2})$ is the interatomic collisional mean free path[1], σ is the interatomic elastic collisional cross-section, and w is the relevant physical length scale. For the condition $\tilde{\lambda} \gg w$ ($Kn \gg 1$), where w represents the characteristic dimension of the source aperture (for a slit this is simply its width), the flow through the aperture is relatively void of interatomic collisions and molecular effusion, also termed free molecular or Knudsen flow, ensues. At higher source densities, $\tilde{\lambda}$ is eventually reduced below w and gas–gas collisions lead to a viscous flow regime ($Kn \ll 1$), described in the framework of hydrodynamics.

For the simple case of an aperture of negligible thickness and moderate source pressure, such that molecular effusion occurs, the aperture approximates a cosine-emitter. The number of atoms effusing from the source per second in a solid angle $\mathrm{d}\Theta$ at angle θ to the

[1] $\tilde{\lambda}$ is derived from a simple "billiard ball" model of particle collisions. For a particle approximated by a hard sphere with diameter d, a collision with an identical particle occurs when particle centres are separated by twice their radius. The collision boundary or collisional cross section is then $\sigma = \pi d^2$. A particle travelling with velocity $\tilde{v}$ sweeps out a volume $\tilde{v}\sigma$ per second. In a unit volume V, occupied by N particles, the number of collisions per second is then given by $z = n\tilde{v}\sigma$, where $n = N/V$. As other particles in the volume are also moving we must transform into the two-body reduced mass frame and consider the relative particle motion. We replace mass in Eq. 3.4 (for $\tilde{v}$) with the reduced mass m/2 (for identical particles). The average distance between collisions, or mean free path, is then given by $\tilde{v}/z = \tilde{\lambda}$.

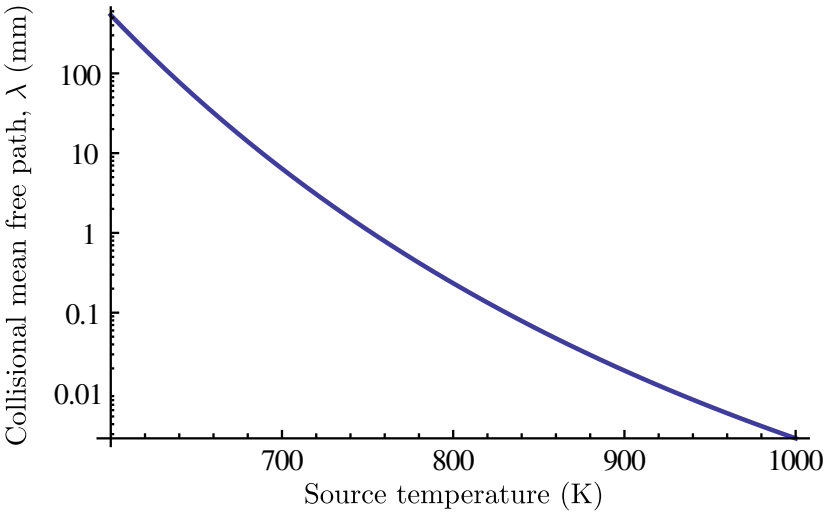


Figure 1: **Sr collisional mean free path versus source temperature** - ^{88}Sr – ^{88}Sr interatomic collisional mean free path. Collisional cross section data taken from Ref. [198]

normal of the plane of the aperture is [173],

$$\mathrm{d}F = \frac{\mathrm{d}\Theta}{4\pi}\, n_0 \tilde{v} A_s \cos\theta \tag{2}$$

where A_s is the area of the source aperture, $\tilde{v}$ the mean source velocity, and n_0 the particle density at entry to the source exit. The total flow rate, or flux, F_{tot}, is then found by integrating $\mathrm{d}F$ over a 2π solid angle in the forward direction (taking Θ as $2\pi \sin\theta\, d\theta$ and integrating over $\mathrm{d}\theta$ from 0 to $\pi/2$), which gives,

$$F_{tot} = \frac{1}{4}\, n_0 \tilde{v} A_s \tag{3}$$

For a circular channel nozzle of non-negligible length (thickness) L and radius r, direct escape trajectories are increasingly constrained with decreasing r/L, resulting in a beam with higher collimation, such that the total atomic flux is diminished for a given axial beam intensity. In addition, assuming diffuse scattering[1] throughout the channel, such that the cosine law describes the angular distribution of atoms leaving the channel wall following an atom–wall collision [254], the total transmission probability, W, of an atom which enters the nozzle later emerging in the forward direction at the nozzle exit, depends only on the nozzle geometry [255]. For a circular channel nozzle, with $L > r$, the so-called

[1] In contrast to reflection, where reflection refers to atom–wall interactions with characteristics of emergence dependent on the incident collision.

Clausing factor is found to be [255],

$$W \approx \frac{8r}{3L}\left(1+\frac{8r}{3L}\right)^{-1} \tag{4}$$

The resulting atomic flux, which holds for $\tilde{\lambda} \gtrsim L$, where gas–gas collisions are negligible throughout the nozzle, is then given by [173],

$$F_{tot} = W\,\frac{1}{4}\,n_0\tilde{v}A_s \tag{5}$$

which in the limit $L \gg r$ is,

$$F_{tot} \approx \frac{2\pi}{3}\,\frac{n_0\tilde{v}r^3}{L} \tag{6}$$

and the axial peak beam intensity $I(0)$, where $I(\theta)$ is the atomic flux per steradian at angle θ (in radians) to the central beam axis,

$$I(0) = \frac{1}{4\pi}\,n_0\tilde{v}(\pi r^2) \tag{7}$$

The angle $\theta_{1/2}$, satisfying $I(\theta_{1/2}) = I(0)/2$, is the beam full-width half-maximum (FWHM) and is useful in characterising the beam divergence, given as [256],

$$\theta_{1/2} = 1.68\,\frac{r}{L} \tag{8}$$

To ease the comparison of channels in different operating conditions it is useful to introduce the peaking factor κ, which normalises the axial beam intensity to the total flow rate as,

$$\kappa = \pi(I(0)/F_{tot}) \tag{9}$$

where the factor of π ensures $\kappa = 1$ for a cosine emitter. The a circular channel nozzle and free molecular flow $\kappa = W^{-1}$. Highly collimated beams are most efficiently created with use of multi-channel nozzle arrays, each with $\kappa \gg 1$ and $L \lesssim \tilde{\lambda}$, where the beam is formed by a superposition of channel flow. It is often desirable to further collimate the beam with an aperture(s) downstream of the source. The axial beam flux, F_a, flowing through an aperture of area A_a at a distance l_a from the source, with $l_a \gg A_a$, is given

by,

$$F_a = \frac{A_a}{l_a^2} I(0) \tag{10}$$

As previously described, two distinct flow regimes, molecular and viscous, are reached depending on the relative dimensions of the source aperture and collisional mean free path (which is a function of the source density, or pressure). In addition, for a circular channel nozzle with characteristic dimensions, length, L, and radius, $r \ll L$, two flow sub-regimes are present within the limits of molecular flow [256],

$$\text{I) Transparent :} \qquad \tilde{\lambda} \gg L \tag{11}$$

$$\text{II) Opaque :} \qquad L \gg \tilde{\lambda} \gg r \tag{12}$$

For the case of transparent flow (for which the above results apply) both the total flux, F, and peak beam intensity, $I(0)$, are proportional to the pressure differential either side of the connecting channel, of conductance C, such that [257],

$$F = C(P - P_{chmbr}) \approx CP \tag{13}$$

and the beam shape and conductance are given simply by the geometrical constraints of the nozzle (a constant), as governed by gas–wall collisions [255].

At higher source pressures, where the probability of an atom passing through the length of the channel without collision is negligible, the opaque flow regime is reached. The total flux remains proportional to source pressure and C remains a constant, however, the beam shape is modified by gas–gas collisions within the nozzle and the peak intensity is no longer proportional to P. We may consider the resulting flow in three contributions, as described by Beijerinck and Verster [258].

i) At large angles of θ the intensity distribution is determined primarily by the gas–wall collision rate near the end of the channel, and remains as in the transparent regime.

ii) As θ decreases towards zero we gain an increasing contribution from atoms scattered into this direction by gas–gas collisions. Those which escape into this direction following a gas–wall collision near the channel entry are increasingly attenuated by subsequent gas–gas collisions.

iii) Finally, in the forward direction where the atom-wall interaction is absent, there are particles which pass without collision. As $L/\tilde{\lambda}$ increases beyond unity this contribution is increasingly diminished and we may consider only the contribution of type-ii particles.

A measure of the channel opacity can be gained by the ratio of channel length to the mean free path, given as a reduced density,

$$n^* = n/n' = L/\lambda \tag{14}$$

where n' is the source density at which $\lambda = L$, such that $n' = 1/(L\sigma\sqrt{2})$. In a simple model [259], which considers only type-ii particles up to a point, we assume a linear density gradient, n/L along the length z of the channel, with local density $n(z)$, such that $n(L) = n_0$ down to a zero exit density $n(0) = 0$. At a distance $z = L'$ the local density satisfies $\lambda[n(L')] = L' = Ln^{*-1/2}$ and is given by $n(L') = nn^{*-1/2}$. We may now make the assumption that the surface πr^2 at position L' acts as the effective channel entry and the subsequent flow is in the transparent regime. Assuming no further attenuation by collisions, we can then estimate the axial beam intensity by,

$$I(0)_{opaque} = I(0)\, n^{*-1/2} \tag{15}$$

As the flow rate is unaffected by the opaque conditions, the peaking factor is given simply by $\kappa = W^{-1}n^{*-1/2}$. In the model of Giordmaine and Wang [256], a full integration over elements of volume $\pi r^2 \mathrm{d}z$ is carried out and the contribution from type-iii particles included. Their result differs from that of Hanes by only a factor of $(\pi/2)^{1/2}$ as,

$$I(0)_{opaque} = \left(\frac{3\tilde{v}r}{64\sigma\sqrt{2}}\, F_{tot}\right)^{1/2} \tag{16}$$

which is valid for,

$$L \geq 2.5 \left(\frac{L\sqrt{2}}{n_0\sigma}\right)^{1/2} = \Lambda \tag{17}$$

where Λ is the critical length at which the channel becomes opaque (previously L'). An increase in L beyond Λ is expected to have a negligible effect on the beam collimation [256]. The beam FWHM can be estimated from [256],

$$\theta_{1/2} \approx \frac{1}{1.78} \left(\frac{3\sigma\sqrt{2}}{\pi\tilde{v}r}\, F_{tot}\right)^{1/2} \tag{18}$$

Finally, for $\tilde{\lambda} < r$ we enter the viscous flow regime and gas–gas collisions dominate throughout the length of the nozzle. The conductance and therefore total flow rate gains a dependence on the source pressure [257]. Calculating the full beam characteristics for

these conditions is non-trivial. At high densities, due to collisions within or just outside the nozzle, a "cloud" is formed whose boundary serves as the effective source of atoms.

.1.2 Beam velocity

For an effusive source with beam exiting along z and Maxwellian source distribution, the longitudinal velocity distribution (to direction of major flow) is [173],

$$I(v_z) = \frac{2I_0}{\beta^4} v_z^3 \exp(-v_z^2/\beta^2) \tag{19}$$

where $I(v_z)$ is the beam intensity at velocity v_z in units of atoms $\mathrm{s}^{-1}\,\mathrm{m}^{-2}$, such that the total intensity $I_0 = \int_0^\infty I(v_z)\,\mathrm{d}v_z$. Characteristic velocities are:

- Most probable velocity: $v_{mp} = \beta\sqrt{(3/2)}$
- Average velocity: $v_{av} = (3/4)\beta\sqrt{\pi}$
- RMS velocity: $v_{\mathrm{RMS}} = \beta\sqrt{2}$

The additional dependence on v in Eq. 19, compared to Eq. 3.2, is apparent from a consideration of the probability of a particle escaping the source (a fast atom has many more attempts at finding an accepted escape trajectory, per unit time, than a slow atom). The transverse velocity distribution is defined by the nozzle geometry, which constrains the allowed escape trajectories from the source, and is dependent on the longitudinal velocity.

For long channels operated with $L > \lambda$ (in opaque or continuum flow regime) it is noted that the axial velocity distribution deviates from the above Maxwellian source distribution as a result of collisions occurring throughout the nozzle [258, 260]. Observations in the opaque flow regime show losses at low velocities moving the mean translational energy to higher velocities. At the transition to continuum flow, losses occur at both high and low velocities towards the mean translational energy [261]. A suggested energy exchange model was used to qualitatively describe the result [261]. The effect is decreasingly observed at increasing beam angles where the distribution is determined by wall collisions towards the exit of the nozzle and at large angles remains unchanged.

References

[1] S.J. Dick. *Sky and Ocean Joined*. Cambridge University Press, 2002. 13

[2] W. Markowitz. Proceedings of the Symposium on the Rotation of the Earth and Atomic Time Standards: Part II. The rotation of the earth: Variations in rotation of the earth, results obtained with the dual-rate moon camera and photographic zenith tubes. *The Astronomical Journal*, 64:106, April 1959. 13

[3] BIPM. Proc.-Verb. Com. Int. Poids et Mesures 25. In *BIPM Proc.-Verb. Com. Int. Poids et Mesures*, page 77, 1956. 13

[4] I. Rabi. Space Quantization in a Gyrating Magnetic Field. *Physical Review*, 51(8):652–654, April 1937. 13

[5] H. Lyons. The Atomic Clock. *Instruments*, 22:133–135, 1949. 14

[6] L. Essen and J.V.L. Parry. An Atomic Standard of Frequency and Time Interval: A Caesium Resonator. *Nature*, 176(4476):280–282, August 1955. 14

[7] N.F. Ramsey. A Molecular Beam Resonance Method with Separated Oscillating Fields. *Physical Review*, 78(6):695–699, June 1950. 14

[8] L. Essen and J.V.L. Parry. The Caesium Resonator as a Standard of Frequency and Time. *Philosophical Transactions of the Royal Society A: Mathematical, Physical and Engineering Sciences*, 250(973):45–69, August 1957. 14

[9] W. Markowitz, R. Glenn Hall, L. Essen, and J.V.L. Parry. Frequency of Cesium in Terms of Ephemeris Time. *Physical Review Letters*, 1(3):105–107, August 1958. 16

[10] S. Leschiutta. The definition of the atomic second. *Metrologia*, 42(3):S10–S19, June 2005. 16

[11] D. Henderson. Essen and the National Physical Laboratory's atomic clock. *Metrologia*, 42(3):S4–S9, June 2005. 16

[12] P. Forman. Atomichron: The atomic clock from concept to commercial product. *Proceedings of the IEEE*, 73(7):1181–1204, 1985. 16, 18

[13] M.A. Lombardi, T.P. Heavner, and S.R. Jefferts. NIST Primary Frequency Standards and the Realization of the SI Second. *Journal of Measurement Science*, 2:74–89, 2007. 16

[14] M. Arditi. A Caesium Beam Atomic Clock with Laser Optical Pumping, as a Potential Frequency Standard. *Metrologia*, 18(2):59–66, April 1982. 17

[15] A. Bauch, H. De Boer, B. Fischer, T. Heindorff, and R. Schroder. Performance of the PTB's primary clocks CS2 and CS1. *Proceedings of the 42nd Annual Frequency Control Symposium*, pages 490–495, 1988. 17

[16] A. De Marchi. A Novel Cavity Design for Minimization of Distributed Phase Shift in Atomic Beam Frequency Standards. *40th Annual Symposium on Frequency Control*, pages 441–446, 1986. 18

[17] J.H. Shirley, W.D. Lee, and R.E. Drullinger. Accuracy evaluation of the primary frequency standard NIST-7. *Metrologia*, 39(1):123–123, February 2002. 18

[18] J. Vanier and C. Audoin. The classical caesium beam frequency standard: fifty years later. *Metrologia*, 42(3):S31–S42, June 2005. 18

[19] T. Hansch and A. Schawlow. Cooling of gases by laser radiation. *Optics Communications*, 13(1):68–69, January 1975. 18

[20] A. De Marchi. The Optically Pumped Caesium Fountain: 10^{-15} Frequency Accuracy? *Metrologia*, 18:103–116, 1982. 18

[21] K. Gibble and S. Chu. Future Slow-atom Frequency Standards. *Metrologia*, 29(2):201–212, 1992. 18

[22] M.A. Kasevich, E. Riis, S. Chu, and R.G. DeVoe. RF spectroscopy in an atomic fountain. *Physical Review Letters*, 63(6):612–615, August 1989. 19

[23] C. Monroe, H. Robinson, and C. Wieman. Observation of the cesium clock transition using laser-cooled atoms in a vapor cell. *Optics Letters*, 16(1):50, January 1991. 19

[24] A. Clairon, C. Salomon, S. Guellati, and W.D. Phillips. Ramsey Resonance in a Zacharias Fountain. *EPL (Europhysics Letters)*, 16(2):165, 1991. 19

[25] A. Clairon, S. Ghezali, G. Santarelli, Ph. Laurent, S.N. Lea, M. Bahoura, E. Simon, S. Weyers, and K. Szymaniec. Proceedings of the 5th Symposium on Frequency Standards and Metrology. pages 49–59, Singapore, 1996. World Scientific. 19

[26] S.R. Jefferts, J. Shirley, T.E. Parker, T.P. Heavner, D.M. Meekhof, C. Nelson, F. Levi, G. Costanzo, A. De Marchi, R. Drullinger, L. Hollberg, W.D. Lee, and F.L. Walls. Accuracy evaluation of NIST-F1. *Metrologia*, 39(4):321, 2002. 20

[27] S. Weyers, U. Hbner, R. Schrder, Chr. Tamm, and A. Bauch. Uncertainty evaluation of the atomic caesium fountain CSF1 of the PTB. *Metrologia*, 38(4):343, 2001. 19

[28] F. Pereira Dos Santos, H. Marion, S. Bize, Y. Sortais, A. Clairon, and C. Salomon. Controlling the Cold Collision Shift in High Precision Atomic Interferometry. *Physical Review Letters*, 89(23):233004, Nov 2002. 20

[29] S.R. Jefferts, T.P. Heavner, T.E. Parker, and J.H. Shirley. NIST Cesium Fountains Current Status and Future Prospects. *Proceedings of SPIE*, 6673:667309, 2007. 20

[30] K. Gibble and B.J. Verhaar. Eliminating cold-collision frequency shifts. *Physical Review A*, 52(4):3370–3373, Oct 1995. 20

[31] K. Szymaniec, W. Chalupczak, S. Weyers, and R. Wynands. Prospects of operating a caesium fountain clock at zero collisional frequency shift. *Applied Physics B: Lasers and Optics*, 89:187–193, 2007. 10.1007/s00340-007-2813-5. 20

[32] K. Szymaniec, W. Chaupczak, E. Tiesinga, C. Williams, S. Weyers, and R. Wynands. Cancellation of the Collisional Frequency Shift in Caesium Fountain Clocks. *Physical Review Letters*, 98(15), April 2007. 20

[33] K. Gibble and S. Chu. Laser-cooled Cs frequency standard and a measurement of the frequency shift due to ultracold collisions. *Physical Review Letters*, 70(12):1771–1774, Mar 1993. 20

[34] S.J.J.M.F. Kokkelmans, B.J. Verhaar, K. Gibble, and D.J. Heinzen. Predictions for laser-cooled Rb clocks. *Physical Review A*, 56(6):R4389–R4392, Dec 1997. 20

[35] Y. Sortais, S. Bize, C. Nicolas, A. Clairon, C. Salomon, and C. Williams. Cold Collision Frequency Shifts in a ^{87}Rb Atomic Fountain. *Physical Review Letters*, 85(15):3117–3120, Oct 2000. 20

[36] C. Fertig and K. Gibble. Measurement and Cancellation of the Cold Collision Frequency Shift in an ^{87}Rb Fountain Clock. *Physical Review Letters*, 85(8):1622–1625, Aug 2000. 20

[37] Y.B. Ovchinnikov and G. Marra. Accurate rubidium atomic fountain frequency standard. *Metrologia*, 48(3):87, 2011. 20

[38] S. Peil, S. Crane, T.B. Swanson, and C.R. Ekstrom. Rubidium-Fountain Characterization Using the USNO Clock Ensemble. In *Frequency Control Symposium, 2007 Joint with 21st European Frequency and Time Forum*, pages 473–476, 2007. 20

[39] S. Bize, Y. Sortais, M.S. Santos, C. Mandache, A. Clairon, and C. Salomon. High-accuracy measurement of the ^{87}Rb ground-state hyperfine splitting in an atomic fountain. *Europhysics Letters*, 45(5):558, 1999. 20

[40] H. Marion, F. Pereira dos Santos, M. Abgrall, S. Zhang, Y. Sortais, S. Bize, I. Maksimovic, D. Calonico, J. Grünert, C. Mandache, P. Lemonde, G. Santarelli, Ph. Laurent, A. Clairon, and C. Salomon. Search for Variations of Fundamental Constants using Atomic Fountain Clocks. *Physical Review Letters*, 90(15), April 2003. 20, 22

[41] A. Wallard. News from the BIPM2006. *Metrologia*, 44(1):97–103, February 2007. 22

[42] K. Beloy. *Theory of the ac Stark Effect on the Atomic Hyperfine Structure and Applications to Microwave Atomic Clocks*. PhD thesis, University of Nevada, Reno, 2009. 22, 44

[43] F. Levi, C. Calosso, D. Calonico, L. Lorini, E.K. Bertacco, A. Godone, G.A. Costanzo, B. Mongino, S.R. Jefferts, T.P. Heavner, and E.A. Donley. Cryogenic fountain development at NIST and INRIM: preliminary characterization. *Ultrasonics, Ferroelectrics and Frequency Control, IEEE Transactions on*, 57(3):600 –605, march 2010. 22

[44] T.E. Parker. Long-term comparison of caesium fountain primary frequency standards. *Metrologia*, 47(1):1, 2010. 22

[45] A.N. Luiten, A.G. Mann, and D.G. Blair. Cryogenic sapphire microwave resonator-oscillator with exceptional stability. *Electronics Letters*, 30(5):417–419, 1994. 22

[46] B. Lipphardt, G. Grosche, U. Sterr, C. Tamm, S. Weyers, and H. Schnatz. The Stability of an Optical Clock Laser Transferred to the Interrogation Oscillator for a Cs Fountain. *Instrumentation and Measurement, IEEE Transactions on*, 58(4):1258 –1262, april 2009. 22

[47] G. Santarelli, Ph. Laurent, P. Lemonde, A. Clairon, A.G. Mann, S. Chang, A.N. Luiten, and C. Salomon. Quantum Projection Noise in an Atomic Fountain: A High Stability Cesium Frequency Standard. *Physical Review Letters*, 82(23):4619–4622, Jun 1999. 22

[48] T.P. Heavner, S.R. Jefferts, E.A. Donley, J.H. Shirley, and T.E. Parker. NIST-F1: recent improvements and accuracy evaluations. *Metrologia*, 42(5):411–422, October 2005. 22

[49] C. Vian, P. Rosenbusch, H. Marion, S. Bize, L. Cacciapuoti, S. Zhang, M. Abgrall, D. Chambon, I. Maksimovic, P. Laurent, G. Santarelli, A. Clairon, A. Luiten, M. Tobar, and C. Salomon. BNM-SYRTE Fountains: Recent Results. *IEEE Transactions on Instrumentation and Measurement*, 54(2):833–836, April 2005. 22

[50] K. Gibble. The difference between a photon's momentum and an atom's recoil. In *Quantum Electronics and Laser Science Conference, 2007. QELS '07*, pages 1 –2, may 2007. 23

[51] P. Giacomo. News from the BIPM. *Metrologia*, 20(1):25–30, January 1984. 23

[52] D.W. Allan. Time and frequency (time-domain) characterization, estimation, and prediction of precision clocks and oscillators. *IEEE transactions on ultrasonics, ferroelectrics, and frequency control*, 34:647–654, 1987. 27

[53] S.A. Webster, M. Oxborrow, and P. Gill. Vibration insensitive optical cavity. *Physical Review A*, 75(1), January 2007. 31

[54] S.A. Webster and P. Gill. Force-insensitive optical cavity. *Optics Letters*, 2011. 31

[55] R.W.P. Drever, J.L. Hall, F.V. Kowalski, J. Hough, G.M. Ford, A.J. Munley, and H. Ward. Laser phase and frequency stabilization using an optical resonator. *Applied Physics B: Lasers and Optics*, 31:97–105, 1983. 10.1007/BF00702605. 29, 99

[56] T. Day, E.K. Gustafson, and R.L. Byer. Sub-hertz relative frequency stabilization of two-diode laser-pumped Nd:YAG lasers locked to a Fabry-Perot interferometer. *Quantum Electronics, IEEE Journal of*, 28(4):1106 –1117, apr 1992. 29

[57] Ch. Salomon, D.G. Hils, and J.L. Hall. Laser stabilization at the millihertz level. *Journal of the Optical Society of America B*, 5(8):1576–1587, Aug 1988. 29

[58] A.D. Ludlow, X. Huang, M. Notcutt, T. Zanon-Willette, S.M. Foreman, M.M. Boyd, S. Blatt, and Jun Ye. Compact, thermal-noise-limited optical cavity for diode laser stabilization at 1×10^{-15}. *Optics Letters*, 32(6):641–3, March 2007. 31, 141

[59] S. Vogt, C. Lisdat, T. Legero, U. Sterr, I. Ernsting, A. Nevsky, and S. Schiller. Demonstration of a Transportable 1 Hz-Linewidth Laser. *ArXiv e-prints*, October 2010. 31

[60] B. Parker. Transportable cavity for stable frequency transfer at 1.5μm. (Unpublished). 31

[61] S. Schiller. Optical Clocks in Space. In *ESA Special Publication*, volume 621 of *ESA Special Publication*, June 2006. 31

[62] D.R. Leibrandt, M.J. Thorpe, M. Notcutt, R.E. Drullinger, T. Rosenband, and J.C. Bergquist. Spherical reference cavities for frequency stabilization of lasers in non-laboratory environments. *Optics Express*, 19(4):3471–3482, Feb 2011. 31

[63] D.R. Leibrandt, M.J. Thorpe, J.C. Bergquist, and T. Rosenband. Field-test of a robust, portable, frequency-stable laser. *Optics Express*, 19(11):10278–10286, May 2011. 31

[64] M.J. Thorpe, D.R. Leibrandt, T.M. Fortier, and T. Rosenband. Measurement and real-time cancellation of vibration-induced phase noise in a cavity-stabilized laser. *Optics Express*, 18(18):18744–18751, Aug 2010. 31

[65] B. Young, F. Cruz, W. Itano, and J. Bergquist. Visible Lasers with Subhertz Linewidths. *Physical Review Letters*, 82(19):3799–3802, May 1999. 31

[66] S.A. Webster, M. Oxborrow, and P. Gill. Subhertz-linewidth Nd:YAG laser. *Optics Letters*, 29(13):1497, 2004. 31

[67] S.A. Webster, M. Oxborrow, S. Pugla, J. Millo, and P. Gill. Thermal-noise-limited optical cavity. *Physical Review A*, 77(3), March 2008. 31

[68] Y.Y. Jiang, A.D. Ludlow, N.D. Lemke, R.W. Fox, J.A. Sherman, L.-S. Ma, and C.W. Oates. Making optical atomic clocks more stable with 10^{-16}-level laser stabilization. *Nature Photonics*, 5(3):158–161, March 2011. 31

[69] K. Numata, A. Kemery, and J. Camp. Thermal-Noise Limit in the Frequency Stabilization of Lasers with Rigid Cavities. *Physical Review Letters*, 93(25):1–4, December 2004.

[70] M. Notcutt, L.-S. Ma, A.D. Ludlow, S.M. Foreman, Jun Ye, and J.L. Hall. Contribution of thermal noise to frequency stability of rigid optical cavity via Hertz-linewidth lasers. *Physical Review A*, 73(3):031804, Mar 2006. 31

[71] H. Dehmelt. Proposed 10^{14} $\Delta\nu/\nu$ laser fluorescence spectroscopy on Tl+ mono-ion oscillator. *Bulletin of the American Phyiscal Society*, 20:637, 1975. 32, 37, 40

[72] W.M. Itano, J.C. Bergquist, J.J. Bollinger, J.M. Gilligan, D.J. Heinzen, F.L. Moore, M.G. Raizen, and D.J. Wineland. Quantum projection noise: Population fluctuations in two-level systems. *Physical Review A*, 47(5):3554–3570, May 1993. 32

[73] H. Katori. Optical lattice clocks and quantum metrology. *Nature Photonics*, 5(4):203–210, April 2011. 33, 50, 162

[74] G. Dick. Local oscillator induced instabilities in trapped ion frequency standards. In *Precise Time and Time Interval*, pages 133–147, Redondo Beach, 1987. 33

[75] C. Audoin, V. Candelier, and N. Dimarcq. A limit to the frequency stability of passive frequency standards. In *Precision Electromagnetic Measurements, 1990. CPEM '90 Digest., Conference on*, page 93, jun 1990.

[76] A. Quessada, R.P. Kovacich, I. Courtillot, A. Clairon, G. Santarelli, and P. Lemonde. The Dick effect for an optical frequency standard. *Journal of Optics B: Quantum and Semiclassical Optics*, 5(2):S150–S154, 2003. 33

[77] P.G. Westergaard, J. Lodewyck, and P. Lemonde. Minimizing the dick effect in an optical lattice clock. *Ultrasonics, Ferroelectrics and Frequency Control, IEEE Transactions on*, 57(3):623 –628, march 2010. 33

[78] H. Schnatz, S. Ohshima, H.R. Telle, and F. Riehle. Extension of the PTB frequency chain towards the Ca intercombination line at 657 nm. *Instrumentation and Measurement, IEEE Transactions on*, 42(2):273 –275, apr 1993. 35

[79] L.-S. Ma, L. Robertsson, S. Picard, M. Zucco, Z. Bi, S. Wu, and R.S. Windeler. First international comparison of femtosecond laser combs at the International Bureau of Weights and Measures. *Optics Letters*, 29(6):641–643, Mar 2004. 35

[80] J. Ye and S.T. Cundiff. *Femtosecond optical frequency comb: principle, operation, and applications*. Springer, 2005. 35

[81] R. Dicke. The Effect of Collisions upon the Doppler Width of Spectral Lines. *Physical Review*, 89(2):472–473, January 1953. 37

[82] J. Bergquist, W. Itano, and D. Wineland. Recoilless optical absorption and Doppler sidebands of a single trapped ion. *Physical Review A*, 36(1):428–430, July 1987. 37

[83] F. Diedrich, J.C. Bergquist, W.M. Itano, and D.J. Wineland. Laser Cooling to the Zero-Point Energy of Motion. *Physical Review Letters*, 62(4):403–406, Jan 1989. 37

[84] S.A. King. NPL internal communication. 38

[85] C.W. Chou, D.B. Hume, T. Rosenband, and D.J. Wineland. Optical Clocks and Relativity. *Science*, 329(5999):1630–1633, 2010. 38, 39

[86] Y.H. Wang, R. Dumke, T. Liu, A. Stejskal, Y.N. Zhao, J. Zhang, Z.H. Lu, L.J. Wang, Th. Becker, and H. Walther. Absolute frequency measurement and high resolution spectroscopy of $^{115}In^{+}$ $5s^2$ $^1S_0$ - 5s5p $^3P_0$ narrowline transition. *Optics Communications*, 273(2):526 – 531, 2007. 38, 39

[87] R.J. Rafac, B.C. Young, J.A. Beall, W.M. Itano, D.J. Wineland, and J.C. Bergquist. Sub-dekahertz Ultraviolet Spectroscopy of $^{199}Hg^{+}$. *Physical Review Letters*, 85(12):2462–2465, Sep 2000. 38

[88] T. Schneider, E. Peik, and Chr. Tamm. Sub-Hertz Optical Frequency Comparisons between Two Trapped $^{171}Yb^{+}$ Ions. *Physical Review Letters*, 94(23), June 2005. 38

[89] K. Hosaka, S.A. Webster, P.J. Blythe, A. Stannard, D. Beaton, H.S. Margolis, S.N. Lea, and P. Gill. Optical Frequency Standard Based on an Electric Octupole Transition in $^{171}Yb^{+}$. *Precision Electromagnetic Measurements Digest, 2004 Conference on*, pages 289–290, June 2004. 38

[90] T. Rosenband, D.B. Hume, P.O. Schmidt, C.W. Chou, A. Brusch, L. Lorini, W.H. Oskay, R.E. Drullinger, T.M. Fortier, J.E. Stalnaker, S.A. Diddams, W.C. Swann, N.R. Newbury, W.M. Itano, D.J. Wineland, and J.C. Bergquist. Frequency Ratio of Al^{+} and Hg^{+} Single-Ion Optical Clocks; Metrology at the 17th Decimal Place. *Science*, 319(5871):1808–1812, March 2008. 38, 39

[91] C.W. Chou, D.B. Hume, J.C.J. Koelemeij, D.J. Wineland, and T. Rosenband. Frequency Comparison of Two High-Accuracy Al^{+} Optical Clocks. *Physical Review Letters*, 104(7):070802, Feb 2010. 39

[92] J.E. Stalnaker, S.A. Diddams, T.M. Fortier, K. Kim, L. Hollberg, J.C. Bergquist, W.M. Itano, M.J. Delany, L. Lorini, W.H. Oskay, T.P. Heavner, S.R. Jefferts, F. Levi, T.E. Parker, and J. Shirley. Optical-to-microwave frequency comparison with fractional uncertainty of 10^{-15}. *Applied Physics B: Lasers and Optics*, 89:167–176, 2007. 10.1007/s00340-007-2762-z. 39

[93] Chr. Tamm, S. Weyers, B. Lipphardt, and E. Peik. Stray-field-induced quadrupole shift and absolute frequency of the 688-THz $^{171}Yb^{+}$ single-ion optical frequency standard. *Physical Review A*, 80(4):043403, Oct 2009. 39

[94] M. Chwalla, J. Benhelm, K. Kim, G. Kirchmair, T. Monz, M. Riebe, P. Schindler, A.S. Villar, W. Hänsel, C.F. Roos, R. Blatt, M. Abgrall, G. Santarelli, G.D. Rovera, and Ph. Laurent. Absolute Frequency Measurement of the $^{40}Ca^{+}$ $4s^2S_{1/2}$ - 3d $^2D_{5/2}$ Clock Transition. *Physical Review Letters*, 102(2):023002, Jan 2009. 39

[95] H.S. Margolis, G.P. Barwood, G. Huang, H.A. Klein, S.N. Lea, K. Szymaniec, and P. Gill. Hertz-level measurement of the optical clock frequency in a single $^{88}Sr^{+}$ ion. *Science*, 306(5700):1355–8, November 2004. 39

[96] S.A. King, R.M. Godun, S.A. Webster, H.S. Margolis, L.A.M. Johnson, K. Szymaniec, P.E.G. Baird, and P. Gill. Absolute frequency measurement of the $^2S_{1/2}$ $^2F_{7/2}$ electric octupole transition in a single ion of $^{171}Yb^{+}$ with 10^{15} fractional uncertainty. *New Journal of Physics*, 14(1):013045, 2012. 39

[97] J. von Zanthier, Th. Becker, M. Eichenseer, A.Yu. Nevsky, Ch. Schwedes, E. Peik, H. Walther, R. Holzwarth, J. Reichert, Th. Udem, T.W. Hänsch, P.V. Pokasov, M.N. Skvortsov, and S.N. Bagayev. Absolute frequency measurement of the In^{+} clock transition with a mode-locked laser. *Optics Letters*, 25(23):1729–1731, Dec 2000. 39

[98] J.C. Bollinger J.J. Drullinger R.E. Wineland, D.J. Bergquist and W.M. Itano. In P. Gill, editor, *Proceeding of the 6th Symposium on Frequency Standards and Metrology*, pages 361–368. World Scientific, 2002. 38

[99] P.O. Schmidt, T. Rosenband, C. Langer, W.M. Itano, J.C. Bergquist, and D.J. Wineland. Spectroscopy Using Quantum Logic. *Science*, 309(5735):749–752, 2005. 38

[100] T. Rosenband, P.O. Schmidt, D.B. Hume, W.M. Itano, T.M. Fortier, J.E. Stalnaker, K. Kim, S.A. Diddams, J.C.J. Koelemeij, J.C. Bergquist, and D.J. Wineland. Observation of the $^1S_0 \rightarrow {}^3P_0$ Clock Transition in $^{27}Al^+$. *Physical Review Letters*, 98(22):220801, May 2007. 38

[101] H. Dehmelt. Mono-ion oscillator as a potential ultimate laser frequency standard. In *Proceedings of the 35th Annual Frequency Control Symposium*, 1981. 40

[102] H. Dehmelt, N. Yu, and W. Nagourney. The $6^1S_0 - 6^3P_0$ transition in thallium isotope ion $^{204}Tl^+$: A superior atomic clock. In *Proceedings of the National Academy of Sciences of the United States of America*, 1989. 40

[103] K. Hayasaka. New Approaches To An Indium Ion Optical Frequency Standard. In *1st European Conference on Trapped Ions*, 2010. 40

[104] C.W. Oates, F. Bondu, R.W. Fox, and L. Hollberg. A diode-laser optical frequency standard based on laser-cooled Ca atoms: Sub-kilohertz spectroscopy by optical shelving detection. *European Physical Journal D*, 7(3):449–460, 1999. 40

[105] F. Riehle, H. Schnatz, B. Lipphardt, G. Zinner, T. Trebst, T. Binnewies, G. Wilpers, and J. Helmcke. The optical Ca frequency standard. In *Frequency and Time Forum, 1999 and the IEEE International Frequency Control Symposium, 1999., Proceedings of the 1999 Joint Meeting of the European*, volume 2, pages 700 –705 vol.2, 1999. 40

[106] Ch. Bordé, Ch. Salomon, S. Avrillier, A. Van Lerberghe, Ch. Bréant, D. Bassi, and G. Scoles. Optical Ramsey fringes with traveling waves. *Physical Review A*, 30(4):1836–1848, October 1984. 40

[107] C.W. Oates, E.A. Curtis, and L. Hollberg. Improved short-term stability of optical frequency standards: approaching 1 Hz in 1 s with the Ca standard at 657 nm. *Optics Letters*, 25(21):1603, November 2000. 41

[108] E.A. Curtis, C.W. Oates, and L. Hollberg. Quenched narrow-line second- and third-stage laser cooling of ^{40}Ca. *Journal of the Optical Society of America B*, 20(5):977, 2003. 41

[109] N.L. Manakov, V.D. Ovsiannikov, and L.P. Rapoport. Atoms in a laser field. *Physics Reports*, 141(6):320 – 433, 1986. 41

[110] H. Katori, M. Takamoto, V. Palchikov, and V. Ovsiannikov. Ultrastable Optical Clock with Neutral Atoms in an Engineered Light Shift Trap. *Physical Review Letters*, 91(17), October 2003. 42, 45, 47, 48

[111] A. Brusch, R. Le Targat, X. Baillard, M. Fouche, and P. Lemonde. Hyperpolarizability Effects in a Sr Optical Lattice Clock. *Physical Review Letters*, 96(10):103003, 2006. 42, 47

[112] P.G. Westergaard, J. Lodewyck, L. Lorini, A. Lecallier, E.A. Burt, M. Zawada, J. Millo, and P. Lemonde. Lattice-Induced Frequency Shifts in Sr Optical Lattice Clocks at the 10^{-17} Level. *Physical Review Letters*, 106(21):210801, May 2011. 42, 46, 47, 55

[113] H. Katori. Spectroscopy of strontium atoms in the Lamb-Dicke confinement. *Proceedings of the 6th Symposium in Frequency Standards and Metrology*, pages 323–330, 2001. 42, 45, 48, 106

[114] M. Takamoto, H. Katori, S.I. Marmo, V.D. Ovsiannikov, and V.G. Pal'chikov. Prospects for Optical Clocks with a Blue-Detuned Lattice. *Physical Review Letters*, 102(6):63002, 2009. 42, 48, 55, 147

[115] H. Katori, K. Hashiguchi, E.Yu. Il'inova, and V.D. Ovsiannikov. Magic Wavelength to Make Optical Lattice Clocks Insensitive to Atomic Motion. *Physical Review Letters*, 103(15):153004, Oct 2009. 42, 46, 55

[116] M. Takamoto, F.-L. Hong, R. Higashi, and H. Katori. An optical lattice clock. *Nature*, 435(7040):321–324, May 2005. 42, 52, 59

[117] A.D. Ludlow, M.M. Boyd, T. Zelevinsky, S.M. Foreman, S. Blatt, M. Notcutt, T. Ido, and Jun Ye. Systematic Study of the ^{87}Sr Clock Transition in an Optical Lattice. *Physical Review Letters*, 96(3), January 2006. 42, 48, 49, 59

[118] S.G. Porsev, A. Derevianko, and E.N. Fortson. Possibility of an optical clock using the $6^1S_0 \rightarrow 6^3P_0^o$ transition in ^{171,173}Yb atoms held in an optical lattice. *Physical Review A*, 69:021403, Feb 2004. 42

[119] Z.W. Barber, J.E. Stalnaker, N.D. Lemke, N. Poli, C.W. Oates, T.M. Fortier, S.A. Diddams, L. Hollberg, C.W. Hoyt, A.V. Taichenachev, and V.I. Yudin. Optical Lattice Induced Light Shifts in an Yb Atomic Clock. *Physical Review Letters*, 100(10):103002, Mar 2008. 47

[120] H. Hachisu, K. Miyagishi, S.G. Porsev, A. Derevianko, V.D. Ovsiannikov, V.G. Palchikov, M. Takamoto, and H. Katori. Trapping of Neutral Mercury Atoms and Prospects for Optical Lattice Clocks. *Physical Review Letters*, 100(5):053001, February 2008. 53, 55, 59

[121] C. Degenhardt, H. Stoehr, U. Sterr, F. Riehle, and C. Lisdat. Wavelength-dependent ac Stark shift of the $^1S_0$ - $^3P_1$ transition at 657 nm in Ca. *Physical Review A*, 70(2):023414, Aug 2004.

[122] Y. Geng-Hua, Z. Jia-Qi, L. Run-Bing, W. Jin, and Z. Ming-Sheng. Magic Wavelength of an Optical Clock Transition of Barium. *Chinese Physics Letters*, 28(7):073201, 2011. 42

[123] A. Derevianko and H. Katori. *Colloquium* : Physics of optical lattice clocks. *Reviews of Modern Physics*, 83:331–347, May 2011. 42

[124] M.M. Boyd. *High Precision Spectroscopy of Strontium in an Optical Lattice: Towards a New Standard for Frequency and Time*. PhD thesis, University of Colorado, 2007. 44, 45, 110

[125] P.G. Westergaard. *Horloge à r eseau optique au Strontium : en quete de la performance ultime*. PhD thesis, l'Edite de Paris, 2010. 44, 110, 161

[126] M. Takamoto, F.-L. Hong, R. Higashi, Y. Fujii, M. Imae, and H. Katori. Improved Frequency Measurement of a One-Dimensional Optical Lattice Clock with a Spin-Polarized Fermionic ^{87}Sr Isotope. *Journal of the Physical Society of Japan*, 75(10):104302, 2006. 44, 48, 49, 55, 59

[127] M.M. Boyd, A.D. Ludlow, S. Foreman, T. Zelevinsky, S. Blatt, T. Zanon, G. Campbell, M. Miranda, M. Martin, and Jun Ye. Strontium Optical Lattice Clock at JILA. In *Frequency Control Symposium, 2007 Joint with the 21st European Frequency and Time Forum. IEEE International*, pages 1269–1273, 2007. 45

[128] A.V. Taichenachev, V.I. Yudin, V.D. Ovsiannikov, V.G. Pal'chikov, and C.W. Oates. Frequency Shifts in an Optical Lattice Clock Due to Magnetic-Dipole and Electric-Quadrupole Transitions. *Physical Review Letters*, 101(19):193601, Nov 2008. 45, 55, 111, 113, 114

[129] P. Lemonde and P. Wolf. Optical lattice clock with atoms confined in a shallow trap. *Physical Review A*, 72(3):033409, Sep 2005. 47

[130] A.V. Taichenachev, V.I. Yudin, V.D. Ovsiannikov, and V.G. Pal'chikov. Optical Lattice Polarization Effects on Hyperpolarizability of Atomic Clock Transitions. *Physical Review Letters*, 97(17):173601, 2006. 47, 55

[131] G.K. Campbell, A.D. Ludlow, S. Blatt, J.W. Thomsen, M.J. Martin, M.H.G. De Miranda, T. Zelevinsky, M.M. Boyd, Jun Ye, S.A. Diddams, T.P. Heavner, T.E. Parker, and S.R. Jefferts. The absolute frequency of the ^{87}Sr optical clock transition. *Metrologia*, 45(5):539–548, 2008. 48, 49, 59

[132] R. Le Targat, X. Baillard, M. Fouche, A. Brusch, O. Tcherbakoff, G.D. Rovera, and P. Lemonde. Accurate optical lattice clock with ^{87}Sr atoms. *Physical Review Letters*, 97:130801, 2006. 48, 49

[133] F.-L. Hong, M. Musha, M. Takamoto, H. Inaba, S. Yanagimachi, A. Takamizawa, K. Watabe, T. Ikegami, M. Imae, Y. Fujii, M. Amemiya, K. Nakagawa, K. Ueda, and H. Katori. Measuring the frequency of a Sr optical lattice clock using a 120 km coherent optical transfer. *Optics Letters*, 34(5):692–694, 2009. 48

[134] X. Baillard, M. Fouché, R. Le Targat, P.G. Westergaard, A. Lecallier, F. Chapelet, M. Abgrall, G.D. Rovera, P. Laurent, P. Rosenbusch, S. Bize, G. Santarelli, A. Clairon, P. Lemonde, G. Grosche, B. Lipphardt, and H. Schnatz. An optical lattice clock with spin-polarized ^{87}Sr atoms. *The European Physical Journal D - Atomic, Molecular, Optical and Plasma Physics*, 48(1):11–17, June 2008. 48, 113

[135] S. Falke, H. Schnatz, J.S.R. Vellore Winfried, T. Middelmann, S. Vogt, S. Weyers, B. Lipphardt, G. Grosche, F. Riehle, U. Sterr, and C. Lisdat. The ^{87}Sr optical frequency standard at PTB. *ArXiv e-prints*, April 2011. 48, 49, 59

[136] N.D. Lemke, A.D. Ludlow, Z.W. Barber, T.M. Fortier, S.A. Diddams, Y. Jiang, S.R. Jefferts, T.P. Heavner, T.E. Parker, and C.W. Oates. Spin-1/2 Optical Lattice Clock. *Physical Review Letters*, 103(6):063001, Aug 2009. 48, 49, 59

[137] T. Kohno, M. Yasuda, K. Hosaka, H. Inaba, Y. Nakajima, and F.-L. Hong. One-Dimensional Optical Lattice Clock with a Fermionic ^{171}Yb Isotope. *Applied Physics Express*, 2(7):072501, 2009. 48, 49

[138] N. Poli, Z.W. Barber, N.D. Lemke, C.W. Oates, L.S. Ma, J.E. Stalnaker, T.M. Fortier, S.A. Diddams, L. Hollberg, J.C. Bergquist, A. Brusch, S. Jefferts, T. Heavner, and T. Parker. Frequency evaluation of the doubly forbidden $^1S_0 - {}^3P_0$ transition in bosonic ^{174}Yb. *Physical Review A*, 77(5):050501, 2008. 48, 49

[139] T. Akatsuka, M. Takamoto, and H. Katori. Optical lattice clocks with non-interacting bosons and fermions. *Nature Physics*, 4(12):954–959, December 2008. 48

[140] X. Baillard, M. Fouché, R. Le Targat, P.G. Westergaard, A. Lecallier, Y. Le Coq, G.D. Rovera, S. Bize, and P. Lemonde. Accuracy evaluation of an optical lattice clock with bosonic atoms. *Optics Letters*, 32(13):1812–1814, 2007. 48, 49, 111

[141] C. Diddams S. Bartels A. Fortier T. Oskay W. Bergquist J. Jefferts S. Heavner T. Parker T. Hollberg L. Wilpers, G. Oates. Absolute frequency measurement of the neutral ^{40}Ca optical frequency standard at 657 nm based on microkelvin atoms. *Metrologia*, 44:146–151, 2007. 48

[142] C. Degenhardt, H. Stoehr, C. Lisdat, G. Wilpers, H. Schnatz, B. Lipphardt, T. Nazarova, P.-E. Pottie, U. Sterr, J. Helmcke, and F. Riehle. Calcium optical frequency standard with ultracold atoms: Approaching 10^{-15} relative uncertainty. *Physical Review A*, 72(6):062111, Dec 2005. 48

[143] M. Takamoto and H. Katori. Spectroscopy of the ^{1}S$_0$ - ^{3}P$_0$ Clock Transition of ^{87}Sr in an Optical Lattice. *Physical Review Letters*, 91(22):223001, November 2003. 48

[144] Report of the 98th meeting of the Comité International des Poids et Mesures (CIPM). *Bureau International des Poids et Mesures (BIPM)*, (ISSN 1016-5893 ISBN 13-978-92-822-2238-6), 2009. 49

[145] M.M. Boyd, T. Zelevinsky, A.D. Ludlow, S.M. Foreman, S. Blatt, T. Ido, and Jun Ye. Optical Atomic Coherence at the 1-Second Time Scale. *Science*, 314(5804):1430–1433, December 2006. 49, 50

[146] S.G. Porsev and A. Derevianko. Hyperfine quenching of the metastable ^{3}P$_{0,2}$ states in divalent atoms. *Physical Review A*, 69(4):042506, Apr 2004. 50, 110, 117

[147] Z.W. Barber. *Ytterbium Optical Lattice Clock*. PhD thesis, University of Colorado, 2007. 50, 59, 111, 112, 114

[148] M.C. Bigeon. Probabilit de transition de la raie 6^1S$_0 - 6^3$P$_0$ du mercure. *Le Journal de Physique*, 28(1):51–60, 1967. 50

[149] L. Yi, S. Mejri, J.J. McFerran, Y. Le Coq, and S. Bize. Optical Lattice Trapping of ^{199}Hg and Determination of the Magic Wavelength for the Ultraviolet ^{1}S$_0 \leftrightarrow ^3$P$_0$ Clock Transition. *Physical Review Letters*, 106(7):073005, Feb 2011. 50, 59

[150] G. Wang and A. Ye. Possibility of using Zn as the quantum absorber for a laser-cooled neutral atomic optical frequency standard. *Physical Review A*, 76(4):043409, Oct 2007. 50, 81

[151] S.G. Porsev and A. Derevianko. Multipolar theory of blackbody radiation shift of atomic energy levels and its implications for optical lattice clocks. *Physical Review A*, 74(2):4–7, August 2006. 51, 52, 53, 154

[152] S.G. Porsev, A.D. Ludlow, M.M. Boyd, and Jun Ye. Determination of Sr properties for a high-accuracy optical clock. *Physical Review A*, 78(3):032508, Sep 2008. 51, 54, 114, 147, 149

[153] Y.B. Ovchinnikov. Towards better characterization of blackbody radiation shift in strontium optical lattice clock. In *Optical clocks: a new frontier in high accuracy metrology*. INRIM, 2010. 54

[154] T. Middelmann, C. Lisdat, S. Falke, J.S.R.V. Winfred, F. Riehle, and U. Sterr. Tackling the Blackbody Shift in a Strontium Optical Lattice Clock. *Instrumentation and Measurement, IEEE Transactions on*, 60(7):2550 –2557, July 2011. 54, 55, 156

[155] W.D. Phillips and H. Metcalf. Laser Deceleration of an Atomic Beam. *Physical Review Letters*, 48:596–599, Mar 1982. 56, 75

[156] E.L. Raab, M. Prentiss, A. Cable, S. Chu, and D.E. Pritchard. Trapping of Neutral Sodium Atoms with Radiation Pressure. *Physical Review Letters*, 59:2631–2634, Dec 1987. 56

[157] M.H. Anderson, J.R. Ensher, M.R. Matthews, C.E. Wieman, and E.A. Cornell. Observation of Bose-Einstein Condensation in a Dilute Atomic Vapor. *Science*, 269(5221):198–201, 1995. 56

[158] K.B. Davis, M.-O. Mewes, M.R. Andrews, N.J. van Druten, D.S. Durfee, D.M. Kurn, and W. Ketterle. Bose-Einstein Condensation in a Gas of Sodium Atoms. *Physical Review Letters*, 75:3969–3973, Nov 1995. 56

[159] Z.W. Barber, C.W. Hoyt, C.W. Oates, L. Hollberg, A.V. Taichenachev, and V.I. Yudin. Direct excitation of the forbidden clock transition in neutral ^{174}Yb atoms confined to an optical lattice. *Physical Review Letters*, 96(8):083002, March 2006. 59, 111

[160] M. Yasuda, T. Kohno, K. Hosaka, H. Inaba, Y. Nakajima, and F.-L. Hong. Yb Optical Lattice Clock at NMIJ, AIST. In *Conference on Lasers and Electro-Optics*, page CMD4. Optical Society of America, 2010. 59

[161] *Chemical Properties Handbook*. McGraw-Hill, 1999. 59, 60

[162] J.A. Neuman, P. Wang, and A. Gallagher. Robust high temperature sapphire cell for metal vapors. *Review of Scientific Instruments*, 66(4):3021 –3023, apr 1995. 61

[163] K.R. Vogel. *Laser Cooling on a Narrow Atomic Transition and Measurement of the Two-Body Cold Collision Loss Rate in a Strontium Magneto-Optical Trap*. PhD thesis, University of Colorado, 1999. 61, 83, 84

[164] D.A. Reay and P.A. Kew. *Heat Pipes: Theory, Design and Applications*. Elsevier, 5th edition, 2006. 61

[165] C.R. Vidal. *Atomic, Molecular, and Optical Physics: Atoms and Molecules*, volume 29B. Academic Press, 1996. 61

[166] Y. Li, T. Ido, T. Eichler, and H. Katori. Narrow-line diode laser system for laser cooling of strontium atoms on the intercombination transition. *Applied Physics B: Lasers and Optics*, 78:315–320, 2004. 61

[167] H. Katori and F. Shimizu. Lifetime measurement of the $1s_5$ metastable state of argon and krypton with a magneto-optical trap. *Physical Review Letters*, 70(23):3545–3548, Jun 1993. 62

[168] T.A. Giorgi, B. Ferrario, and B. Storey. An updated review of getters and gettering. *Journal of Vacuum Science & Technology A*, 3(2):417–423, 1985. 62

[169] J.C. Turnbull. Barium, strontium, and calcium as getters in electron tubes. *Journal of Vacuum Science and Technology*, 14(1):636 –639, jan 1977. 62

[170] J. Van Dongen, C. Zhu, D. Clement, G. Dufour, J.L. Booth, and K.W. Madison. Trap-depth determination from residual gas collisions. *Physical Review A*, 84(2):022708, Aug 2011. 62

[171] X. Xu, T.H. Loftus, J.L. Hall, A. Gallagher, and Jun Ye. Cooling and trapping of atomic strontium. *Journal of the Optical Society of America B (Optical Physics)*, 20(5):968 – 76, 2003. 62

[172] M. Yasuda and H. Katori. Lifetime Measurement of the $^3P_2$ Metastable State of Strontium Atoms. *Physical Review Letters*, 92(15):153004, Apr 2004. 62, 116, 117

[173] N.F. Ramsey. *Molecular Beams*. Oxford University Press, 1956. 63, 166, 167, 170

[174] E.M. Bridge, J. Millen, C.S. Adams, and M.P.A. Jones. A vapor cell based on dispensers for laser spectroscopy. *Review of Scientific Instruments*, 80(1):013101 –013101–3, jan 2009. 63

[175] K.I. Lee, J.A. Kim, H.R. Noh, and W. Jhe. Single-beam atom trap in a pyramidal and conical hollow mirror. *Optics Letters*, 21(15):1177–1179, Aug 1996. 63

[176] M.P.A. Jones. Private communication. 63

[177] See for example the Nobel Lecture by W.D. Phillips. Laser Cooling and Trapping of Neutral Atoms. 1997. 69

[178] A. Aspect, E. Arimondo, R. Kaiser, N. Vansteenkiste, and C. Cohen-Tannoudji. Laser Cooling below the One-Photon Recoil Energy by Velocity-Selective Coherent Population Trapping. *Physical Review Letters*, 61:826–829, Aug 1988. 73

[179] M.A. Kasevich and S. Chu. Laser cooling below a photon recoil with three-level atoms. *Physical Review Letters*, 69:1741–1744, Sep 1992. 73

[180] V.S. Letokhov, V.G. Minogin, and B.D. Pavlik. Cooling and trapping of atoms and molecules by a resonant laser field. *Optics Communications*, 19(1):72 – 75, 1976. 73

[181] J.V. Prodan and W.D. Phillips. Chirping the light - fantastic? Recent NBS atom cooling experiments. *Progress in Quantum Electronics*, 8(3-4):231 – 235, 1984. 74

[182] J. Hoffnagle. Proposal for continuous white-light cooling of an atomic beam. *Optics Letters*, 13(2):102–104, Feb 1988. 74

[183] M. Zhu, C.W. Oates, and J.L. Hall. Continuous high-flux monovelocity atomic beam based on a broadband laser-cooling technique. *Physical Review Letters*, 67:46–49, Jul 1991. 74

[184] W.D. Phillips. Proposal to the Office of Naval Research from the National Bureau of Standards, Laser cooling and trapping of neutral atoms. 1979. 75

[185] Y.B. Ovchinnikov. A Zeeman slower based on magnetic dipoles. *Optics Communications*, 276(2):261–267, August 2007. 76, 96

[186] I.R. Hill, Y.B. Ovchinnikov, E.M. Bridge, S. Donnellan, E.A. Curtis, and P. Gill. A Simple, Configurable, Permanent Magnet Zeeman Slower for Sr. In *EFTF 2012*, 2012. 97

[187] I.R. Hill, Y.B. Ovchinnikov, E.M. Bridge, E.A. Curtis, and P. Gill. In preparation. 2012. 76, 97

[188] X. Xu, T.H. Loftus, J.W. Dunn, C.H. Greene, J.L. Hall, A. Gallagher, and Jun Ye. Single-Stage Sub-Doppler Cooling of Alkaline Earth Atoms. *Physical Review Letters*, 90(19), May 2003. 80, 83, 85, 114, 116

[189] R. Maruyama, R.H. Wynar, M.V. Romalis, A. Andalkar, M.D. Swallows, C.E. Pearson, and E.N. Fortson. Investigation of sub-Doppler cooling in an ytterbium magneto-optical trap. *Physical Review A*, 68(1):011403, Jul 2003. 80

[190] J.J. McFerran, L. Yi, S. Mejri, and S. Bize. Sub-Doppler cooling of fermionic Hg isotopes in a magneto-optical trap. *Optics Letters*, 35(18):3078–3080, Sep 2010. 80, 81

[191] M. Yasuda, T. Kishimoto, M. Takamoto, and H. Katori. Photoassociation spectroscopy of ^{88}Sr : Reconstruction of the wave function near the last node. *Physical Review A*, 73(1):011403, Jan 2006. 81, 146, 149

[192] R. Drozdowski, M. Ignaciuk, J. Kwela, and J. Heldt. Radiative lifetimes of the lowest $^3P_1$ metastable states of Ca and Sr. *Zeitschrift fr Physik D Atoms, Molecules and Clusters*, 41:125–131, 1997. 10.1007/s004600050300. 81, 149

[193] K.-A. Brickman, M.-S. Chang, M. Acton, A. Chew, D. Matsukevich, P.C. Haljan, V.S. Bagnato, and C. Monroe. Magneto-optical trapping of cadmium. *Physical Review A*, 76(4):043411, Oct 2007. 81

[194] T. Kurosu and F. Shimizu. Laser Cooling and Trapping of Alkaline Earth Atoms. *Japanese Journal of Applied Physics*, 31(Part 1, No. 3):908–912, 1992. 84

[195] A.D. Ludlow. *The Strontium Optical Lattice Clock: Optical Spectroscopy with Sub-Hertz Accuracy*. PhD thesis, University of Colorado, 2008. 84, 144

[196] H.G.C. Werij, C.H. Greene, C.E. Theodosiou, and A. Gallagher. Oscillator strengths and radiative branching ratios in atomic Sr. *Physical Review A*, 46(3):1248–1260, Aug 1992. 84, 146, 147, 149

[197] P.G. Mickelson, Y.N. Martinez de Escobar, P. Anzel, B.J. DeSalvo, S.B. Nagel, A.J. Traverso, M. Yan, and T.C. Killian. Repumping and spectroscopy of laser-cooled Sr atoms using the (5s5p) $^3P_2$ - (5s4d) $^3D_2$ transition. *Journal of Physics B: Atomic, Molecular and Optical Physics*, 42(23):235001, 2009. 85

[198] F. Sorrentino, G. Ferrari, N. Poli, R. Drullinger, and G.M. Tino. Laser Cooling and Trapping of Atomic Strontium for Ultracold Atoms Physics, High-Precision Spectroscopy and Quantum Sensors. *Modern Physics Letters B*, 20:1287–1320, 2006. 85, 166

[199] P.G. Mickelson, Y.N. Martinez de Escobar, M. Yan, B.J. DeSalvo, and T.C. Killian. Bose-Einstein condensation of ^{88}Sr through sympathetic cooling with ^{87}Sr. *Physical Review A*, 81:051601(R), May 2010. 85

[200] F. Buchinger, R. Corriveau, E.B. Ramsay, D. Berdichevsky, and D.W.L. Sprung. Influence of the *N=50* shell closure on mean square charge radii of strontium. *Physical Review C*, 32:2058–2066, Dec 1985. 85

[201] Y. Tsuda, M. Ohta, P.O. Vaccaro, S. Ito, S. Hirukawa, Y. Kawaguchi, Y. Fujishiro, Y. Takahira, Y. Ueta, T. Takakura, and T. Yuasa. Blue Laser Diodes Fabricated on *m*-Plane GaN Substrates. *Applied Physics Express*, 1(1):011104, 2008. 89

[202] M. Kubota, K. Okamoto, T. Tanaka, and H. Ohta. Continuous-Wave Operation of Blue Laser Diodes Based on Nonpolar *m*-Plane Gallium Nitride. *Applied Physics Express*, 1(1):011102, 2008. 89

[203] K.G. Libbrecht and J.L. Hall. A low-noise high-speed diode laser current controller. *Review of Scientific Instruments*, 64(8):2133–2135, 1993. 91

[204] S.G. Cox, P.F. Griffin, C.S. Adams, D. DeMille, and E. Riis. Reusable ultrahigh vacuum viewport bakeable to 240 °C. *Review of Scientific Instruments*, 74(6):3185–3187, 2003. 94

[205] K.J. Weatherill, J.D. Pritchard, P.F. Griffin, U. Dammalapati, C.S. Adams, and E. Riis. A versatile and reliably reusable ultrahigh vacuum viewport. *Review of Scientific Instruments*, 80(2):026105, 2009. 94

[206] M. Schioppo. *Development of a Transportable Strontium Optical Clock*. PhD thesis, University of Florence, 2010. 96

[207] T.H. Loftus, T. Ido, M.M. Boyd, A.D. Ludlow, and Jun Ye. Narrow line cooling and momentum-space crystals. *Physical Review A*, 70:063413, Dec 2004. 99

[208] K.R. Vogel, T.P. Dinneen, A. Gallagher, and J.L. Hall. Narrow-line Doppler cooling of strontium to the recoil limit. In *IEEE Transactions on Instrumentation and Measurement*, volume 48, pages 618 – 21, Washington, DC, USA, 1999.

[209] H. Katori, T. Ido, Y. Isoya, and M. Kuwata-Gonokami. Magneto-Optical Trapping and Cooling of Strontium Atoms down to the Photon Recoil Temperature. *Physical Review Letters*, 82:1116–1119, Feb 1999. 99

[210] T. Day. *Frequency Stabilized Solid State Lasers for Coherent Optical Communications*. PhD thesis, Stanford University, 1991. 99, 137, 138

[211] R.W. Fox, C.W. Oates, and L.W. Hollberg. *Cavity-Enhanced Spectroscopies*, chapter Stabilizing diode lasers to high finesse cavities. Elsevier Science, New York, 2002. 99

[212] J.C. Owens. Optical Refractive Index of Air: Dependence on Pressure, Temperature and Composition. *Applied Optics*, 6(1):51–59, Jan 1967. 101

[213] J. Alnis, A. Matveev, N. Kolachevsky, Th. Udem, and T.W. Hänsch. Subhertz linewidth diode lasers by stabilization to vibrationally and thermally compensated ultralow-expansion glass Fabry-Pérot cavities. *Physical Review A*, 77:053809, May 2008. 102

[214] N.C. Wong and J.L. Hall. Servo control of amplitude modulation in frequency-modulation spectroscopy: demonstration of shot-noise-limited detection. *Journal of the Optical Society of America B*, 2(9):1527–1533, Sep 1985. 103

[215] C. Ishibashi, Jun Ye, and J.L. Hall. Analysis/reduction of residual amplitude modulation in phase/frequency modulation by an EOM. In *Quantum Electronics and Laser Science Conference, 2002. QELS '02. Technical Digest. Summaries of Papers Presented at the*, pages 91 – 92, 2002. 103

[216] H. Kogelnik and T. Li. Laser Beams and Resonators. *Applied Optics*, 5(10):1550, October 1966. 103

[217] R. Grimm, M. Weidemller, and Y.B. Ovchinnikov. Optical Dipole Traps for Neutral Atoms. volume 42 of *Advances In Atomic, Molecular, and Optical Physics*, pages 95 – 170. Academic Press, 2000. 104

[218] V. Letokhov. Narrowing of the Doppler width in a standing light wave. *JETP Letters*, 7:272, 1968. 104

[219] A. Ashkin. Trapping of Atoms by Resonance Radiation Pressure. *Physical Review Letters*, 40:729–732, Mar 1978. 104

[220] A. Derevianko. Feasibility of Cooling and Trapping Metastable Alkaline-Earth Atoms. *Physical Review Letters*, 87(2):023002, Jun 2001. 110, 116

[221] T. Hong, C. Cramer, W. Nagourney, and E.N. Fortson. Optical Clocks Based on Ultranarrow Three-Photon Resonances in Alkaline Earth Atoms. *Physical Review Letters*, 94(5), February 2005. 111

[222] A.V. Taichenachev, V.I. Yudin, C.W. Oates, C.W. Hoyt, Z.W. Barber, and L. Hollberg. Magnetic Field-Induced Spectroscopy of Forbidden Optical Transitions with Application to Lattice-Based Optical Atomic Clocks. *Physical Review Letters*, 96(8), March 2006. 111

[223] J.E. Sansonetti and G. Nave. Wavelengths , Transition Probabilities , and Energy Levels for the Spectrum of Neutral Strontium Sr I. *Journal of Physical and Chemical Reference Data*, 39(3), 2010. 113, 146, 147, 149, 151

[224] X. Baillard, A. Gauguet, S. Bize, P. Lemonde, Ph. Laurent, A. Clairon, and P. Rosenbusch. Interference-filter-stabilized external-cavity diode lasers. *Optics Communications*, 266(2):609 – 613, 2006. 118

[225] T.M. Hard. Laser Wavelength Selection and Output Coupling by a Grating. *Applied Optics*, 9(8):1825–1830, Aug 1970. 118, 120, 121

[226] N.G. Littman and H.J. Metcalf. Spectrally narrow pulsed dye laser without beam expander. *Applied Optics*, 17:2224–2227, 1978. 118

[227] S. Lecomte, E. Fretel, G. Mileti, and P. Thomann. Self-Aligned Extended-Cavity Diode Laser Stabilized by the Zeeman Effect on the Cesium D2 Line. *Applied Optics*, 39(9):1426–1429, Mar 2000. 119

[228] C.J. Hawthorn, K.P. Weber, and R.E. Scholten. Littrow configuration tunable external cavity diode laser with fixed direction output beam. *Review of Scientific Instruments*, 72(12):4477–4479, 2001. 119

[229] A. Takamizawa, G. Yonezawa, H. Kosaka, and K. Edamatsu. Littrow-type external-cavity diode laser with a triangular prism for suppression of the lateral shift of output beam. *Review of Scientific Instruments*, 77(4):046102, 2006. 119

[230] L. Levin. Mode-hop-free electro-optically tuned diode laser. *Optics Letters*, 27(4):237–239, Feb 2002. 121

[231] L. Nilse, H.J. Davies, and C.S. Adams. Synchronous Tuning of Extended Cavity Diode Lasers: The Case for an Optimum Pivot Point. *Applied Optics*, 38(3):548–553, Jan 1999. 122, 123, 124

[232] H. Loh, Y.-J. Lin, I. Teper, M. Cetina, J. Simon, J.K. Thompson, and V. Vuletić. Influence of grating parameters on the linewidths of external-cavity diode lasers. *Applied Optics*, 45(36):9191–9197, Dec 2006. 127

[233] J.G. Ziegler, N.B. Nichols, and N.Y. Rochester. Optimum Settings for Automatic Controllers. *American Society of Mechanical Engineers*, November, 1942. 131

[234] B.D. Tyreus and L.L. Luyben. Tuning PI Controllers for Integrator/Dead Time Processes. *Industrial & Engineering Chemistry Research*, 31:2625–2628, 1992. 131

[235] M. Notcutt, L.-S. Ma, Jun Ye, and J.L. Hall. Simple and compact 1-Hz laser system via an improved mounting configuration of a reference cavity. *Optics Letters*, 30(14):1815–1817, 2005. 141

[236] I.I. Sobelman. *Atomic Spectra and Radiative Transitions*. Springer, 1979. 144

[237] For example, see www-stone.ch.cam.ac.uk/wigner.html. 144

[238] T. Ido and H. Katori. Recoil-Free Spectroscopy of Neutral Sr Atoms in the Lamb-Dicke Regime. *Physical Review Letters*, 91(5):053001, Jul 2003. 147

[239] G. Jönsson, C. Levinson, A. Persson, and C.-G. Wahlström. Natural radiative lifetimes in the $^1P_1$ and $^1F_3$ sequences of Sr I. *Zeitschrift für Physik A Hadrons and Nuclei*, 316:255–258, 1984. 10.1007/BF01439897. 148

[240] D.A. Miller, L. You, J. Cooper, and A. Gallagher. Collisional energy transfer between excited-state strontium and noble-gas atoms. *Physical Review A*, 46:1303–1309, Aug 1992. 149

[241] H.J. Andrä, H.-J. Plöhn, W. Wittmann, A. Gaupp, J.O. Stoner, and M. Gaillard. Lifetimes of levels in neutral strontium (Sr I). *Journal of the Optical Society of America*, 65(12):1410–1412, Dec 1975. 149

[242] J.W. Farley and W.H. Wing. Accurate calculation of dynamic Stark shifts and depopulation rates of Rydberg energy levels induced by blackbody radiation. Hydrogen, helium, and alkali-metal atoms. *Physical Review A*, 23(5):2397–2424, May 1981. 152

[243] J.A. Sherman, N.D. Lemke, N. Hinkley, M. Pizzocaro, R.W. Fox, A.D. Ludlow, and C.W. Oates. High accuracy measure of atomic polarizability in an optical lattice clock. *ArXiv e-prints*, December 2011. 156

[244] L. Windholz and C. Neureiter. A field assembly for Stark effect investigations, allowing a precise determination of high electric field strengths. *Journal of Physics E: Scientific Instruments*, 17(3):186, 1984. 156

[245] S. Schmid, G. Thalhammer, K. Winkler, F. Lang, and J. Hecker Denschla. Long distance transport of ultracold atoms using a 1D optical lattice. *New Journal of Physics*, 8(8):159, 2006. 161

[246] J. Lodewyck, P.G. Westergaard, and P. Lemonde. Non-destructive measurement of the transition probability in a Sr optical lattice clock. *Physical Review*, 79, February 2009. 161

[247] Simon Stellmer, Meng Khoon Tey, Bo Huang, Rudolf Grimm, and Florian Schreck. Bose-Einstein Condensation of Strontium. *Physical Review Letters*, 103(20):200401, Nov 2009. 163

[248] Y. de Escobar, P. Mickelson, M. Yan, B. DeSalvo, S. Nagel, and T. Killian. Bose-Einstein Condensation of ^{84}Sr. *Physical Review Letters*, 103(20):3–6, November 2009. 163

[249] Christiane P. Koch. Perspectives for coherent optical formation of strontium molecules in their electronic ground state. *Phys. Rev. A*, 78:063411, Dec 2008. 163

[250] J. Millen. *A cold strontium Rydberg gas*. PhD thesis, Durham University, 2011. 163

[251] M.D. Swallows, G.K. Campbell, A.D. Ludlow, M.M. Boyd, J.W. Thomsen, M.J. Martin, S. Blatt, T.L. Nicholson, and Jun Ye. Precision measurement of fermionic collisions using an ^{87}Sr optical lattice clock with 1×10^{-16} inaccuracy. *Ultrasonics, Ferroelectrics and Frequency Control, IEEE Transactions on*, 57(3):574 –582, march 2010. 163

[252] M. Bishof, Y. Lin, M. D. Swallows, A. V. Gorshkov, J. Ye, and A. M. Rey. Resolved Atomic Interaction Sidebands in an Optical Clock Transition. *Physical Review Letters*, 106:250801, Jun 2011. 163

[253] E. Peik, K. Zimmermann, M. Okhapkin, and C. Tamm. Prospects for a Nuclear Optical Frequency Standard Based on THORIUM-229. In L. Maleki, editor, *Frequency Standards and Metrology*, pages 532–538, April 2009. 164

[254] S. Adamson, C. O'Carroll, and J.F. McGilp. The angular distribution of thermal molecular beams formed by single capillaries in the molecular flow regime. *Vacuum*, 38(6):463 – 467, 1988. 166

[255] P. Clausing. The flow of highly rarefied gases through tubes of arbitrary length. *The Journal of Vacuum Science and Technology*, 8:636, 1931. 166, 167, 168

[256] J.A. Giordmaine and T.C. Wang. Molecular Beam Formation by Long Parallel Tubes. *Journal of Applied Physics*, 31(3):463–471, 1960. 167, 168, 169

[257] J.M. Guevremont, S. Sheldon, and Z. Francisco. Design and characterization of collimated effusive gas beam sources: Effect of source dimension and backing pressure on total flow and beam profile. *Review of Scientific Instruments*, 71(10):3869–3881, 2000. 168, 169

[258] H.C.W. Beijerinck and N.F. Verster. Velocity distribution and angular distribution of molecular beams from multichannel arrays. *Journal of Applied Physics*, 46(5):2083–2091, 1975. 168, 170

[259] G.R. Hanes. Multiple Tube Collimator for Gas Beams. *Journal of Applied Physics*, 31(12):2171–2175, 1960. 169

[260] D.R. Olander, R.H. Jones, and W.J. Siekhaus. Molecular Beam Sources Fabricated from Multichannel Arrays. IV. Speed Distribution in the Centerline Beam. *Journal of Applied Physics*, 41(11):4388–4391, 1970. 170

[261] G.C. Angel and R.A. Giles. The velocity distribution of atoms issuing from a multichannel glass capillary array and its implication on the measurement of atomic beam scattering cross sections. *Journal of Physics B: Atomic and Molecular Physics*, 5(1):80, 1972. 170